STRONGLY LENSED SUPERNOVAE: A POWERFUL PROBE OF ASTROPHYSICS AND COSMOLOGY

MAX FOXLEY-MARRABLE

A thesis submitted in partial fulfilment of the requirements for the award of the degree of Doctor of Philosophy

Institute of Cosmology and Gravitation
Faculty of Technology
University of Portsmouth

December 2020

Max Foxley-Marrable: *Strongly Lensed Supernovae: A Powerful Probe of Astrophysics and Cosmology*. A thesis submitted in partial fulfilment of the requirements for the award of the degree of Doctor of Philosophy, © December 2020

SUPERVISORS:

Dr. Thomas Collett

Prof. Bob Nichol

Prof. David Bacon

"The best scientific minds of the system were staring at the data with their jaws slack, and the reason no one was panicking yet was that no one could agree on what they should panic about."

— James S.A. Corey, Caliban's War

ABSTRACT

Strongly lensed supernovae (gLSNe) are a remarkable phenomenon capable of cutting-edge cosmological and astrophysical science. The time delays between the multiple lensed images are a direct and independent probe of the Hubble constant (H_0). As a standardisable candle, Type Ia gLSNe promise to measure H_0 with tightly constrained systematics. This is vital to resolve the ongoing tensions between indirect early-Universe and direct late-Universe measurements of H_0, potentially signalling physics beyond the Λ cold dark matter (ΛCDM) model of cosmology. A 1% measurement of H_0 acquired through gLSNe Ia provides a stringent test of ΛCDM. Additionally, gLSNe discovered before the reappearance of the supernova (SN) explosion in the later lensed images provides a unique window into observing the earliest moments of SNe. Such early observations are critical in constraining the progenitor populations of SNe.

This thesis investigates the practicality of using gLSNe to make the above observations. I begin with an introduction to the Hubble constant, supernovae and strong lensing to provide the reader with the context for my research. I then detail the research from Foxley-Marrable et al. (2018), where we discuss the usefulness of gLSNe Ia as a cosmological probe, given the obstacle of stellar microlensing. We show that by considering a sample $\sim$ 140 gLSNe Ia with asymmetric image configurations, we can measure H_0 with systematics constrained at the 0.5% level. I then present research from Foxley-Marrable et al. (2020), where we discuss whether gLSNe can be used to observe the earliest moments of SNe. We predict that Legacy Survey of Space and Time (LSST) will find $\sim$ 110 candidate systems per year, with $11.7^{+29.8}_{-9.3}$ days between discovery and the SN reappearance. We argue that whilst this will be a challenging undertaking, with significant investment from the astronomical community, deep observations of gLSNe are capable constraining the progenitor populations of SNe. This thesis demonstratively proves the future power of gLSNe when applied to both astrophysics and cosmology.

PUBLICATIONS

Chapters 4 and 5 have appeared previously in the following publications:

Foxley-Marrable, Max, Thomas E. Collett, Chris Frohmaier, Daniel A. Goldstein, Daniel Kasen, Elizabeth Swann, and David Bacon (May 2020). "Observing the earliest moments of supernovae using strong gravitational lenses." In: *MNRAS*. DOI: 10.1093/mnras/staa1289. arXiv: 2003.14340 [astro-ph.HE].

Foxley-Marrable, Max, Thomas E. Collett, Georgios Vernardos, Daniel A. Goldstein, and David Bacon (Aug. 2018). "The impact of microlensing on the standardization of strongly lensed Type Ia supernovae." In: *Monthly Notices of the RAS* 478.4, pp. 5081–5090. DOI: 10.1093/mnras/sty1346. arXiv: 1802.07738 [astro-ph.CO].

ACKNOWLEDGEMENTS

I am forever indebted to my first supervisor Thomas Collett. Your guidance and expertise has allowed me to achieve what I frequently believed to be an insurmountable task. My frequent struggles with mental health and self-confidence have not made this process an easy road, however you remained patient and supportive throughout. Considering I was your first student, the way you have adapted to provide a level of supervision expected from those beyond your years of experience, is nothing short of commendable. I am so proud of what we have achieved over the years.

I also want to extend my heartfelt thanks to David Bacon. You have been a constant source of emotional guidance and have always made time out of your busy schedule to aid me in my times of need. Even during moments of utter despair, meetings with you always left me hopeful and optimistic about the future.

I want to express sincere gratitude towards my collaborators: Daniel Goldstein, Chris Frohmaier, Georgios Vernardos, Daniel Kasen and Elizabeth Swann, whose key contributions and thoughtful insights made the published works presented a reality. I also want to thank my colleagues at the Institute of Cosmology and Gravitation and all of my friends, both in and outside of academia. I want to extend a special mention to my UK Tech-Fest and ArcTanGent family. Getting to hang out with you guys every year, nerding out to incredible music and laughing until I can't breathe - I truly feel myself and at home.

To my loved ones, in particular my Mum and Dad, whose support over the past ~ 27 years have enabled me to pursue my passion and without I would not be here today... quite literally. To my partner Alexandra, I cannot even begin to express how much your love and words of encouragement enabled me to keep on going. Even during my darkest moments you remained a rock and kept me grounded. You have enriched my life beyond words and I look forward to the day when there isn't an ocean separating us. I'm extremely lucky to be with someone as wonderful as you.

Simply put, without all your support, this thesis would not exist. I dedicate this work to all of you.

CONTENTS

LIST OF FIGURES

LIST OF TABLES

ACRONYMS

AGB	Asymptotic Giant Branch
AGN	Active Galactic Nucleus
BAO	Baryon Acoustic Oscillations
BBN	Big Bang Nucleosynthesis
BOSS	Baryon Oscillation Spectroscopic Survey
CC	Core-Collapse
CD	Core-Degenerate
CDM	Cold Dark Matter
CE	Common Envelope
CMB	Cosmic Microwave Background
C-O	Carbon-Oxygen
DD	Double-Degenerate
DTD	Delay Time Distribution
DES	Dark Energy Survey
DSFG	Dusty Star-Forming Galaxy
gLSN	Gravitationally Lensed Supernova
GPU	Graphics Processing Unit
GR	General Relativity
GW	Gravitational Wave
HoLiCOW	H_0 Lenses in COSMOGRAIL's Wellspring

HST	Hubble Space Telescope
H-R	Hertzsprung–Russell
IMF	Initial Mass Function
iPTF	Intermediate Palomar Transient Factory
ΛCDM	Λ Cold Dark Matter
LIGO	Laser Interferometer Gravitational-Wave Observatory
LMC	Large Magellanic Cloud
LSST	Legacy Survey of Space and Time
MACHO	Massive Compact Halo Object
MS	Main Sequence
O-Ne	Oxygen-Neon
PDF	Probability Density Function
P-L	Period-Luminosity
RG	Red Giant
RGB	Red Giant Branch
SIS	Singular Isothermal Sphere
SD	Single-Degenerate
SN	Supernova
SZ	Sunyaev–Zel'dovich
TRGB	Tip of the Red Giant Branch
VLBI	Very Long Baseline Interferometry
WD	White Dwarf
ZTF	Zwicky Transient Facility

NOMENCLATURE

M_{Ch} Chandrasekhar Mass

θ_{Ein} Einstein Radius

H_o Hubble Constant

Part I

INTRODUCTION

"In the beginning there was nothing, which exploded."

— Terry Pratchett, Lords and Ladies

1

THE HUBBLE CONSTANT

1.1 A BRIEF HISTORY

The discovery of the relationship between an object's distance and recession velocity, known as the Hubble Law (Hubble, 1929), arguably set the foundations for modern day cosmology. This was considered first piece of direct observational proof that the Universe was expanding. Whilst this landmark discovery is often solely credited to Edwin Hubble, it can be argued that this work was built on many years of previous research and hence the proper accreditation is a source of significant controversy (Way, 2013). This section will best attempt to summarise the most important historical contributions, however for extensive historical coverage see Rowan-Robinson (1985).

Slipher (1913, 1915, 1917) measured radial velocities of multiple spiral "nebulae" and discovered that the large majority of galaxies were receding from Earth. Einstein (1917) and de Sitter (1917) suggested that the Universe could be described by a set of relativistic field equations proposed by Einstein (1915). Friedmann (1922) presented solutions of the field equations from Einstein (1915), showing that the Universe was meant to be expanding, as opposed to the then favoured static model of the Universe. Lemaître (1927) later independently derived similar solutions and presented the first derivations of the 'Hubble' law and the first predictions of the 'Hubble' constant (H_0). Hubble (1929) (with Milton L. Humason) confirmed these findings by combining Cepheid distance measurements with the (uncredited) Doppler-shift observations of Slipher (1915, 1917). They found that objects located further away from Earth were receding at higher velocities than closer objects. By plotting the distances of these objects against their velocities (see Figure 1), they noticed a linear relationship between the two quantities. The local rate of expansion was determined by evaluating the slope of the 'Hubble Diagram'. They evaluated $H_0 = 500$ km s^{-1} Mpc^{-1}, a factor of ~ 7 discrepant from modern day calculations. This was due to incorrect zero-point calibrations of the standard candles used at the time.

Since then, further measurements have driven down the value of H_0, settling around 70 km s^{-1} Mpc^{-1} (see Figure 2). However, as the precision on measurements have im-

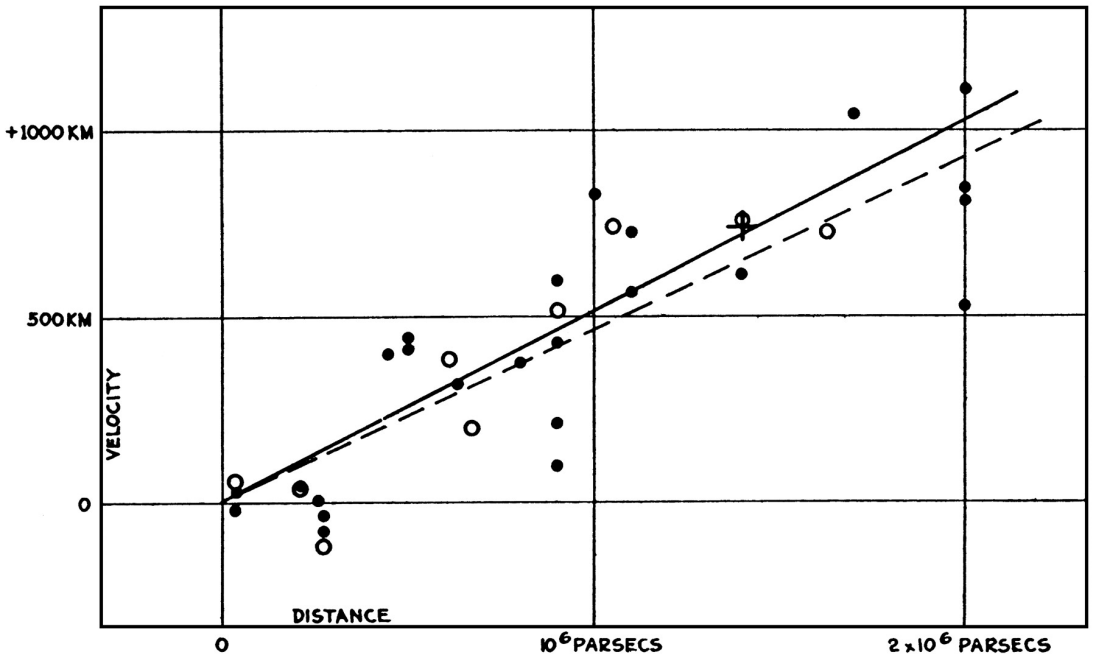

Figure 1: The first 'Hubble Diagram' used in the original determination of H_0 by Hubble (1929). Plotted is the velocity-distance relation for extra-galactic 'nebulae', taking into account the motion of the Earth about the Sun. The black circles and solid best-fit line are from taking into account each individual nebula. The circles and dashed line come from combining the nebulae into groups. The cross represents the mean for 22 nebulae whose distances could not be measured individually. In this case, H_0 is determined from the slope of the best-fit lines.

proved over time, tensions have begun to arise in H_0 between indirect early-Universe and direct late-Universe measurements (see Section 1.2).

1.2 TENSIONS IN THE HUBBLE CONSTANT

The Λ cold dark matter (ΛCDM) model is the standard model of cosmology today and is favoured due to its robustness to observations (Planck Collaboration et al., 2018). ΛCDM is a six-parameter model that describes a universe containing the following (see Figure 3 for a timeline):

1. ~ 70% dark energy, associated with the cosmological constant Λ. An unknown form of energy that seemingly exerts a negative pressure on the Universe, providing an explanation for the accelerated expansion of the Universe (see Huterer and Shafer, 2018, for a recent review).

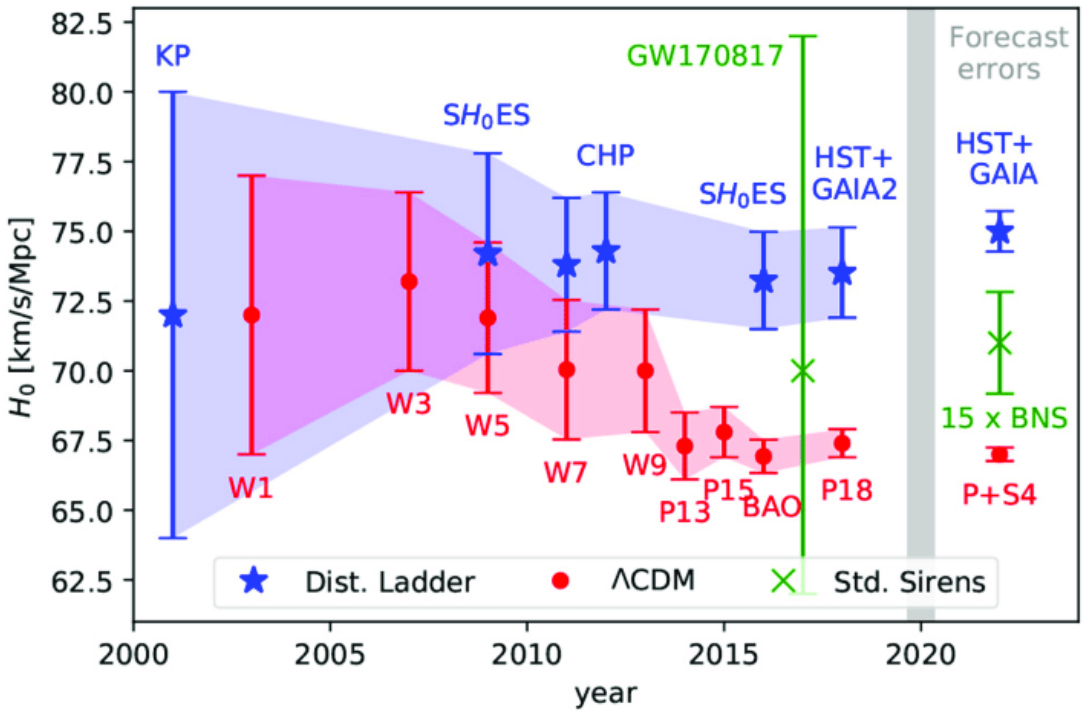

Figure 2: History of modern H_0 measurements from 2000 - 2018. Notice tensions begin to arise between the distance ladder and ΛCDM around 2013. Figure taken from Ezquiaga and Zumalacárregui (2018), originally adapted from Beaton et al. (2016) and Freedman (2017). Note: figure has been edited to correct 'CPH' to 'CHP'.

2. ~ 25% cold dark matter (CDM). Non-baryonic matter that interacts very weakly with ordinary matter, primarily through the force of gravity. Its existence has not been directly observed, but inferred indirectly through observations that cannot be explained with ordinary matter alone (see Peter, 2012, for a review).

3. ~ 5% ordinary/baryonic matter.

The validity of ΛCDM is however being called into question with the ever increasing tensions between early-Universe and late-Universe measurements of H_0. With the improving precision in H_0 measurements over time, the value of H_0 between the local distance ladder (SH_0ES) and the CMB has been consistently diverging. The first clear hint of tensions began to arise in ~ 2013 (Riess et al., 2011; Freedman et al., 2012; Bennett et al., 2013; Hinshaw et al., 2013), especially when the Planck 2013 result (Planck Collaboration et al., 2014) yielded an unexpectedly low value of $H_0 = 67.3 \pm 1.2$ km s^{-1} Mpc^{-1}. Subsequent measurements from Planck Collaboration et al. (2016, 2018) and measurements from the analyses of baryon acoustic

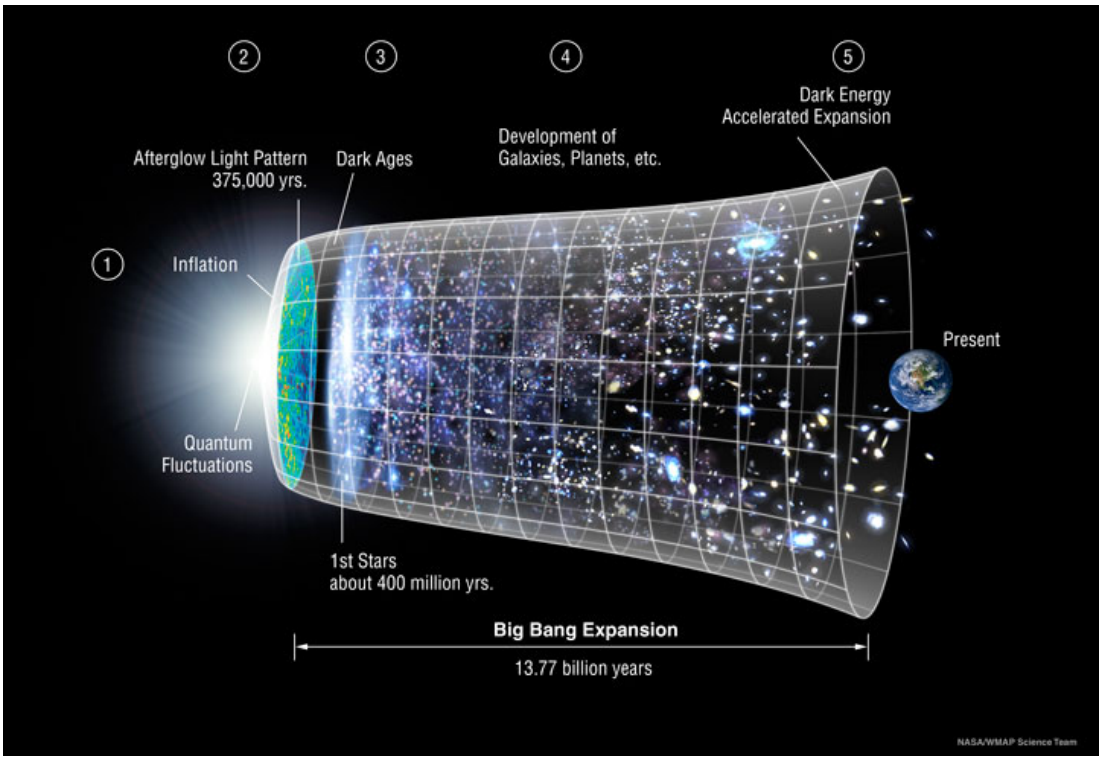

Figure 3: Timeline of the ΛCDM Universe. 1) The Universe begins as a hot, dense and opaque plasma, containing baryons and photons coupled together. Density fluctuations in the plasma are believed to originate from initial quantum fluctuations seeded into the structure of the Universe during a period of rapid expansion called inflation (see Tsujikawa, 2003; Baumann, 2009, for reviews). Matter begins to in-fall towards overdensities and becomes rebounded by subsequent increases in radiation pressure. The resulting spherical sound waves propagate outwards (Hu and White, 2004). 2) The epoch of recombination. The Universe cools enough such that baryons and photons decouple. Photons are able to free-stream. The Universe becomes transparent. The acoustic waves are no longer radiation-driven and propagation stops. The resulting overdensities become ingrained into the large scale structure of the Universe (Eisenstein and Hu, 1998). 3) A period known as the 'Dark Ages' where the Universe contains no sources of light beyond residual radiation from the CMB. CDM collapses into regions of overdensity. Baryonic matter collapses into CDM halos and form the first stars, ending the Dark Ages and beginning the 'Cosmic Dawn' (Miralda-Escudé, 2003). 4) The large scale structure of the Universe continues to evolve under the influence of gravity. Matter substructures collapse further to form the first galaxies (Bromm and Yoshida, 2011). 5) The negative pressure from Dark Energy dominates over gravitational forces. The Universe begins to expand at an accelerated rate (Riess et al., 1998; Perlmutter et al., 1999). *Image Credit*: Original by NASA WMAP Science Team. Adapted by NASA LAMBDA Archive Team.

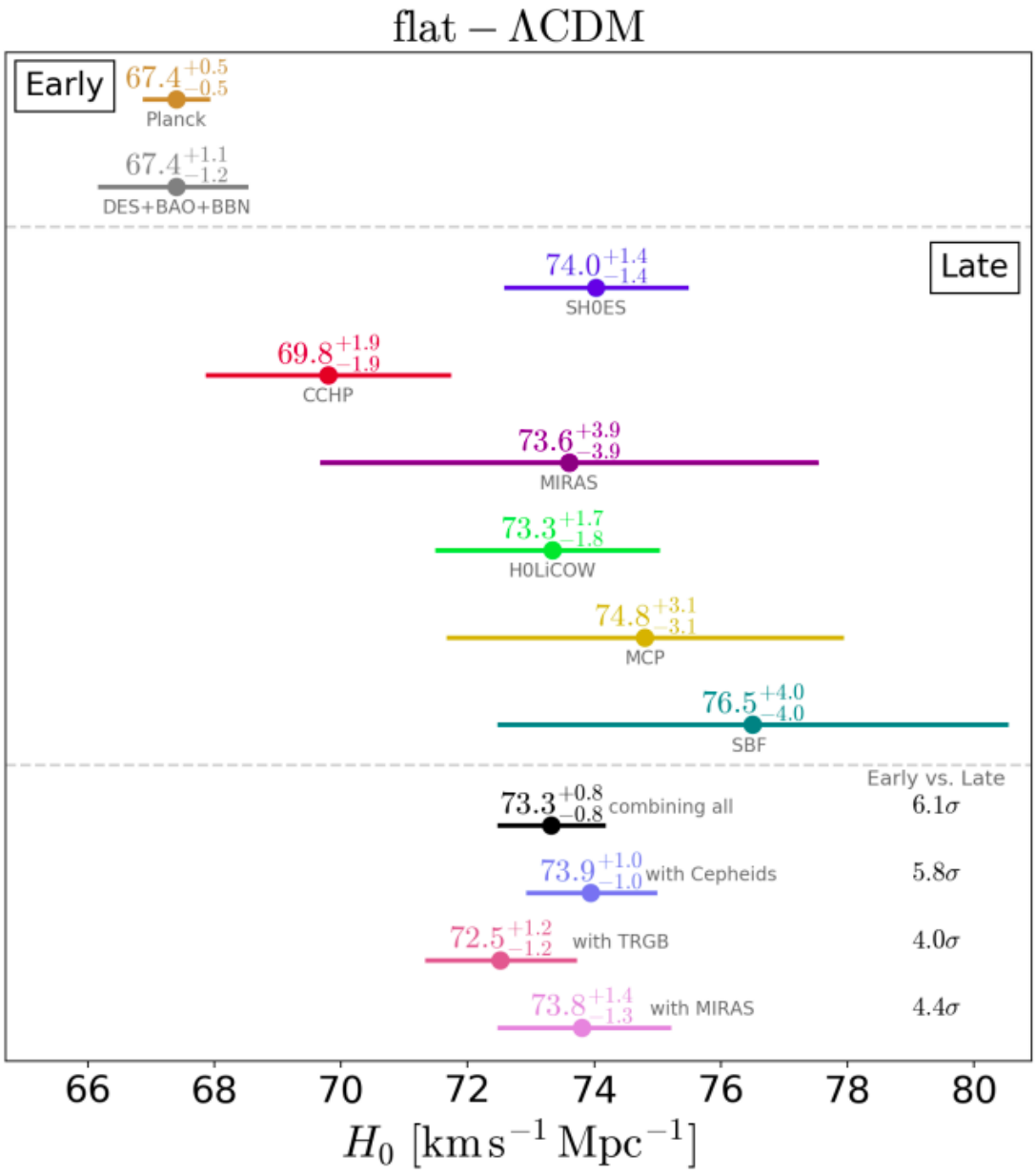

Figure 4: Comparison of H_0 measurements highlighting the tensions between early (top panel) and late (middle panel) Universe, as of September 2019. The bottom panel gives combinations of late-Universe measurements and the resulting 4-6σ tensions with Planck Collaboration et al. (2018) and Abbott et al. (2018). Figure taken from Verde, Treu, and Riess (2019).

oscillations (BAO) (e.g. Alam et al., 2017; Abbott et al., 2018) have remained consistent with Planck Collaboration et al. (2014). Subsequent SH_0ES measurements (Riess et al., 2016, 2018; Riess et al., 2019) and independent local probes of H_0 (e.g. Wong et al., 2019; Pesce et al., 2020) have remained consistent with Riess et al. (2011). At the time of writing, early-Universe (Planck Collaboration et al., 2018; Abbott et al., 2018) and late-Universe (e.g. Riess et al., 2019; Wong et al., 2019; Pesce et al., 2020) measurements of H_0 are in 4-6σ tension, as highlighted in Figure 4 (also refer to Verde, Treu, and Riess 2019).

For early-Universe estimates, Planck Collaboration et al. (2018) derives H_0 from measurements of the cosmic microwave background (CMB) and Abbott et al. (2018) derives H_0 by combining data from Dark Energy Survey (DES) Year 1 clustering/weak lensing with BAO and big bang nucleosynthesis (BBN). For late-Universe estimates, Riess et al. (2019) measures H_0 from Type Ia supernovae (SNe) calibrated with Cepheid variable stars, Wong et al. (2019) uses time delays from strongly lensed quasars and Pesce et al. (2020) uses maser distances to measure H_0. In other words, early-Universe measurements derive H_0 indirectly assuming ΛCDM, whilst late-Universe measurements probe H_0 directly. In essence, these measurements are obtained at two different distance scales at the opposite ends of the expanding observable Universe. Whilst this tension could be attributed to unaccounted systematics, another plausible explanation is the presence of new physics beyond ΛCDM. Hence, the need for *independent* measurements of H_0 is greater than ever in order to test concordance cosmology.

1.3 THEORY

From Einstein's field equations of general relativity, Friedmann derived two solutions explaining the dynamics of the Universe, known as the Friedmann equations:

$$\left(\frac{\dot{a}}{a}\right)^2 = \frac{8\pi G}{3}\rho - \frac{kc^2}{a^2} + \frac{\Lambda c^2}{3}, \tag{1}$$

$$\frac{\ddot{a}}{a} = -\frac{4\pi G}{3}\left(\rho + \frac{3p}{c^2}\right) + \frac{\Lambda c^2}{3}, \tag{2}$$

where $a = a(t)$ is the scale factor parameterising the relative expansion of the Universe, G is Newton's gravitational constant, c is the speed of light and Λ is the cosmological constant. ρ and p represent the total density and pressure of the Universe,

respectively. k = -1, 0 or 1 is a curvature term describing an open, flat or closed Universe, respectively. We define the Hubble Parameter $H(t)$ as:

$$H(t) \equiv \frac{\dot{a}(t)}{a(t)}. \tag{3}$$

From Equation 1 if we assume a spatially flat (k = 0) Universe with no cosmological constant (Λ = 0), then the Universe will have a specific density, known as the critical density:

$$\rho_c \equiv \frac{3H^2}{8\pi G}. \tag{4}$$

We then define the density parameter Ω_i as the ratio of the density components with the critical density:

$$\Omega_i \equiv \frac{\rho_i}{\rho_c} = \frac{8\pi G}{3H^2}\rho_i. \tag{5}$$

It is more useful to see how the first Friedmann equation relates to the the present day density parameters ($\Omega_{i,0} = \rho_{c,0}/\rho_{i,0}$) and their evolution with redshift. The density component ρ_i is related to the present day density $\rho_{i,0}$ (hence $\Omega_{i,0}$) by:

$$\rho_i = \frac{\rho_{i,0}}{a^\alpha} = \rho_{i,0}(1+z)^\alpha = \rho_{c,0}\Omega_{i,0}(1+z)^\alpha, \tag{6}$$

where for a radiation dominated Universe α = 4 and for matter-dominated Universe α = 3. Hence, for a Universe that contains radiation, matter and a cosmological constant, Equation 1 can be re-written as such:

$$\begin{aligned} H^2(t) &= \frac{8\pi G}{3}[\rho_r + \rho_m] - \frac{kc^2}{a^2} + \frac{\Lambda c^2}{3} \\ &= \frac{8\pi G}{3}\rho_{c,0}\left[\Omega_{r,0}(1+z)^4 + \Omega_{m,0}(1+z)^3\right] - \frac{kc^2}{a^2} + \frac{\Lambda c^2}{3}. \end{aligned} \tag{7}$$

From general relativity we define the density parameters for both the cosmological constant and curvature:

$$\Omega_\Lambda \equiv \frac{\Lambda c^2}{3H^2}\ ;\ \Omega_k \equiv -\frac{kc^2}{H^2}. \tag{8}$$

The Hubble constant is simply the Hubble parameter taken at present day. Hence, by rearranging Equation 4 at present day:

$$H_0 \equiv \frac{8\pi G}{3}\rho_{c,0}. \tag{9}$$

Hence, by substituting these definitions at present day into Equation 7 and rearranging, we obtain the redshift dependent Hubble Parameter, related to the Hubble constant H_0:

$$H(z) = H_0\sqrt{\Omega_{r,0}(1+z)^4 + \Omega_{m,0}(1+z)^3 + \Omega_{k,0}(1+z)^2 + \Omega_{\Lambda,0}}. \tag{10}$$

1.3.1 *Measuring Distances*

Hubble's law states that the recession velocity v of an object evolves with distance d from the observer via the following relationship:

$$v = H(z)d. \tag{11}$$

At low redshift, this relationship is established to be linear i.e. $v = H(z \approx 0)d \approx H_0 d$ (also refer to Figures 1 and 10). Since H_0 has units of inverse time (km s^{-1} Mpc^{-1}), we can therefore define the Hubble time t_H and roughly estimate the age of the Universe:

$$t_H \equiv \frac{1}{H_0}. \tag{12}$$

We can estimate the distance to the edge of the observable Universe by defining the Hubble distance D_H:

$$D_H \equiv \frac{c}{H_0}. \tag{13}$$

The co-moving distance D_C between an observer and a distant object at redshift z in an expanding universe is calculated by integrating along the line of sight:

$$D_C = D_H \int_0^z \frac{dz'}{E(z')}, \tag{14}$$

where $E(z) \equiv H(z)/H_0$ is the dimensionless Hubble parameter. Assuming a spatially flat Universe, the angular diameter distance D_A is given by the comparison of an object's physical size r to its angular size θ on the sky:

$$D_A \equiv \frac{r}{\theta} = \frac{D_C}{1+z}. \tag{15}$$

We can measure the luminosity distance D_L of an object by comparing its measured flux F with its intrinsic luminosity L:

$$D_L \equiv \sqrt{\frac{L}{4\pi F}} = (1+z)\, D_C. \tag{16}$$

The luminosity distance is related to the angular diameter distance via the equation:

$$D_L = (1+z)^2\, D_A. \tag{17}$$

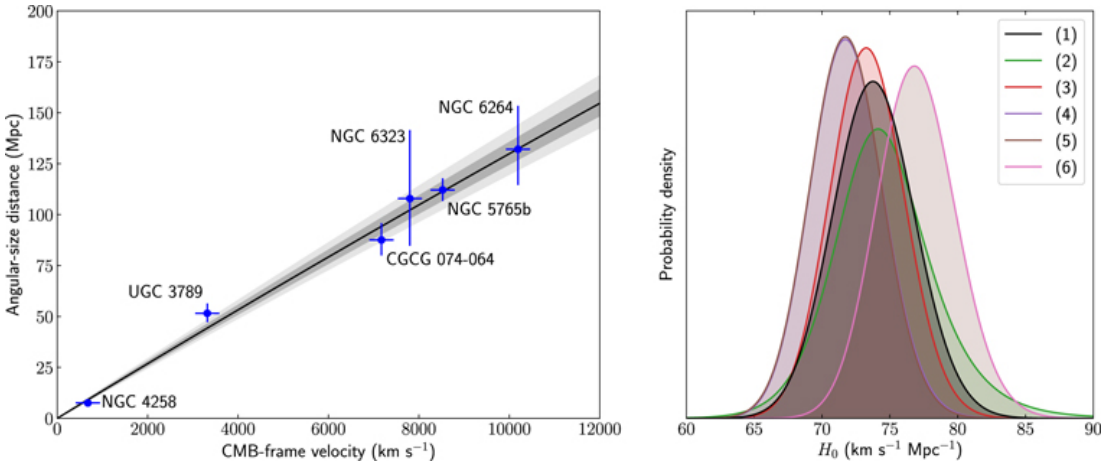

Figure 5: *Left*: Hubble diagram using 6 systems from the Megamaser Cosmology Project plotted with 1σ uncertainties in distance and 250 km s^{-1} uncertainties in peculiar motions. The black line shows the best-fit with the shaded regions showing the 1σ and 2σ confidence regions. *Right:* H_0 posterior distributions for six different treatments of peculiar velocities (see Table 2 of Pesce et al. 2020 for more details). Figure taken from Pesce et al. (2020).

1.4 ONE-STEP DISTANCE METHODS

In this section I will summarise a few key 'one-step' methods of measuring H_0. These methods rely on well understood objects residing in the Hubble flow, i.e. their distances/redshifts can be tightly measured and are far enough away ($z \gtrsim 0.01$ or $d \gtrsim 50$ Mpc) such that cosmic expansion dominates over peculiar motion. Therefore, they can be used to measure H_0 without any need for external calibration, e.g. a cosmic distance ladder (see Section 1.5). For further discussions on one-step distance methods see Freedman and Madore (2010) and Jackson (2015), and references within.

1.4.1 *Megamasers*

Megamasers are sources of stimulated spectral line emission with typical luminosities of 10^3 $L_\odot$. They occur when large clumps of molecular gas are excited by nearby sources of photons, emitting additional photons at the same energy as the incident photons. Known megamasers are typically composed of hydroxyl (OH), water (H_20), formaldehyde (H_2CO) and methine (CH). Water megamasers are useful for cosmology because they are typically located close to the vicinity (within ~ 0.1 pc) of super-

massive black holes in the centre of spiral galaxies with active galactic nuclei (AGN), emitting narrow linewidths around 22 GHz (Herrnstein et al., 1999). They can therefore be observed at milliarcsecond resolution using very long baseline interferometry (VLBI) techniques to gain good understanding of their spatial and kinematic profiles. Assuming Keplerian motion, we can determine the velocity, radius and angular separation from the centre of the AGN for each clump. With this information we can calculate the angular diameter distance from the centre of the AGN to the observer. The black hole mass can also be obtained as a result.

This method is dependent on the sample of water megamasers being observed relatively edge-on, otherwise observing Doppler shifting in the orbiting clumps required for kinematic profiling is impossible. Also modelling the morphology of the host spiral galaxy is non-trivial, requiring up to eight parameters (e.g. Humphreys et al., 2013; Reid, Pesce, and Riess, 2019) to describe the properties and warping of the disk, which are potentially vulnerable to systematics. At the time of writing, from the combined distance measurements of six water megamasers: UGC 3789, NGC 6264, NGC 6323, NGC 5765b, CGCG 074-064 and NGC 4258, the Megamaser Cosmology Project have measured $H_0 = 73.9 \pm 3.0$ km s^{-1} Mpc^{-1}, consistent with other local Universe measures of H_0 (Pesce et al., 2020, also see Figure 5).

1.4.2 *Strong Gravitational Lensing*

Strong gravitational lensing is a direct consequence of Einstein's theory of general relativity. Large objects (e.g. galaxies) can distort spacetime enough such that rays of light interacting with the gravitational potential of the lens will have their paths altered. Therefore background objects situated along the line of sight to a large foreground object (lens) will appear distorted to the observer. If the background and foreground objects are well aligned, multiple images of the background source will form. For more detailed discussion of the physics and associated systematics, see Chapter 3.

Gravitational lenses are very sensitive to the ratio of distances between the source, lens and observer and are therefore sensitive to H_0 (Refsdal, 1964). We can probe these distance ratios through time delay cosmography. For each strongly lensed image, the light travel time is affected by geometrical changes in the path length due to the

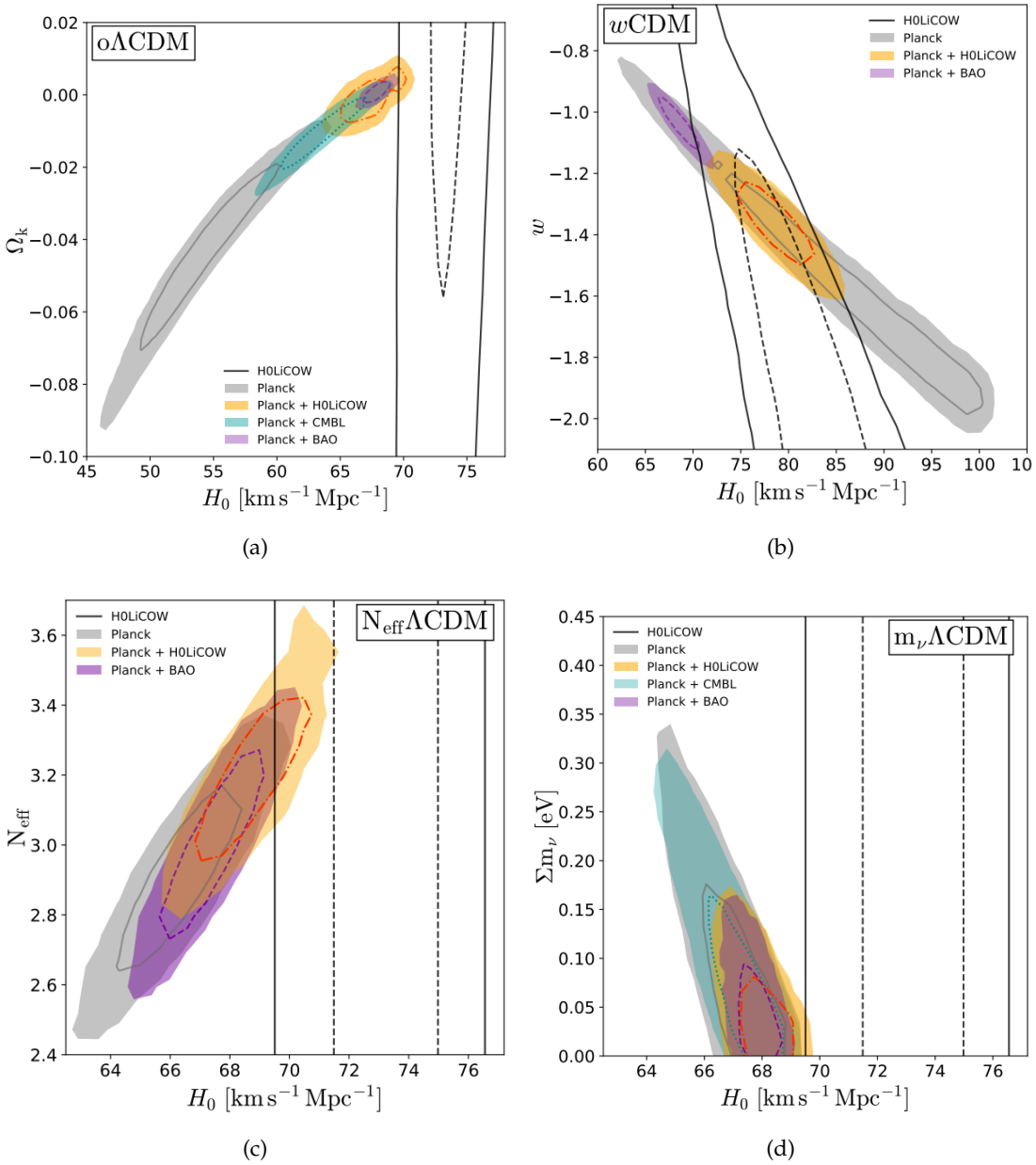

Figure 6: Cosmological constraints on H_0 across a range of possible cosmologies, including variations on: a) the curvature Ω_k, b) the dark energy equation of state w, c) the effective number of relativistic particle species N_{eff} and d) the total mass of neutrinos Σm_ν. Note the relative insensitivity of H_0 to the choice of cosmology when measured with strong lens time delays (HoLiCOW), compared to other cosmological probes. Figures from Wong et al. (2019).

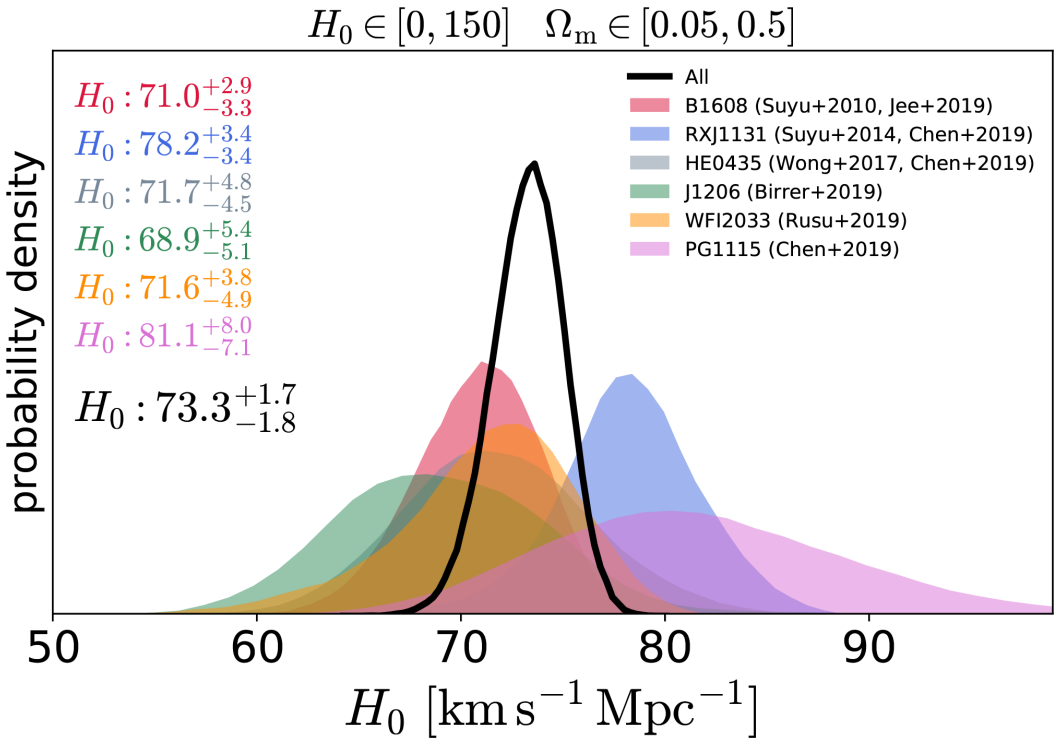

Figure 7: Probability density functions for six HoLiCOW lenses assuming a flat ΛCDM cosmology with uniform priors. The given value of H_0 for each lens comes from the median of their respective PDF, with errors given by the 16th and 84th percentiles. The combined measurement is shown in black. Figure taken from Wong et al. (2019).

Lens Name	H_0 (km s^{-1} Mpc^{-1})	Reference
B1608+656	$71.0^{+2.9}_{-3.3}$	Suyu et al. (2010) and Jee et al. (2019)
RXJ1131-1231	$78.2^{+3.4}_{-3.4}$	Suyu et al. (2014) and Chen et al. (2019)
HE 0435-1223	$71.7^{+4.8}_{-4.5}$	Wong et al. (2017) and Chen et al. (2019)
SDSS 1206+4332	$68.9^{+5.4}_{-5.1}$	Birrer et al. (2019)
WFI2033-4723	$71.6^{+3.8}_{-4.9}$	Rusu et al. (2019b)
PG 1115+080	$81.1^{+8.0}_{-7.1}$	Chen et al. (2019)
Combined	$73.3^{+1.7}_{-1.8}$	Wong et al. (2019)

Table 1: Table of H_0 measurements from the HoLiCOW collaboration using six strongly lensed quasars.

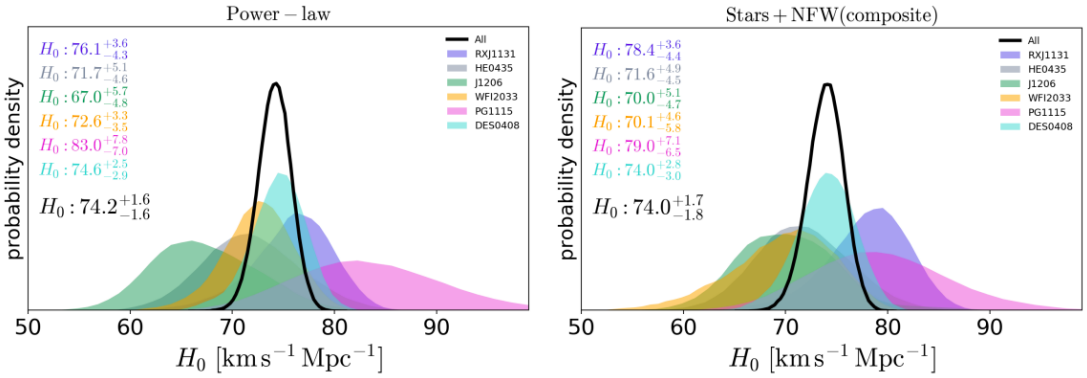

Figure 8: Marginalised posterior distributions on H_0 through reanalyses of seven lensed quasars using power-law mass models (left) and composite mass models (right). The distributions assume a flat ΛCDM cosmology with uniform priors. The given value of H_0 for each lens comes from the median of their respective PDF, with errors given by the 16th and 84th percentiles. The combined measurement is shown in black. Figure taken from Millon et al. (2019).

curvature of spacetime around the lens, as well as additional time dilation effects from the gravitational potential of the lens. As a result each lensed image shows the source at a different point in time. If the source was to vary in brightness, the brightness of the lensed images will vary asynchronously relative to each other. In principle, this time delay can be measured by marking down the appearance of an intrinsic source variation in each image and calculating the relative time difference (see Section 3.5). The time delay between two images Δt_{ij} is inversely proportional to H_0 and is completely independent of the cosmological distance ladder. Another major strength of strong lensing time delays compared to other cosmological probes is that the measured value of H_0 is relatively insensitive to the choice of cosmology (see Figure 6).

The H_0 Lenses in COSMOGRAIL's Wellspring (HoLiCOW) collaboration measured $H_0 = 73.3^{+1.7}_{-1.8}$ km s^{-1} Mpc^{-1} to a 2.4% precision using time delays from six strongly lensed quasars (see Table 1 for a list of measurements with references). This measurement is in 3.1σ tension with Planck Collaboration et al. (2018) and Abbott et al. (2018). The combined measurement with Riess et al. (2019) $H_0 = 73.38^{+1.1}_{-1.1}$ km s^{-1} Mpc^{-1} is in 5.3σ tension with Planck and BAO (Wong et al., 2019). Shajib et al. (2020) measured $H_0 = 74.2^{+2.7}_{-3.0}$ km s^{-1} Mpc^{-1} at 3.8% precision through time delay analysis of the strongly lensed quasar DES J0408-5354, providing the most precise constraint

on H_0 with single lens system. A recent collaboration to emerge is TDCOSMO, a merger of the COSMOGRAIL, HoLiCOW, STRIDES and SHARP collaborations (Millon et al., 2019). Through a reanalysis of the six HoLiCOW lenses (Table 1) and the single STRIDES lens DES J0408-5354, Millon et al. (2019) produced a combined measurement of $H_0 = 74.0^{+1.7}_{-1.8}$ km s^{-1} Mpc^{-1} using simple power-law mass models and $H_0 = 74.2^{+1.6}_{-1.6}$ km s^{-1} Mpc^{-1} using more complex composite lens models (see Figure 8).

1.4.3 *Gravitational Waves*

The acceleration of mass will create a disturbance in the fabric of space-time that propagates at the speed of light, known as a gravitational wave (GW). Events capable of producing a detectable GW signal include the coalescence of massive compact binary objects such as neutron stars and black holes. The first detection of GWs was performed by the Laser Interferometer Gravitational-Wave Observatory (LIGO) and Virgo collaborations in 2016, who detected a GW signal originating from the merger of two $\gtrsim 25$ $M_\odot$ binary black holes (Abbott et al., 2016; Abbott et al., 2016). At the time of writing about 11 GW detections have been reported in total. GW events from the coalescence of massive compact binary objects will also produce a counterpart electromagnetic emission, known as a 'kilonova', detectable through follow up observations (e.g. see Troja et al., 2018).

The physics behind the in-spiralling of compact objects is well understood and the resulting GW signal allows direct constraints on the luminosity distance (since amplitude $h \propto D_L^{-1}$). GWs can therefore be referred to as 'standard sirens' due to the aural nature of these signals (Schutz, 1986; Holz and Hughes, 2005; MacLeod and Hogan, 2008; Nissanke et al., 2010; Sathyaprakash, Schutz, and Van Den Broeck, 2010). Unfortunately, these signals alone cannot be used to measure H_0 as they lend no constraints on the recession velocity. However, combined with redshift measurements (and potentially improved constraints on the luminosity distance) from the electromagnetic counterpart and its host, these 'multi messenger' systems can be used to place constraints on H_0 completely independently of the cosmic distance ladder and early-Universe physics. However, the constraining power of GWs on H_0 is limited by the small sample size. A binary neutron star merger GW170817, alongside

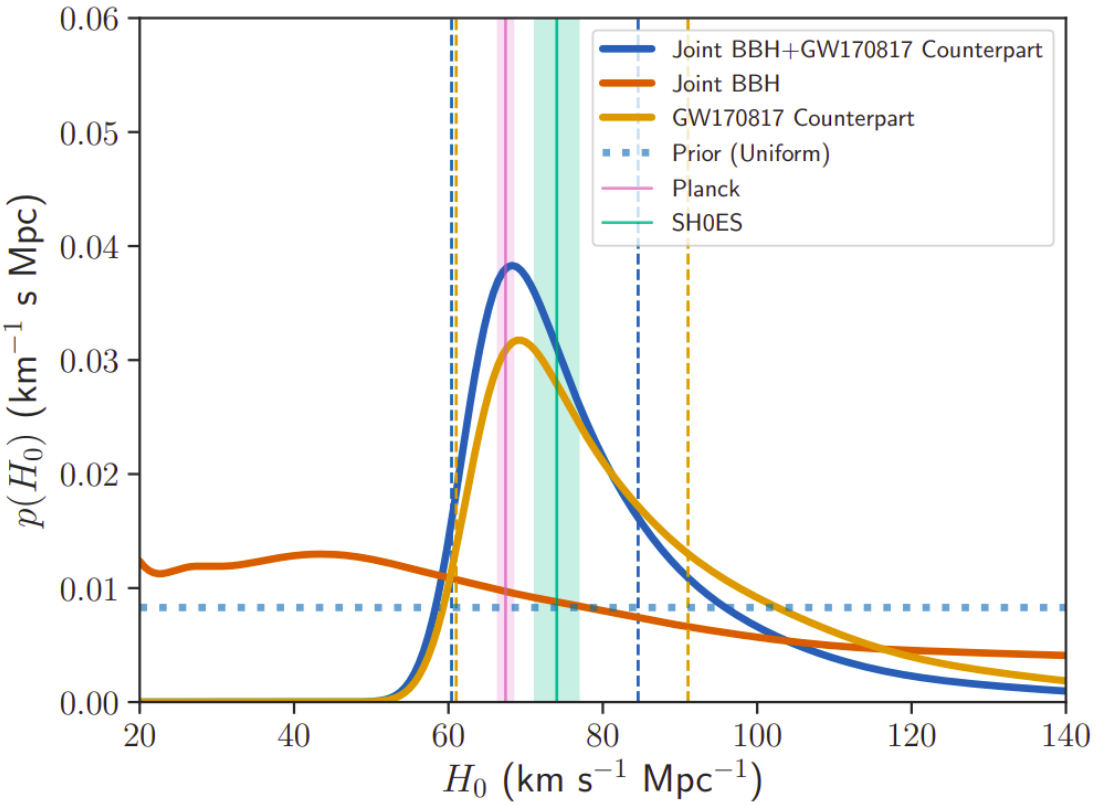

Figure 9: Constraints on H_0 from the first two observing runs by the LIGO and Virgo collaborations. Shown are the constraints from GW170817 (in orange) from Abbott et al. (2017) and the joint constraint from five binary black hole mergers (in dark orange). The final joint constraint between the two is given in dark blue. For comparison, H_0 measurements from both Planck Collaboration et al. (2018) and Riess et al. (2019) are shown. Figure from The LIGO Scientific Collaboration et al. (2019).

its electromagnetic counterpart associated with host galaxy NGC4993, was used to measure $H_0 = 70.0^{+12}_{-8}$ km s^{-1} Mpc^{-1} (Abbott et al., 2017). At the time of writing, the latest standard siren result measures $H_0 = 68^{+14}_{-7}$ km s^{-1} Mpc^{-1} , using constraints from GW170817 and five binary black hole mergers (see Figure 9), taken from the first two observing runs by the LIGO and Virgo collaborations (The LIGO Scientific Collaboration et al., 2019). These results are in broad agreement with both early and late-Universe measures of H_0. However, the errors from the standard siren method are currently too large to provide a competitive constraint. This will hopefully improve over time with the detection of further GW events with electromagnetic counterparts.

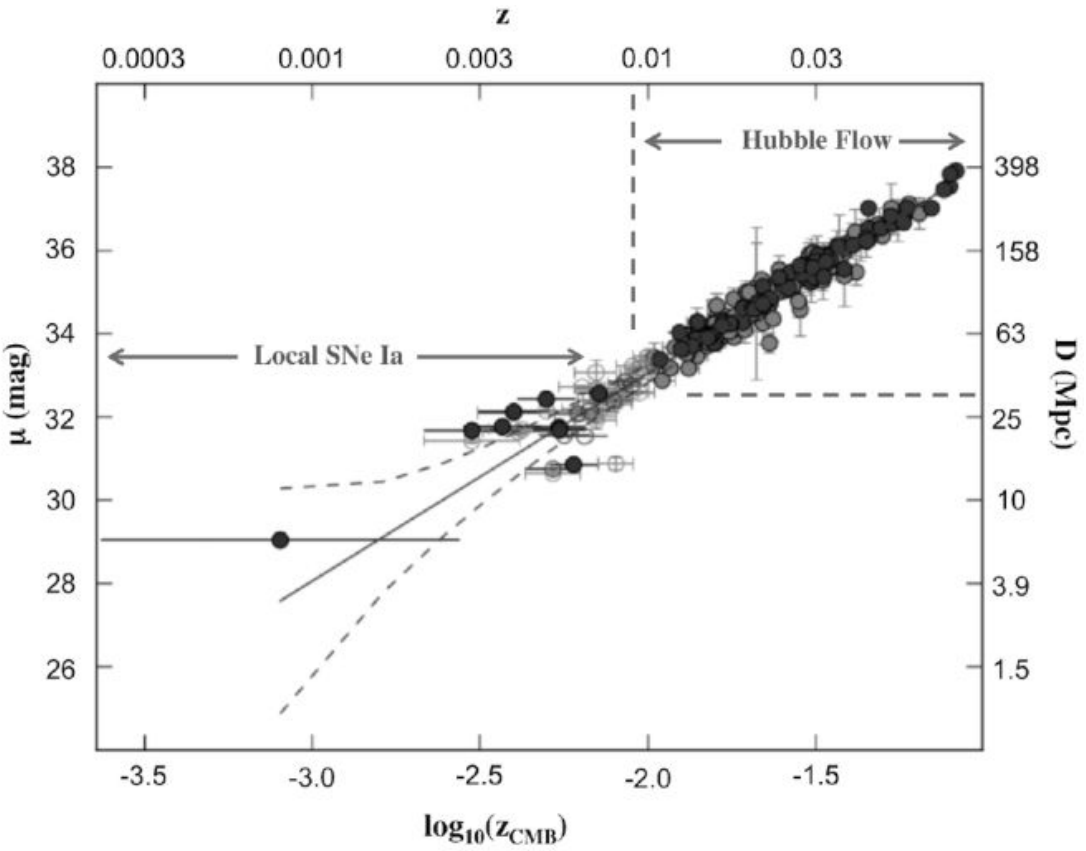

Figure 10: Modern day Hubble diagram using Type Ia SNe. Note the large scatters on the recession velocities ($v \approx cz$) for local SNe due to the effect of peculiar motion, highlighting the importance of additional calibrations from other standard candles located in the SNe Ia host galaxy, e.g. Cepheid variable stars and TRGB stars. SNe in the 'Hubble flow' ($z \gtrsim 0.01$) have recession velocities dominated by cosmic expansion, contributing little to systematics. H_0 is calculated by the slope of the best-fit (solid black line). Figure taken from Czerny et al. (2018), adapted from Beaton et al. (2016).

1.5 THE COSMIC DISTANCE LADDER

1.5.1 *Overview*

We can in principle measure H_0 for any object with a known value of distance, either from a source with well understood brightness or size, and a measure of recession velocity from the object's redshift. However, this is dependent on the object being located in the Hubble flow ($z \gtrsim 0.01$) where cosmic expansion dominates over peculiar motion. Objects that fit all these criteria are uncommon and don't allow us to probe

the distance-redshift relation across a wide range of distance scales, especially locally. It is possible to probe a range of distances across the observable Universe through a complimentary succession of methods i.e. a cosmological distance ladder, containing a collection of local, intermediate and cosmological distance measures. The distance ladder method also provides the means to calibrate the luminosities of distant objects through observations of more local objects, therefore not requiring the idealised objects used in one-step methods. The succession of objects on the cosmological distance ladder can then be used to form a Hubble diagram, allowing inference on H_0 (see Figure 10). As methods have become more robust over time, as of today measuring H_0 to a high-accuracy requires only 3 steps:

1. A local zero point calibration, e.g. from stellar parallax.
2. Intermediate distances to Type Ia SNe located in galaxies with other standard candles such as Cepheid variables or tip of the red giant branch (TRGB) stars.
3. Cosmological distances to Type Ia SNe located well into the Hubble flow, where the expansion of the Universe dominates over peculiar velocities.

In this section we will solely focus on the distance measurements required for the above three steps, with particular focus on the first two steps. This is because the error budget on H_0 from the cosmic distance ladder is almost entirely dominated by errors from low-z and zero-point distance calibrations. We will also briefly look into an alternative 'inverse' distance ladder calibrated at intermediate z using the standard ruler of BAO measurements. For extensive discussions on the cosmic distance ladder, refer to Freedman and Madore (2010), Jackson (2015), Zhang et al. (2017), and Freedman et al. (2019) and references therein.

1.5.2 *Stellar Parallax*

According to an observer in motion, objects closer to the observer appear to be moving more rapidly compared to objects located further away. By comparing the angular shift of a nearby object relative to the position of the slower moving background objects across a period of time, it is possible to measure the distance to the nearby object through trigonometry. This principle can be applied to the motion of stars relative

to the Earth's orbit around the Sun. By noting the position of a nearby star on the sky, and then again six months later when the Earth is located at the opposite side of the Sun, we would observe an angular shift of the nearby star against the static background of more distant stars according to the Earth's reference frame. The distance to the nearby star is can be approximated as the reciprocal of half of the total angular shift in arcseconds i.e. $d(\mathrm{pc}) = 1(\mathrm{AU})/\theta(\mathrm{arcsec})$. This method provides an effective zero-point calibration for the modern day Hubble diagram due to its high-accuracy, with the main limitation being its relatively short range compared to other distance measures. However, this has been steadily improving over time with recent generations of space-based telescopes. The launch of the Gaia satellite increased the distance limit from $\sim$ 100 pc to $\sim$ 10 kpc, a significant improvement over Earth based telescopes, due to increased astrometric precision and thus higher sensitivity to shifts in angular position. The sample of stars with well-measured distances also increased significantly with Gaia, with the second data release providing the positions, proper motions and parallaxes for $\sim$ 1.3 billion stars (Gaia Collaboration et al., 2018; Luri et al., 2018).

1.5.3 *Type Ia Supernovae*

Type Ia SNe are the explosions of carbon-oxygen (C-O) white dwarfs (WDs) on approach to the Chandrasekhar mass limit ($M_{Ch} \sim 1.4\ M_{\odot}$), through accretion of mass or direct collision with another object (see Section 2.4 for further discussion of the physics). Their light-curves are standardisable, due to their homogeneous light curves and an established correlation between the maximum brightness and the width/decline rate of the Type Ia light curve (Pskovskii, 1984; Phillips, 1993; Hamuy et al., 1996). Intrinsically brighter SN Ia have typically broader light curves than dimmer ones, irrespective of distance to the observer. Therefore by taking advantage of this relation and applying empirical corrections, we can standardise the SN Ia light curve such that its peak brightness is only distance dependent, as opposed to being a function of the intrinsic properties of the SN.

As a result, Type Ia SNe are excellent cosmological distance indicators and were instrumental in discovering the accelerated expansion of the Universe, a keystone of modern day cosmology (Riess et al., 1998; Perlmutter et al., 1999). Type Ia SNe

arguably form the foundation of the modern day Hubble diagram, however the intrinsic luminosity of each individual SN Ia is not directly known and can vary for example with progenitor populations and host environments (e.g. see Sullivan et al., 2006; Childress, Wolf, and Zahid, 2014). Additionally at local distances their recession velocities become more and more contaminated by peculiar velocities (see Figure 10). Therefore local SNe outside of the Hubble flow ($z \lesssim 0.01$) require additional calibrations from other standard candles sharing the same host galaxy in order to properly anchor them to the Hubble diagram. This is especially important since the sample of low-z SNe Ia is very small. SNe Ia are rare, with only 19 published Cepheid distances for nearby SNe Ia across ~ 4 decades of searches (Riess et al., 2016). No SN Ia has occurred close enough to Earth to be calibrated with parallax. Therefore the low-z SNe Ia sample dominates the error budget in H_0 (e.g. see Zhang et al., 2017; Czerny et al., 2018, and references therein for extensive discussions).

1.5.4 *Distance Ladder Calibrators*

1.5.4.1 *Cepheid Variables*

Cepheid variables are a class of pulsating variable stars that typically lie in a small, luminous region of the Hertzsprung–Russell (H-R) diagram known as the instability strip. Stars are normally self regulating in size, however stars lying in this region are prone to expand and contract, resulting in periodic fluctuations in their luminosity. The light curves of Cepheid variables have a well understood period-luminosity (P-L) relationship (also referred to as Leavitt's Law Leavitt, 1908; Leavitt and Pickering, 1912) characterised by a sharp rise, followed by a more gradual fall in luminosity. The more luminous a Cepheid is, the longer its period of oscillation.

The physics behind Cepheid pulsation is driven by the changing temperature and opacity in the star's helium layer. When the helium layer is ionised, it becomes opaque and subsequently traps energy, increasing the star's internal pressure. This results in a radial expansion as the ionised helium pushes against the outer layers of the star. As the star expands, the ionised helium layer cools until it recombines and becomes subsequently transparent, allowing photons to escape to the outer layers. The photon pressure drops and the star re-contracts, compressing and re-ionising

the helium layer, increasing its opacity and thus repeating the cycle. This results in the Cepheid having a variable luminosity. From the established P-L relationship it's possible to calculate the intrinsic luminosity of the Cepheid and therefore its distance, establishing its position as a standard candle.

Cepheids are an important component of the cosmic distance ladder and are primarily used to calibrate the distances of local Type Ia SN outside the Hubble flow ($z \lesssim 0.01$). However, they are subject to systematics (e.g. metalicity and reddening), which if not accounted for can significantly impact measurements of H_0. The error budget in H_0 from the cosmic distance ladder is dominated by analyses of low-z objects. Using low-z SNe Ia calibrated with Cepheids in the Large Magellanic Cloud (LMC), Riess et al. (2019) have best estimated $H_0 = 74.03 \pm 1.42$ km s^{-1} Mpc^{-1}. For further discussion of Cepheids and their role in the cosmic distance ladder, including a discussion of systematics, see e.g. Freedman and Madore (2010) and Jackson (2015), and references therein.

1.5.4.2 *Tip of the Red Giant Branch*

The accuracy of the cosmic distance ladder determinations of H_0 are effectively dependent on calibrations from low-z objects. Whilst Cepheid variables have classically been used to anchor the distance ladder, they are subject to systematics including metalicity and reddening. Even if all these known systematics were under control, all future analyses will be blind to unknown systematics. Therefore alternative low-z objects capable of calibrating the distance ladder (independently of Cepheids) are a vital indicator of unknown systematics.

The TRGB marks a key transition point in the stellar evolution of low mass stars evolving into red giants. This is marked by a 'helium flash', signifying core helium burning becoming the dominant energy mechanism in the star. This feature is observed as discontinuity in the luminosity function of stars evolving up the red giant branch (RGB) and is well understood. The luminosity of TRGB stars are essentially independent of their metalicity and mass, being driven primarily by nuclear physics. They are also distinctly bright and red, making them easily identifiable when observed in the *I*-band. As a result they are a viable alternative to Cepheid variables as standard candles and calibrators of low-z SNe Ia. For more detailed discussion on the

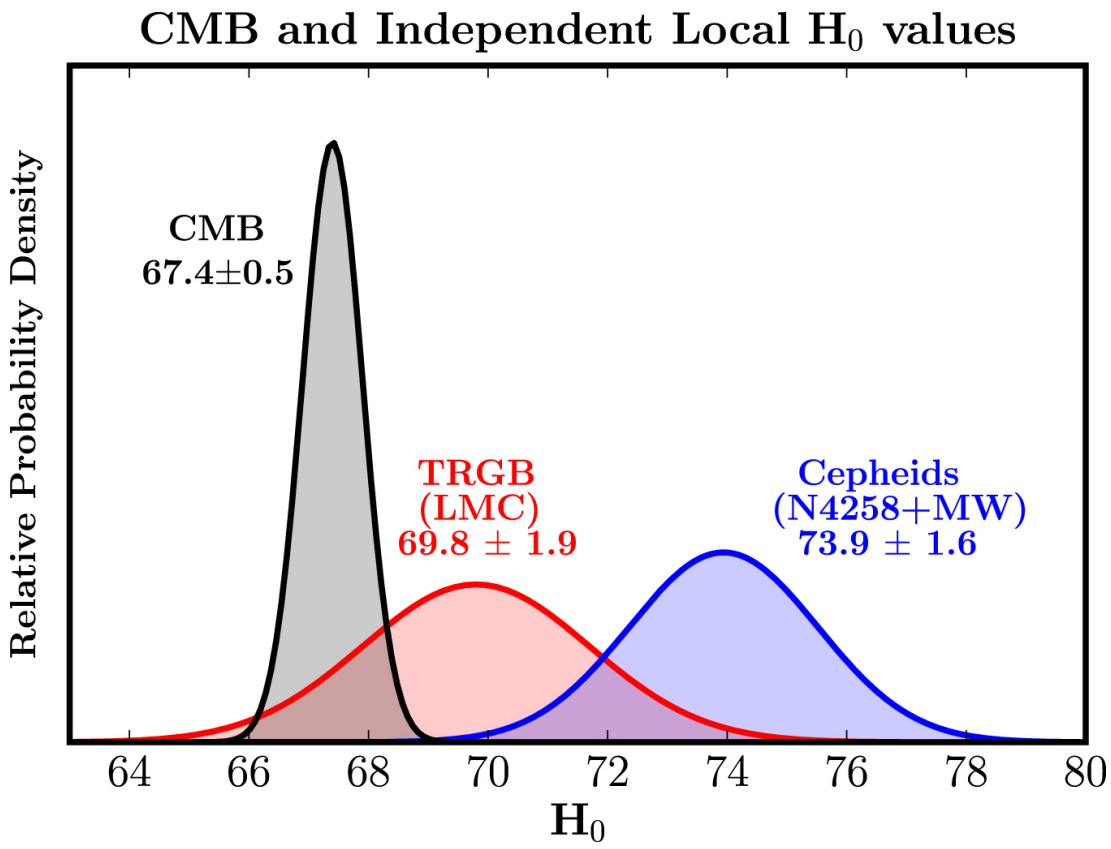

Figure 11: Calibrations of H_0 obtained through completely independent methods. Shown in red is the PDF from Freedman et al. (2019), using calibrations from LMC TRGB. Shown in blue is the PDF from Riess et al. (2019), using additional calibrations from Milky Way parallaxes and the maser distance to NGC 4258, however excluding LMC detached eclipsing binaries. The Planck Collaboration et al. (2018) PDF is shown in black. Figure from Freedman et al. (2019).

TRGB method, including systematics, see Freedman and Madore (2010), Beaton et al. (2018), Freedman et al. (2019), and McQuinn et al. (2019) and references therein.

Freedman et al. (2019) have measured $H_0 = 69.8 \pm 1.9$ km s^{-1} Mpc^{-1} using a distance ladder calibrated with TRGB stars in the LMC. This results agrees at the 1.2σ level with Planck Collaboration et al. (2018) and at the 1.7σ level with Riess et al. (2019) (see Figure 11). Alternatively Yuan et al. (2019) have measured $H_0 = 72.5 \pm 1.9$ km s^{-1} Mpc^{-1}, in stronger agreement with the cosmic distance ladder. Like Freedman et al. (2019), Yuan et al. (2019) use LMC TRGB calibrators, however they apply different treatments of TRGB extinction and calibrations between Hubble Space Telescope and ground-based photometry. These results highlight the significant impact on H_0, not only based on the choice of low-z SNe Ia calibrators, but also on the subsequent han-

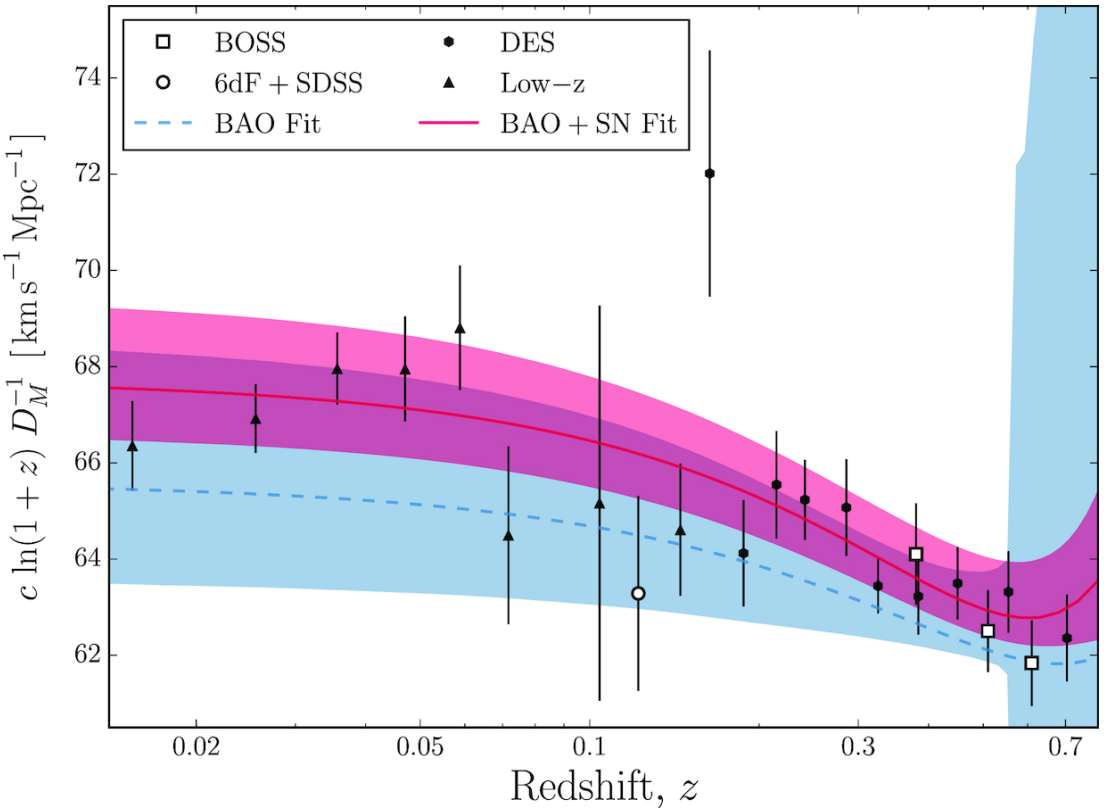

Figure 12: The inverse distance ladder method as illustrated by Macaulay et al. (2019). The red line shows the best cosmological fit model using DES SNe (black markers) anchored with BAO (white markers). The blue line shows the same, but with only BAO. The respective shaded regions give the 68% confidence regions. For each best-fit model, H_0 is determined by the y-axis intercept.

dling of systematics. Therefore highlighting the importance of further independent measurements of H_0.

1.5.5 *Inverse Distance Ladder*

The inverse distance ladder is an alternate model-insensitive way of measuring H_0. Whilst the local distance ladder is calibrated using absolute distance measurements to Cepheid variable stars, the inverse distance ladder is calibrated using absolute distance measurements from BAO, with physical scales set by the sound horizon from CMB measurements (as illustrated in Figure 12). The systematics of BAO are completely independent of Cepheids, therefore the inverse distance ladder provides a complimentary measurement of H_0 and a further test of unknown systematics. Inter-

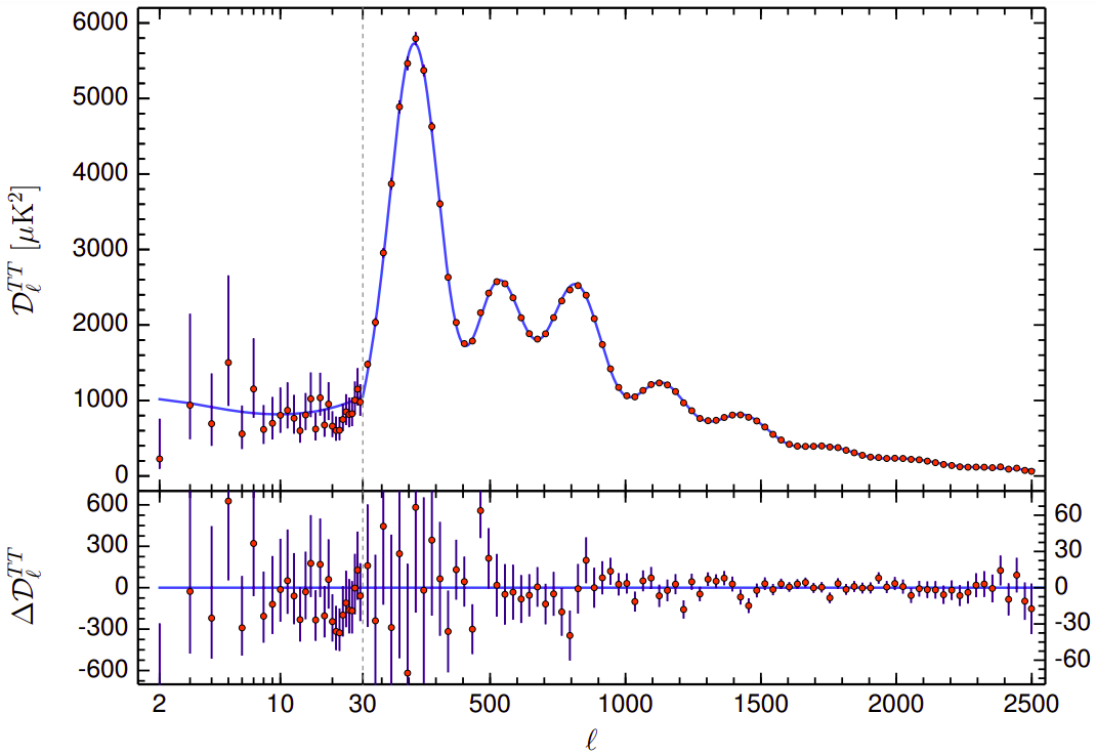

Figure 13: CMB temperature power spectrum. Figure taken from Planck Collaboration et al. (2018).

estingly, measurements of H_0 through the inverse distance ladder have been consistent with early-Universe measurements (see Aubourg et al., 2015; Cuesta et al., 2015; Alam et al., 2017; Macaulay et al., 2019). However, since the calibration of the inverse distance ladder is dependent on the knowing the absolute scale of the sound horizon, it could be argued this method doesn't produce a value of H_0 that is entirely independent of early-Universe measurements.

1.6 EARLY-UNIVERSE MEASUREMENTS

1.6.1 *Cosmic Microwave Background*

After the Big Bang, the early Universe was composed of a hot plasma containing both baryons and photons. The extreme temperatures meant that photons were constantly scattered by charged particles, making the early Universe completely opaque. As the Universe expanded it began to cool and the first atoms began to form. Since the photons were no longer coupled to baryons, they were finally allowed to free

stream and the Universe became transparent as a result. This is known as the epoch of recombination.

In the Universe's hot and fluid state, baryons would fall into gravitational overdensities and were subsequently rebounded due to the increase in radiation pressure. These opposing forces resulted in spherical oscillations that propagated at a relativistic sound speed of approximately half the speed of light (Hu and White, 2004). At the epoch of recombination, the Universe became transparent and the radiation-driven spherical sound waves stopped propagating. The size of the resulting shells of mass became dictated purely by the expansion of the Universe (Eisenstein and Hu, 1998). The observed temperature anisotropies in the CMB map are a result of these acoustic oscillations and therefore can be described by a series of spherical harmonics (see e.g. Challinor, 2013, for a review of the physics).

The temperature power spectrum of the CMB is shown in Figure 13. The second and third acoustic peaks are sensitive to the baryon density and the total matter density respectively, multiplied by the square of the Hubble Constant i.e. $\Omega_b H_0^2$ and $\Omega_m H_0^2$. In order to disentangle H_0 from the cosmological parameters, either additional data or assumptions on the cosmological model is required, e.g. assuming a spatially flat Universe where the spectrum of the initial perturbations follow a power-law profile. Combining the CMB data with other independent probes of H_0 (e.g. BAO measurements) allows relaxation on the cosmological assumptions. Assuming a flat ΛCDM cosmology, Planck Collaboration et al. (2018) have measured $H_0 = 67.4 \pm 0.5$ km s^{-1} Mpc^{-1}, in 4.4σ tension with Riess et al. (2019).

1.6.2 *Baryonic Acoustic Oscillations*

As previously discussed in Section 1.6.1, the oscillating tensions between gravity and radiation in overdense regions of the early Universe produced spherical acoustic waves that travelled at relativistic speeds (Hu and White, 2004). When the Universe cooled to around 3000K, the sound speed was reduced to the point where the propagation of the spherical waves effectively froze. Afterwards, the radius of these shells were dictated solely by the expansion of the Universe (Eisenstein and Hu, 1998). This signal is directly ingrained into the large scale structure of the Universe (see Figure 14). The gas in the central overdensities and the outer shells of the frozen acous-

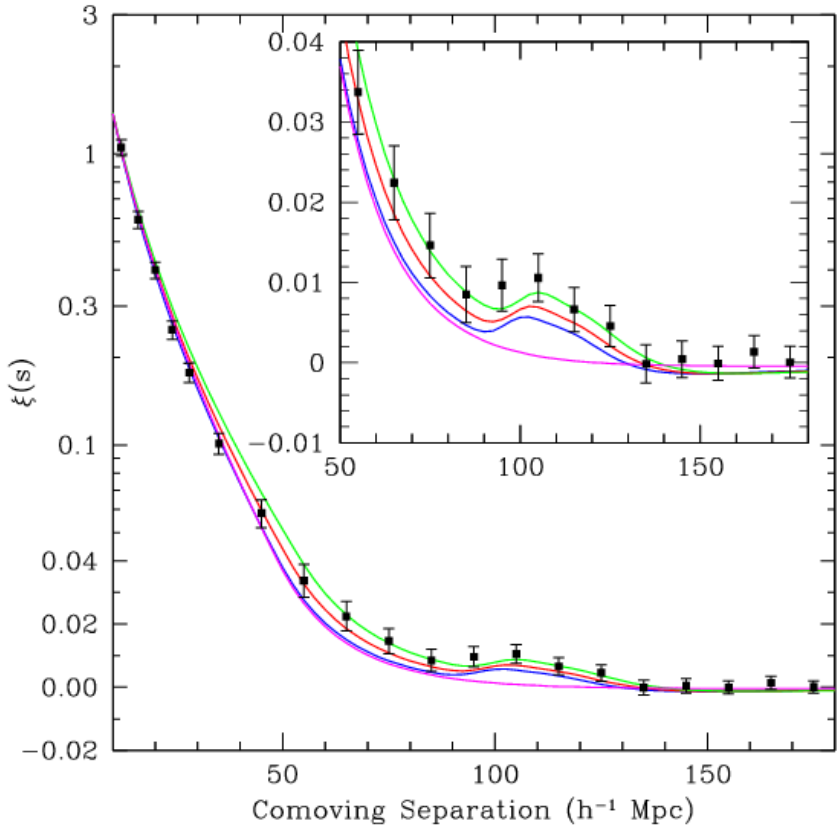

Figure 14: Large-scale redshift-space correlation function of the SDSS LRG sample. The secondary peak provided a 10σ detection of the BAO signal, proving that overdensities from initial perturbations from the early Universe were frozen into the the distribution of galaxies in the late Universe. Figure from Eisenstein et al. (2005).

tic waves collapsed to form galaxies. The distances between these central and outer galaxies are set by the expansion of the Universe and provide a standard ruler that can be used to calculate H_0.

Using the inverse distance ladder method highlighted in Section 1.5.5 and assuming flat ΛCDM, Alam et al. (2017) measured $H_0 = 67.6 \pm 0.5$ km s^{-1} Mpc^{-1} using clustering data from the Baryon Oscillation Spectroscopic Survey (BOSS). Combining BAO (using BOSS priors from Alam et al. 2017) with DES Year 1 clustering/weak lensing data and Big Bang nucleosynthesis experiments, Abbott et al. (2018) measured $H_0 = 67.6 \pm 0.5$ km s^{-1}. In general, BAO measurements are in strong agreement with the CMB (Planck Collaboration et al., 2018), but are in tension with the local distance ladder (e.g. Riess et al., 2019). This is illustrated in Figure 15.

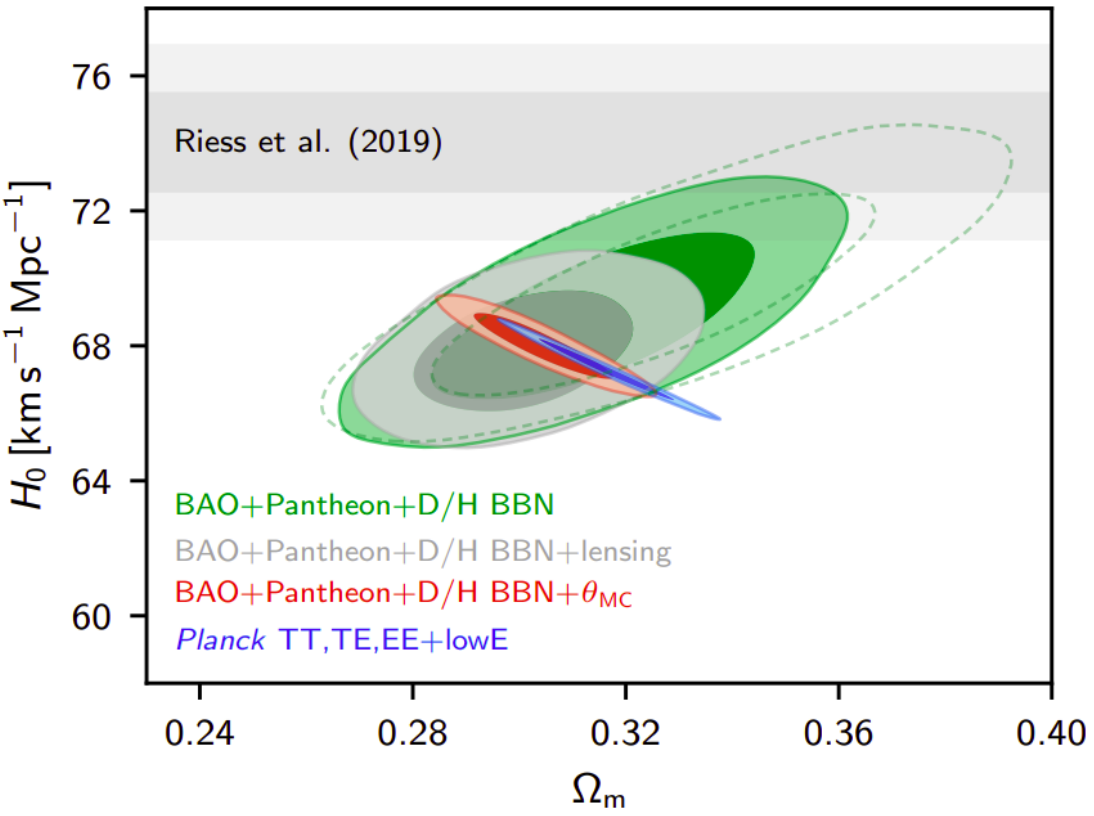

Figure 15: Constraints on H_0 and the total matter density Ω_M from the inverse distance ladder using BAO and the CMB power spectrum (see Planck Collaboration et al., 2018, for further details), against the local distance ladder result from Riess et al. (2019). Both early-Universe constraints are complimentary, in significant agreement with each other and in tension with the local distance ladder. Figure taken from Planck Collaboration et al. (2018).

2

SUPERNOVAE

A star ending its life with a powerful and luminous explosion is known as a supernova (SN). SNe can occur as the result of collapsing cores in massive stars ($\gtrsim 8M_{\odot}$), typically leaving behind a neutron star or a black hole in its place (see Heger et al., 2003). If the explosion is particularly violent, no compact remnant is left behind at all. SNe can also occur through the thermonuclear explosions of white dwarfs (WDs) upon obtaining sufficient mass, leaving no compact remnant behind (Maguire, 2017). For individual galaxies, SNe are rare events, occurring at rates of ~ 2 per galaxy per century (Li et al., 2011). Most SNe eject significant amounts of gaseous material into their surrounding environments, influencing the chemical evolution of galaxies (see Heger et al., 2003). SNe are a major source of many elements in the periodic table. Elements heavier than iron are primarily synthesised in SN explosions (see Alsabti and Murdin, 2017). The ejected material provides foundations for the formation of planetary and even other stellar systems. Radiation expelled from nearby SNe explosions ($\sim$ 100 parsecs) have even had an effect on the climate and evolution of life of our own planet (Thomas et al., 2016). For a recent and exceedingly comprehensive set of articles discussing the various aspects of SNe, refer to the 'Handbook of Supernovae' (see Alsabti and Murdin, 2017).

2.1 A BRIEF HISTORY

'Nova' is the Latin word for 'new'. In an astronomical context the usage of the word derives from the Latin phrase 'nova stella', since the first observations of SNe were visible to the naked eye such that a 'new star' seemed to appear on the sky (sometimes even during the day), lasting up to several months before fading. In modern astronomy, the word 'nova' specifically refers to explosions that occur in the outer hydrogen layers of a WD, accreted from a non-degenerate binary companion star. The term 'supernovae' was conceived to describe a new class of novae that were $\sim 10^4$ times more radiant than the sun (e.g. Baade and Zwicky, 1934).

There have been many observations of SNe over the course of human history. The earliest possible sighting, known as HB9, could have been observed by a group of unknown Indian astronomers back in ~ 4500 BC (see Joglekar, Vahia, and Sule, 2011). However, the first SN on record was SN 185 (see Zhao, Strom, and Jiang, 2006) which was observed by Chinese astronomers back in 185 AD, who at the time referred to the phenomenon as a 'guest star', lasting for around 8 months in the sky. The remnant of SN 185 is believed to be the gaseous shell RCW 86, as X-ray observations suggest a good match for the expected age (Vink et al., 2006).

The most notable examples of historic SNe, hosted in the Milky Way and visible to the naked eye, include: SN 1006, possibly the brightest recorded transient event in history, reaching an estimated V-band magnitude of -7.5 (see Katsuda, 2017); SN 1054, which produced the Crab Nebula (see Blandford and Bühler, 2017); SN 1181, which likely produced the synchrotron nebula 3C 58 (see Kothes, 2017); SN 1572, a.k.a Tycho's SN (see Decourchelle, 2017) and SN 1604, a.k.a. Kepler's SN, the most recent galactic supernova according to historical record (see Vink, 2017). These five historic supernovae have well studied remnants, recorded histories and precisely known ages that have significantly helped our understanding of SN astrophysics (see Stephenson and Green 2002, Stephenson 2017 and Green 2017 for further reading on historical SNe).

The most recent SN observable by the naked eye was SN 1987A (Kunkel et al., 1987), occurring in the Large Magellanic Cloud, a satellite galaxy of the Milky Way about 50 kiloparsecs from Earth. SN 1987A is unique in that it was the first SN to be observed in detail in every band of the electromagnetic spectrum and the first SN with an observable neutrino signature, appearing before a few hours first light (Bionta et al., 1987; Hirata et al., 1987; Alexeyev et al., 1988). The detection of the initial neutrino burst confirmed that a component of the SN population was formed from the collapse of massive stars into neutron stars. In general, observations of SN 1987A were instrumental in the understanding of core-collapse supernovae. For further discussion on the various aspects of SN 1987A and its impact on SN astrophysics, refer to Arnett et al. (1989), McCray (1993), McCray and Fransson (2016), Podsiadlowski (2017), and McCray (2017).

2.2 CORE-COLLAPSE SUPERNOVAE

Massive stars (~ 8-140 $M_\odot$) end their life as a core-collapse (CC) SNe. Progenitor stars with mass beyond 140 $M_\odot$ are believed to result in electron-positron production in the core, leading to violent 'pair-instability' explosions that completely rip apart the star, however this yet to be confirmed by observation (e.g. Rakavy and Shaviv, 1967; Gal-Yam et al., 2009; Moriya et al., 2010). The degenerate core of a progenitor star is typically composed primarily of iron, but sometimes a mixture of oxygen, magnesium, neon and silicon. The electron degeneracy pressure from the core cannot support surrounding non-degenerate matter, resulting in catastrophic collapse and violent explosion. Detailed discussion on the physics and explosion mechanisms of CC SNe is beyond the remit of this chapter, if the reader is interested there is an abundance of review articles available for further reference (e.g. Janka 2012, Burrows 2013, Janka, Melson, and Summa 2016 and a range of chapters from Alsabti and Murdin 2017).

CC SNe have a wide range of progenitor configurations and therefore their observational characteristics (e.g. luminosity, spectra, etc) can vary significantly. Typically they manifest themselves as Type II SNe from the hydrogen detectable in their spectra. However, if the hydrogen is significantly dispersed from the envelope, due to strong stellar winds or interaction with another astronomical object during the star's life cycle, then it can be classified as a Type I SN.

There are many subclasses of CC SNe, however only the most common types (Type IIP, IIL, IIn, IIb and Ib/c) will be briefly discussed in this section (see e.g. Arcavi 2017 and Pian and Mazzali 2017 for further discussions on the CC subclasses, see Smartt 2009 and Leonard 2011 for discussions on their respective progenitors, also see Figure 16 for a comparison of model light-curves). The most common type of CC SNe (and in fact SNe in general) are Type IIP explosions, with light curves that plateau for approximately 100 days after peak (see Figure 17, left), likely indicative of a thick hydrogen envelope. From observations, the progenitor stars of SNe IIP have been identified as red supergiants with masses in the range 10-17 $M_\odot$ (see Arcavi, 2017). These stars have extended hydrogen envelopes and are likely to be directly responsible for the observed plateau in the light curve. Type IIL SNe have light curves that decline linearly after peak (see Figure 17, right) and this was one of the initial

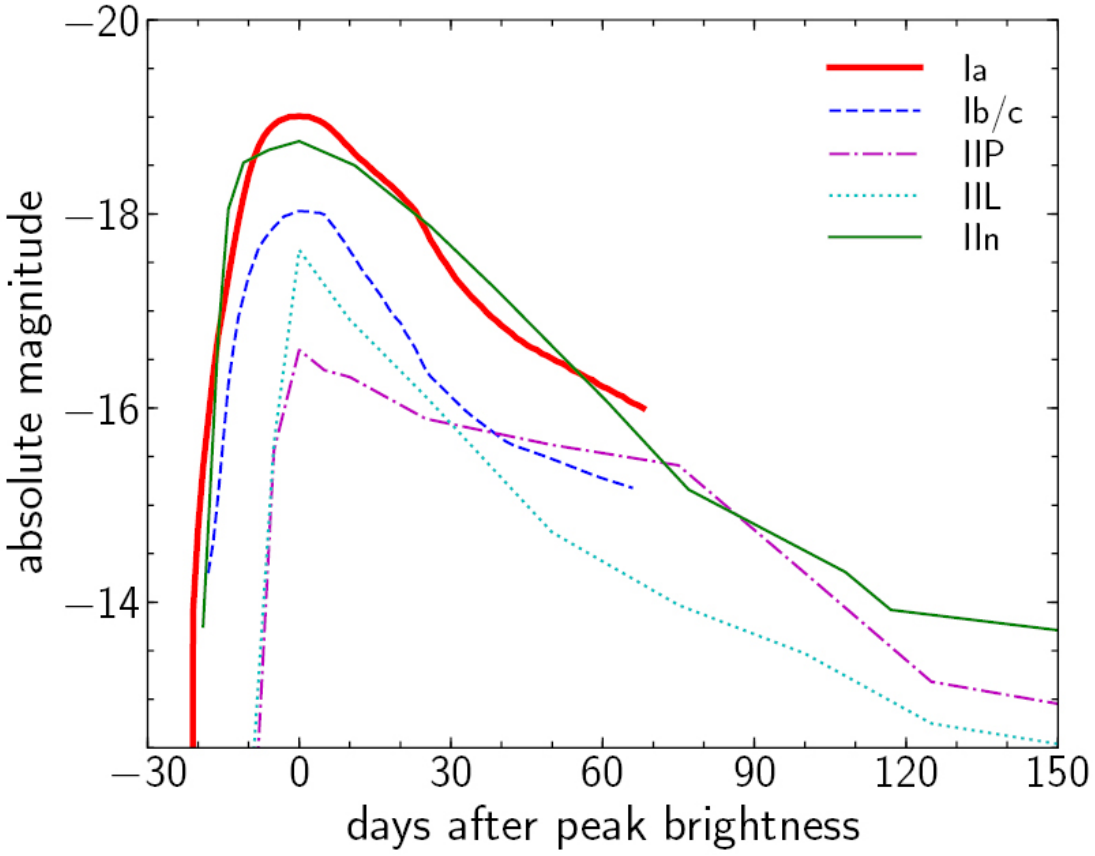

Figure 16: Absolute V-band magnitude template light curves across a range of SN subtypes (from Nugent, 2007). Peak absolute magnitudes are taken from Richardson et al. (2002). Figure from Oguri (2019)

classifications for Type II SNe, along with Type IIPs (Barbon, Ciatti, and Rosino, 1979). The progenitors for Type IIL SNe are unclear and it still remains an open question whether the progenitors of Type IIP and IIL SNe span a continuous distribution, or are two separate populations entirely (Arcavi, 2017).

Type IIn SNe contain narrow hydrogen emission lines in their spectra (Schlegel, 1990), likely due to interaction of the SN ejecta with a sufficiently thick circumstellar medium ejected by the progenitor before the explosion (Chugai, 1991). Only one Type IIn progenitor has been detected thus far. Gal-Yam et al. (2007) and Gal-Yam and Leonard (2009) identified the progenitor of SN2005gl as a luminous blue variable star. These are massive, evolved stars that undergo periods of heavy mass loss, resulting in a significant amount of circumstellar hydrogen. This is a natural explanation for the observed hydrogen emission lines of Type IIn SNe and their long, luminous and blue light curves.

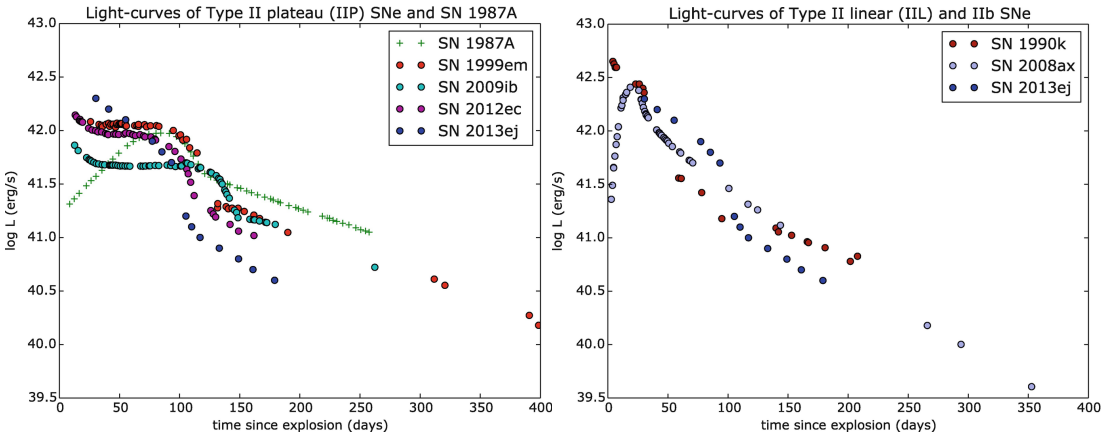

(a) (b)

Figure 17: (a) Bolometric light curves of a representative sample of Type IIP SNe (Leonard et al., 2003; Takáts et al., 2015; Barbarino et al., 2015; Huang et al., 2015), alongside the light curve for SN 1987A (Hamuy et al., 1988). (b) Bolometric light curves for a Type IIL SN (SN 1990K; Cappellaro et al., 1995), Type IIb SN (SN 2008ax; Pastorello et al., 2008; Taubenberger et al., 2011) and a Type IIP SN for comparison (SN2013ej; Huang et al., 2015). Figures taken from Zampieri (2017).

Types IIb, Ib and Ic are all different forms of hydrogen-poor or stripped envelope CC SNe. They exhibit little (IIb) to no hydrogen (Ib/c) in their spectra. Type IIb SNe initially have broad hydrogen lines in their spectra, however these fade away over time and become dominated by helium to represent a Type Ib SN, suggesting an intermediate stripping stage between H-rich Type II and H-poor Type Ib SNe. Type Ic SNe are stripped of both hydrogen and helium. A few Type IIb progenitors have been identified as yellow supergiants with a binary companion (e.g. Podsiadlowski et al., 1993; Crockett et al., 2008; Folatelli et al., 2014, 2015). An interacting binary companion that strips the envelope of the progenitor star would explain the low amount of hydrogen observed in the spectra of Type IIb SNe. The progenitors of Type Ib/c stars have been proposed to be massive Wolf-Rayet stars (Gaskell et al., 1986) that have shed their hydrogen/helium envelope through strong stellar winds. An alternate explanation is a low mass star that has its hydrogen/helium envelope stripped through close binary interaction with a companion (e.g. Podsiadlowski, Joss, and Hsu, 1992; Nomoto, Iwamoto, and Suzuki, 1995).

2.3 SUPERLUMINOUS SUPERNOVAE

Superluminous SNe are a relatively new class of extremely bright and rare SNe, with typical peak *B*-band magnitude $\gtrsim$ -21 (Quimby et al., 2011). Superluminous SNe are believed to evolve from massive stars ($\gtrsim$ 30-40 $M_\odot$; e.g. Heger et al. 2003) and can explode as both Type I and Type II SNe (Gal-Yam, 2012; Howell, 2017). They are also extremely rare, occurring a factor of 10^{-3} less often than CC SNe (Prajs et al., 2017). The current favored power source is the spin down of a highly magnetic compact object known as a magnetar, however there also exists ^{56}Ni and interaction-powered models to explain the extreme luminosities (e.g. see Moriya, Sorokina, and Chevalier, 2018, and references therein). They can be found at redshift $z \gtrsim 2$ (e.g. Cooke et al., 2012; Pan et al., 2017; Smith et al., 2018; Moriya et al., 2019; Curtin et al., 2019) and could for example be used to probe the cosmic star formation at very high redshifts. They even have potential as future standard candles, allowing measurement of cosmological distances well beyond the reach of SNe Ia (Quimby et al., 2013a; Inserra and Smartt, 2014; Wei, Wu, and Melia, 2015; Scovacricchi et al., 2016; Inserra et al., 2018). Further discussion regarding superluminous SNe is beyond the remit of this chapter. For the interested reader, there exists a number of recent reviews that cover both the observational and theoretical aspects of superluminous SNe (e.g. Gal-Yam, 2012; Howell, 2017; Moriya, Sorokina, and Chevalier, 2018).

2.4 TYPE IA SUPERNOVAE

Type Ia SNe have long been used as cosmological distance measures and were critical in the discovery of the accelerating expansion of the universe (Riess et al., 1998; Perlmutter et al., 1999). Their light curves are remarkably homogeneous and can be standardised by applying empirical corrections, albeit with a small scatter in intrinsic brightness ($\sigma_M \sim 0.15$ mag; e.g. Betoule et al. 2014; Macaulay et al. 2017; Jones et al. 2018). This makes them powerful distance indicators, as their light curves can be corrected to be purely distance-dependent and therefore are commonly used as standard candles.

Despite being a trusted measurement of extragalactic distances, the formation mechanism for Type Ia SNe remains an open problem. The progenitor star is ex-

pected to most likely be a carbon-oxygen (C-O) WD (e.g. Woosley, Taam, and Weaver, 1986) that explodes when its mass approaches the Chandrasekhar mass limit, M_{Ch} ~ 1.4 $M_{\odot}$. This can be the result of the WD accreting mass or directly merging (possibly even colliding) with another stellar object, believed to be a companion in binary orbit with the WD. Whilst there is no direct observational evidence to confirm this, observations of the early phases of SN 2011fe, a nearby and well-studied SN Ia, have placed strong constraints on possible progenitor stars, with the consensus being that the progenitor star was a compact degenerate star, most likely a WD (Bloom et al., 2012).

WDs come in three flavours: the lower-mass helium WDs, the intermediate mass C-O WDs and the higher-mass oxygen-neon (O-Ne) WDs. The ejecta of a exploding helium WD would consist entirely of He, ^{56}Ni and other decay products (e.g. Woosley, Taam, and Weaver, 1986; Nomoto and Sugimoto, 1977) and hence helium WDs have been completely ruled out by observations - SNe Ia are characterised by the lack of hydrogen and helium (but with an additional silicon component, unlike Type Ib/c SNe) in their spectra. According to simulations, O-Ne WDs accreting mass become gravitationally unstable, leading to 'accretion-induced collapse' resulting in the formation of a neutron star instead of a SN (e.g. Nomoto and Kondo, 1991; Gutierrez et al., 1996; Saio and Nomoto, 1985; Saio and Nomoto, 2004; Sato et al., 2015). Even if the results of the simulations were untrue, the population of O-Ne WDs would unlikely reproduce the observed SN Ia rate (e.g. Livio and Truran, 1992). This leaves C-O WDs as the primary candidate progenitor star for Type Ia SNe, which is supported by simulations (e.g. Nomoto and Kondo, 1991; Nomoto et al., 2007; Hillman et al., 2016).

Upon reaching the M_{Ch}, carbon ignition and burning occurs which rapidly propagates through the C-O WD. Since the electron degeneracy pressure is independent of temperature, the fusion of carbon and oxygen cannot be regulated. As a result the burning turns into a runaway process that ultimately triggers a thermonuclear explosion ($E \sim 10^{51}$ ergs), completely unbinding the WD and leaving no compact remnant behind. Assuming all C-O WDs explode on approach to M_{Ch}, they should produce the similar amount of nuclear energy upon explosion, and therefore all have similar luminosities ($\sim 10^{43}$ erg s^{-1}).

The observed SN Ia luminosity is not powered directly from the explosion, but from the decay of radioactive ^{56}Ni synthesised in the inner regions of the WD during the

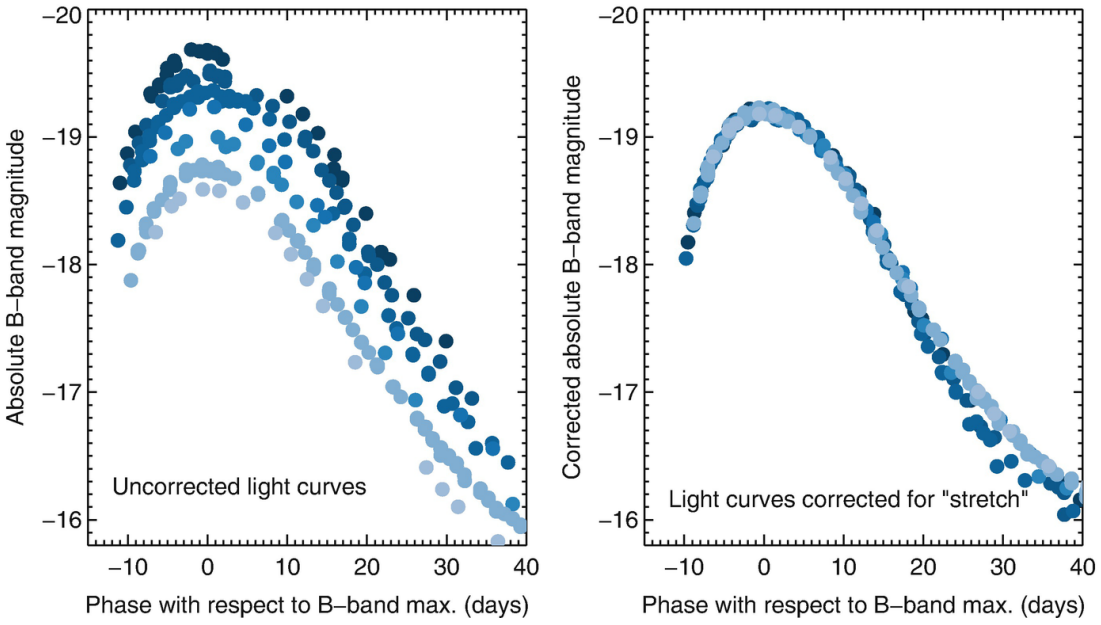

Figure 18: Absolute *B*-band magnitude for a sample of SNe Ia, using data from Hicken et al. (2009) and Stritzinger et al. (2011). The left panel shows the uncorrected light curves. The luminosity-width relation is clearly demonstrated here, with fainter SNe Ia declining faster after peak compared to the more luminous SNe Ia. The right panel shows the light curves after 'stretch' corrections have been performed, the scatter between the light curves is now minimised. Figure taken from Maguire (2017).

explosion (Colgate and McKee, 1969). Initially, the luminosity is powered by the decay of ^{56}Ni (half life, $t_{1/2} = 6.1$ days) to ^{56}Co and is then later powered by the decay of ^{56}Co ($t_{1/2} = 77.3$ days) to stable ^{56}Fe. The decay process produces gamma rays that are reprocessed by the optically thick ejecta into optical photons that dominate the luminosity ($\sim 85\%$ between the *U* and *I* bands, e.g. Howell et al. 2009).

The rise time to light curve peak for SNe Ia is typically ~ 20 days after explosion in the *B*-band, followed by a rapid decline of ~ 3 magnitudes in 1 month and then a more steady decline of ~ 1 magnitude every month. Type Ia SNe have a tight correlation between peak luminosity and decline rate after peak (known as the 'width-luminosity' and/or Phillips relation, e.g. Phillips 1993; Phillips et al. 1999; Kattner et al. 2012), as shown in Figure 18. Brighter SNe Ia decline more slowly, i.e. have broader light curves than fainter ones. The peak of the luminosity is determined by the amount of synthesised ^{56}Ni and in parallel, the rate of luminosity evolution is determined by the synthesis of iron-group elements which contribute to the bulk of the opacity,

slowing down the light-curve evolution (e.g. Arnett, 1982; Hoeflich and Khokhlov, 1996; Kasen and Woosley, 2007).

The evolution of SN Ia light curves was first quantified by measuring the difference in *B*-band magnitude between peak and 15 days after peak ($\Delta m_{15}(B)$, Phillips 1993). Over time, this relation has evolved across multiple light curve models (e.g. MCLS, Riess, Press, and Kirshner 1996; Jha, Riess, and Kirshner 2007; SALT2, Guy et al. 2007 & SIFTO, Conley et al. 2008) to take into account the time evolution in multiple band-passes (e.g. colour correction factor, $CL(\lambda)$) and the overall shape of the SN Ia light curve (e.g. the luminosity correction factor Δ or the 'stretch' factor, s). Since the intrinsic properties of the light-curves are distance-independent, the width-luminosity relation (and its equivalents) can be used to infer the intrinsic luminosity of the SN Ia, therefore allowing us to calculate its luminosity distance from Earth.

Type Ia SNe are known to form in both young (with active star formation) and old (little to no star formation) stellar populations unlike core-collapse SNe, which are hosted only by young galaxies (e.g. late/spiral types) (Li et al., 2011). The observed properties of SNe Ia have been shown to be dependent on the properties of their host galaxies, including galaxy morphology, metalicity, stellar mass and mean star formation rates (Hamuy et al., 1996, 2000; Sullivan et al., 2006). For example, SNe Ia occurring in younger populations are more luminous than their counterparts found in older populations. The rates of SNe Ia are also dependent on the host, being more common in younger star forming galaxies by an order of magnitude compared to older populations (Mannucci et al., 2005; Sullivan et al., 2006).

Whilst the majority of SNe Ia behave as expected, there exists a small subset of 'weirdos' that do not conform to the width-luminosity relation and/or have peculiar features in their spectra, e.g. 1991T-like SNe and 1991bg-like SNe. 1991T-likes (e.g. Filippenko et al., 1992a; Phillips et al., 1992; Ruiz-Lapuente et al., 1992) are over-luminous SNe Ia with broad light curves and iron lines dominating their early spectrum, likely due to a large amount of ^{56}Ni synthesised during their explosions. On the other hand 1991bg-likes (e.g. Filippenko et al., 1992b; Leibundgut et al., 1993; Turatto et al., 1996) are under-luminous with rapidly declining light curves, likely due to a low amount of synthesised ^{56}Ni, however they are spectroscopically similar to normal SNe Ia. For further discussion of 1991T-likes 1991bg-likes and other sub-classes of weirdos, see Taubenberger (2017) and references therein.

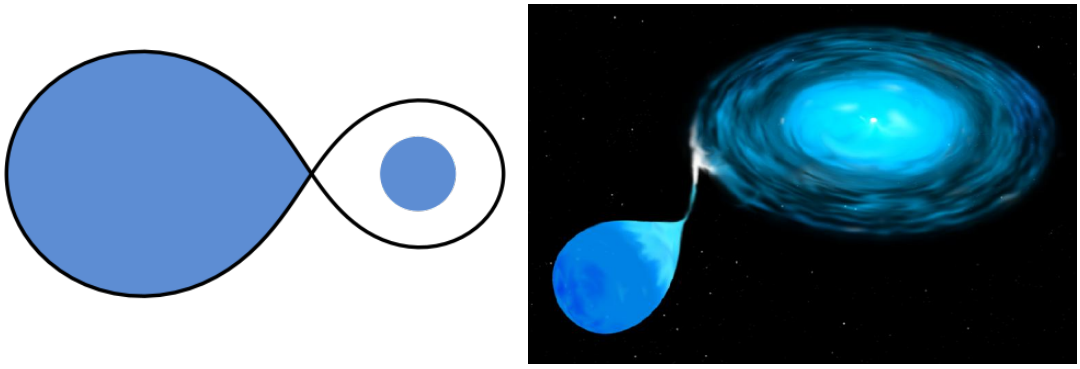

(a) (b)

Figure 19: (a) In the SD scenario, the non-degenerate companion star (left) is large enough to fill its Roche lobe (shown by the black line) and material at the outer edges of the companion become gravitationally bound to the primary WD (right). (b) As a result, the primary WD accretes mass from the companion, forming an accretion disk around the WD. *Credit*: (a) Philip D. Hall (b) NASA.

2.4.1 *Progenitors*

In this subsection, I outline 3 plausible progenitor scenarios that lead to a normal Type Ia SN explosion. For extensive reviews on the progenitors of Type Ia SNe, see Maoz, Mannucci, and Nelemans (2014) and Livio and Mazzali (2018). Also the 'Handbook of Supernovae' has several chapters discussing Type Ia progenitor channels and their subsequent explosion mechanisms (e.g. Maguire, 2017; Hoeflich, 2017; García-Berro and Lorén-Aguilar, 2017; Pakmor, 2017).

2.4.1.1 *Single-Degenerate Channel*

The single-degenerate (SD) channel comprises of a C-O WD accreting mass from a non-degenerate binary companion and exploding on approach to the Chandrasekhar mass limit, M_{Ch} (Whelan and Iben, 1973; Nomoto, 1982; Maguire, 2017). Mass transfer from the companion star onto the surface of the WD can occur through Roche-lobe overflow (see Figure 19) or through strong stellar winds originating from the companion (e.g. Li and van den Heuvel, 1997). The companion can in principle be a main sequence (MS) star, a subgiant, a red giant (RG), a helium star and or an asymptotic giant branch (AGB) star (Livio and Mazzali, 2018). The progenitor system can also have a have a range of possible configurations for each companion type, dependent on any

common envelope (CE) and mass transfer phases that have previously occurred (e.g. Wang and Han, 2012).

In order for the WD to have a net gain in mass from its companion, the accretion rate needs to lie in the range that allows for stable burning i.e. the rate of hydrogen converted into helium is comparable to the rate of accretion from the companion (e.g. Paczynski and Zytkow, 1978; Nomoto, 1982; Fujimoto, 1982; Livio, 1989; Nomoto et al., 2007; Shen and Bildsten, 2007; Wolf et al., 2013). Simulations have shown that that stable burning typically occurs in the relatively narrow range of $10^{-8} \lesssim \dot{M} \lesssim 10^{-7}$ $M_\odot$ yr^{-1} (e.e. Nomoto et al., 2007; Wolf et al., 2013; Hillman et al., 2016).

Accretion rates below this range can result in a net loss of mass for the WD. Hydrogen accumulating on the surface can ignite and burn in a thermonuclear runaway 'nova' eruption (Starrfield et al., 1972), stripping away most of the accreted mass. If the accumulated hydrogen diffuses down and mixes in with the C-O layers of the WD, then further mass loss could occur due to stripping of the original WD material (e.g. Yaron et al., 2005). Accretion rates above the ideal range can result in the WD expanding into a RG configuration (Nomoto, Nariai, and Sugimoto, 1979; Wolf et al., 2013), engulfing the companion in a CE which is eventually ejected, resulting in the suppression or complete interruption of mass growth towards M_{Ch}. However, an optically thick wind originating from the accreted layers of the WD could regulate the growth of high accretion systems (Hachisu, Kato, and Nomoto, 1996).

2.4.1.2 *Double-Degenerate Channel*

The double-degenerate (DD) channel occurs when a WD approaches or exceeds M_{Ch} as a result of merging with a secondary WD, therefore exploding as a Type Ia SN. The classical model involves two C-O WDs of different masses in a binary system that inspiral through radiation of gravitational waves (Iben and Tutukov, 1984; Webbink, 1984; Maguire, 2017). Eventually, the less-massive WD fills its Roche lobe and becomes totally tidally disrupted by the higher-mass WD, resulting in the formation of an accretion disk around the primary WD (e.g. Rasio and Shapiro, 1994; Pakmor et al., 2012).

Accretion of carbon and oxygen rich material avoids the problems of inefficient mass growth from the SD model (see Section 2.4.1.1), however this still doesn't guarantee whether the system will evolve into an SN Ia , which will be largely dependent

on the WD masses and the rate of accretion. Some studies have argued that large accretion rates could result in off-center carbon ignition and burning in the primary WD, transforming it into an O-Ne WD on approach to M_{Ch}, ultimately leading to gravitational instability and accretion-induced collapse to a neutron star (e.g. Nomoto and Iben, 1985; Saio and Nomoto, 1985; Saio and Nomoto, 1998; Yoon, Podsiadlowski, and Rosswog, 2007; Shen et al., 2012). However, if the WD masses and accretion rates are favourable, central carbon ignition in the primary WD can occur and produce a SN Ia explosion (e.g. Yoon, Podsiadlowski, and Rosswog, 2007; Sato et al., 2015).

Explosive carbon detonation can sometimes occur if the interaction of material accreted onto the primary WD results in compressional heating during a so-called 'violent merger' phase (e.g. Pakmor et al., 2012; Raskin et al., 2014; Sato et al., 2015; Pakmor, 2017), resulting in central carbon ignition and a Type Ia SN explosion, or an off-center runaway explosion that detonates the centre regardless. This can occur even if the primary WD is far below M_{Ch} and shares many similarities with the sub-M_{Ch} detonation scenario (e.g. Fink, Hillebrandt, and Röpke, 2007; Sim et al., 2010).

The two C-O WDs could even, in principle, directly collide to produce a Type Ia SN. These collisions are only likely to occur in dense cluster environments Rosswog et al. (e.g. 2009), Raskin et al. (2010), and Lorén-Aguilar, Isern, and García-Berro (2010), or in progenitor systems with third gravitational body that influences the orbits of the two WDs enough to cause a direct collision (e.g. Thompson, 2011; Katz and Dong, 2012; Kushnir et al., 2013).

2.4.1.3 *Core-Degenerate Channel*

The core-degenerate (CD) channel is the merger of a WD and the hot core of an AGB star that results in a Type Ia SN (Livio and Riess, 2003; Kashi and Soker, 2011; Ilkov and Soker, 2012). The initial evolutionary path of the CD channel is identical to the DD channel, where an AGB star fills its Roche lobe and begins to transfer material over to the companion WD. During the mass transfer phase, the AGB star expands and the system evolves into a CE configuration, in which the WD and AGB core inspiral inside the CE (e.g. Rasio and Livio, 1996; Taam and Sandquist, 2000). In the DD scenario, this results in the ejection of CE, followed by the cooling and shrinking of the hot AGB core, resulting in the formation of a close WD-WD binary system, which merges to produce a Type Ia SN. For a graphical representation, refer to Figure 20.

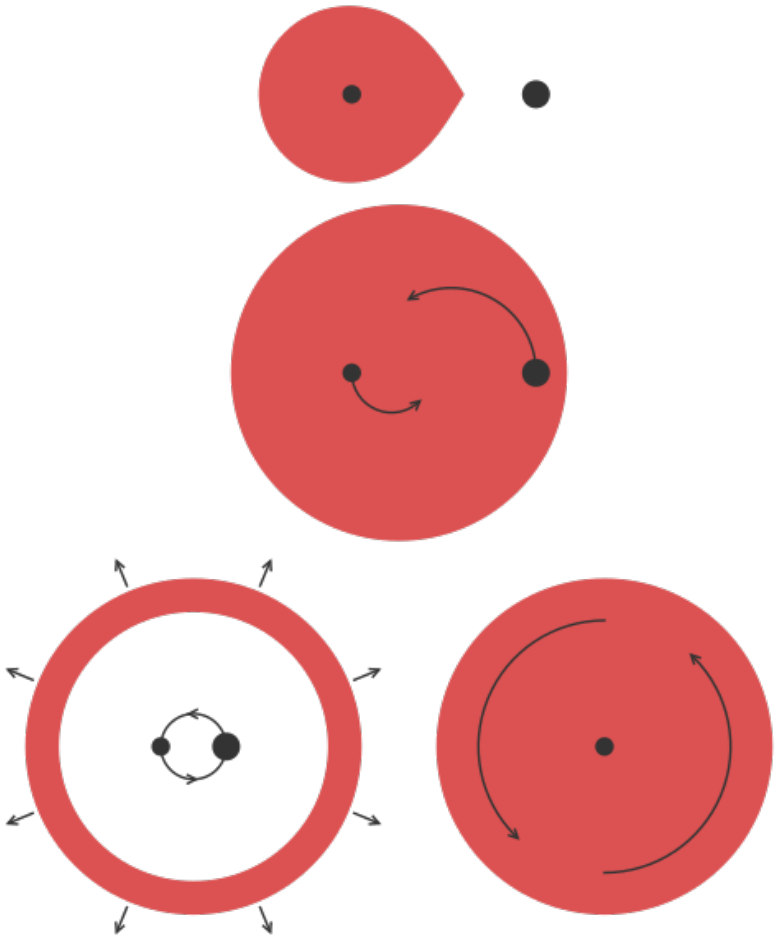

Figure 20: *Top*: An AGB star (left) fills its Roche lobe and begins mass-transfer to the primary WD (right). *Middle*: The mass transfer process is unstable, causing the AGB star to expand and form a CE configuration with the primary WD *Bottom*: In the DD scenario, the envelope is ejected, leaving behind two WDs that eventually inspiral and merge (left). In the CD scenario, the WD merges with the hot AGB core, forming a super-M_{Ch} WD that's supported by angular momentum. *Credit*: Philip D. Hall.

In the CD scenario, the WD and hot AGB core merge during the CE phase, $\sim 10^5$ years after formation of the CE. The resulting merger produces a super-M_{Ch} object that doesn't collapse due to being supported by its high angular momentum (e.g. Yoon and Langer, 2005). Over time the merged object 'spins down' through magnetic dipole radiation until it can no longer be supported by rotation, eventually leading to collapse and detonation of the core (Kashi and Soker, 2011). This scenario has been suggested to explain the detection of a broad Hα component in the spectra of some Type Ia SNe, where the explosion occurred while there was enough CE material around for the SN ejecta to interact with (e.g. Livio and Riess, 2003; Hamuy et al., 2003).

The big drawback to this scenario is that it is yet to be well understood, as no detailed simulations have been performed beyond the initial merger phase of the CD channel (see Aznar-Siguán et al., 2015). Therefore it is still uncertain whether this channel leads to a Type Ia SN explosion.

2.4.1.4 *Cosmological Implications & Constraining Progenitor Models*

Type Ia SNe are standardisable candles used in the measurement of distances at cosmological scales. However, this is dependent on the assumption that the light curves are homogeneous after standardisation ($\sigma_M \sim 0.15$ mag; e.g. Betoule et al. 2014; Macaulay et al. 2017; Jones et al. 2018). If the peak brightness of SNe Ia varies significantly with progenitor model and the progenitor population varies with redshift, then this introduces a major systematic into the standardisation process that would significantly bias cosmological analyses (Childress, Wolf, and Zahid, 2014). In other words the intrinsic properties of the SN Ia light curve is not distance-independent, as previously thought. This is especially problematic, since the standardisation process corrects the peak absolute *B*-band magnitude of the SN Ia light curve based on observations of low-z populations (e.g. see Zhang et al., 2017, and references therein).

One of the major differences between progenitor models is the 'delay time' between the formation of the progenitor system from an instantaneous burst of star formation in the host, to the subsequent explosion as a Type Ia SN. Measuring the delay time is impossible to do on a case-by-case basis for each SNe Ia, however analysing the delay time distribution (DTD) for entire populations can provide inference into the underlying progenitor systems (Maoz and Mannucci, 2012). Scannapieco and Bildsten (2005),

Mannucci et al. (2005), Mannucci, Della Valle, and Panagia (2006), and Sullivan et al. (2006) have all suggested that the DTD can be described by a two-component distribution, containing both 'prompt' and 'delayed' channels (with short and long delay times respectively). This suggests that the dominant progenitor channel could vary with redshift, i.e. progenitors with long delay times will likely explode at lower redshifts compared to progenitors with shorter delay times.

This is a very natural explanation as the DD channel is more likely to exhibit longer delay times compared to the SD channel. The SD channel is dependent on Roche lobe overflow, which is expected to occur towards the end of the MS life for the companion. The DD channel depends on the transformation of the companion to a WD that inspirals with the primary WD through radiation of gravitational waves, leading to an eventual merger (either dynamically or violently) and a Type Ia SN. Therefore it's plausible that the SD progenitor channel traces the cosmic star formation rate and the DD will likely have a longer delay between star formation and explosion (Sullivan et al., 2006; Strolger et al., 2020). The CD channel is also likely to have a long delay time, mainly due to the time predicted for a super M_{Ch} WD to spin down enough to no longer be supported by angular momentum ($10^6 < t < 10^{10}$ years; Ilkov and Soker 2012). However, no plausible inferences can be made regarding the DTD of the CD channel until it is better understood through observations and simulation.

A simpler parameterisation of the DTD, follows a t^{-1} relation, where t is the delay time. This power law is in good in reproducing the observed SN Ia rate (Maoz, Mannucci, and Brandt, 2012; Graur and Maoz, 2013; Graur et al., 2014; Frohmaier et al., 2019) although this relation breaks down when $t < 10^9$ years. This is also in good agreement to theoretical predictions of the DTD for the DD channel (e.g. Yungelson and Livio, 1998; Greggio, 2005). Binary population synthesis models predict the delay time of the SD channel to typically be between 10^8 and 10^9 years after formation (e.g. Mennekens et al., 2010; Claeys et al., 2014). The longer delay time SD systems (e.g. with a RG donor) can reproduce the t^{-1} relation, but binary population synthesis models predict very few of them. However, there is still potential for contribution for SD systems with short delay times ($t < 10^9$ years), as this region of parameter space is not well constrained (see Maoz, Mannucci, and Nelemans, 2014).

However, analysis of the DTD for SN Ia populations is not yet enough to truly discriminate between progenitor channels. Direct observations from the moment of ex-

plosion will provide a stronger insight into the nature of the progenitor channels compared to inference from late-time observations. Early photometry obtained within the initial hours/days of the explosion will allow constraints on properties like the radii of the progenitor star and its possible companion (e.g. Kasen, 2010; Nugent et al., 2011; Bloom et al., 2012; Goobar et al., 2014, 2015; Fausnaugh et al., 2019; Yao et al., 2019). The shape and duration of the rising light curve can be used to infer the radial distribution of ^{56}Ni and the existence of any circumstellar material (e.g. Dessart et al., 2014; Piro and Nakar, 2014; Firth et al., 2015; Piro and Morozova, 2016; Miller et al., 2018, 2020; Magee et al., 2020). The early colour evolution can also provide a direct way of discriminating between progenitor models, by probing the location of ^{56}Ni in the SN ejecta (Dessart et al., 2014; Bulla et al., 2020). The prospect of performing early-time observations of gravitationally lensed SNe is discussed in Chapter 5.

3

STRONG GRAVITATIONAL LENSING

3.1 A BRIEF HISTORY

Gravitational lensing occurs when the path of a ray of light is deflected from its original path due to the influence of an intervening gravitational body and is a direct consequence of general relativity (GR) (Einstein, 1915). The initial hypothesis of lensing could arguably date back to 1704 as a result of the corpuscular theory of light, where a 'particle' of light was subject to the gravitational field of a body of mass (Newton, 1704). Soldner (1804) is credited for the initial calculation for the deflection angle of light, who used a Newtonian derivation. Einstein (1915) re-derived the deflection angle (Equation 18) using the field equations from GR, which differed from the Soldner (1804) calculation by a factor of 2. The first observation of gravitational lensing took place in 1919, where a scientific collaboration fronted by Arthur Eddington and Frank Watson Dyson witnessed a deviation of 1.7″ in the position of stars about the sun's corona during a total solar eclipse, confirming Einstein's predictions (Dyson, Eddington, and Davidson, 1920).

The possibility of multiple images resulting from gravitational lensing was acknowledged by Einstein (1936). However, he only considered the phenomenon on a stellar scale and hence dismissed the possibility of observation, stating that multiple imaging of stars required a very precise, and hence negligibly probable alignment of two stellar objects. This hypothesis was widely accepted until Zwicky (1937a,b) postulated that extended objects such as galaxies have a non-negligible probability of being observed as multiple distinct images if gravitationally lensed by a foreground galaxy cluster. This idea was later extended to include individual galaxies as foreground lenses with observable effects (Rubin and Ford, 1970; Rubin, Ford, and Thonnard, 1978). Zwicky's work largely fell into obscurity until Refsdal (1964, 1966) proposed that gravitational lenses could be used to measure the Hubble constant (H_0), independently of other methods. This technique relied on using a variable source, e.g. a supernova (SN), exploiting that the lensing effect imparts a 'time delay' between the arrival time of photons between each image.

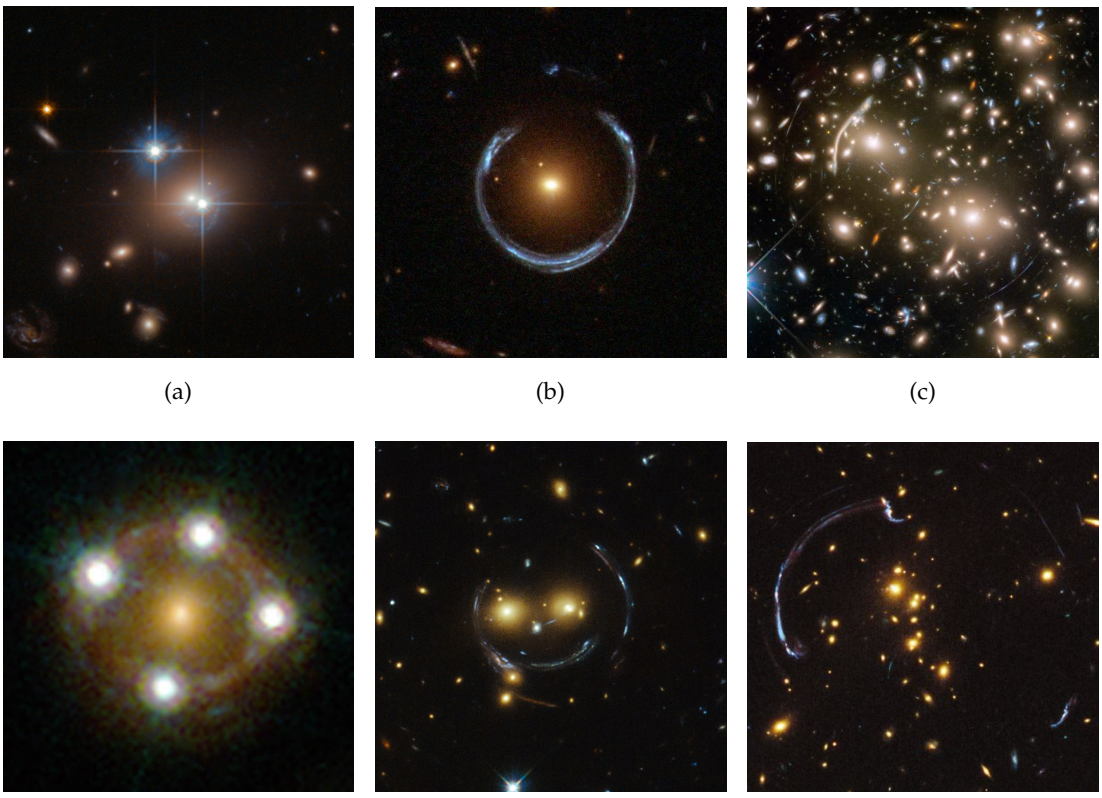

(a) (b) (c)

(d) (e) (f)

Figure 21: Colour composite images of gravitational lenses taken by the Hubble Space Telescope: (a) QSO 0957+561 a.k.a. the 'Twin Quasar'; (b) LRG 3-757 a.k.a. the 'Cosmic Horseshoe'; (c) Abel 370 (d) HE0435-1223; (e) SDSS J1038+4849; (f) RCS2 032727-132623. *Image Credits*: NASA, ESA, Hubble, J. Lotz and the HFF Team, Suyu et al., J. Rigby (NASA Goddard Space Flight Center), K. Sharon (Kavli Institute for Cosmological Physics, University of Chicago), M. Gladders and E. Wuyts (University of Chicago), and the Hubble Heritage Team (STScI/AURA).

The first observation of strong gravitational lensing, i.e. with multiple images, occurred when Walsh, Carswell, and Weymann (1979) observed a set of two identical quasars QSO 0957+561, dubbed the 'Twin Quasar' (see Figure 21 for Hubble Space Telescope (HST) images of the 'Twin Quasar' and a selection of other strong gravitational lenses). To date, several hundred strong lenses have been discovered by various surveys including: Cosmic Lens All-Sky Survey (Myers et al., 2003; Browne et al., 2003), Sloan Digital Sky Survey (Bolton et al., 2006, 2008; Hennawi et al., 2008; Kubo et al., 2009; Brownstein et al., 2011; Shu et al., 2016), COSMOS (Faure et al., 2008; Jackson, 2008), Canada-France-Hawaii Telescope Legacy Survey (More et al., 2012), Herschel Astrophysical Terahertz Large Area Survey (Negrello et al., 2010; Wardlow

et al., 2012), South Pole Telescope (Wardlow et al., 2012; Hezaveh et al., 2013), Gaia (Lemon et al., 2018; Lemon, Auger, and McMahon, 2019; Delchambre et al., 2019), Dark Energy Survey (Diehl et al., 2017; Treu et al., 2018; Anguita et al., 2018; Jacobs et al., 2019), Kilo-Degree Survey (Petrillo et al., 2019), Pan-STARRS1 (Rusu et al., 2019a), and Subaru Hyper Suprime-Cam survey (Sonnenfeld et al., 2018; Wong et al., 2018).

3.2 APPLICATIONS OF STRONG LENSING

In this section I will be discussing the applications of strong lensing, in particular by galaxies. Gravitational lensing has a plethora of applications in astronomy, however this section only covers a small selection, with time delay cosmography and microlensing covered in later sections. For the interested reader, there exists reviews and textbooks which cover the applications of strong lensing in further depth (e.g. see Treu, 2010; Treu and Marshall, 2016; Congdon and Keeton, 2018, and the extensive references therein).

The first major application of strong lensing is that it is an excellent probe of mass at galactic and sub-galactic scales. The lensing effect is extremely sensitive to the mass of the foreground lensing galaxy, therefore the mass contained within the Einstein radius of the lens can be well measured (to within a few percent). The mass measured with lensing often exceeds the visible stellar mass, providing a strong argument for the existence of dark matter (e.g Kochanek, 1995). A powerful method to detect the presence of a dark matter halo is to combine lensing measurements with other observations, particularly the stellar lens kinematics of the lens galaxy. The lens kinematics probes the mass distribution of the lens galaxy on smaller scales and is effective at constraining degeneracies such as the mass-anisotropy degeneracy when combined with lensing (e.g. see Treu and Koopmans, 2004; Beaulieu et al., 2006).

Not only is strong lensing an effective probe of the presence of dark matter, the lensing observables are also sensitive to the presence of substructure in the lens, leading to inconsistencies with a predicted smooth mass model. We discuss this effect on the smallest observable scales (i.e. microlensing) in Section 3.4, however the intermediate angular scales between 'macrolensing' and microlensing lies the regime of 'millilensing'. Millilensing results in anomalous flux-ratios between lensed images that are not predictable with a smooth macro mass model (e.g. Mao and Schneider,

1998; Metcalf and Madau, 2001; Dalal and Kochanek, 2002; Chiba, 2002). However, research has shown that the anomalies can also affect other observables such as time delays (e.g. Keeton and Moustakas, 2009) and image positions (e.g. Chen et al., 2007). Therefore, strong lensing is an effective way to test for the existence of dark matter 'subhalos', providing a critical test for the model of cold dark matter. This is especially important due to the 'missing satellites' or 'excess subhalos' problem where cold dark matter (CDM) models predict a larger number of satellite galaxies than is observationally present (see Kravtsov, 2010, for a review).

Strong lenses also make effective cosmic telescopes due to the effect of magnification, capable of increasing the brightness of background sources by orders of magnitude (see Treu, 2010). This enables the better study of faint objects at high redshift and can even make observations of previously undetectable objects possible. As a consequence, strong lensing can aid the understanding of source populations and their evolution as a function of redshift. For example, one source population of interest are dusty star-forming galaxies (DSFGs). These galaxies are responsible for a substantial fraction of star formation in the early universe and are critical in the understanding of galaxy evolution, however they are completely obscured at optical wavelengths (see Casey, Narayanan, and Cooray, 2014, for a review). Strong lensing has allowed these objects to be studied in much higher resolution and the brightest observed DSFGs are strongly lensed (e.g. see Negrello et al., 2010; Hezaveh and Holder, 2011; Hezaveh et al., 2013). In particular, the increased signal-to-noise due to strong lensing magnification has enabled spectroscopic and kinematic studies of distant DSFGs (e.g. Geach et al., 2018; Rivera et al., 2019).

The main limitation of strong lensing analyses are the lack of suitable systems in the known lens sample. However, there is significant promise to dramatically increase the known lens sample size with the next generation of wide-field surveys including the Legacy Survey of Space and Time (LSST) and Euclid. LSST, part of the Vera Rubin Observatory, is a ground-based survey that will image the whole southern sky ($\sim$ 20000 deg) in multiple filters every few days with sub-arcsecond resolution (0.7" median seeing limit) to a total point source depth of $r \sim 27.5$. Euclid is a space-based telescope with a 1.2m diameter primary mirror, operating a wide-field optical imager (VIS) and a near infrared photometer and spectrograph (NISP). Euclid will perform four high-cadence surveys: one wide-field survey ($\sim$ 15000 deg) and three deep-field

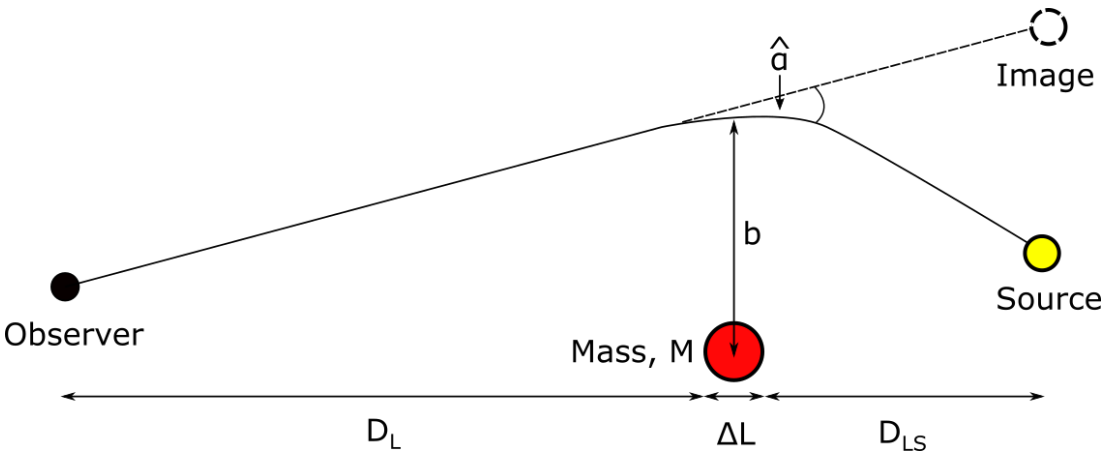

Figure 22: Diagram showing the deflection of a light ray due to an intervening point mass along the line of sight. The light ray at distance b from the point mass M is deflected by angle $\hat{\alpha}$.

surveys ($\sim$ 40 deg) across the night sky. VIS has a field of view of 0.57deg^2 (almost 180x that of Hubble) with a mean resolution limit of 0.23" across one broadband filter to a depth of $\sim$ 24.5, proving very useful for follow-up imaging of strong lenses. LSST and Euclid are predicted to find $\sim 10^5$ galaxy-galaxy strong lens systems over the next decade (Collett, 2015).

3.3 STRONG LENSING THEORY

According to GR, a light ray passing at distance b from a point mass M is deflected by angle $\hat{\alpha}$ (as illustrated in Figure 22), where:

$$\hat{\alpha} \equiv \frac{4GM}{c^2 b}. \tag{18}$$

Note this equation only holds for small $\hat{\alpha}$. To produce multiple imaging on an observable scale, extended and diffuse bodies are required. Since the size of the lens is negligible compared to the relative distances between the observer/lens/source, we can assume the thin lens approximation, i.e. we can project the 3D mass distribution as a 2D sheet of mass on the sky. The total deflection angle can therefore be calculated by summing over all mass elements m_i on the projected 2D mass-sheet:

$$\vec{\hat{\alpha}}(\vec{\xi}) = \sum_i \frac{4Gm_i}{c^2} \frac{\vec{\xi} - \vec{\xi}_i}{|\vec{\xi} - \vec{\xi}_i|^2}, \tag{19}$$

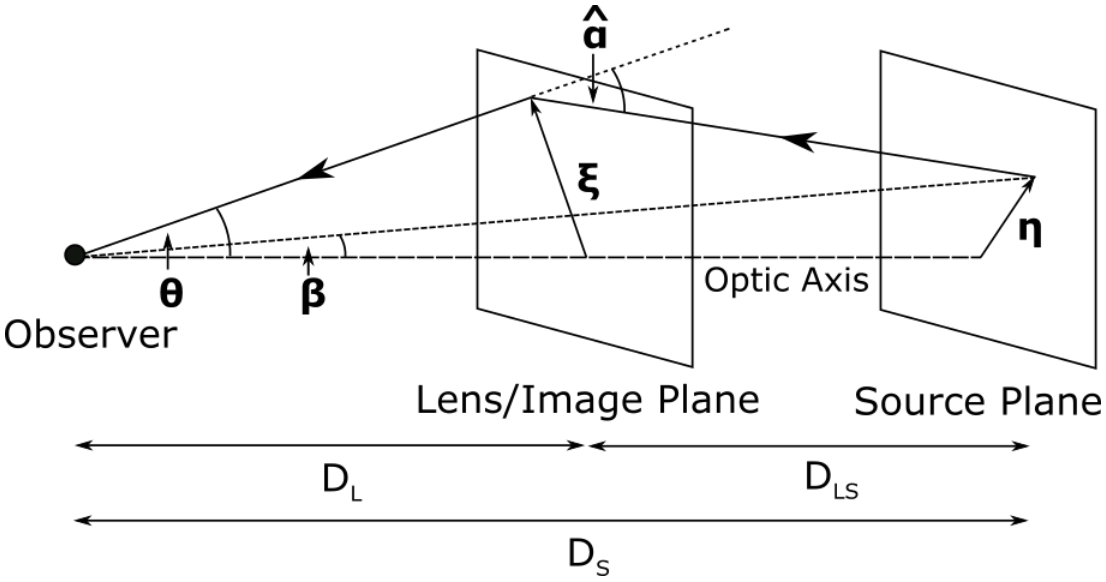

Figure 23: Diagram of a simple gravitational lensing system.

where $\vec{\xi}$ and $\vec{\xi}_i$ respectively denote the positions of the light ray and the mass element m_i on the lens plane, i.e. $b = \vec{\xi} - \vec{\xi}_i$. We characterise the mass-sheet in terms of its surface mass density:

$$\Sigma(\vec{\xi}) \equiv \int \rho(\vec{\xi}, z)\,dz. \tag{20}$$

In the small mass limit we can define $dm = d^2\xi\,\Sigma(\vec{\xi})$, where $d^2\xi$ is a surface element on the lens plane, and replace the sum with an integral:

$$\vec{\alpha}(\vec{\xi}) = \frac{4G}{c^2}\int d^2\xi'\,\Sigma(\vec{\xi}')\frac{\vec{\xi}-\vec{\xi}'}{|\vec{\xi}-\vec{\xi}'|^2}. \tag{21}$$

The gravitational lensing effect is described by the lens equation, with characteristic length scale determined by the Einstein radius θ_{Ein}:

$$\vec{\beta} = \vec{\theta} - \vec{\alpha}(\vec{\theta}), \tag{22}$$

$$\theta_{Ein} \equiv \sqrt{\frac{4GM}{c^2}\frac{D_{LS}}{D_L D_S}}, \tag{23}$$

where the two dimensional vectors $\vec{\beta}$ and $\vec{\theta}$ denote the angular positions on the source and image plane, respectively. $\vec{\alpha} \equiv \vec{\hat{\alpha}}(D_L\vec{\theta})\frac{D_{LS}}{D_S}$ is the scaled deflection angle, hereby referred to as the deflection angle. D_L, D_S, D_{LS} are the angular diameter

distances between the observer/lens, observer/source and lens/source. Figure 23 shows that the lens equation (Equation 22) can be derived geometrically by observing that $\vec{\theta}D_S = \vec{\beta}D_S + \vec{\alpha}D_{LS}$. The lens equation effectively describes the lensing effect as a remapping of the source plane coordinates onto the observed image plane.

The deflection angle $\vec{\alpha}$ can be written terms of the observed angular position $\vec{\theta}$ on the image plane:

$$\vec{\alpha}(\vec{\theta}) = \frac{1}{\pi}\int d\vec{\theta}' \frac{\vec{\theta} - \vec{\theta}'}{|\vec{\theta} - \vec{\theta}'|^2}\kappa(\vec{\theta}'), \tag{24}$$

where κ, often referred to as convergence, is the projected surface mass density distribution Σ in units of the critical surface density Σ_{cr}:

$$\kappa(\vec{\theta}) \equiv \frac{\Sigma(D_L\vec{\theta})}{\Sigma_{cr}}, \tag{25}$$

where

$$\Sigma_{cr} \equiv \frac{c^2}{4\pi G}\frac{D_S}{D_L D_{LS}}. \tag{26}$$

We define the lens potential, which can be described as a scaled projection of the Newtonian gravitational potential Φ:

$$\psi(\vec{\theta}) \equiv \frac{2}{c^2}\frac{D_{LS}}{D_L D_S}\int \Phi(D_L\vec{\theta}, z)dz = \frac{1}{\pi}\int d^2\theta' \kappa(\vec{\theta}')\ln|\vec{\theta} - \vec{\theta}'|, \tag{27}$$

such that the deflection angle $\vec{\alpha}$ is simply the gradient of the lens potential ψ, and the convergence κ is half the laplacian of the lens potential ψ:

$$\vec{\alpha}(\vec{\theta}) = \vec{\nabla}\psi(\vec{\theta}), \tag{28}$$

$$\kappa(\vec{\theta}) = \frac{1}{2}\vec{\nabla}^2\psi(\vec{\theta}). \tag{29}$$

We define the Jacobian of the lens equation, A:

$$A \equiv \frac{\partial\vec{\beta}}{\partial\vec{\theta}}. \tag{30}$$

The magnification by lensing is related to the determinant of the lensing Jacobian A:

$$\mu = \frac{1}{\det(A)}, \tag{31}$$

where the flux is magnified by a factor of $|\mu|$ and the sign denotes the image parity, i.e. whether the image is flipped or not. The magnification is formally infinite when

$\det(A) = 0$. On the image plane, these regions form closed curves called 'critical curves'. The corresponding regions on the source place when acted on via the lens equation (Equation 22) are referred to as 'caustics'. The source position relative to the caustics determines the multiplicity of the images on the image plane (see Figure 24). Sources located outside the outer caustic form will not be strongly lensed. As the source crosses the outer and inner caustics, the number of images will increase or decrease by two. Typically, sources located close to caustics are most often observed due to magnification bias, i.e. the magnification is large enough to surpass detection limits of most telescopes. Additional central images can be observed if the density profile about the center of the lens is shallow enough, resulting in systems with an odd number of observable images. Central images are typically heavily demagnified, however there exists rare scenarios where the lens produces a central image that is magnified (e.g. Collett et al., 2017).

3.4 MICROLENSING

Most lensing theory is dependent on the assumption that the foreground lensing objects have smooth mass distributions, i.e. they follow the regime of 'macrolensing'. However, in reality, these mass distributions are not smooth and in fact are composed of many individual sub-structures. As the size of a background source decreases relative to the foreground, it becomes sensitive to lensing by structures on smaller and smaller scales. In particular, this section will be discussing the regime of 'microlensing' by individual stars, where the typical image separations are too small to be resolved and the only observable is the total magnification of a background source (see e.g. Wambsganss, 2006; Congdon and Keeton, 2018, for further reading).

In a strong lensing system, individual stars in the foreground lensing galaxy can introduce additional microlensing events to each of the multiple images (Schechter and Wambsganss, 2002; Kochanek, 2004). Due to the random relative motion of stars in the lensing galaxy, the effect and precise time-frames of microlensing events is often stochastic and seldom predictable (e.g. Dobler and Keeton, 2006). Each image is affected independently, such that understanding the microlensing of one lensed images yields no information on the other images. As alluded to previously, the amount of microlensing is dependent on the source size, and is most significant for

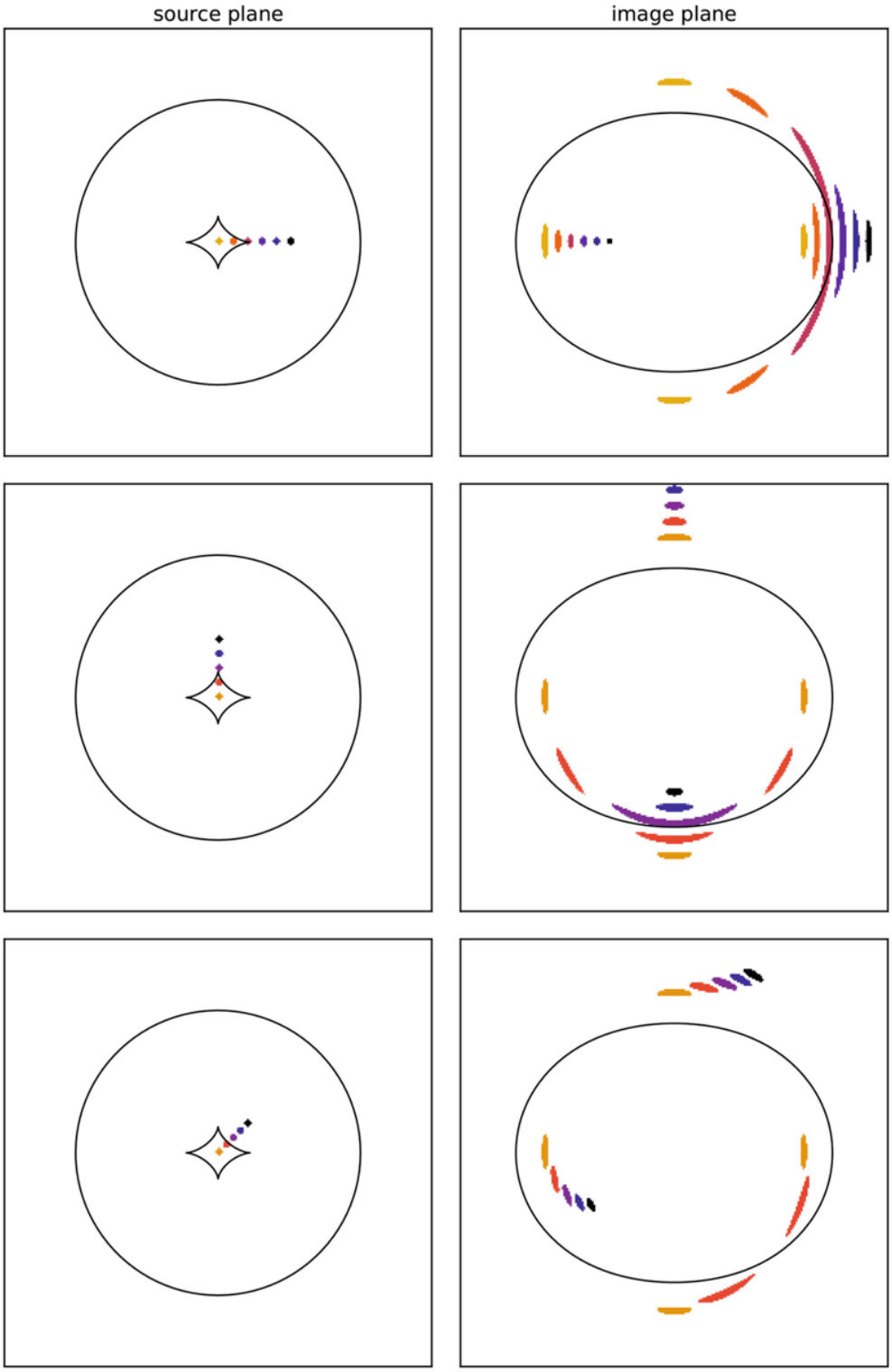

Figure 24: Image configurations for an singular isothermal sphere (SIS) lens with external shear. The caustics/critical curves in the source/image plane are represented by the solid black lines. Note as the source crosses the inner caustic in the source plane, the number of images in the image plane increases or decreases by 2. Figure taken from Congdon and Keeton (2018).

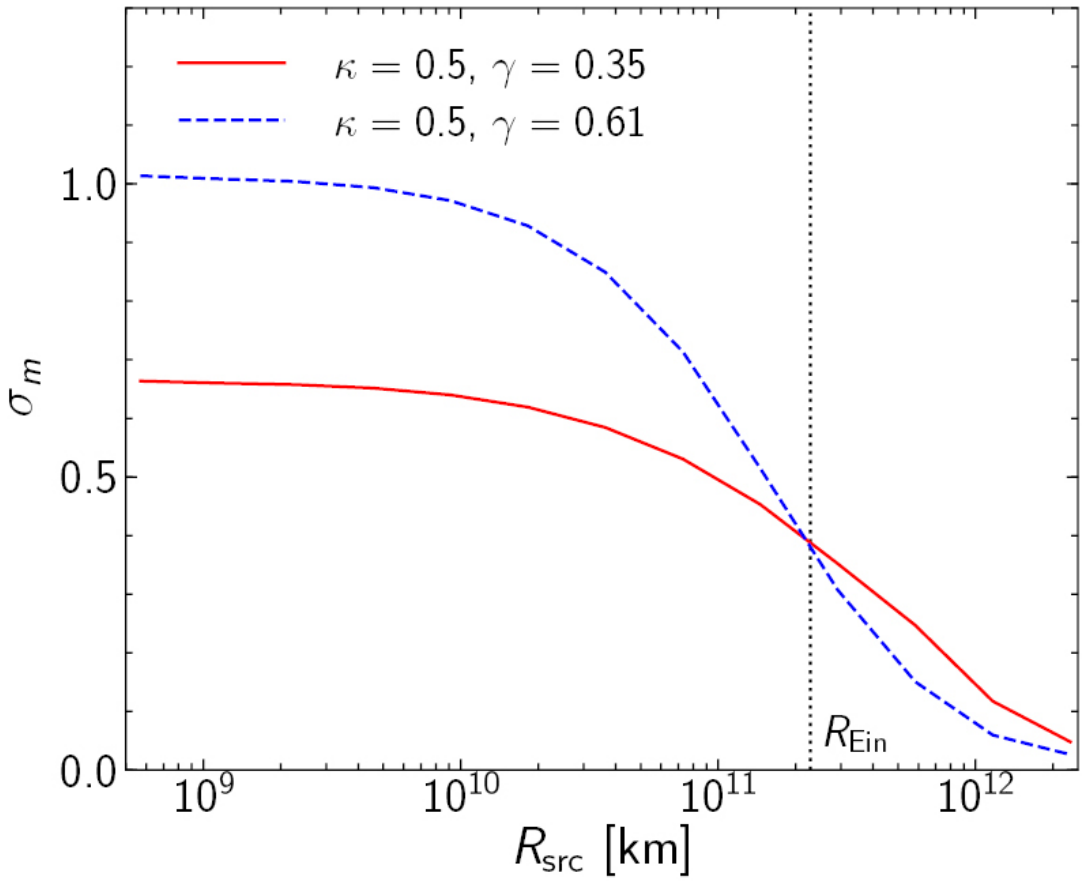

Figure 25: Microlensing scatter (in magnitudes) as a function of source size, computed using microlensing maps from the GERLUMPH project (Vernardos et al., 2014, 2015). This is assumed for a source at redshift $z_s = 1$, a lens at redshift $z_l = 0.5$, and an average stellar mass of 0.3 $M_\odot$ in the foreground lens. The solid line represents an image with positive parity and the dashed line represents a negative parity image. The mass projected onto the images is split 50/50 between dark matter and stellar matter. The source is assumed as a disk with uniform brightness. Figure taken from Oguri (2019).

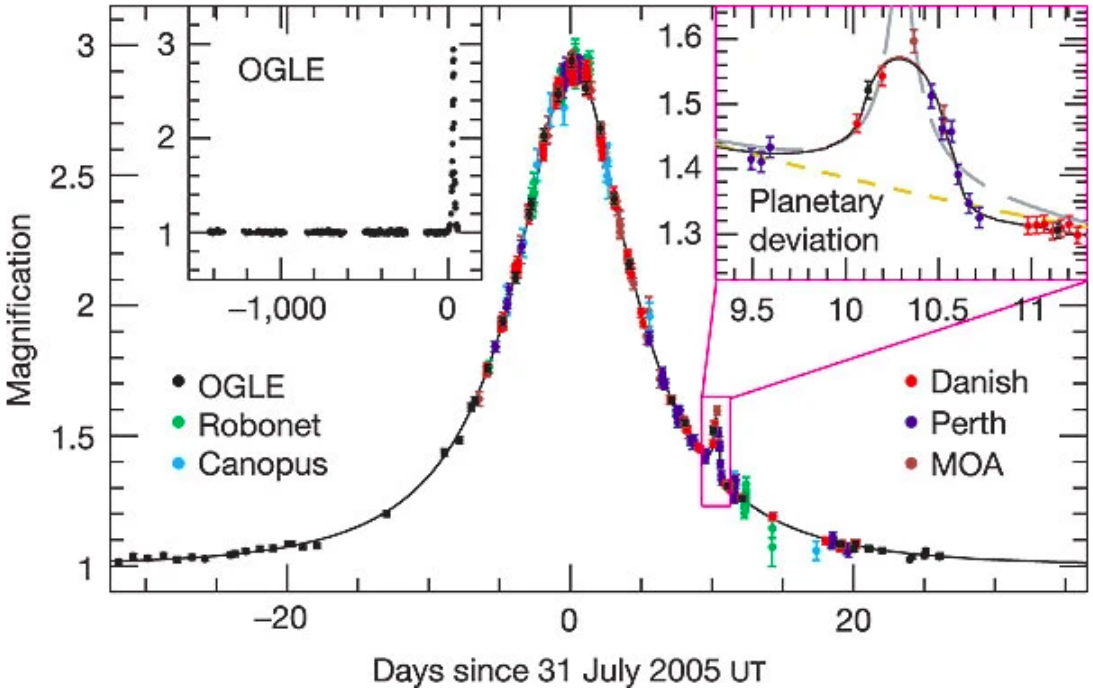

Figure 26: A microlensing event caused by the exoplanet OGLE-2005-BLG-390. Note the initial magnification from the foreground star and the secondary magnification as a result of the exoplanet crossing the line of sight. Figure from Beaulieu et al. (2006).

sources smaller than the Einstein radius of the lens (Chang and Refsdal, 1979; Mortonson, Schechter, and Wambsganss, 2005), however the effect becomes significantly suppressed for sources larger than the Einstein radius. This is illustrated in Figure 25.

Microlensing of lensed images will not perturb the image positions on an observable scale, but will have a significant impact on other strong lensing observables. For example, the additional magnifications can introduce anomalous flux ratios between the lensed images, biasing any lens models, and significantly distorting the light curves of the background source (e.g. Dobler and Keeton, 2006). In particular, microlensing can also affect measurements of the time delay between the multiple images. This has significant cosmological implications when using time delays to measure H_0, since the transverse motion of stars makes microlensing magnifications a time-domain effect, potentially mimicking intrinsic source variations (e.g. Bonvin et al., 2017).

Whilst microlensing is often a source of systematics in strong lensing, it does have other useful applications in astronomy (see Treu, 2010; Congdon and Keeton, 2018,

for in-depth discussions). Initially, microlensing was used to search for and place constraints on massive compact halo objects (MACHOs), a candidate form of dark matter in the Milky Way, by monitoring the brightness of stars in the Magellanic Clouds (e.g. see Paczynski and Zytkow, 1978; Alcock et al., 2000; Tisserand et al., 2007; Wyrzykowski et al., 2011a; Wyrzykowski et al., 2011b). Microlensing has also been a tool for finding extrasolar planets (e.g. see Beaulieu et al., 2006; Gaudi et al., 2008; Batista et al., 2011; Udalski et al., 2015), where foreground stars with an orbiting planet will create observable features when they gravitationally lens the light from background sources. The foreground star will initially magnify the light from the background source and the planet will add further, more rapid magnifications to the light curve as it crosses the line of sight (see Figure 26). For a discussion of the methods and results of microlensing searches of exoplanets, see Gaudi (2012). For further discussions of the general astrophysical applications of microlensing see e.g. Mao (2012) and Congdon and Keeton (2018).

3.5 TIME DELAY COSMOGRAPHY

Strong lenses can be used to directly measure H_0, independently of the cosmic distance ladder, due to their sensitivity to the ratio of angular diameter distances between the observer, the lens and the background source (see Section 1.4.2, Refsdal 1964 and Treu and Marshall 2016 for a comprehensive and recent review). Whilst the time delays are dependent on the choice of cosmology, its effects are sub-dominant compared to the dependence on H_0 and measurements are largely non-degenerate with the other cosmological parameters (see Figure 6, also see Bonvin et al. 2017; Wong et al. 2017).

For each image in a lensing system, the rays of light take a different set of paths in order to reach the observer. As a result, the arrival time for each image is affected by geometrical changes in the path length of the light (due to the local changes in the curvature around the lens) and additional time dilation effects due to the light's interaction through the gravitational potential of the lens (Shapiro, 1964), i. e.:

$$t = t_{\text{geometric}} + t_{\text{gravitational}}. \tag{32}$$

For a given position on the source place $\vec{\beta}$, position on the image plane $\vec{\theta}$ and lensing potential $\psi(\vec{\theta})$, the excess time delay can be derived using Fermat's principle:

$$t = \frac{D_{\Delta t}}{c}\left(\frac{1}{2}|\vec{\theta} - \vec{\beta}|^2 - \psi(\vec{\theta})\right), \tag{33}$$

where c is the speed of light and $D_{\Delta t}$ is a quantity known as the time delay distance (see Equation 37). The lensing potential obeys the 2D Poisson equation $\nabla^2\psi = 2\kappa$. Images will form at the stationary points of the time delay surface, i.e. where the path length of the light is minimised. By taking the derivative of Equation 33 at extrema we can derive the lens equation (Equation 22):

$$\begin{aligned} 0 &= \vec{\nabla}_\theta\left(\frac{1}{2}|\vec{\theta} - \vec{\beta}|^2 - \psi(\vec{\theta})\right) \\ &= \vec{\theta} - \vec{\beta} - \vec{\nabla}_\theta\psi(\vec{\theta}). \end{aligned} \tag{34}$$

If the unlensed source was to vary in luminosity, then the luminosity of each image would also vary, however not at the same time. The variation in each image would occur asynchronously relative to the other images. Hence in principle, the time delay between two lensed images can be measured noting the time difference of the same event in each lensed image. The time delay between angular positions $\vec{\theta}_i$ and $\vec{\theta}_j$ on the image plane is given by:

$$\Delta t_{ij} = t(\vec{\theta}_i, \vec{\beta}) - t(\vec{\theta}_j, \vec{\beta}). \tag{35}$$

By substituting Equation 33 into Equation 35, we obtain the time delay as a function of the angular positions on the image/source plane $(\vec{\theta}, \vec{\beta})$, the lensing potential $\psi(\vec{\theta})$ and the time delay distance $D_{\Delta t}$:

$$\Delta t_{ij} = \frac{D_{\Delta t}}{c}\left[\frac{(\vec{\theta_i} - \vec{\beta})^2}{2} - \psi(\vec{\theta_i}) - \frac{(\vec{\theta_j} - \vec{\beta})^2}{2} + \psi(\vec{\theta_j})\right], \tag{36}$$

where the time delay distance $D_{\Delta t}$ is defined as:

$$D_{\Delta t} = (1 + z_L)\frac{D_L D_S}{D_{LS}} \propto \frac{1}{H_0}, \tag{37}$$

where z_L is the redshift of the lens.

3.6 MASS-SHEET DEGENERACY

One inherent problem in the analysis of strong lensing systems is the various degeneracies associated with the lens equation. One such degeneracy is the mass-sheet

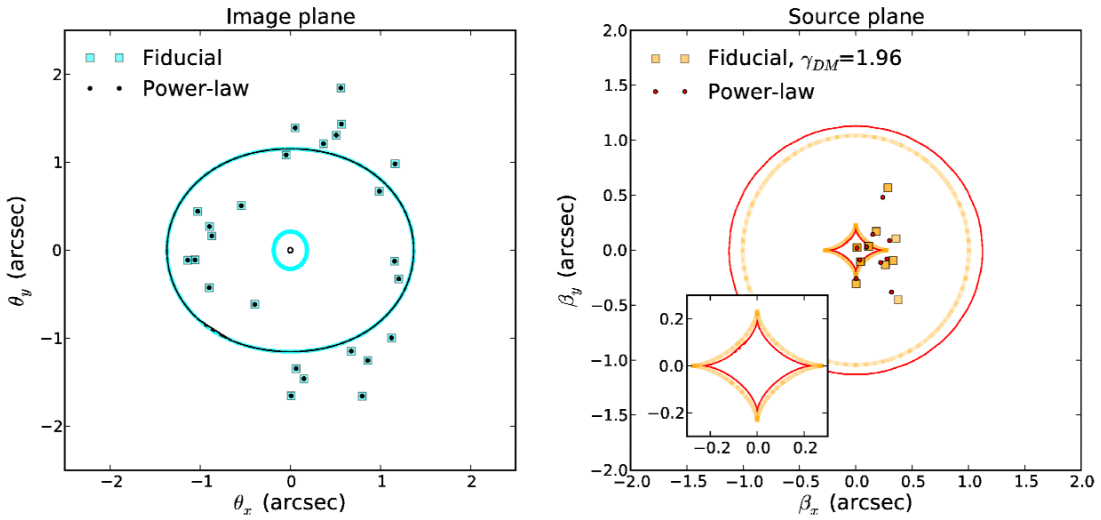

Figure 27: Example of a fiducial complex mass model lensing 10 background point sources, with observables that are well reproduced by a simpler power law mass profile. *Left:* The power-law mass model correctly reproduces the observed image configuration of the more complicated fiducial mass profile. *Right:* The true source positions and caustics however are significantly less well produced by the power-law mass profile. This has implications on the time delays and hence any measurement of H_0. Figure taken from Schneider and Sluse (2014).

degeneracy (Falco, Gorenstein, and Shapiro, 1985). Let's consider a lensing system where we add an external mass sheet of constant convergence and infinite area along the line of sight. The external lensing potential is defined as follows (see Congdon and Keeton, 2018, for a derivation):

$$\psi_{\text{ext}} = \frac{1}{2}\kappa_{\text{ext}}|\vec{\theta}|^2. \tag{38}$$

The lens equation for the combined potential then becomes:

$$\begin{aligned}\vec{\beta} &= \vec{\theta} - \vec{\nabla}\left(\psi(\vec{\theta}) + \frac{1}{2}\kappa_{\text{ext}}|\vec{\theta}|^2\right) \\ &= (1-\kappa_{\text{ext}})\vec{\theta} - \vec{\nabla}\psi(\vec{\theta}).\end{aligned} \tag{39}$$

We can recover the lens equation (Equation 22) by applying the following transformations:

$$\vec{\beta} \to (1-\kappa_{\text{ext}})\vec{\beta}, \tag{40}$$

$$\psi \to (1-\kappa_{\text{ext}})\psi(\vec{\theta}) + \frac{1}{2}\kappa_{\text{ext}}|\vec{\theta}|^2. \tag{41}$$

In other words we have rescaled the above lensing system to produce identical image configurations to a seemingly equivalent system without an external mass sheet. This is particularly problematic, since the transformation affects time delays as follows:

$$\Delta t_{ij} \rightarrow (1 - \kappa_{ext})\Delta t_{ij}, \tag{42}$$

which has strong implications to bias cosmological analyses, as the transformation carries through to any measurement of H_0 through time delay cosmography, i.e.:

$$\Delta H_0 \rightarrow (1 - \kappa_{ext})H_0. \tag{43}$$

Determining the value of κ_{ext} is impossible from modelling of the image configuration alone. The observer could choose to make an assumption about the overall mass model and assume no mass sheet (i.e. $\kappa_{ext} = 0$), however this carries significant uncertainty. Whilst an infinite mass sheet isn't physically plausible, the effect could be reproduced for example by an unknown quantity of mass along the line of sight with constant convergence, e.g. a distribution of smooth dark matter. However, it's important to explicitly state that the mass-sheet degeneracy isn't exclusive to external forms of convergence that may exist along the line of sight. The degeneracy stems from different scalings of the foreground mass distribution producing indistinguishable observables and is ultimately mathematical in nature (e.g. see Schneider and Sluse, 2014, for an alternative formalism for the mass-sheet transformation and further discussion). In other words, the degeneracy also exists in the choices of lens models themselves (see Figure 27). Therefore, in order to obtain any reliable measurement of the time delays and H_0, breaking the mass-sheet degeneracy (by determining κ_{ext}) is of particular importance.

Breaking the mass-sheet degeneracy is possible thorough obtaining additional information about the lensing system. One method is to determine the magnification factor μ, which is affected by the transformation as follows:

$$\mu \rightarrow (1 - \kappa_{ext})^{-2}\mu. \tag{44}$$

Since the transformation does not affect the flux ratios between the multiple images, obtaining the intrinsic brightness of the background source will allow determination of κ_{ext}. This is possible if the background was a standard candle such as a Type Ia SN (see Section 3.7 and Chapter 4). Another key method is to obtain an independent

mass estimate of the lens. This is achievable for example by understanding the kinematics of the lens through spectroscopy and obtaining a measurement of the velocity dispersion (e.g. see Schneider and Sluse, 2014, and references therein for further discussion). Another way to break the mass-sheet degeneracy is through the strong lensing of an additional background source at an independent redshift to lensing system components (e.g. AbdelSalam, Saha, and Williams, 1998).

3.7 STRONGLY LENSED SUPERNOVAE

As mentioned in Section 3.6, lens models are subject to the mass-sheet degeneracy. One of the key methods to break the mass-sheet degeneracy is obtaining the absolute magnifications of the lensed images, which is achievable by knowing the intrinsic luminosity of the source. As mentioned in Section 2.4, Type Ia SNe are standardisable candles in which the intrinsic luminosity can be inferred after applying empirical corrections to their relatively homogeneous light curves. Hence if a Type Ia SN was to be strongly lensed by a foreground mass distribution, it would be extremely effective in breaking the mass-sheet degeneracy if standardised (see Oguri, 2019, for a recent and extensive review on the strong lensing of transients, including SNe).

The concept of gravitationally lensed supernovae (gLSNe) originally dates back to Refsdal (1964), when he suggested that the time delays of gLSNe could be used to independently directly probe H_0. However, these systems were exceptionally rare and none were discovered for almost half a century since. As a result the field of time delay cosmography became dominated by quasar sources (see Section 1.4.2).

The first detection of a gLSN occurred in 2010 with the discovery of PS1-10afx by the Pan-STARRS1 Medium Deep Survey (Chornock et al., 2013), originally believed to be a superluminous SN at $z = 1.388$ due to its extreme brightness and unusual light curve. However, after re-inspecting the photometric and spectroscopic data, Quimby et al. (2013b) proposed that the unusual transient was a gravitationally lensed normal SN Ia magnified by a factor of ~ 31. This was supported by further spectroscopic analysis of the 'host' galaxy, where an additional foreground galaxy at $z = 1.117$ along the line of sight was discovered (Quimby et al., 2014). However, the multiple images were never resolved due to very small image separations ($\theta_{\rm Ein} < 0.4''$).

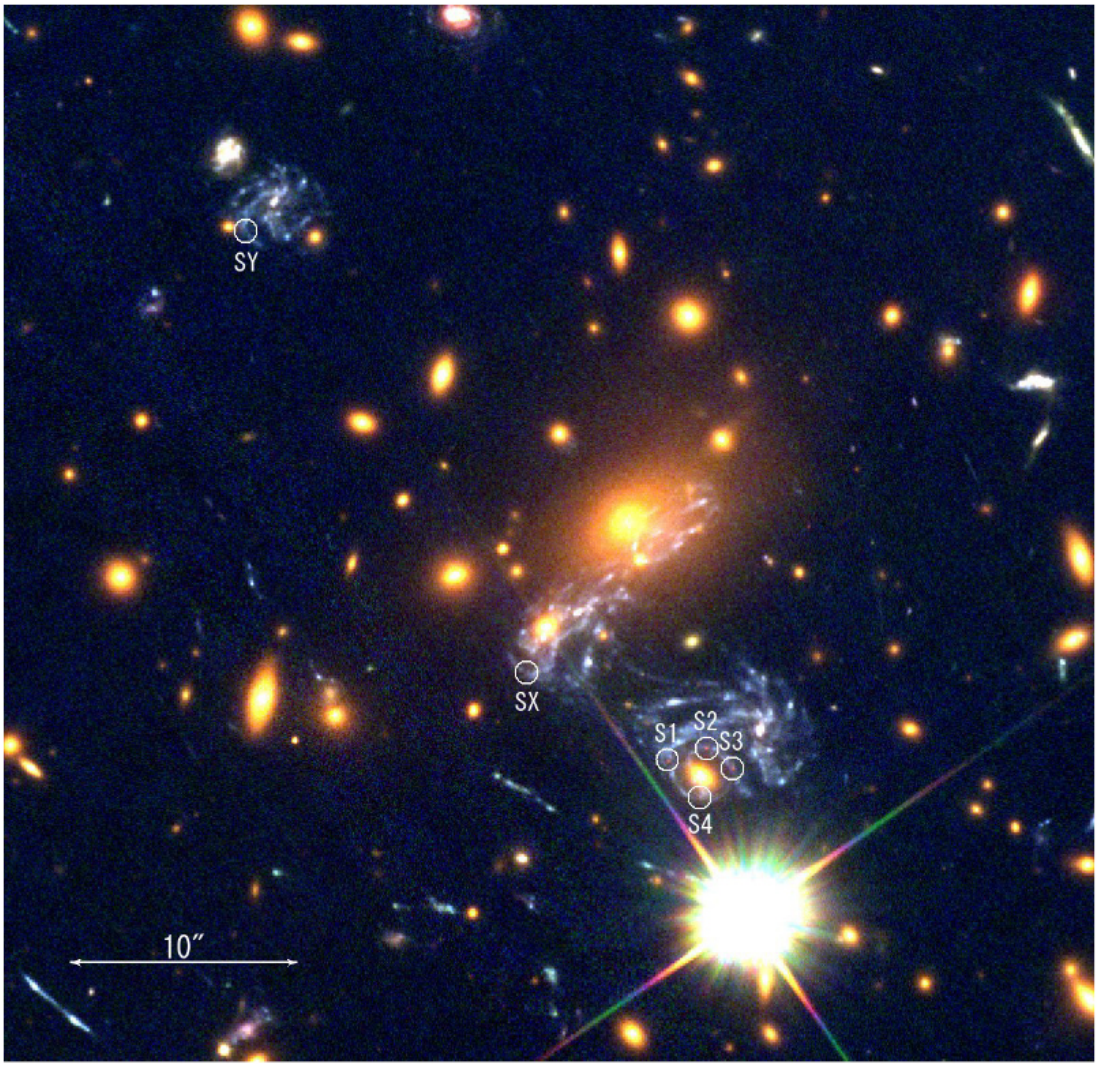

Figure 28: Color-composite image of SN Refsdal and foreground lensing cluster MACS J1149+2223, taken by the Hubble Frontier Fields program (Lotz et al., 2017). Images S1-S4 were initially discovered by Kelly et al. (2015), with image SX appearing approximately a year later (Kelly et al., 2016), as predicted by cluster lens models (Treu et al., 2016). Image SY was never observed, but predicted to have appeared ~ 10 years before the initial discovery. Figure taken from Oguri (2019).

The first gLSN with fully resolved images was SN Refsdal, a core-collapse supernova at $z = 1.49$ that was multiply imaged by the foreground galaxy cluster MACS J1149+2223 at $z = 0.54$ (see Figure 28), one of the six clusters targeted by the Hubble Frontier Fields program, aimed at studying the distant universe. In the initial discovery (Kelly et al., 2015), four lensed images (S1-S4) were observed with a fifth image (SX) predicted to appear approximately a year later by multiple lens models (Treu et al., 2016). The prediction was confirmed by the appearance of image SX $\sim$ 350 days later (Kelly et al., 2016). A sixth image (SY) was never observed, but predicted by mass models to have appeared approximately 10 years prior to discovery. SN Refsdal presented a unique opportunity to test current lens modelling methods for complicated cluster environments against observation, and the relatively successful predictions regarding the location and time of appearance of image SX is particularly encouraging. Especially since if the mass distributions of clusters and the systematics inherent to lens models are well constrained, then the cluster lens time delays could be used to measure H_0, adding to the sample of independent distance measures to test the Λ cold dark matter (ΛCDM) model of cosmology (Vega-Ferrero et al., 2018; Grillo et al., 2018). However, the errors on the time delays were sufficiently large (see Table 6 of Treu et al. 2016) such that any constraint on H_0 would struggle to be competitive without additional information, especially if assumptions on the cluster mass model were relaxed (Williams and Liesenborgs, 2019).

The third and most recent[1] gLSN is iPTF16geu, a Type Ia SN at $z = 0.409$ that was strongly lensed into four images and magnified by a factor of $\sim$ 52 by a foreground galaxy at $z = 0.216$. iPTF16geu was discovered by the intermediate Palomar Transient Factory in 2016 (Goobar et al., 2017), and is also the first Type Ia gLSN to be discovered with spatially resolved images (see Figure 29). The median image separations are particularly small ($\sim$ 0.3″) due to the compact sub-kpc foreground galaxy, also resulting in small time delays of $\lesssim$ 1 day (Dhawan et al., 2020; Johansson et al., 2020), making cosmography measurements difficult. Initial mass modelling by More et al. (2017) noted that the flux ratios between the images were inconsistent with lens modelling, concluding that this was due to the effect of microlensing by stars in the foreground galaxy. Some studies concluded that microlensing alone couldn't explain this flux anomaly, suggesting for example that substructure in the foreground lens

1 At the time of writing.

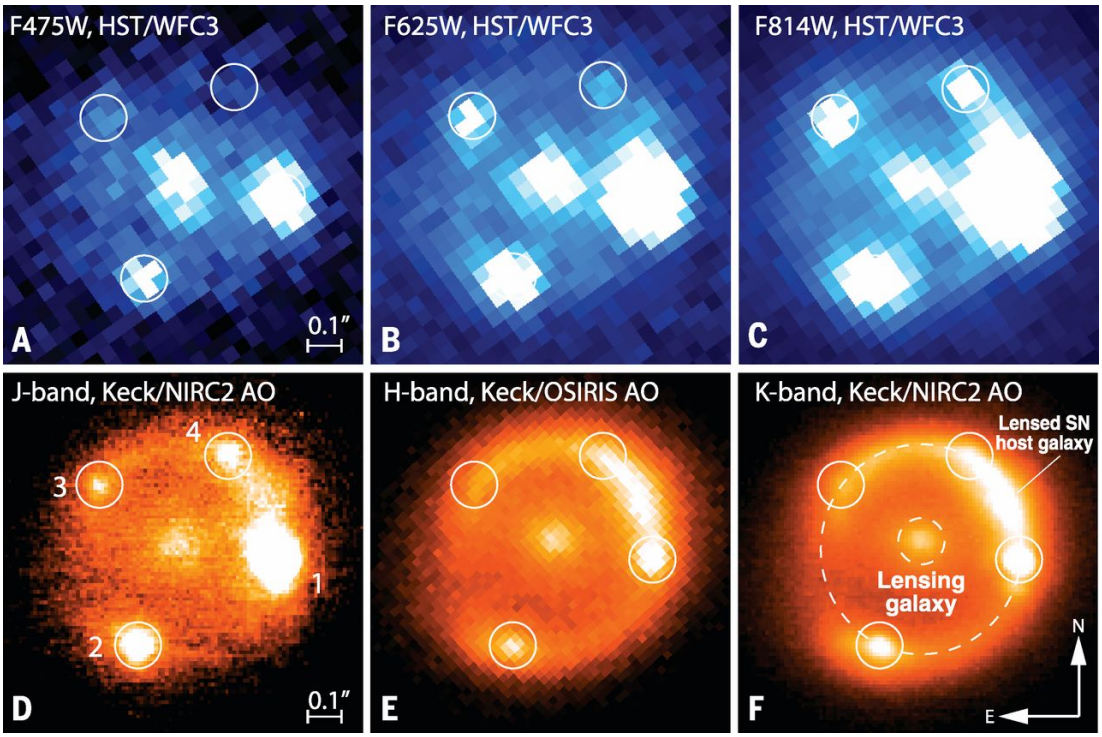

Figure 29: HST and Keck imaging of iPTF16geu across a range of bandpasses. The transient was strongly lensed into a quadruple image configuration. Figure taken from Goobar et al. (2017).

could contribute additional millilensing effects (e.g. Yahalomi, Schechter, and Wambsganss 2017, also see Chapter 4). However, Mörtsell et al. (2019) have alternatively suggested that microlensing can produce the observed flux anomaly if the radial density of the mass model is shallower than the isothermal model. Unfortunately the utility of iPTF16geu in cosmology is limited due to short time delays, anomalous flux ratios and the fact that individual images are highly susceptible to microlensing, introducing significant light curve scatter and hence severely affecting the standardisable nature of the source (see Chapter 4). The unique nature of this system highlights the importance of fully understanding systematics regarding the analyses of gLSNe. This is especially important when using Type Ia gLSN to produce a competitive, independent measurement of H_0 in order to test ΛCDM. This is achievable for example by having tighter constraints on the foreground lens mass model (e.g. through independent observation or by modelling with more complex mass profiles), or by being selective with the gLSN Ia sample such that systems with high probability of systematics are ignored (e.g. compact systems with sub-arcsec Einstein radii, see Chapter 4).

3.7.1 *Impact of gLSNe on Time Delay Cosmography*

The major application of gLSNe discussed in this section is the field of time delay cosmography and measurements of H_0 (see Oguri, 2019, for a further discussion on the applications of gLSNe and lensed transients in general). As of today, the field is dominated by quasar sources. gLSNe are incredibly rare with only SN Refsdal producing a H_0 measurement (Vega-Ferrero et al., 2018). However, since the sample size of gLSNe is expected to increase by several orders of magnitude with future wide-field surveys, high cadence surveys such as LSST (e.g. Goldstein et al. 2018; Goldstein, Nugent, and Goobar 2019, also see Section 3.7.2), it is expected that gLSNe will likely outperform quasars in the field of time delay cosmography. Firstly, the light curves of quasars are heterogeneous and stochastic, and their compact size makes them susceptible to microlensing. Therefore to measure time delays with percent level precision and produce competitive estimates of H_0, quasars need to be monitored over many years, if not decades (e.g. see Bonvin et al., 2017). The light curves of supernovae are simple and well understood and usually evolve over a timescale of $\sim$ 30 days, allowing for robust time delay measurements that can be obtained more trivially and at a far faster rate compared to quasars (Holz, 2001; Oguri, Suto, and Turner, 2003; Huber et al., 2019).

Additionally quasars are so bright they can often dominate the flux over the host, and even the lens galaxy, making it difficult to constrain the properties of the lens/host. Since gLSN are transient events, the properties of the host and lens galaxy can be observed and analysed before and after the transient event with greater ease and in much better detail (Holz, 2001). Time delay cosmography with gLSNe could even yield better cosmological constraints than quasars. The standardisable nature of SNe Ia means the magnification factor can be measured directly if strongly lensed, breaking degeneracies such as the mass-sheet degeneracy (e.g. Holz 2001; Schneider and Sluse 2014, also see Section 3.6) and the H_0-slope degeneracy (Oguri and Kawano, 2003). In reverse, gLSN could even be used to further constrain the peak absolute magnitude of SNe Ia (Wen and Liao, 2020). Thus the systematics with gLSNe Ia are likely to be far better controlled in comparison to quasars.

However, the most problematic source of systematics regarding gLSNe is that their compact source sizes makes them very sensitive to microlensing, and their shorter

light curves mean the microlensing effect can't be averaged out over years of observations unlike quasars. The microlensing effect is also time-dependent due to the transverse motions of the source relative to the foreground stars and the fact that the emitting region changes over time as the SN expands. This has potential to introduce significant scatter into the light curve shape (Dobler and Keeton, 2006). For the case of Type Ia SNe, this can affect their ability to be standardised. However, recent studies have shown that the multi-band observations allow for time delay measurements that are insensitive to microlensing during early times (e.g. Goldstein et al., 2018), however directly correcting for the microlensing effect remains an open problem (see Chapter 4).

3.7.2 *Future Prospects*

Unfortunately the largest limitation with gLSNe so far is shared with strong lensing in general, i.e. the lack of known, well resolved samples with accurately measured redshifts. At the time of writing only three gLSNe are known (Chornock et al., 2013; Kelly et al., 2015; Goobar et al., 2017), and only two systems have spatially resolved images. However, future wide-field, high cadence surveys such as LSST and the Zwicky Transient Facility (ZTF) could allow us to dramatically increase the gLSNe sample size by orders of magnitude over the next decade or so.

Goldstein, Nugent, and Goobar (2019) predicts that $\sim 10^1$ yr^{-1} and $\sim 10^2$ yr^{-1} gLSNe will be discovered by LSST and ZTF respectively, with a total projected sample size of $\sim 10^3$ gLSN systems over the next decade (seen Table 2 for a detailed breakdown by SN type). This prediction relies on a novel strategy of identifying gLSNe in LSST in elliptical galaxies without the need to resolve multiple imaging, taking advantage of the fact that elliptical galaxies dominate the lensing cross-section (see Oguri, 2019, and references therin) For a detailed description of the proposed observing strategy, see Goldstein et al. 2018 and Chapter 5. Predicted all-sky rates for gLSNe, as calculated by Oguri (2019), are given by Table 3. Oguri (2019) predicts that $\sim 10^3$ yr^{-1} Type Ia, $\sim 10^4$ yr^{-1} core-collapse (CC) and $\sim 10^1$ yr^{-1} superluminous gLSNe with total magnifications $\mu_{\rm tot} \gtrsim 10$ will appear on the sky within $z < 3$. The all-sky rate as a function of redshift and SN type is given by Figure 30.

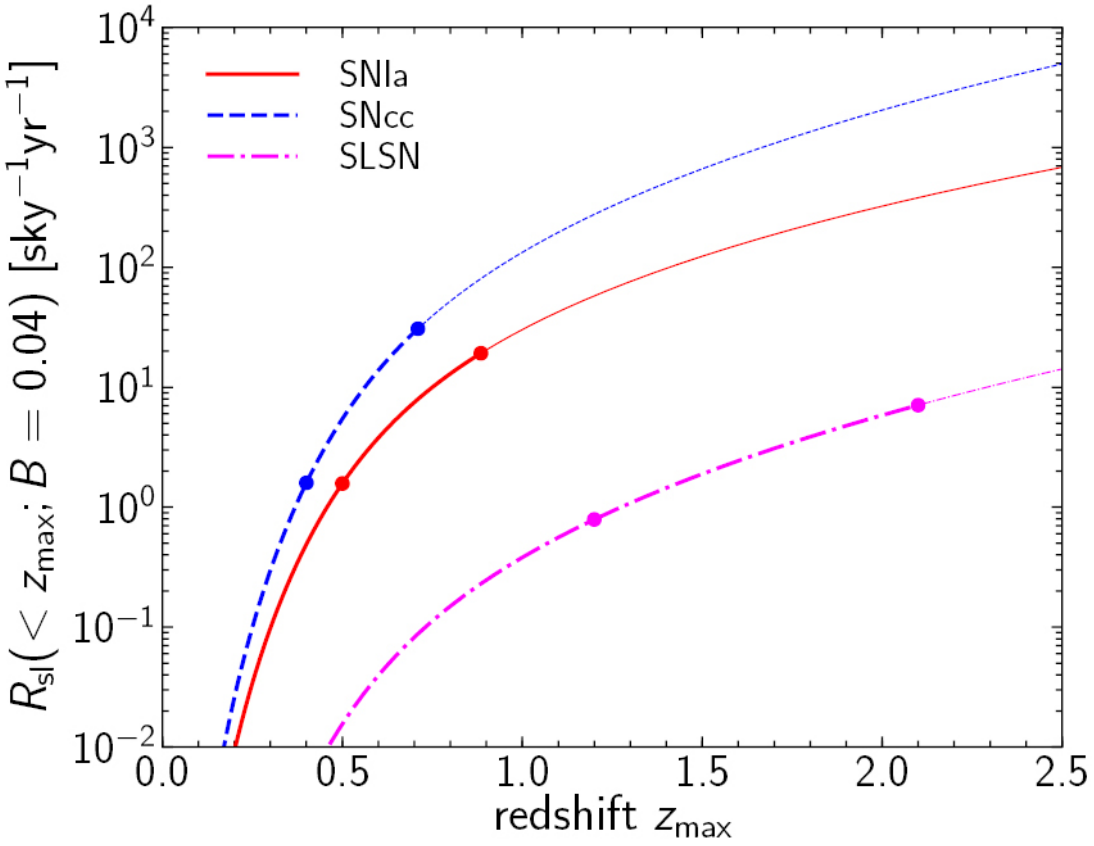

Figure 30: Predicted all-sky gLSNe rates as a function of redshift for systems where the total magnification $\mu_{tot} \gtrsim 10$ (B = 0.04), across a range SNe types (Type Ia, Core-collapse and Superluminous SNe, respectively). The thick parts of each line approximately represent the observable regions for LSST. The two dots on each line represent the limiting redshifts for unlensed and lensed SNe to be discovered by LSST, respectively. Figure taken from Oguri (2019).

This dramatic increase of gLSNe sample size will prove invaluable to the field of astronomy and cosmology, for example allowing sub-percent measurements on H_0 with tightly constrained systematics (see Chapter 4). However, this is dependent on the community's willingness and ability to invest further resources into obtaining high-resolution imaging and lens/source redshifts of many systems through follow-up observations. The increase in sample size will also introduce further demand for more efficient lens modelling, which is a particularly time intensive task. However, the promise of automated lens modelling software (e.g. `Autolens` Nightingale, Dye, and Massey, 2018) could significantly reduce modelling time, especially if there is a time pressure to quickly model a lens in time for a follow up observation (e.g. when predicting image reappearance, see Chapter 5).

SN Type	ZTF	LSST	
		`minion_1016`	`altsched`
Type Ia	1.23	47.84	47.42
Type IIP	2.76	88.51	91.06
Type IIn*	3.75	209.31	166.54
Type IIL	0.31	11.69	13.10
Type Ib/c	0.36	14.00	16.15
SN 1991bg-like	0.02	0.79	0.89
SN 1991T-like	0.17	5.41	6.09
Total*	8.60	380.60	341.27

Table 2: Yearly gLSNe rates to be discovered by LSST and ZTF across a range of SN types, as forecast by Goldstein, Nugent, and Goobar (2019). For LSST, the rates for the `minion_1016` and `altsched` observing strategies are presented. Note: * denotes the lower limit.

SN Type	R_{sl} (sky^{-1} yr^{-1})			
	$z < 0.5$	$z < 1$	$z < 2$	$z < 3$
Ia	1.6	30	320	1300
Core-collapse	5.4	130	2000	10000
Superluminous	0.02	0.38	5.8	29

Table 3: All-sky gLSNe rates predicted by Oguri (2019) for systems where the total magnification $\mu_{tot} \gtrsim 10$.

Part II

RESEARCH

"All I've really ever wanted was to know what it feels like to be human. And now we're going to do the must human thing of all: attempt something futile with a ton of unearned confidence and fail spectacularly!"

— Michael, The Good Place

4

THE STANDARDISATION OF STRONGLY LENSED TYPE IA SUPERNOVAE

Note: A previous version of this chapter was published in Foxley-Marrable et al. (2018).

Abstract

We investigate the effect of microlensing on the standardisation of strongly lensed Type Ia supernovae (gLSNe Ia). We present predictions for the amount of scatter induced by microlensing across a range of plausible strong lens macromodels. We find that lensed images in regions of low convergence, shear and stellar density are standardisable, where the microlensing scatter is $\lesssim 0.15$ magnitudes, comparable to the intrinsic dispersion of for a typical SN Ia. These standardisable configurations correspond to asymmetric lenses with an image located far outside the Einstein radius of the lens. Symmetric and small Einstein radius lenses ($\lesssim 0.5$ arcsec) are not standardisable. We apply our model to the recently discovered gLSN Ia iPTF16geu and find that the large discrepancy between the observed flux and the macromodel predictions from More et al. (2017) cannot be explained by microlensing alone. Using the mock gLSNe Ia catalogue of Goldstein et al. (2018), we predict that $\sim 22\%$ of gLSNe Ia discovered by LSST will be standardisable, with a median Einstein radius of 0.9 arcseconds and a median time delay of 41 days. By breaking the mass-sheet degeneracy the full LSST gLSNe Ia sample will be able to detect systematics in H_0 at the 0.5% level.

4.1 INTRODUCTION

The value of the Hubble constant (H_0) is a major point of contention in cosmology today, bringing the validity of the Λ cold dark matter (ΛCDM) model of cosmology into question. This particularly arises from the 3.4σ tension between the Planck Collaboration et al. (2016) result of $H_0 = 67.8 \pm 0.9$ km s^{-1} Mpc^{-1}, derived from the cosmic microwave background, and the Riess et al. (2016) result of $H_0 = 73.2 \pm 1.7$ km s^{-1} Mpc^{-1}, measured from low redshift supernovae (SNe) and Cepheids. The Planck Collaboration et al. (2016) result infers H_0 assuming ΛCDM, whilst the Riess et al. (2016) result probes H_0 directly. Whilst this tension could be attributed to statistical fluke or

unaccounted systematics, it potentially signals new physics beyond the ΛCDM model. Hence the need for precise and independent measurements of H_0 is greater than ever, such that the validity of the ΛCDM model can be tested.

Strong gravitational lenses are powerful probes of cosmology (Oguri et al., 2012; Suyu et al., 2013; Collett and Auger, 2014) and are particularly sensitive to H_0 through time delay cosmography (Treu and Marshall, 2016). The light from each image in a lensing system takes a different path through the lens before reaching the observer. If the lensed object is a variable source, the images vary asynchronously with a geometrical time delay based on these path differences. Time delays have an additional component caused by the gravitational potential of the lens (Shapiro, 1964). When a background source peaks sharply in luminosity, the time delay between each image can in principle be measured by observing the time difference between the peaks of each image.

Time delays allow strong gravitational lenses to measure H_0 independently of assumptions made in the cosmological model: the value of H_0 is mostly invariant to other cosmological parameters such as the curvature and the dark energy equation of state (Bonvin et al., 2017). A recent example is Wong et al. (2019), who used time delays from six lensed quasars to independently measure $H_0 = 73.3^{+1.7}_{-1.8}$ km s^{-1} Mpc^{-1} to within a 2.4% precision. In order to obtain a value for H_0 through strong lens time delays, one needs to know the 2D lens potential and the unlensed source position, neither of which can be observed directly. The use of lens modelling is therefore required in order to infer these quantities.

However strong lens models are subject to degeneracies, which are a major source of uncertainty for time delay cosmography (Schneider and Sluse, 2014). The main component of the degeneracy is the mass-sheet degeneracy: when rescaling the mass of the lens with an additional sheet of mass of constant density, the image configurations remain exactly the same but the projected mass on each image (also known as the convergence κ) changes, affecting the time delay (Falco, Gorenstein, and Shapiro, 1985). Put simply, two lens models producing identical image configurations can have very different time delays. Breaking the mass-sheet degeneracy is therefore necessary to constrain H_0. In order to break the mass-sheet degeneracy additional information is required, such as the intrinsic luminosity of the background source (Kolatt and Bartelmann, 1998).

Originally proposed by Refsdal (1964), the prospect of using strong gravitationally lensed supernovae (gLSNe) to precisely measure H_0 is promising, especially after the discovery of the Type Ia gLSN iPTF16geu by the Intermediate Palomar Transient Factory (iPTF) in October 2016 (Goobar et al., 2017). The light curves of Type Ia SNe are standardisable (Phillips, 1993), allowing us to infer their intrinsic luminosity, hence gLSNe Ia can potentially lift the mass-sheet degeneracy (Oguri and Kawano, 2003) and enable a test of systematic uncertainties in time delay cosmography.

gLSNe are advantageous over the lensed active galactic nuclei (AGN) currently used for time delay cosmography (Vuissoz et al., 2008; Suyu et al., 2010; Tewes et al., 2013a; Bonvin et al., 2016). SN light curves have a strong peak before they decay, occurring over a time-scale of several weeks, whilst AGN light curves vary stochastically and heterogeneously, with weak variations in luminosity. Hence gLSN time delays can be obtained in a single observing season, whilst AGN must be monitored over several years in order to acquire accurate time delays (Liao et al., 2015a).

Goldstein et al. (2018) predicts that ~ 930 gLSNe Ia will be discovered by the Legacy Survey of Space and Time (LSST) over its 10 year survey, with 70% of the gLSNe Ia having time delays that can be measured precisely.

Despite the potential power of gLSNe Ia there exists one major theoretical barrier to their use as cosmological probes: microlensing caused by stars in the foreground lensing galaxy. Microlensing can independently magnify or demagnify individual images of the background source (Dobler and Keeton, 2006; Bagherpour, Branch, and Kantowski, 2006), introducing scatter into the shape and amplitude of the resulting light curves. The effect of microlensing on each lensed image can be inferred by obtaining its convergence κ[1], shear γ and smooth matter fraction s through lens modelling. κ and γ represents the amount of mass projected on and near the image respectively while s represents the projected fraction of mass in dark matter as opposed to stellar matter (see Figure 31). Due to the distribution and random motion of the stars in the foreground galaxy, inferring the effect of microlensing on one image does not infer the effect of microlensing on the other image(s). This can significantly reduce the reliability of any time delay and luminosity measurement, as microlensing can randomly distort the light curve of each image, such that the intrinsic magnification and luminosity of the source can be difficult to determine. This effect also evolves

1 κ is composed of both stellar and dark matter components.

over time. As the background SN Ia grows, the number of microlensing caustics that its light profile intersects with increases with time (see Figure 32). Recently, Goldstein and Nugent (2017) have shown that time delays can be robustly measured using early time colour curves.

More et al. (2017) modelled iPTF16geu using the GLAFIC (Oguri, 2010) and GLEE (Suyu et al., 2010, 2012) macro lens models. Whilst the models themselves were in agreement, they were in contention with the Goobar et al. (2017) observations, with a discrepancy of almost 2 magnitudes for the brightest image. Their conclusion was that the disparity between their lens models and the observations was primarily due to microlensing from foreground stars in the lensing galaxy[2].

In this chapter, we examine the effect microlensing has on an expanding SN Ia profile across a wide range of image configurations corresponding to particular values of κ, γ and s. We provide the first predictions for regions of parameter space where the SN Ia image has a standardisable light curve, allowing us to infer its intrinsic luminosity and hence break the mass-sheet degeneracy. We define a standardisable SN as one where the scatter due to microlensing is $\lesssim 0.15$ magnitudes, comparable to the intrinsic dispersion for an unlensed SN Ia after standardisation (Betoule et al., 2014; Macaulay et al., 2017). We also present predictions for the fraction of gLSNe Ia discovered by LSST that will be standardisable. Finally we analyse the effect of microlensing on iPTF16geu and compare our results against the More et al. (2017) prediction. In Section 4.2 we describe our microlensing simulations. In Section 4.3 we present and discuss our subsequent analysis with results and conclude in Section 4.4. Throughout this chapter we report results in the observer time frame assuming a source redshift of 0.409.

2 More et al. (2017) also mention the possibility of milli-lensing.

4.2 SIMULATIONS

Disclaimer: This section was jointly written with Georgios Vernardos.

To simulate the effect of microlensing by stars in the lens galaxy, we use magnification maps generated by the GERLUMPH project[3] as shown in Figure 31 (Vernardos et al., 2014; Vernardos and Fluke, 2014). These are pixelated maps of the source plane where the magnification per pixel has been calculated using the inverse ray-shooting technique (Kayser, Refsdal, and Stabell, 1986). A field of randomly distributed point masses is used to simulate the star field, with each star having the same mass. The deflections for each microlens are computed directly and in parallel using the graphics processing Unit (GPU) implementation of Thompson et al. (2010, 2014).

Each magnification map used in this work is square with 10000 pixels on a side, with a side corresponding to 13.7 $\theta_{\mathrm{Ein},\odot}$. $\theta_{\mathrm{Ein},\odot}$ is the Einstein radius for a 1 $M_\odot$ microlens; for a lens at $z_l = 0.216$ and a source at $z_s = 0.409$. This corresponds to a physical scale of $\theta_{\mathrm{Ein},\odot} = 4 \times 10^{11}$ km $= 2 \times 10^{-6}$ arcseconds on the sky, with each map pixel covering an area of 2.5×10^{17} km^2 $= 9 \times 10^{-18}$ arcseconds^2 on the sky[4].

To sample a wide range of possible gLSN configurations we use the GD1 set of maps (described in detail in Vernardos et al., 2014). This set covers κ, γ space on a uniform grid with $\Delta\kappa, \Delta\gamma = 0.05$ and $0 \lesssim \kappa, \gamma \lesssim 1.7$. For each κ, γ combination there are 11 values of s available: $0 \leqslant s \leqslant 0.9$, in steps of 0.1, and $s = 0.99$. For each κ, γ pair we use maps with a smooth matter fraction $s = 0.2, 0.4, 0.6, 0.8$. This results in a total of 4488 magnification maps.

To obtain the SN microlensing light curves we convolve the magnification maps with a time varying profile of the background source[5] (see Figure 32). We use an expanding uniform disc to approximate the SN brightness profile. This simple model is sufficient for our purposes since the observed luminosity of a microlensed source is mostly sensitive to the average size and largely independent of any specific shape of the source profile (Mortonson, Schechter, and Wambsganss, 2005). We do not consider sources with clumpy profiles.

3 `http://gerlumph.swin.edu.au`

4 Here we assume the best-fit ΛCDM cosmological parameters of Planck Collaboration et al. (2016).

5 **Disclaimer**: The convolutions used in our analyses were performed by Georgios Vernardos.

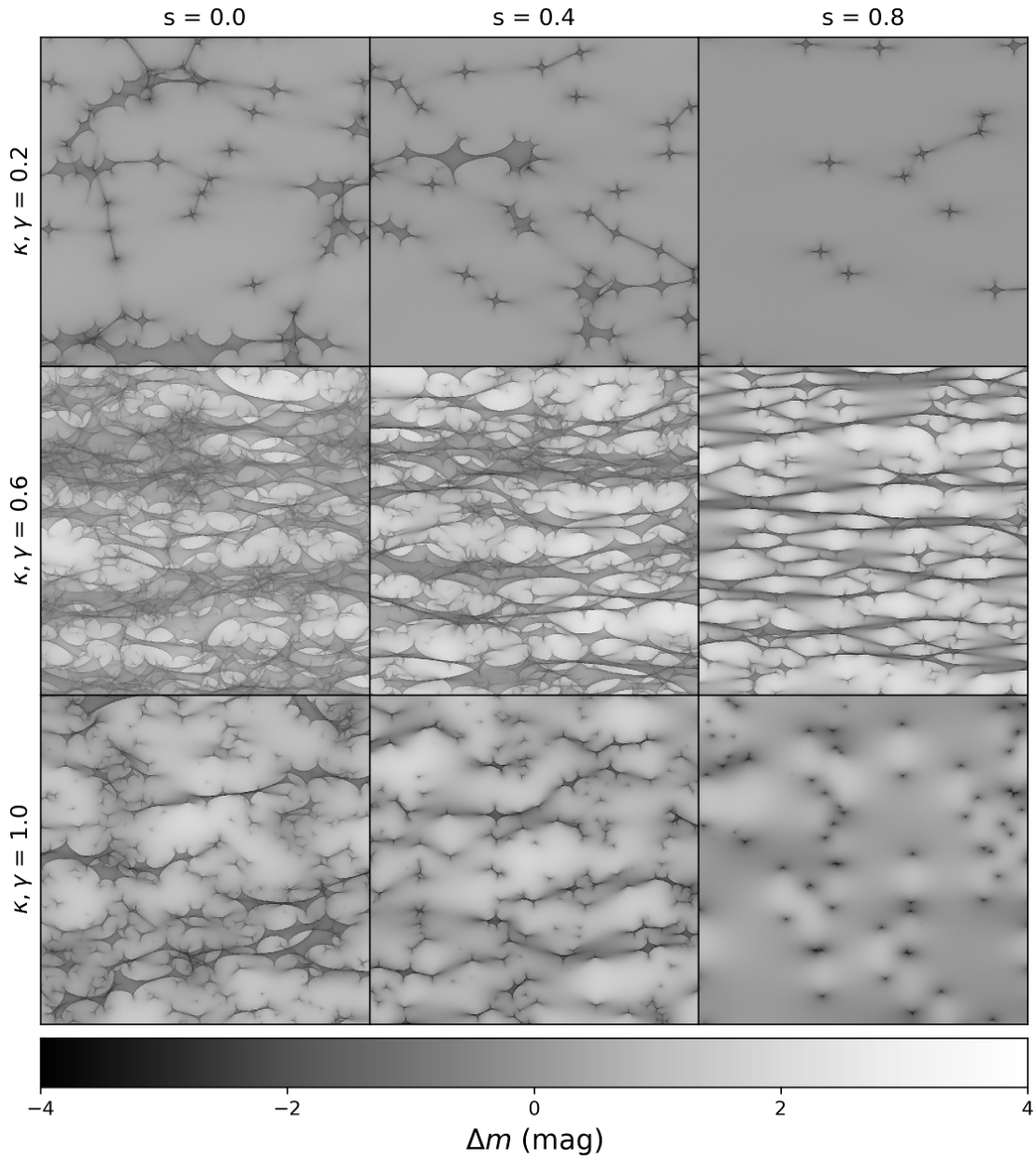

Figure 31: Example microlensing maps corresponding to various combinations of the convergence κ, shear γ and smooth (dark) matter fraction s. Each side in a subpanel spans a physical range of 13.7 $\theta_{\mathrm{Ein},\odot}$ (5×10^{12} km). The maps show microlensing caustics projected onto the source plane as a result of inverse ray-tracing through a foreground star field. Background sources will be magnified/demagnified with amplitudes determined by the position and size of the light profile cross-section relative to the microlensing caustics. The colour scale represents the deviation in magnitudes from the smooth macromodel magnification.

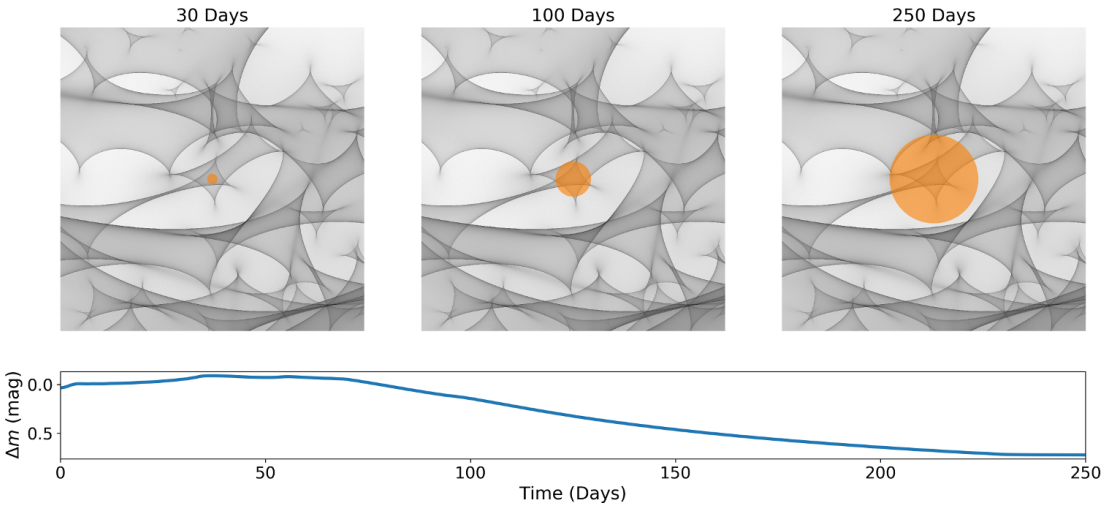

Figure 32: A zoomed in microlensing map (each side corresponding to 2.75 $\theta_{Ein,\odot} = 1 \times 10^{12}$ km) with a SN Ia profile superimposed on top, expanding at a rate of 2.5×10^{-8} $\theta_{Ein,\odot}$ s^{-1} = 10^4 km s^{-1}. At each time step, the SN Ia profile is convolved with the microlensing background: the magnifications inside the disc are summed up and averaged. As the SN Ia profile grows, it crosses more and caustics, causing the microlensing magnification to vary over time. The resulting magnifications are shown in the bottom panel.

The SN expansion rate is set to 10^4 km s^{-1} (2.5×10^{-8} $\theta_{Ein,\odot}$ s^{-1}). Since this is much larger than any of the velocities involved (i.e. the peculiar velocity of the lens and the source, the velocity of the observer, and the proper motions of the microlenses), we can approximate the microlensing map as time invariant, and the centroid of a SN as constant; only the radius of the SN changes with time. At this expansion rate we are able to place 10^4 SNe per magnification map without profile overlap within the first 60 days.

To obtain a light curve for an individual SN, we choose a position on the magnification map, and evaluate the product of its profile and the magnification map at each time step. This is done for a total of 55 time steps: $0 < t < 16$ days with $\delta t = 1$ day, $16 < t < 60$ days with $\delta t = 2$ days, and $60 < t < 200$ days with $\delta t = 7$ days. A total of $\approx 250,000$ convolutions between maps and profiles have been performed, requiring roughly 300 GPU hours.

We normalize all of our unlensed source fluxes to unity at all times, such that our light curves depend only on the microlensing rather than intrinsic variations in the unlensed source. We show a range of example microlensing light curves in Figure 33.

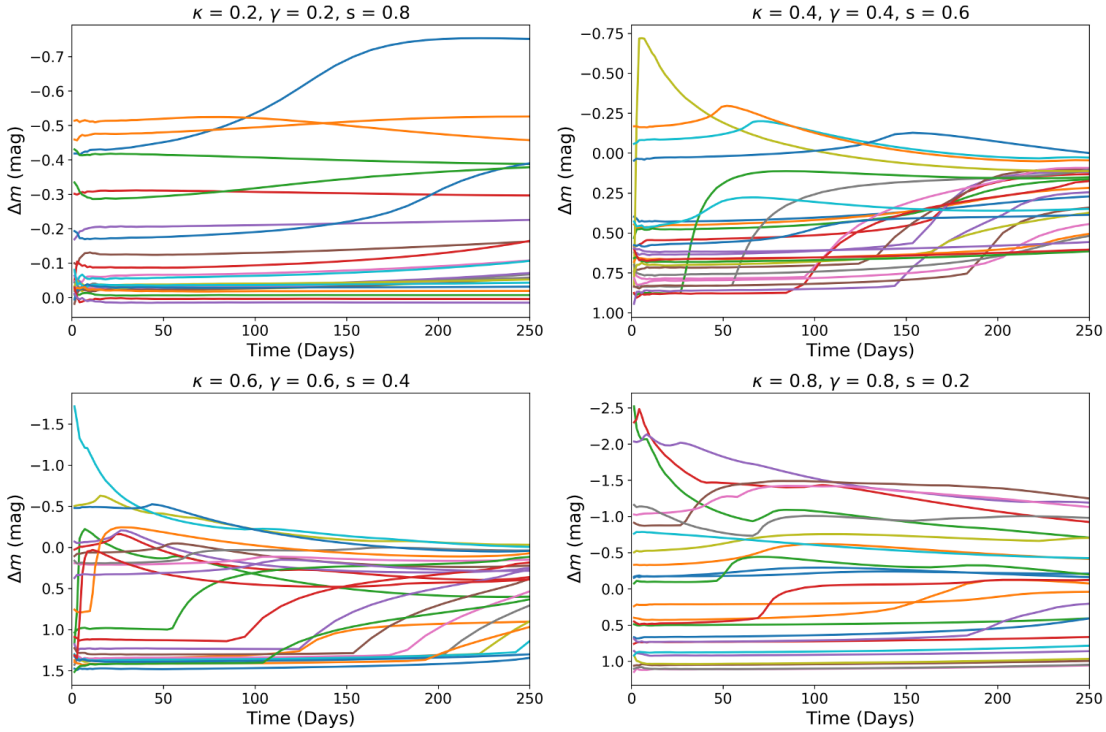

Figure 33: A selection of simulated microlensing light curves for an expanding uniform disk. The four panels correspond to different values of the convergence κ, shear γ and smooth matter fraction s. Each light curve within a panel has the same macrolensing parameters but a different realisation of the microlensing by stars.

4.3 RESULTS AND DISCUSSION

4.3.1 *Microlensing Scatter*

For each $\kappa - \gamma$ pair, time-step and value of the smooth matter fraction s, we measured the scatter by taking half the difference of the 16th and 84th percentile of the resulting probability density function (PDF)[6].

In Figure 34, we show how the microlensing scatter σ_{ML} varies with κ, γ and s, across a range of times t. We find that there is a region of parameter space where the light curves from gLSNe Ia are standardisable as the scatter due to microlensing is comparable to the typical intrinsic dispersion for a SN Ia after standardisation (Betoule et al., 2014; Macaulay et al., 2017). Therefore, with the correct lensing configuration, it is possible to infer the unlensed magnitude of the source SN Ia. This

6 Equivalent to calculating a 1σ standard deviation for a Gaussian distribution.

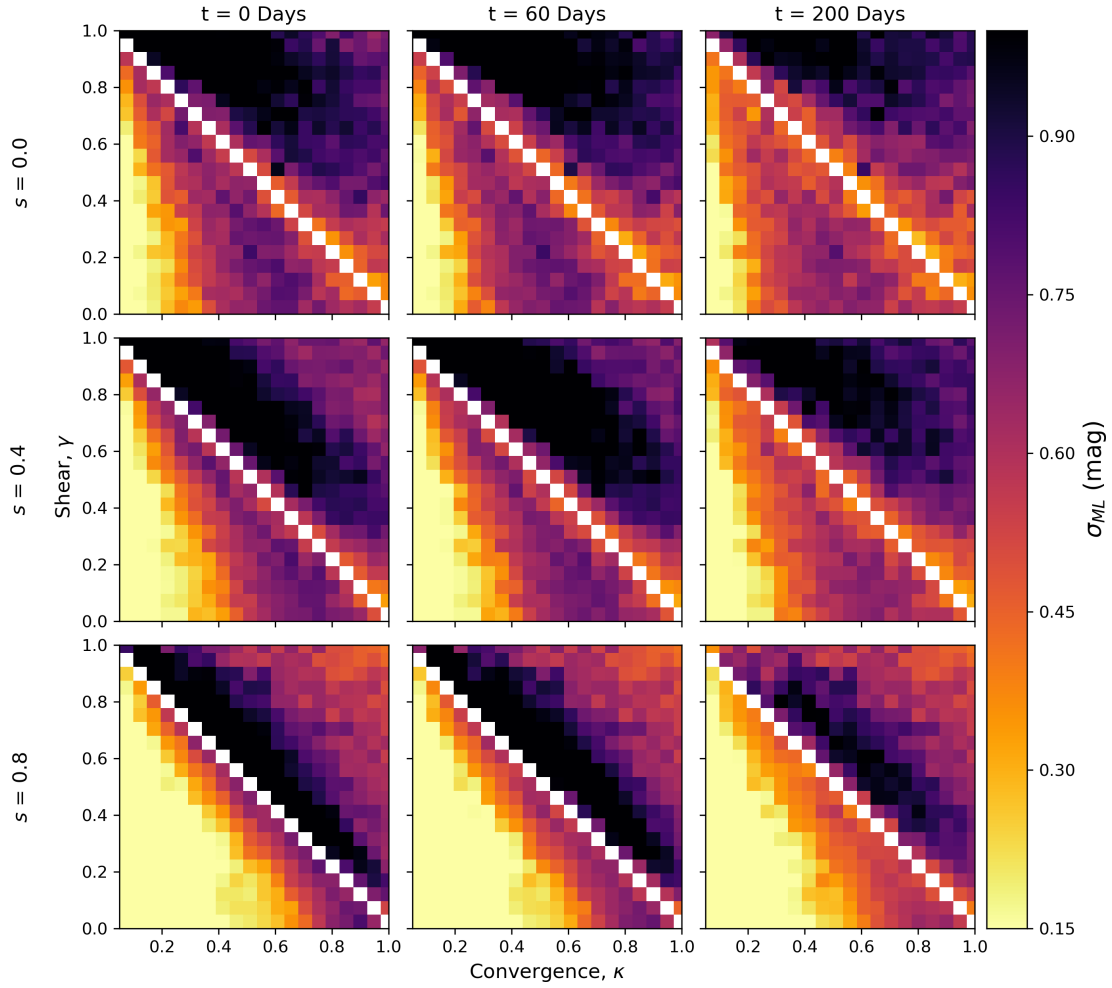

Figure 34: The microlensing scatter in the observed luminosity of a lensed SN image. Each subpanel shows the scatter as a function of the convergence κ and shear γ at fixed smooth matter fraction s and time t after explosion. The smooth matter fraction increases from top to bottom and the time of observation increases from left to right. The white pixels along the diagonal correspond to regions of infinite magnification: lensed images do not form here.

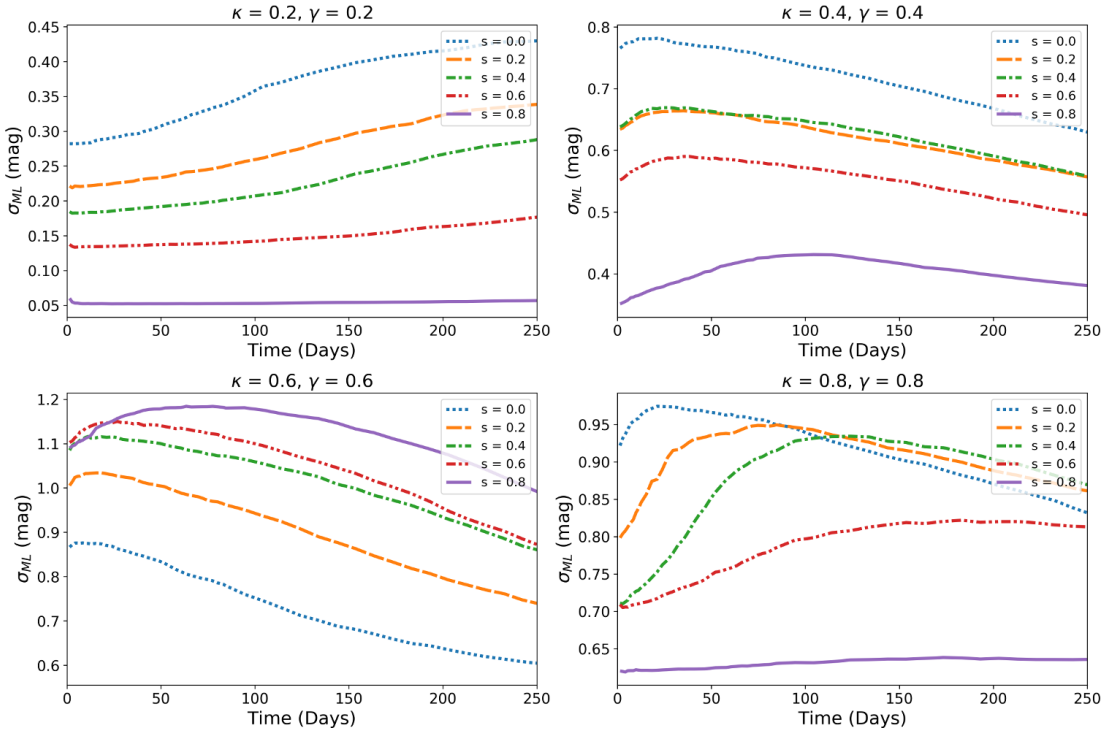

Figure 35: The microlensing induced scatter in the observed luminosity as a function of time. The different lines correspond to different values of the smooth matter fraction s.

will lift the mass-sheet degeneracy and allow us to acquire an accurate, precise and independent measurement of H_0.

We find that the standardisable region corresponds to lensed images with low κ and γ, with the size of the standardisable region increasing with s, i.e. images forming in regions of lower stellar density are less susceptible to microlensing. Physically, this corresponds to a lens with an asymmetric image configuration, with at least one image located far outside the Einstein radius of the lens. This outermost image experiences the least amount of microlensing due to being far away from the high stellar density region of the lensing galaxy and hence could be used to infer the unlensed magnitude of the background SN Ia.

As highlighted in Figure 35, the microlensing scatter in low κ, γ regions increases over time, meaning early time measurements of the SN image fluxes are optimal for cosmography. This counter-intuitive result is because there are few caustics in these situations and a small source will typically fall in the smooth region between caustics (see Figure 31). A small number of systems will be highly magnified but these are excluded by our choice to define width as half the 68% confidence region. As the source expands it is more likely to cross a caustic, creating a larger spread of

magnifications at late time. The scatter does not decrease at late times as the source is still too small to average over many caustics. However, in higher κ, γ regions, the scatter decreases with time and increases with s. This behaviour is due to the increased density of microlensing caustics. As the source expands it averages over more caustics and the scatter shrinks, but this still does not reach a standardisable level even after 200 days.

4.3.2 *How Many Lensed Supernovae are Standardisable?*

To investigate the fraction of lensed SNe that will be standardisable, we first use a simple lens model to relate lensed image position to the expected microlensing scatter. We assume a singular isothermal sphere (SIS) lens model and iPTF16geu redshifts of $z_l = 0.216$ and $z_s = 0.409$ for the lens and source respectively.

For each point on the image plane κ and γ can be inferred from the macro lens model, however the macro model is sensitive only to the total mass and not the partition between stars and dark matter. The smooth matter fraction is given by the fraction of the surface density not in stars:

$$s = 1 - \frac{\kappa_*}{\kappa_{tot}}. \tag{45}$$

The total mass distribution is modelled using an SIS lens profile:

$$\kappa_{tot} = \kappa_{SIS} = \frac{\theta_{Ein}}{2r}, \tag{46}$$

where r denotes a position in the image plane in polar coordinates. For the stellar component of Equation 45 we assume a de Vaucouleurs profile:

$$\kappa_* = \kappa_{deV}(r) = Ae^{-k(r/R_e)^{1/4}}, \tag{47}$$

where A is a normalisation constant, R_e is the effective radius of the lens and k=7.669 (Dobler and Keeton, 2006). To calculate the normalisation constant A, we match the dark matter fractions to those found in typical strong lensing ellipticals in the Sloan Lens ACS (SLACS) sample
(Auger et al., 2010):

$$A = (1 - f_{DM})\frac{M_{tot}}{M_*}, \tag{48}$$

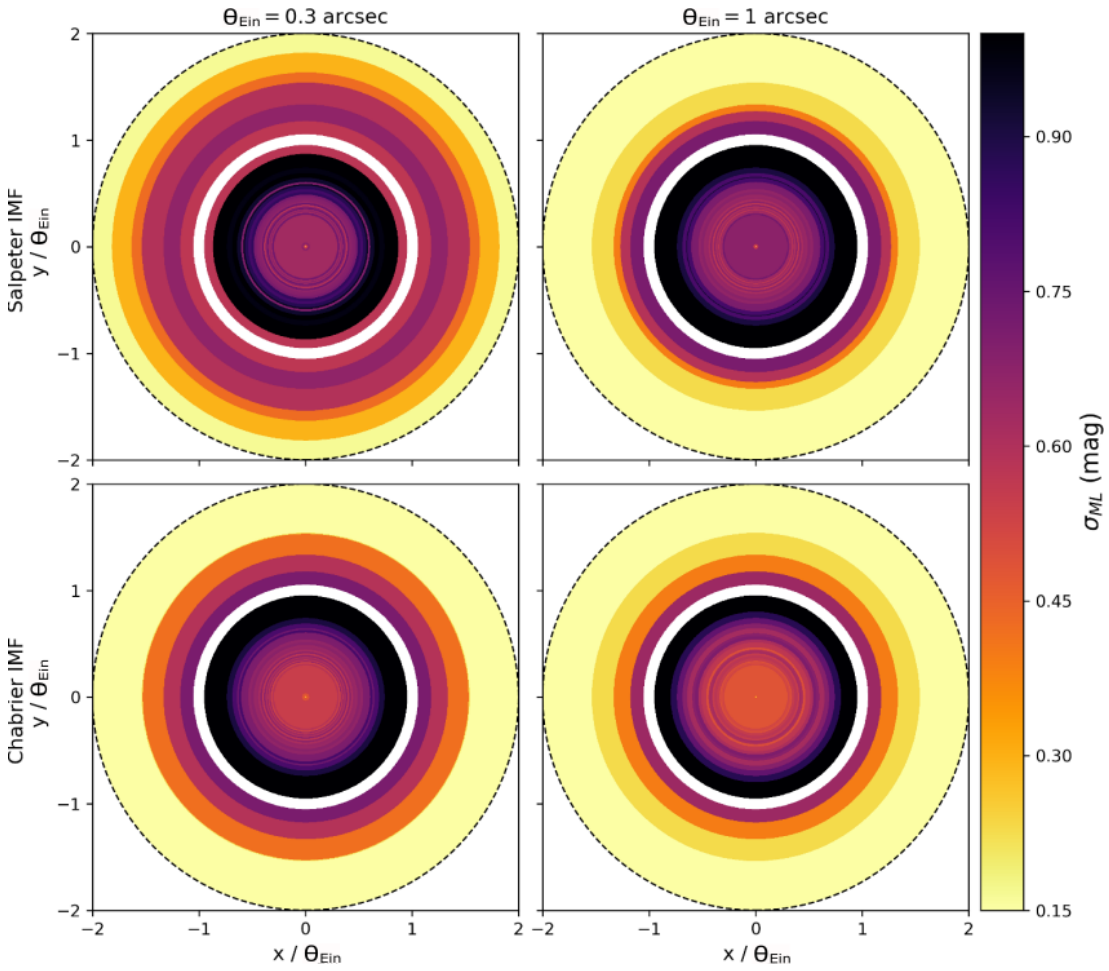

Figure 36: The amount of microlensing scatter induced on any lensed image at any point on the image plane, assuming an SIS lens and a SN 30 days after explosion. The four panels show the effect of varying the Einstein radius $\theta_{\rm Ein}$ and the IMF. The black dashed line represents the outermost boundary for multiple imaging. The inner white circle corresponds to the critical curve and infinite magnification. The Salpeter and Chabrier IMFs correspond to the dark matter fractions derived in Auger et al. (2010).

where M_{tot} and M_* were inferred by integrating Equations 46 and 47 in polar coordinates from 0 to $R_e/2$. f_{DM} is the total projected fraction of dark matter within half the effective radius of the galaxy. Our f_{DM} is then matched to the fit derived in Auger et al. (2010):

$$f_{DM} = a \times \log(\sigma_{R_e/2}) + b, \tag{49}$$

where a and b are fitting parameters that depend on the initial mass function (IMF) of the lens and $\sigma_{R_{e/2}}$ is the velocity dispersion[7] within half the effective radius of the lens (Auger et al., 2010). Assuming a Salpeter IMF, $a = 0.80 \pm 0.44$ and $b = -0.05 \pm 0.18$ while for a Chabrier IMF, $a = 0.46 \pm 0.22$ and $b = 0.40 \pm 0.09$ (Auger et al., 2010).

Using our model for κ, γ and s across the image plane and the results of Section 4.3.1, we determine the microlensing scatter as a function of gLSN image plane position. Figure 36 shows that standardisable images form beyond the Einstein radius corresponding to an asymmetric configuration. More of the image plane is standardisable if the Einstein radius is large or if the IMF is Chabrier rather than Saltpeter. The Chabrier IMF has a lower mass-to-light ratio, so places a larger fraction of the total mass in dark matter whereas the Salpeter IMF places more mass in low mass stars.

In order to infer how often standardisable images form we must determine the fraction of the source plane that is standardisable. We solve the lens equation for a range of source positions and Einstein radii. For each source position we infer the microlensing scatter for all images formed. Figure 37 shows the fraction of the source plane that is standardisable as a function of θ_{Ein}, for a SN 30 days after explosion, assuming either a Salpeter or Chabrier IMF. For a Salpeter IMF $\sim$ 70% of the source plane is standardisable provided $\theta_{Ein} \gtrsim 1$ arcsecond on the sky. Decreasing θ_{Ein} causes the standardisable fraction of the source plane to sharply decline to zero at $\theta_{Ein} \sim 0.5$ arcseconds. More of the source plane is standardisable if the IMF is Chabrier: lenses as small as $\theta_{Ein} \sim 0.4$ arcseconds can have a source plane which is 70% standardisable, but sharply dropping to 0% at $\theta_{Ein} \sim 0.2$ arcseconds.

In principle, measuring the scatter for a sample of gLSNe Ia with $\theta_{Ein} \sim 0.5$ arcseconds will allow us to discriminate between IMFs in the lensing galaxy. If the Auger et al. (2010) Salpeter fit is correct then no lensed SNe with $\theta_{Ein} < 0.5$ arcseconds should have a scatter of less than 0.15 mags whilst most lensed SNe will if the Chabrier fit is correct.

7 In units of 100 km s^{-1}.

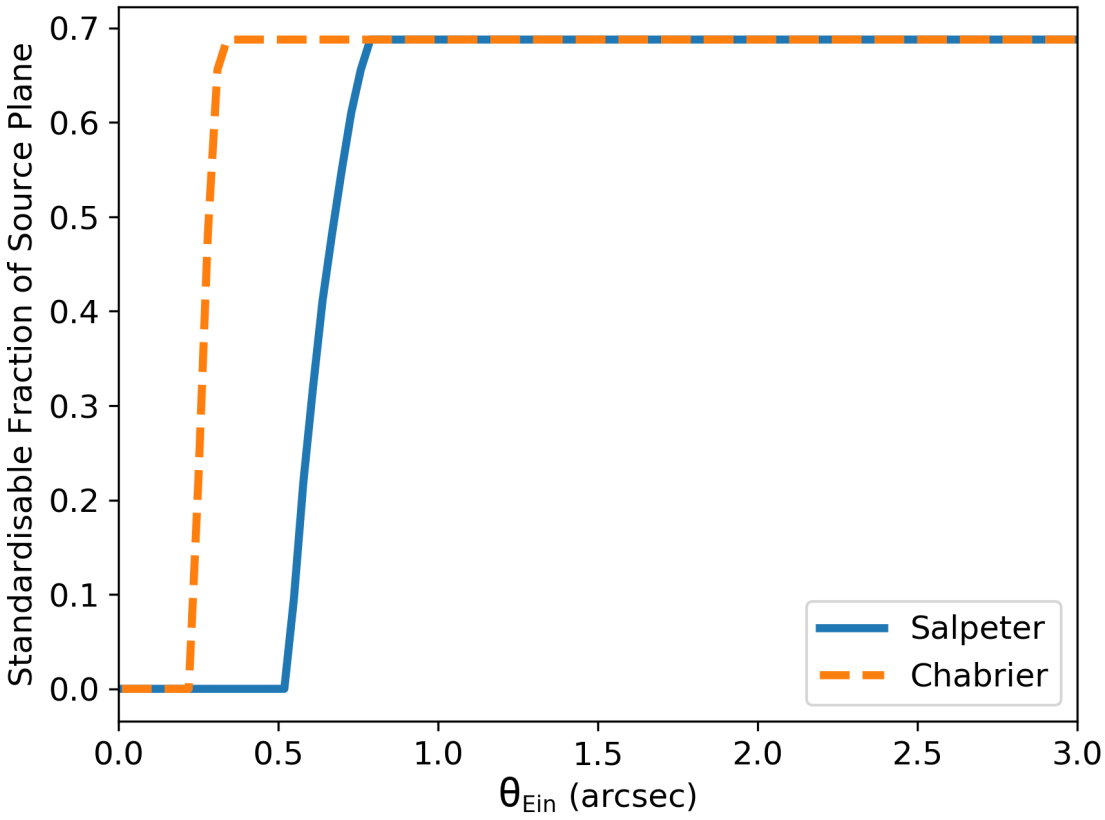

Figure 37: The percentage of the source plane that is standardisable as a function of the Einstein radius θ_{Ein} of the lens 30 days after explosion. The result is sensitive to the dark matter fraction in the lens: the solid blue and dashed orange lines correspond to the dark matter fractions derived in Auger et al. (2010) for a Salpeter and Chabrier IMF respectively.

The above toy model neglects magnification bias. Whilst asymmetric configurations dominate the source plane, they are less highly magnified and therefore harder to detect than more symmetric configurations. To illustrate this we take the mock gLSNe catalogue of Goldstein et al. (2018) and assess the standardisable fraction of systems where the brightest SN image reaches a peak apparent *i*-band magnitude of 22.15. This choice roughly approximates the LSST discovery threshold for gLSNe. We predict that that 22% of the ~ 930 gLSNe Ia to be discovered by LSST will be standardisable, of which approximately 1 in 5 will be quads. The median time delay for a standardisable LSST gLSN Ia is 44 days, compared to 18 days for all LSST gLSN Ia. The median Einstein radius for a standardisable LSST gLSN Ia is 0.9 arcseconds, compared to 0.7 arcseconds for all LSST gLSN Ia. The catalogue spans a range of Einstein radii between 0.06 arcsec $\leqslant \theta_{Ein} \leqslant$ 2.54 arcsec.

4.3.3 *Lifting the Mass-Sheet Degeneracy with LSST gLSN Ia: Predictions for* H_0

Disclaimer: This section was jointly written with Thomas Collett.

The fundamental gain of a gLSNe Ia over a standard time delay lens is the ability to test for the presence of systematic uncertainties in the lens model. Since lens models have typical errors of a few percent (Wong et al., 2017), a 0.15 mag uncertainty on the flux of a single lensed image will not provide statistically relevant improvement on H_0. Averaging over many lensed SNe will be required to constrain H_0 with interesting accuracy.

To investigate the expected constraints on H_0 from the final LSST gLSNe Ia sample, we draw 650 gLSNe Ia from our mock LSST catalogue. This is the number of gLSNe Ia forecast to be discovered by LSST early enough to measure reliable time delays (Goldstein et al., 2018). Taking a typical 7% error per system (Bonvin et al., 2017) and scaling by root N, gives $\sigma_{H_0} = 0.3\%$, however this neglects residual systematics from the mass-sheet degeneracy.

Given the individual magnification probability $P(\mu)$ for each image of a gLSN, the expected PDF for the unlensed magnitude of the SN is given by:

$$P(M_{SN}) = \prod_{\forall i} P(\mu_i). \tag{50}$$

Adding this in quadrature to an intrinsic SN Ia scatter of 0.1 magnitudes (Betoule et al., 2014), gives the expected uncertainty on the macromodel magnifications for the lens.

Constraining the true macromodel magnifications gives constraints on the mass-sheet degeneracy parameter λ, since

$$\mu_{True} = \mu_{Model}/\lambda^2, \tag{51}$$

where μ_{True} is the true magnification and μ_{Model} is the macromodel magnification assuming $\lambda = 0$. This implies that a system with a microlensing scatter of 0.15 magnitudes gives a constraint on λ with 17% precision that is insensitive to the the mass-sheet transformation.

The time delays - and hence $1/H_0$ - are proportional to λ. The product of $P(\lambda)$ over all the systems gives the level at which the mass-sheet degeneracy can be broken for the final constraint on H_0. This product has a width of $\sigma_\lambda = 0.5\%$. Combined, the 650

Table 4: Table of parameters used for iPTF16geu simulations. κ and γ were taken from More et al. (2017). Values of the smooth matter fraction s were inferred from our lens model of iPTF16geu.

Image	κ	γ	s
A	0.56	0.56	0.22
B	0.43	0.43	0.23
C	0.57	0.56	0.27
D	0.46	0.45	0.23

LSST gLSNe Ia will therefore be able to detect systematics in H_0 due to the mass-sheet transformation at the 0.5% level. If we restrict the sample to the 140 gLSNe with a microlensing scatter of less than 0.15 mags, the constraints on H_0 degrade to $\sigma_{H_0} = 0.6\%$. If only the 44 standardisable quad image systems are used, the constraints H_0 degrade to $\sigma_{H_0} = 1.1\%$.

We have not considered the possibility of multiple progenitor channels in these calculations. If the intrinsic brightness of the SN Ia depends on the progenitor, and the dominant progenitor channel varies with redshift, then this can introduce a redshift-dependant bias into the distance measures of SNe Ia. This will therefore bias the slope of the resulting Hubble diagram used in the calculation of H_0. If this bias is significant, then this could potentially affect the ability of gLSNe Ia to produce a competitive sub-percent measurement of H_0 unless accounted for. This further motivates the study presented in Chapter 5.

4.3.4 *iPTF16geu*

The recent observations of iPTF16geu, give us a first opportunity to test the analysis methods developed in this paper. Since the images have high magnification and form in regions of high stellar density, we should not expect this system to be standardisable. The values of κ and γ for each of the iPTF16geu images have been estimated from the macro lens model published in More et al. (2017). We use the same prescription as in Section 4.3.2 to infer the likely smooth matter fractions at the image locations (Table 4).

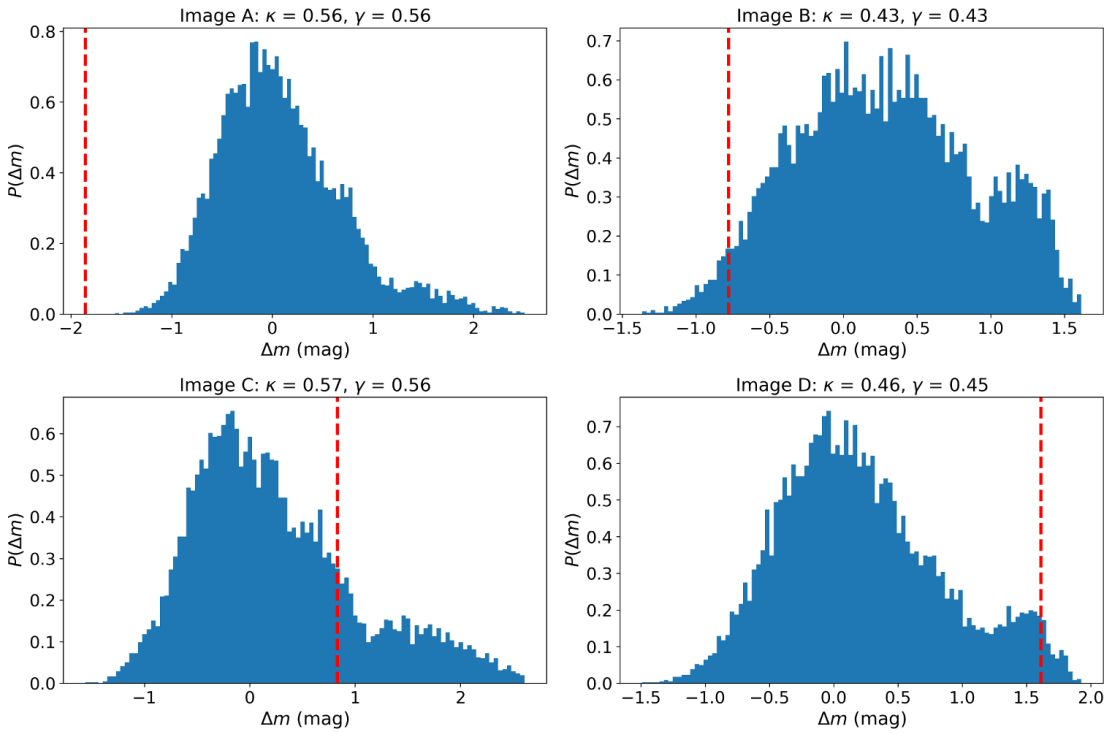

Figure 38: Histograms showing the typical magnifications for 10^4 microlensed SN for each image in iPTF16geu, around the time of HST imaging. The magnifications are in units of magnitudes and show the microlensing deviation from the smooth macromodel. The red dashed lines give the corresponding observations from Goobar et al. (2017).

In Figure 38 we show the PDF of the change in magnitude due to microlensing for each image of iPTF16geu. These PDFs are generated assuming a time of 60 days after explosion approximately corresponding to the Hubble Space Telescope (HST) data analysed in More et al. (2017). More et al. (2017) noted that there is a significant discrepancy between the observed fluxes in iPTF16geu and those predicted by their lens macromodel assuming iPTF16geu is a typical SN Ia, with image A being almost 2 magnitudes brighter than the macromodel prediction for a SN Ia. Figure 38 shows that this discrepancy cannot be due to microlensing alone. A similar analysis by Yahalomi, Schechter, and Wambsganss (2017) reaches the same conclusion using a point source, however the tension increases for a finite sized source. We find that the discrepancies between the observed and macromodel predicted fluxes of the other three images are consistent with microlensing.

If iPTF16geu has a standard Type Ia luminosity, then at least some of the the disagreement in the observed and predicted fluxes must be due to deficiencies in the

macromodel. The presence of a dark substructure or a stellar disk close to image A may explain this flux anomaly (Vegetti et al., 2010; Hsueh et al., 2017).

iPTF has an *r*-band discovery limit of 21st magnitude (Goobar et al., 2017); without the extreme magnification of image A, iPTF16geu still would have been identified as a transient by iPTF, but only marginally. The transient was only added to the spectroscopic follow-up queue when the system reached an *r*-band magnitude of 19.3 Goobar et al. (2017). iPTF16geu would likely had not been confirmed as a gLSNe Ia without the extreme magnification of image A. The demagnification of image D is another atypical feature of iPTF16geu. Whilst microlensing can plausibly explain the observed brightness of D, the presence of dust may also contribute to the dimming. Therefore, the micro- and macro-lensing of iPTF16geu are therefore unlikely to be representative of a future population of lensed SNe. However this result does demonstrate that breaking the mass-sheet degeneracy with future lensed SNe Ia will also require a detailed reconstruction of disks and dark matter substructures in the lenses.

4.4 CONCLUSIONS

We have evaluated the effect of microlensing on gLSNe Ia for various image configurations, corresponding to values of the convergence κ, the shear γ and the smooth matter fraction s, across multiple time intervals. We have found that there are regions of parameter space where the effect of microlensing is suppressed enough for the gLSN Ia to be standardisable. Specifically, regions of low κ, γ and high s are subject to microlensing scatter of $\sigma_{ML} \lesssim 0.15$, particularly at early times (see Figure 34). Physically this corresponds to asymmetric configurations with at least one image located far outside the Einstein radius, which will experience the least amount of microlensing.

Combining our microlensing models with the gLSNe Ia catalogue from Goldstein et al. (2018) we predict that $\sim 22\%$ of the ~ 930 gLSNe Ia to be discovered by LSST will be standardisable. From the sample of 650 gLSNe Ia, of which accurate time delays can be measured, the mass-sheet degeneracy can be broken at the 0.5% level. The LSST gLSNe Ia sample will thus be robust against systematics in H_0 at the 0.5% level. The assumed fraction of standardisable systems with accurate time delays may be

somewhat pessimistic, since we found that standardisable gLSNe have larger Einstein radii (median 0.9 arcseconds) and time delays (median 44 days), than the general population.

Our result assumes a SN Ia light profile that expands at a constant velocity of 10^4 km s^{-1}. Whilst simple, more complicated models can be extracted from our results by rescaling the time axis. We have not considered sources with clumpy profiles, however, since the standardisable region of Figure 34 varies only weakly with time, our results should not be heavily influenced by the choice of source model. If the SN profile contains any small, bright, fast moving clumps then additional scatter may be introduced. However, microlensing of such clumps would introduce rapid temporal variation in the light curve which should be easy to detect.

Whilst this paper does not focus on the IMF, we found a sharp sensitivity to the IMF for lenses with Einstein radii between 0.2 and 0.5 arcseconds, assuming a lens and source with the same redshifts as in iPTF16geu. Measuring the scatter in a sample of such gLSNe Ia should trivially discriminate between the Salpeter and Chabrier fits of Auger et al. (2010).

We also applied our microlensing analysis to the gLSN Ia iPTF16geu and compared our results against the More et al. (2017) analysis, who found a strong discrepancy between the observations and their lens model, attributing the discrepancy to microlensing. Our analysis suggests that the discrepancy cannot be due to microlensing primarily (see Figure 38) and signals potential deficiencies in the use of simple lens macromodels, as suggested by More et al. (2017).

This work shows that it is possible to infer the intrinsic luminosity for a significant sample of $\sim$ 200 LSST gLSNe Ia, suppressing the mass-sheet degeneracy of the lens model. This will allow for accurate and precise measurements of H_0 with significantly reduced systematics through time delay cosmography, thus enabling a stringent test of the ΛCDM model of cosmology.

5

OBSERVING THE EARLIEST MOMENTS OF SUPERNOVAE USING STRONG GRAVITATIONAL LENSES

Note: A previous version of this chapter was published in Foxley-Marrable et al. (2020).

Abstract

We determine the viability of exploiting lensing time delays to observe strongly gravitationally lensed supernovae (gLSNe) from first light. Assuming a plausible discovery strategy, the Legacy Survey of Space and Time (LSST) and the Zwicky Transient Facility (ZTF) will discover $\sim$ 110 and $\sim$ 1 systems per year before the supernova (SN) explosion in the final image respectively. Systems will be identified $11.7^{+29.8}_{-9.3}$ days before the final explosion. We then explore the possibility of performing early-time observations for Type IIP and Type Ia SNe in LSST-discovered systems. Using a simulated Type IIP explosion, we predict that the shock breakout in one trailing image per year will peak at $\lesssim$ 24.1 mag ($\lesssim$ 23.3) in the *B*-band (*F218W*), however evolving over a timescale of $\sim$ 30 minutes. Using an analytic model of Type Ia companion interaction, we find that in the *B*-band we should observe at least one shock cooling emission event per year that peaks at $\lesssim$ 26.3 mag ($\lesssim$ 29.6) assuming all Type Ia gLSNe have a 1 $M_\odot$ red giant (main sequence) companion. We perform Bayesian analysis to investigate how well deep observations with 1 hour exposures on the European Extremely Large Telescope would discriminate between Type Ia progenitor populations. We find that if all Type Ia SNe evolved from the double-degenerate channel, then observations of the lack of early blue flux in 10 (50) trailing images would rule out more than 27% (19%) of the population having 1 $M_\odot$ main sequence companions at 95% confidence.

5.1 INTRODUCTION

Early observations of supernovae (SNe) light curves are critical in constraining the properties of SN progenitor systems and their pre-explosion evolution in a way that cannot be inferred from late-time observations (e.g. Kasen 2010; Piro, Chang, and Weinberg 2010; Rabinak and Waxman 2011; Piro and Morozova 2016; Kochanek 2019;

Fausnaugh et al. 2019; Yao et al. 2019; Miller et al. 2020; Bulla et al. 2020). In addition, the physics of SN explosion mechanisms are still yet to be well understood (see Smartt 2009; Janka 2012; Hillebrandt et al. 2013; Burrows 2013; Maoz, Mannucci, and Nelemans 2014; Livio and Mazzali 2018 for recent reviews).

The earliest expected SN emission should comprise of a bright X-ray/UV flash as the initial radiation-mediated shock propagates to the outer edges of the star, ejecting the envelope in a process known as the 'shock breakout' (see Colgate 1968, 1975; Grassberg, Imshennik, and Nadyozhin 1971; Lasher and Chan 1975; Lasher and Chan 1979; Imshennik and Utrobin 1977; Falk 1978; Klein and Chevalier 1978; Epstein 1981; Ensman and Burrows 1992; Piro, Chang, and Weinberg 2010). This process occurs over a timescale of order seconds to a fraction of an hour, dependent on the progenitor size. If there is significant circumstellar material surrounding the progenitor prior to the moment of explosion, the breakout timescale could be extended to a number of days. After the initial shock breakout, as the ejected envelope expands, we expect to observe UV/optical cooling emission evolving over a timescale of order days (see Waxman and Katz 2017 and references therein for a comprehensive theoretical overview on the topic of shock breakout and cooling emission).

The progenitors of Type Ia SNe remain an unsolved problem in astrophysics (Maoz, Mannucci, and Nelemans, 2014; Livio and Mazzali, 2018), with the single-degenerate (SD) and double-degenerate (DD) channels being plausible explanations for the post-explosion light curves. The SD scenario occurs when a carbon-oxygen (C-O) white dwarf (WD) accretes mass from a non-degenerate companion star, triggering an explosion via thermonuclear detonation on the approach to the Chandrasekhar Mass, M_{Ch} (Whelan and Iben, 1973; Nomoto, 1982; Maguire, 2017). In the DD scenario, a WD approaches M_{Ch} due to accretion of mass or directly merging with a secondary WD (Iben and Tutukov, 1984; Webbink, 1984; Maguire, 2017). Another plausible model is the sub-M_{Ch} 'double-detonation' scenario, where an initial detonation in the outer helium layers accreted onto the surface of the WD triggers a secondary detonation in the C-O core (Nomoto, 1980; Taam, 1980; Woosley, Taam, and Weaver, 1986; Livne, 1990; Woosley and Weaver, 1994; Fink et al., 2010; Moll and Woosley, 2013). This mechanism has been used to explain the unusual colour evolution and spectra of three recent Type Ia SN (Jiang et al., 2017; De et al., 2019; Jacobson-Galan et al., 2019).

Type Ia SNe are used to measure cosmological distances (e.g. Riess et al., 1998; Perlmutter et al., 1999) on the assumption their peak magnitudes are all effectively homogeneous after standardisation ($\sigma_M \sim 0.1$ mag; e.g. Betoule et al. 2014; Macaulay et al. 2017; Jones et al. 2018). Therefore, if the mean intrinsic brightness of the Type Ia SN significantly varies with progenitor model, and the progenitor population varies with redshift (Childress, Wolf, and Zahid, 2014), cosmological analyses dependent on SNe Ia will be inherently biased. Since neither the SD or DD channels have been ruled out conclusively, it is entirely plausible that both scenarios are valid, and that traces of the population could even come from other channels (e.g. the core-degenerate channel, see Livio and Mazzali, 2018, and references therein). Early photometry obtained within hours or days of the SN Ia explosion could provide insight into the presence of a potential companion star and constrain properties such as the companion radius (e.g. Nugent et al., 2011; Bloom et al., 2012; Goobar et al., 2014, 2015; Marion et al., 2016; Hosseinzadeh et al., 2017; Dimitriadis et al., 2019; Shappee et al., 2019).

Even with the development of wide-field optical surveys, observing the earliest moments of SNe is still non-trivial and heavily reliant on chance. Ideally, we would like to systematically predict the precise moment a SN will appear on a particular patch of sky and start performing high-cadence observations in the moments prior to and at first light. Such a prediction could be possible if the SN was subject to strong gravitational lensing (Suwa, 2018).

Gravitational lensing occurs because massive objects, e.g. elliptical galaxies, deform the local curvature of spacetime such that nearby rays of light become deflected from their original path. When a sufficiently dense object is precisely aligned between the observer and a background source, multiple images of the background object form. This effect is known as strong gravitational lensing (Einstein, 1936; Zwicky, 1937a). The light travel time from the source to the observer varies between lensed images due to geometrical differences in the path length and differences in gravitational time dilation. Both effects are a function of the path of the light through the gravitational potential of the lens (Shapiro, 1964; Blandford and Narayan, 1986; Treu and Marshall, 2016).

When a strongly lensed supernova (gLSN) explodes, an observer will witness the SN from first light once in each lensed image, but with a time delay between the images. Hence, if a gLSN is identified before the appearance of the SN in any of the

multiple images, and the mass distribution of the lens is well understood, it should be possible to predict the explosion time of the SN in the remaining images.

SN Refsdal, a core-collapse SN multiply imaged by a foreground galaxy cluster (Kelly et al., 2015), was predicted to have a fifth image appear ~ 1 year from the appearance of the first image (Treu et al., 2016). This prediction was later confirmed by the reappearance of the SN in the fifth lensed image (Kelly et al., 2016). However, the errors on the predictions ranged from 5-20% of the year-long time delay between the first and fifth image, dependent on the choice of lens model (Treu et al., 2016). This can be attributed to the dense and complicated mass profile of the foreground galaxy cluster lens. Therefore lens systems with significantly simpler mass profiles (e.g. elliptical galaxies) and shorter time delays are more suited for very early observations of lensed SN light curves.

To date, only one other gLSN with resolved images has been discovered (iPTF16geu, Goobar et al., 2017), and this was identified after the appearance of the last image. A sample of gLSN with followup triggered before the reappearance of the SN in the remaining images is required to constrain progenitor populations. The Legacy Survey of Space and Time (LSST) and Zwicky Transient Facility (ZTF) are the next generation of wide-field, high-cadence imaging surveys which together are expected to yield thousands of gLSNe over the next decade (Goldstein et al., 2018; Goldstein, Nugent, and Goobar, 2019).

In this paper, we endeavour to answer the following questions:

1. Will LSST and ZTF enable the discovery of gLSNe before the appearance of all multiple images?

2. How long is the time frame between the discovery of the system and explosion of the last image? How precisely can the last explosion time be predicted?

3. How bright will the early phase light curves of Type IIP and Type Ia SNe found in the trailing images of LSST-discovered gLSNe get?

4. Can we use LSST-discovered gLSNe to make inferences on the progenitor population of Type Ia SNe with redshift? How will this compare with constraints from unlensed SNe Ia?

5. Can we measure precise time delays between the rapid early-phase light curves of gLSNe?

In Section 5.2, we use the gLSNe catalogues from Goldstein, Nugent, and Goobar (2019) to provide predictions into the populations of gLSNe in LSST and ZTF that will be discovered before reappearance of the SN explosion in any of the remaining lensed images. In Section 5.3, we make predictions on the magnitude distributions of early phase, LSST-discovered Type IIP and Type Ia SNe, whose light curves were generated using the SuperNova Explosion Code (SNEC) code and the companion emission models of Kasen (2010), respectively. In Section 5.4 we explore how gLSNe can be used to constrain SNe Ia populations. In Section 5.5 we determine whether early phase SNe observations are useful for the field of time delay cosmography. We then conclude in Section 5.6.

5.2 LSST/ZTF POPULATIONS

5.2.1 *gLSN Catalogues*

To make predictions on the populations of LSST/ZTF discovered gLSNe with 'trailing' SN images, i.e. gLSNe discovered before the reappearance of the SN in the remaining lensed images, we use the publicly available simulated gLSN catalogues from Goldstein, Nugent, and Goobar (2019)[1]. These catalogues were created by simulating a population of randomly realised gLSNe systems into mock LSST/ZTF survey data and applying the resolution-insensitive discovery strategy detailed in Section 4.1 of Goldstein et al. (2018) to forecast the properties and rates of gLSNe to be discovered by LSST and ZTF.

Only elliptical galaxies were considered as potential lenses in the catalogues. Ellipticals are the most common type of gravitational lens; the sharp 4000 Å break in their uniform spectra allows their photometric redshifts to be accurately measured; and they are the only lens compatible with the Goldstein et al. (2018) discovery strategy. The projected mass distributions of the ellipticals were modelled as a singular isothermal ellipsoids[2] (Kormann, Schneider, and Bartelmann, 1994), shown to be in good agreement with observations (e.g. Koopmans et al., 2009).

1 https://portal.nersc.gov/project/astro250/glsne/
2 Including an external shear component to replicate additional lensing by line-of-sight structures.

The catalogues contain 7 different subtypes of gLSNe: including 3 subtypes of thermonuclear gLSNe (Type Ia, SN 1991bg-like and SN 1991T-like), with rates and luminosity functions based on Sullivan et al. (2006); and 4 subtypes of core-collapse gLSNe (Type IIP, Type IIL, Type IIn, Type Ib/c) with rates and luminosity functions based on Li et al. (2011). The rates in the gLSN catalogue carry uncertainties of order 10% which carries over to the rates presented in our analysis. Three different types of host galaxies were considered in the catalogues: elliptical galaxies (very little to no star formation), So/a-Sb galaxies (some star formation) and late-type/spiral galaxies (ongoing star formation). The simulations assume elliptical and So/a-SB galaxies only host normal SNe Ia and SN 1991bg-like events, whereas late-type/spiral galaxies host both core-collapse and thermonuclear SNe types.

With the assumptions listed above, for each gLSN system the properties of the lens galaxy, the SN and the host galaxies were realised at random, uniformly distributed on the sky and assigned a reddening value $E(B-V)$ for the host galaxy and Milky Way dust[3].

For ZTF, Goldstein, Nugent, and Goobar (2019) used the simulated survey data and scheduler from Bellm et al. (2019) for the public, partnership and Caltech programs. For LSST, both the `minion1016` (Delgado et al., 2014) and `altsched` (Rothchild, Stubbs, and Yoachim, 2019) observing strategies were considered. For our analysis we only consider the `altsched` observing strategy[4].

5.2.1.1 *Discovery Strategy*

The discovery strategy proposed in Goldstein et al. (2018) and Goldstein, Nugent, and Goobar (2019) is designed to photometrically identify gLSNe in transient survey data without the need to resolve the multiple images through follow-up observations.

The discovery strategy can be summarised as follows: first, identify SNe candidates spatially aligned with elliptical galaxies. Since there is very little to no ongoing star formation in elliptical galaxies, they primarily host only Type Ia SNe (Li et al., 2011). The next step is to test whether the SNe candidate is a Type Ia SN hosted by the elliptical galaxy. This can be achieved by comparing the properties of the SN light curve (e.g. peak brightness, light curve shape and colour evolution) to a SN Ia template (e.g.

3 Lens galaxy dust was neglected.

4 Yields are comparable to `minion1016`, but with better sampled light curves that are discovered earlier.

SN Type	LSST		ZTF	
	Doubles	Quads	Doubles	Quads
IIn	52.0	9.7	0.1	0.5
IIP	18.9	3.3	0.2	0.1
Ia	12.8	1.5	—	0.1
Ibc	3.4	0.9	—	—
IIL	2.2	0.8	—	—
91T	1.6	0.2	—	—
91bg	0.2	0.1	—	—
Total	91.1	16.5	0.3	0.7

Table 5: Number of gLSNe discovered with one or more unexploded trailing images each year. Rates below 0.05 per year are not shown.

SALT2; Guy et al., 2007) at the photometric redshift of the elliptical galaxy. If observations are inconsistent with a SN Ia at the photometric redshift of the apparent host, then it is a candidate for strong lensing. A transient is identified as a gLSN when at least one data point is observed with a 5σ discrepancy from the best fit Ia light curve (consistent with the elliptical's photometric redshift) and at least four data points have signal-to-noise $\geqslant 5$ (see Section 4.2 of Goldstein et al. 2018).

5.2.2 *Trailing gLSNe Populations*

A system in the gLSNe catalogue is determined to contain unexploded trailing images if the arrival time of any lensed image is after the discovery time of the gLSN. The moment of explosion for each image is calculated by adding the time delay to the arrival time of the first image at zero-phase, and subtracting the difference between explosion time and zero-phase time for each model. For Type Ia and Type IIP SNe, the zero-phase time, t_0 is at the peak of the SN light curve, for the other models, t_0 is the explosion time. To determine the time of explosion, we assume the explosion time to be 20 rest frame days before peak for Type Ia SNe and 19 rest frame days for Type IIP

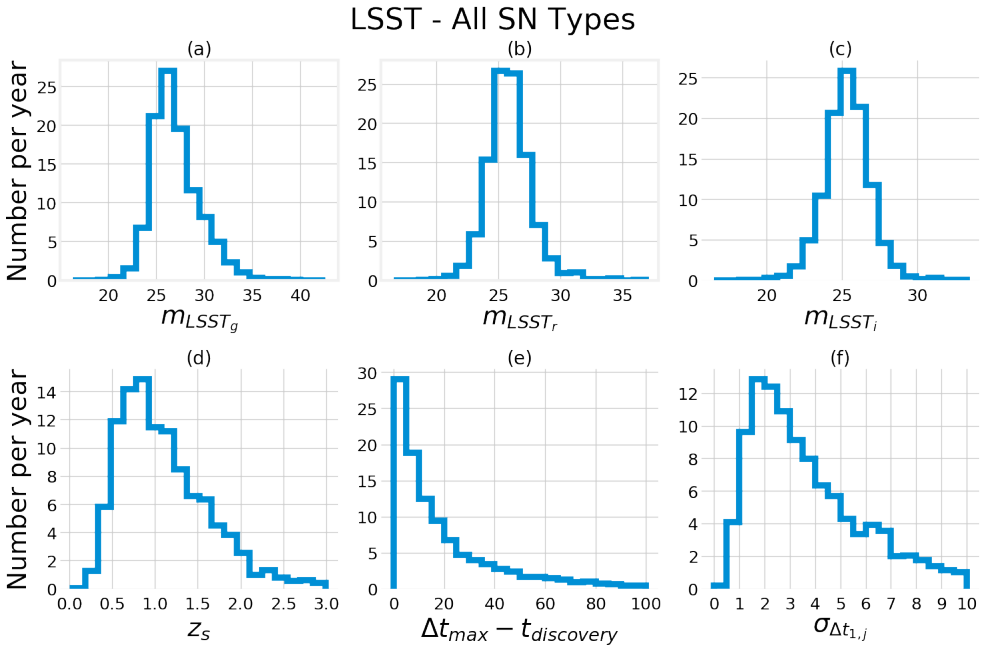

Figure 39: Distributions and annual rates of LSST-discovered gLSNe (of all SN Types) containing trailing images with unexploded SNe. See Table 6 for descriptions of the subplots.

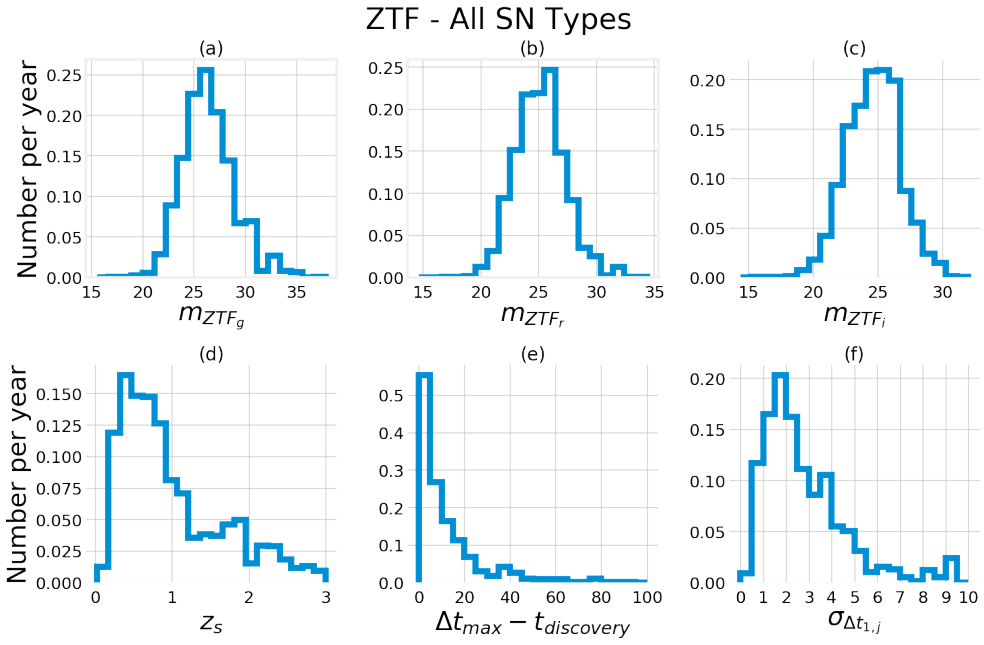

Figure 40: Distributions and annual rates of ZTF-discovered gLSNe (of all SN Types) containing trailing images with unexploded SNe. See Table 6 for descriptions of the subplots.

Subplot	Description
(a) - (c)	Observer frame apparent magnitudes for trailing lensed images in the g, r and i bands respectively.
(d)	Redshift of the background source.
(e)	'Reaction' time between the discovery and confirmation of the gLSNe and the appearance of the final image.
(f)	Error in the time delay relative to the first image for all trailing images.

Table 6: Description of subplots for Figures 39-40 and Figures 48-54.

SNe. This is derived from the difference between peak and the earliest non-zero data point of the Hsiao et al. (2007) and Sako et al. (2011) models respectively.

The populations of gLSNe with unexploded trailing images for all SN types are illustrated in Figures 39 and 40 (see Figures 48 - 54 for a breakdown of the LSST distributions by SN Type[5]). The number of discoveries per year for each instrument and SNe type are shown in Table 5. Across all SN types LSST is expected to find ~ 110 trailing gLSNe per year, whilst ZTF will yield a significantly lower rate of systems at ~ 1 trailing gLSNe per year.

The ZTF sample is dominated by quadruple imaged systems (hereby referred to as 'quads') whereas the LSST sample is dominated by double imaged systems (hereby referred to as 'doubles'). Quads dominate the ZTF sample because ZTF is shallow and quads typically have higher magnification than doubles. The deeper, lower cadence of LSST allows it to find fainter systems but at later times: since doubles typically have longer time delays than quads, they are more likely in LSST. Quads make up ~ 16 % of the total sample with a discovery rate of approximately once every 1.4 years with ZTF and once every 22 days with LSST. Across all quadruple gLSNe types, we expect to find ~ 15 per year in LSST and ~ 1 per year in ZTF with a single trailing image remaining. This falls to ~ 1 quad per year in LSST ($<$ 0.01 in ZTF) with 2 or more images remaining. In many ways, quads are more suited for early phase SN observations, since they are typically more highly magnified, and they are easier to

5 ZTF distributions were purposefully left out due to low sample size, resulting in distributions being dominated by shot noise.

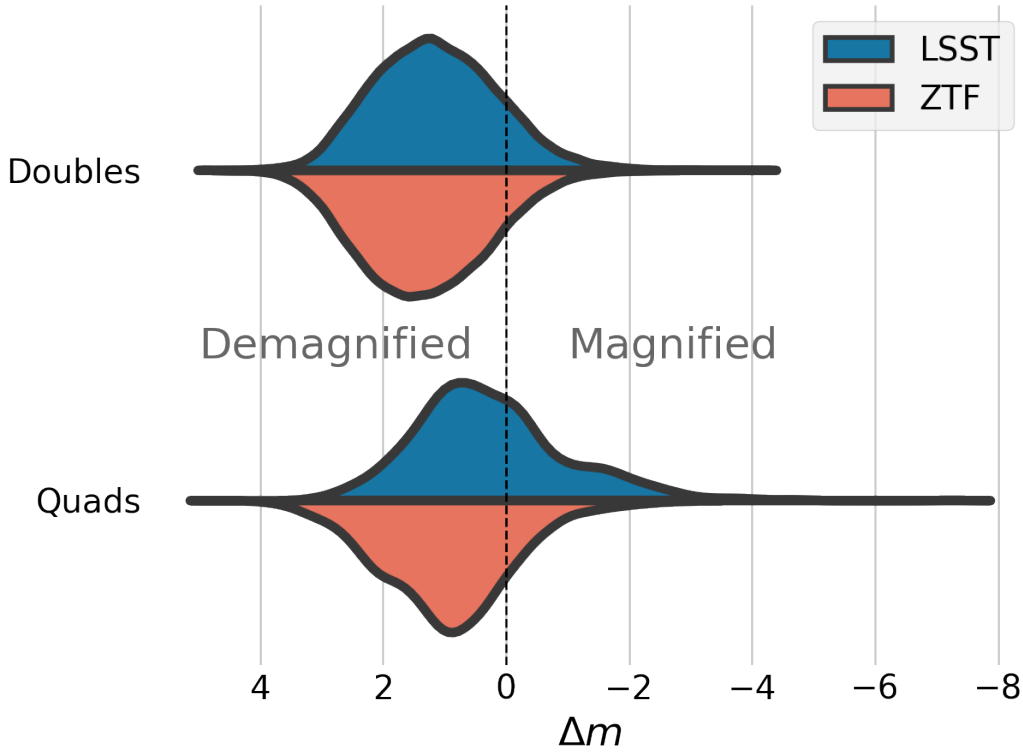

Figure 41: Distribution of trailing image magnifications (shown as deviation in magnitudes, Δm) for double and quadruple image gLSNe after discovery by LSST and ZTF.

accurately model enabling more precise predictions of the time delay. However, the shorter time delays make the rate of quads discovered before the final explosion far lower than the double systems.

Lens modelling of galaxy scale lenses typically yields model time delay estimates at around 5% precision (e.g. Wong et al., 2017; Birrer et al., 2019; Chen et al., 2019). We assume this fractional precision for the predicted reappearance of trailing images. Comparable fractional precision was achieved for predicting the reappearance of SN Refsdal in a much more complicated cluster lensing environment (Treu et al., 2016). Galaxy scale lenses should be easier to precisely model, though the shorter time delay will require a fast turn around between discovery and time delay estimate. Assuming this 5% error is achieved for incomplete systems we find that typically we will be able to predict the time delays to $3.2^{+3.4}_{-1.6}$ days around the appearance of the final image. Very few trailing images are predictable to less than a day (Figures 39f and 40f). The 'reaction' time between discovery of the gLSN and the appearance of the SN in the final lensed image (Figures 39e and 40e) is typically within $11.7^{+29.8}_{-9.3}$ days from discovery.

Performing follow-up observations and modelling lenses within this time scale will pose a challenge, however the promise of automated lens modelling software (e.g. `AutoLens`; Nightingale, Dye, and Massey 2018) could alleviate this time pressure.

The trailing images in the gLSNe sample have a peak median magnitude of $25.4^{+1.4}_{-1.3}$ in the *i*-band, which is typically dimmer than the unlensed SN explosion (see Figures 11 and 25 of Goldstein, Nugent, and Goobar 2019 for comparison). This is due to the vast majority of trailing gLSNe only having one image remaining after discovery, which are commonly demagnified by $\sim$ 1 or 2 magnitudes (see Figure 41). This is because the final image is typically closest to the centre of the lensing galaxy. These images have significant mass density at their location, such that the light rays are over-focused. Small changes in the image plane position result in large changes in the source plane position, so these images are demagnified. As shown in Figure 41 a small number of magnified trailing images exist in the catalogue for both doubles and quads. This can be explained (particularly for doubles) by the systems having more symmetrical image configurations combined with the presence of external shear in the model. However, the magnified trailing images are significantly less abundant when compared to their demagnified counterparts[6]. Coupled with extinction by dust, it is clear that obtaining early phase SN data from the trailing images of gLSNe will be an observationally expensive effort.

5.2.3 *Unknown vs Known Lenses*

Our estimated yields are potentially pessimistic, since the assumed discovery method does not include the possibility that the SN host is already known to be strongly lensed. LSST is expected to discover $\sim$ 100,000 lenses (Collett, 2015) and immediate followup of any transient detected in a known lens system should enable the identification of gLSN at an earlier phase than we have assumed. For LSST-discovered gLSNe, by assuming that all lenses in the Goldstein, Nugent, and Goobar (2019) catalogue are already known and assuming gLSN discovery from the first SN observation with signal-to-noise $\geqslant$ 5, we find that the gLSNe population with trailing images increases by $\sim$ 48% with an average increase in brightness of $\sim$ 0.3 magnitudes (for a detailed breakdown by SN type, see Table 7).

6 By a factor of $\sim$ 4 less for doubles and a factor of $\sim$ 2 less for quads.

SN Type	ΔN		Δm
	Doubles	Quads	
IIn	24.4	6.1	-0.4
IIP	8.7	2.7	-0.4
Ia	4.5	1.1	-0.3
Ibc	1.2	0.4	-0.2
IIL	1.0	0.5	-0.2
91T	0.6	0.1	-0.2
91bg	—	—	-0.5
Total	40.4	10.9	

Table 7: Change in the number and average brightness of gLSNe with trailing images if all lensed SNe in the LSST catalogue were already known lenses. In this scenario, discovery is assumed from the first observation of the SN with a signal-to-noise $\geqslant 5$ in any filter. Rates below 0.05 per year are not shown.

5.3 EARLY PHASE SUPERNOVAE MODELS

In this section of the paper, we apply light curves from a Type IIP detonation model (see Section 5.3.1 and Figure 42) and a Type Ia SD companion cooling model (see Section 5.3.2 and Figure 43) to the ensemble of LSST-discovered gLSN detailed in Section 5.2 in order to determine the early-phase peak brightness and rates of the SNe found in trailing gLSN images (including the effects of magnification and host galaxy/milky way extinction) and determine whether gLSNe can feasibly be used to observe early-phase SNe.

5.3.1 *Type IIP Shock Breakout*

We model an instance of a Type IIP explosion using the SuperNova Explosion Code[7] (`SNEC`), an open-source Lagrangian code for simulating the hydrodynamics and equilibrium-diffusion radiation transport in the expanding envelopes of SNe (Morozova et al.,

7 `http://stellarcollapse.org/SNEC`

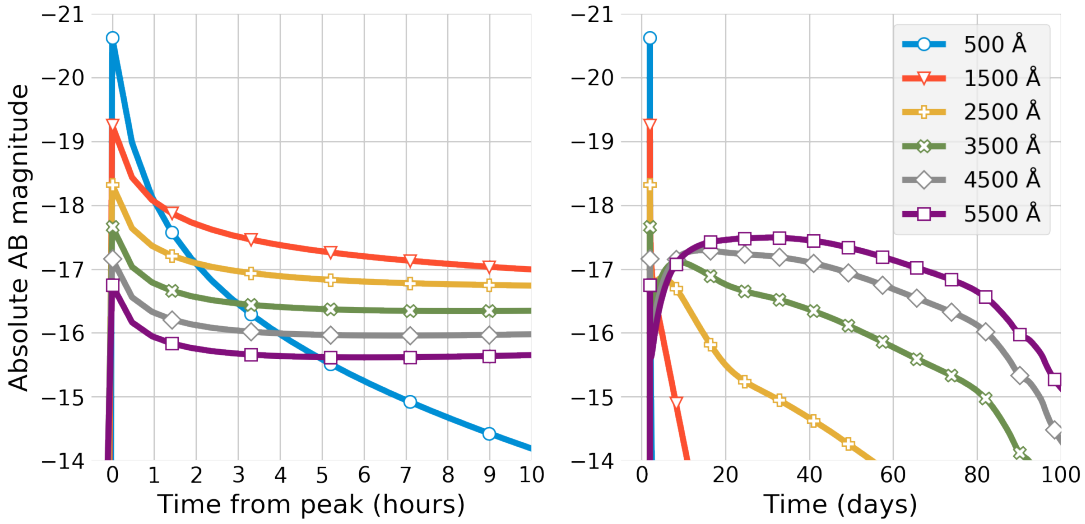

Figure 42: Absolute AB magnitude for a Type IIP SN explosion as a function of rest frame wavelength. The light curve includes the initial shock breakout and was simulated using SNEC (see Morozova et al., 2015). *Left:* The initial hours of the light curve from the peak of the shock breakout, evolving over a timescale of ~ 30 mins in the rest frame. *Right:* The evolution of the full IIP light curve over 100 rest frame days.

2015). For the progenitor star, we use the unstripped zero-age main sequence (ZAMS) reference star ($M_{ZAMS} = 15\ M_\odot$) that was evolved by the open-source stellar evolution code MESA (Paxton et al., 2011, 2013) into a red supergiant with outer radius $R = 7.2 \times 10^{13}$ cm and total mass $M = 12.3\ M_\odot$[8]. We model the explosion as a black body and assume a constant grey opacity.

Figure 42 shows the absolute magnitude of the Type IIP explosion over time, including the initial shock breakout, across a selection of wavelengths. The peak of the Type IIP shock breakout is brightest when observed at ~ 400 Å (extreme ultra-violet) in the source rest frame, with an absolute AB magnitude of ~ -20.5. The rise and decline of the Type IIP shock breakout at early times is extremely rapid, occurring over a timescale of ~ 30 minutes and is clearly distinct from the late-time light curve. The high-energy nature of the shock breakout means that the peak of the emission will be in the extreme UV in the source rest frame.

For strongly lensed images we must also account for microlensing by stars in the lensing galaxy in addition to the macromagnification from the entire lens galaxy. For sources much larger than the Einstein radius of a star, the granularity of the lens

8 Some mass is lost in stellar winds during the star's evolution.

does not affect the total magnification of the source. This is not the case for gLSNe (Foxley-Marrable et al., 2018). Due to conservation of energy, microlensing by stars does not change the average magnification over an ensemble, but it can introduce significant scatter (Foxley-Marrable et al. 2018; Goldstein et al. 2018; Dobler and Keeton 2006). We use the microlensing magnification distributions from Vernardos et al. (2014, 2015) to build the probability density function for microlensing magnification. For simplicity's sake, we assume all trailing images go through the region star field where 80 percent of the mass is in stars and 20% in a smooth (dark matter) component. We assume all of the images have a lensing convergence and shear of 1.65, comparable to the typical values for trailing images found in Section 5.2. The magnification distribution for such a microlensing configuration is shown in Figure 44. We assume the microlensing is achromatic at early times as found by Goldstein et al. (2018), Huber et al. (2019) and Suyu et al. (2020).

Figure 45 shows the distribution of peak apparent magnitudes from applying our IIP shock breakout model to the LSST-discovered trailing gLSNe images, incorporating the effects of magnification (including microlensing by foreground stars) and extinction by dust (using the dust model of Goldstein, Nugent, and Goobar 2019 and the reddening law of Cardelli, Clayton, and Mathis 1989).

Assuming our model is representative of the IIP population, we predict to observe Type IIP shock breakouts at a rate of one per year at $\lesssim$ 24.1 mag in the *B*-band and $\lesssim$ 23.3 in the UV (*F218W*). However, since the shock breakout only lasts for $\sim$ 30 minutes, reaching this depth will require a large collecting aperture if spectroscopy or multiple points on the light curve are desired. Given that reappearance times will only typically be accurate to $2.6^{+3.0}_{-1.4}$ days for Type IIP gLSNe, a network of telescopes would be required to catch the shock breakout.

This result arises from the application of a single IIP detonation to the ensemble of Type IIP SNe from the Goldstein, Nugent, and Goobar (2019) catalogue. The absolute magnitudes of core collapse SNe can vary significantly, with a typical scatter of $\sim \pm 1$ mag for Type IIP SNe (Li et al., 2011; Richardson et al., 2014). This variation in the magnitude of Type IIP SNe implies that our single realisation of the shock breakout is naive, and an ensemble of breakouts may shift, and will broaden the distribution of peak magnitudes shown in Figure 45.

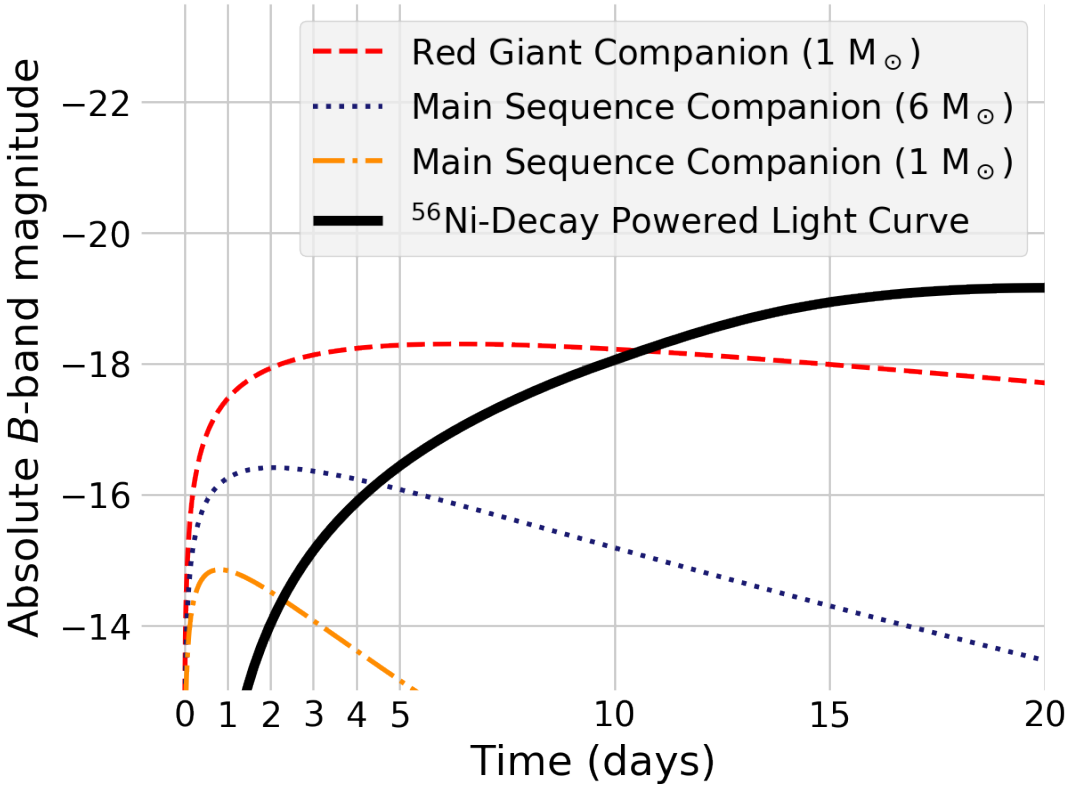

Figure 43: Absolute *B*-band magnitude for a series of analytical companion shock cooling models from Kasen (2010) plotted against a ^{56}Ni-decay powered Type Ia SN light curve (derived from the Hsiao et al. 2007 model, assuming a rise time of 20 rest-frame days from explosion and peak absolute *B*-band magnitude of -19.1). If there is a stellar companion, the observed flux during the earliest phases of the SN Ia will be dominated by the shock cooling component.

5.3.2 *Type Ia Companion Shock Cooling*

Using the analytic models from Kasen (2010) we generate a series of shock cooling light curves for a non-degenerate companion star after shocking by the ejecta from a Type Ia SN. Radiative diffusion after shock-heating produces optical/UV emission. During the earliest phases of a SD Type Ia SN, the shock-heated emission is expected to exceed the radioactively powered luminosity (see Figure 43, also refer to Figure 3 of Kasen 2010). Assuming a constant opacity and that the companion fills its Roche lobe, the luminosity and time scale for the shock cooling depends on the mass and stellar evolution stage of the companion. We investigate a 1 $M_\odot$ red giant (RG) companion, a 1 $M_\odot$ main sequence (MS) subgiant companion and a 6 $M_\odot$ MS subgiant companion.

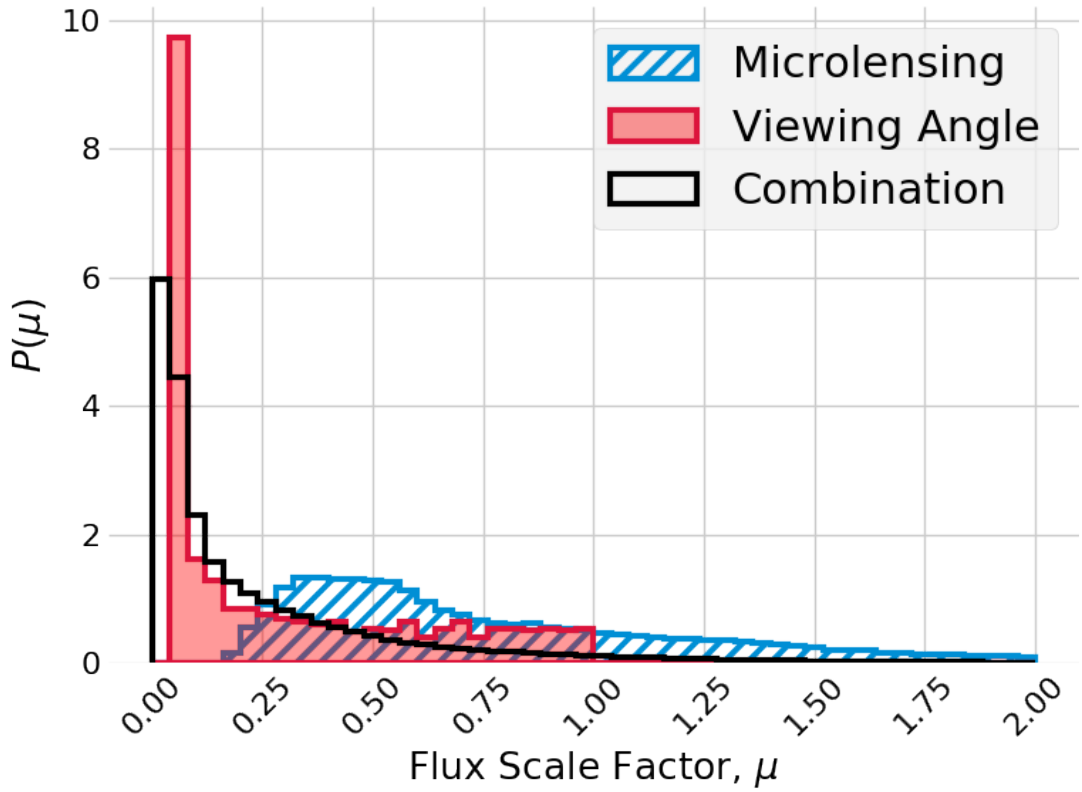

Figure 44: The effect of microlensing and viewing angle on the flux of a lensed SN image, relative to the case of no microlensing and directly viewing the shocked region. The microlensing effect averages to 1, but introduces scatter. The viewing angle introduces scatter and decreases the average flux by a factor of 0.3. The two effects are independent: black shows the convolution of the two effects. **Disclaimer**: This figure is the joint work of myself and Thomas Collett.

The effect of viewing angle is such that companion shock cooling will on average be seen to be fainter than observing directly down onto the shocked region. However, back-scattering means that a few percent of the flux is observed even when observing from the opposite viewing angle to the shocked region (Kasen, 2010). To account for this effect, we assume the shocked region is described by a spherical cap on the surface of an opaque sphere. We assume that the cap has a half opening angle of 30 degrees, therefore covering 7 percent of the sphere. The relative flux observed as a function of viewing angle is proportional to the area of the cap projected onto a plane perpendicular to the viewing angle. Larger opening angles would therefore imply that the shocked region would be visible for more SNe Ia. However, simulations have constrained the half opening angle to within 30-40 degrees, corresponding to ~ 7-12

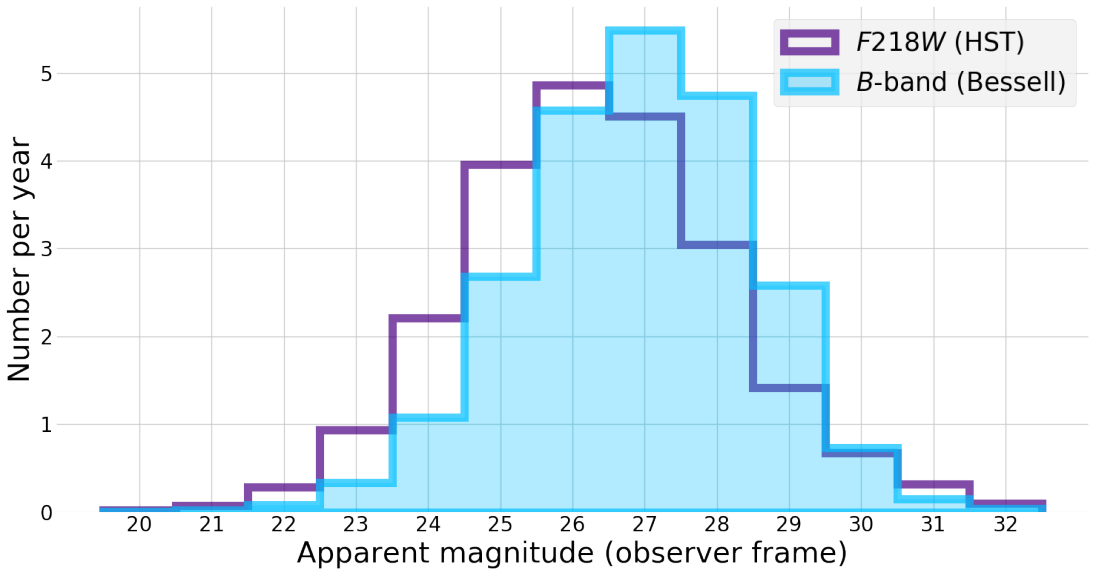

Figure 45: Distribution of peak *B*-band and UV (*F218W*) observer frame magnitudes for a Type IIP shock breakout applied to the catalogue of trailing gLSNe IIP images.

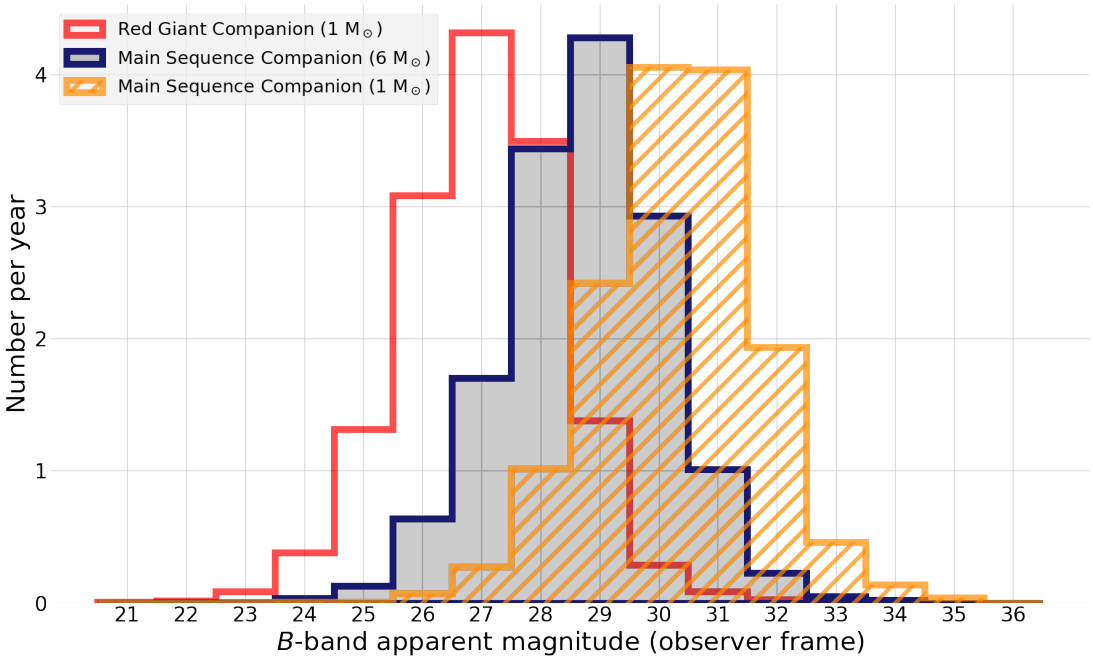

Figure 46: Distribution of peak *B*-band observer frame magnitudes for Type Ia companion shock cooling events in the trailing images of Type Ia gLSNe, within one rest-frame day from explosion. We have performed the analysis across a series of plausible companion models. This figure assumes all Type Ia SNe in LSST are from the SD channel.

percent of the sphere's surface (e.g. see Marietta, Burrows, and Fryxell, 2000; Kasen, 2010). We use the result of Ureña and Georgiev (2018) to perform the projection. The maximum flux is set to the analytic result of Kasen (2010). For viewing angles where the shocked region is occulted, we assume a minimum flux of 5 percent of the peak flux to account for back scattering. The flux scalings for the viewing angle effect are shown in Figure 44[9].

Figure 46 shows the range of peak observer *B*-band magnitudes for Type Ia companion shock cooling curves, predicted to be found in the trailing images of LSST gLSNe Ia, within one rest-frame day of explosion. If SNe Ia only came from the SD channel, we would expect to see at least one instance per year of shock cooling with a *B*-band magnitude of $\lesssim 26.3$ assuming only 1 $M_\odot$ RG companions, $\lesssim 28.0$ assuming only 6 $M_\odot$ MS companions and $\lesssim 29.6$ assuming only 1 $M_\odot$ MS companions.

Since the shock cooling light curves evolve over a timescale of days (as opposed to minutes with the IIP shock breakout), the shock cooling can plausibly be caught with daily cadenced observations spread over the typical $3.3^{+3.1}_{-1.4}$ day time delay uncertainty for Type Ia gLSNe.

On average, the brightness of sources in the *B*-band and the UV (`F218W`) are comparable to the *B*-band magnitude due to extinction by dust. However, if we are able to observe these sources in the UV, this would allow us to better differentiate between the very blue shock cooling light curve and the redder ^{56}Ni driven light curve of the exploding WD (Kasen, 2010).

In this section, we have only considered the possibility of early-time flux excess from ejecta-companion interaction i.e. from the SD channel. For example in the case of SN 2018oh, Dimitriadis et al. (2019) favoured the SD channel as the source of the early-time flux excess. However, Shappee et al. (2019) favoured the DD channel, noting that an off-center ^{56}Ni distribution could produce a redder early-time flux component compared to the SD channel. Further analyses into sources of early-time flux other than ejecta-companion interaction will be left for future studies.

9 **Disclaimer**: The paragraph regarding the viewing angle effect was written and based on the work by Thomas Collett.

5.4 CONSTRAINING SNE IA PROGENITOR POPULATIONS WITH EARLY PHOTOMETRY

Disclaimer: This section (and the following subsections) is written by Thomas Collett and based on his direct contributions to Foxley-Marrable et al. (2020), unless indicated.

Observing companion shock cooling from a single SN Ia would be a demonstration that the SD channel is a viable progenitor system for producing SNe Ia. However, it is plausible that the SN Ia population contains both SD and DD progenitors. Observing - or not observing - shock cooling in a sample of SNe Ia can inform us about the progenitor population.

If both the SD and DD channels are viable, the progenitor population should vary with redshift (Childress, Wolf, and Zahid, 2014). The SD channel relies on Roche lobe overflow which happens at the end of the stellar main sequence life of the companion. The DD channel takes longer: both stars must evolve fully into WDs and then in-spiral due to loss of angular momentum through gravitational wave radiation. Thus the SD Ia population should approximately trace the cosmic star formation history, whereas there should be a longer delay between cosmic star formation and the explosions of DD SNe Ia (Sullivan et al., 2006; Strolger et al., 2020).

If the progenitor population varies as a function of redshift, it is of critical significance for Type Ia SN cosmology - if the mean magnitude of a SN Ia varies with redshift this will bias cosmological constraints derived assuming SNe Ia are standard candles.

In this section we investigate the ability of early time data to constrain the relative fraction of SD to DD populations, assuming the SD models follow the Kasen (2010) shock cooling model and that DD Ia do not show early blue flux. The population of gLSNe Ia in Section 5.2, the microlensing model in Section 5.3.1 and the viewing angle model in Section 5.3.2 give us a a probability density function for the amount of blue flux expected for each SD gLSN Ia. We test a toy model of progenitors where the ratio of SD to DD progenitors is A, and where all SD progenitors are 1 $M_\odot$ MS stars.

The mathematics of this problem are akin to a coin flip experiment, except observational uncertainties mean that each 'flip' is not uniquely identifiable as a SD or a

DD and the SD model does not predict a unique value. The key probability theory is described in Appendix A.

5.4.1 *Constraining SN Ia Progenitor Populations with Unlensed Monitoring of the LSST Deep Drilling Fields*

We first consider how well a blind survey could constrain the ratio of SD to DD progenitors, given a realistic observing strategy. LSST will observe 4 deep drilling fields every night for ten years with a total area of 38.4 square degrees. These fields will be observed ~nightly in multiple filters, enabling high cadence photometry of early SN light curves without prior knowledge that a SN is about to occur.

If the LSST deep drilling fields take *u*-band exposures every night to the ideal 5 sigma detection threshold of 23.9 (Rothchild, Stubbs, and Yoachim, 2019), then LSST-deep would give nightly cadenced photometry of sufficient depth to observe shock cooling for 15 SNe per year, and 150 SNe over the 10 year duration of LSST, up to a limiting redshift limit of 0.115, assuming all SNe Ia are 1 $M_{\odot}$ MS subgiant companions, with optimal viewing angles (see Table 8 for expected rates with limiting redshifts across all previously analysed companion models). The mean redshift of this population is 0.09[10].

The forecast constraints on the ratio of SD to DD progenitors are stochastic, with the mean inferred value of A and the error depending on shot noise in the realisations of the progenitor population, the realisations of the SN redshifts and the realisation of the viewing angles for the SD progenitors. We simulate 1000 realisations of 150 LSST SNe, assuming that ten percent of progenitors are SD ($A = 0.1$; see Livio and Mazzali 2018). Following the probability theory in Appendix A, we then infer $P(A)$ given the data in each realisation. We find that the 68 percent uncertainty on A is 0.037 ± 0.06. The $P(A)$ inferred for 10 random realisations of this population is shown in Figure 47. When we assume there are no SD progenitors we find that the 95 percent upper limit on A is 0.047 ± 0.007.

10 This paragraph (and Table 8) is my own work

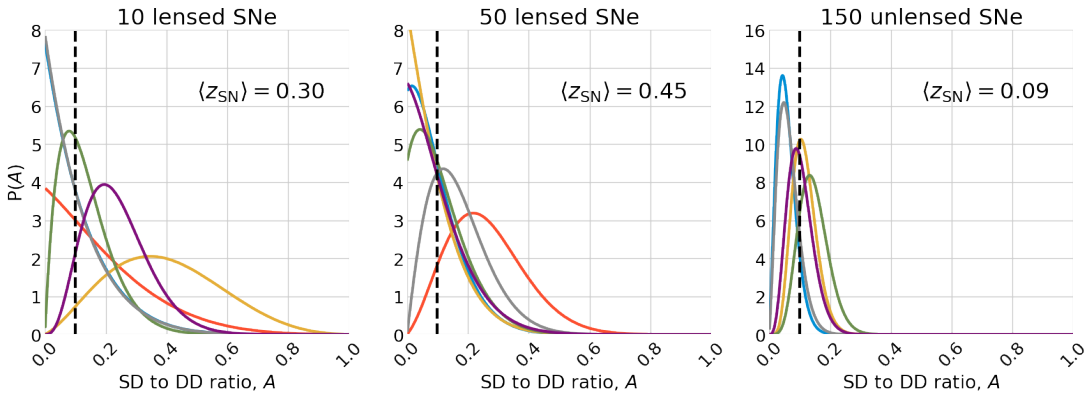

Figure 47: Forecast constraints on the ratio of SD to DD progenitors. From left to right: observations of the 10 best lensed trailing images with a 5 sigma depth of $m_B = 28.7$, 50 lensed images to the same depth, and 150 unlensed images to $m_u = 23.9$ assuming a blind search. Lines show the probability density function from a single realisation of the SN population, accounting for Poisson noise in the population, and randomness in the viewing angle, the SN redshifts and (for the lensed SNe only) magnification due to microlensing. Each PDF shows an equally likely realisation of the inferred P(SD/DD) given the assumed observing conditions. The input truth is shown by the dashed line. **Disclaimer**: This figure is the work of Thomas Collett.

5.4.2 *Constraining SNe Ia Progenitor Populations with Deep Observations of LSST Trailing Images*

We now consider how well observations of the strongly lensed trailing images can be used to constrain the SN Ia progenitor population. As shown in Figures 39, 50 and 46, the trailing images are at higher redshift and much fainter than can be observed during a single LSST exposure. However, the predictive power of lensing means that deep targeted follow-up is plausible. We assume a *B*-band 5 sigma depth of 28.7th magnitude, corresponding to a 60 minute exposure time on the European Extremely Large Telescope, with 0.8 arcsecond seeing and 7 days from new moon (Liske, 2019).

If only a subset of the lenses can be followed up, focusing efforts on the brightest images minimises the uncertainty in $P(A)$. Because both the viewing angle and the microlensing effect are a priori unknown, it is impossible to predict which trailing images will show the brightest shock cooling events. However, an observer targeting

Companion model	LSST deep drilling field rates within $m_u \lesssim 23.9$ (Year^{-1})	Limiting redshift
1 $M_\odot$ MS	15	0.115
6 $M_\odot$ MS	97	0.225
1 $M_\odot$ RG	521	0.440

Table 8: Predicted rates for unlensed Type Ia shock cooling events to be observed in the LSST deep drilling fields, assuming the SN rates from Sullivan et al. (2006) and a limiting u-band magnitude of 23.9 from LSST.

the systems with the brightest trailing images as predicted by the macromodel will achieve the best signal to noise.

Assuming that ten percent of progenitors are SD ($A = 0.1$), and that the 10 lens (macromodel predicted) brightest trailing images are followed up, we find that the 68 percent uncertainty on A is $0.11^{+0.04}_{-0.03}$. The $P(A)$ inferred for 10 random realisations of this population is shown in Figure 47. If the brightest 50 are followed up the uncertainty improves to 0.09 ± 0.02. Despite targeting 5 times more systems, there is only a modest improvement in uncertainty because most of these 50 are too faint for shock breakout to be detected even with a 5 sigma depth of 28.7 in the B-band unless there is significant microlensing magnification.

When we assume there are no SD progenitors we find that the 95 percent upper limit on A is 0.27 ± 0.10 and 0.19 ± 0.05 for followup of 10 and 50 lensed SNe respectively.

Whilst the uncertainties for this lensed sample will be much larger than what a blind LSST deep drilling fields survey can achieve, the lensed sample is at higher redshift. The brightest 10 trailing images will come from SNe with a mean redshift of 0.3; for the brightest 50 it is 0.45.

5.5 TIME DELAY COSMOLOGY WITH EARLY OBSERVATIONS OF LENSED SUPERNOVAE

Strong lensing time delays enable inference on cosmological parameters (Refsdal, 1964). However, measuring these time delays is observationally expensive (Tewes

et al., 2013b), requiring high cadence multi-season monitoring campaigns to yield robust time delays with several day precision. If observed in multiple images, the sharp features of an early phase gLSN would immediately provide a precise time delay estimate. To do this would require identification of a quadruple imaged gLSNe before the explosion in at least 2 of the images. Across all SN types, LSST will discover ~ 1 quad per year with multiple images remaining. Even if a sharp early phase feature were observed for every such system, this rate is too low to compete with the LSST sample of lensed active galactic nucleus (AGN) (Oguri and Marshall, 2010; Liao et al., 2015b).

5.6 CONCLUSIONS

We have investigated the population of gLSNe systems which will be discovered in LSST and ZTF before the explosion occurs in the final image. We are now able to answer our initial questions:

1. Will LSST and ZTF enable the discovery of gLSNe before the appearance of all multiple images?

Across all SN types LSST is expected to find ~ 110 trailing gLSNe per year, whilst ZTF will be finding significantly less at ~ 1 trailing gLSNe per year (see Table 5 for a detailed breakdown). The LSST sample is dominated by doubles, whilst the ZTF sample is dominated by quads.

2. How long is the time frame between the discovery of the system and explosion of the last image? How precisely can the last explosion time be predicted?

Reaction times between discovery and the SN explosion in the final image are typically around $11.7^{+29.8}_{-9.3}$ days (Figures 39e and 40e). Assuming a 5% precision on the time delay prediction from detailed lens modelling, we find that we will be able to predict the reappearance of the SN in the final image to within $3.2^{+3.4}_{-1.6}$ days (Figures 39f and 40f).

3. How bright will the early phase light curves of Type IIP and Type Ia SNe found in the trailing images of LSST-discovered gLSNe get?

The vast majority of trailing images are demagnified by ~ 1 or 2 magnitudes (Figure 41), coupled with extinction by dust this will make obtaining early phase SN data using gLSNe an observationally challenging effort.

For LSST gLSNe IIP, of order 1 trailing image per year will reach $\lesssim$ 24.1 in the *B*-band and $\lesssim$ 23.3 in the UV (*F218W*). Assuming the SD channel only for SNe Ia, we find that the LSST gLSNe population will include trailing images with one instance of a companion shock cooling emission per year in the *B*-band, with magnitude $\lesssim$ 26.3 assuming a 1 $M_\odot$ RG companion, $\lesssim$ 28.0 assuming a 6 $M_\odot$ MS subgiant companion and $\lesssim$ 29.6 assuming a 1 $M_\odot$ MS subgiant companion (Figure 46).

4. Can we use LSST-discovered gLSNe to make inferences on the progenitor population of Type Ia SNe with redshift? How will this compare with constraints from unlensed SNe Ia?

Figure 47 shows that assuming the brightest gLSN trailing images can be observed for 1 hour on the European Extremely Large Telescope, the progenitor population can be constrained. When we assume there are no SD progenitors we find that the 95 percent upper limit on the fraction of 1 $M_\odot$ MS companions is 0.27 ± 0.10 and 0.19 ± 0.05 for followup of 10 and 50 lensed SNe respectively. Nightly *u*-band observations of the LSST deep drilling fields would yield more precise constraints, with 15 unlensed SNe per year bright enough to detect shock cooling from a 1 $M_\odot$ main sequence companion. Such observations would place a 5% upper limit on the fraction of 1 $M_\odot$ main sequence companions at $\langle z \rangle = 0.09$. The gLSNe Ia are at higher redshifts, with even the 10 brightest systems having $\langle z \rangle = 0.30$. Combining lensed and unlensed samples should constrain evolution in the Ia progenitor population and would place limits on progenitor evolution-induced systematics in Type-Ia SN cosmology[11].

5. Can we measure precise time delays between the rapid early-phase light curves of gLSNe?

We find that this is unlikely to produce a cosmologically competitive sample of time delays. The rate of systems with multiple unexploded trailing images is below 1 per year even for LSST gLSNe.

11 **Disclaimer**: This paragraph was written by Thomas Collett.

In summary, during the LSST era catching the earliest phases of lensed SNe and constraining their progenitor physics is possible for Type Ia SNe if the community is willing to invest in deep ($\sim$ 26 to 30 mag in the *B*-band, depending on the progenitor) cadenced imaging for $3.2^{+3.4}_{-1.6}$ days either side of the predicted recurrence.

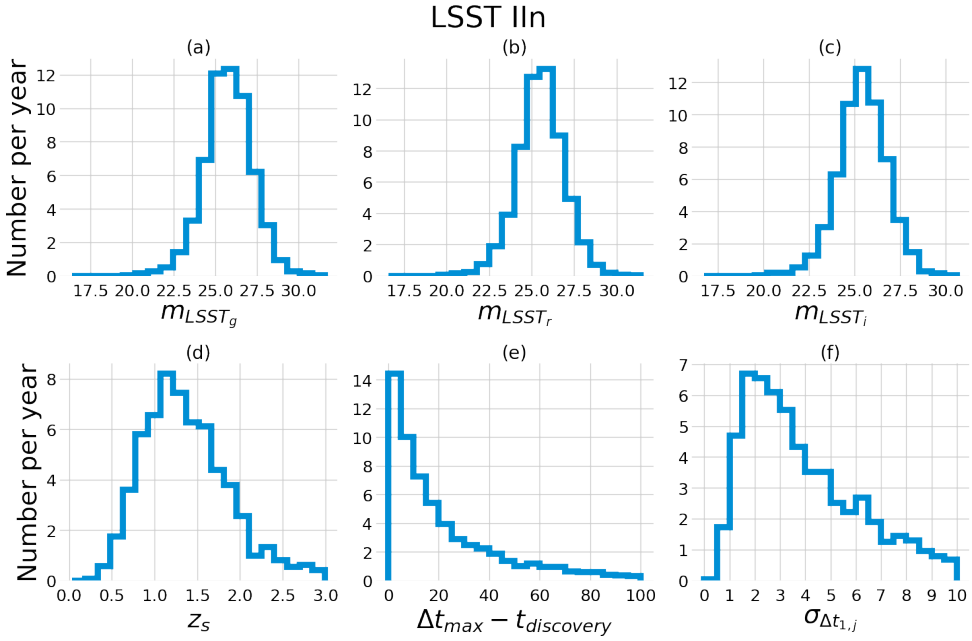

Figure 48: Distributions and annual rates of LSST-discovered Type IIn gLSNe containing trailing images with unexploded SNe. See Table 6 for descriptions of the subplots.

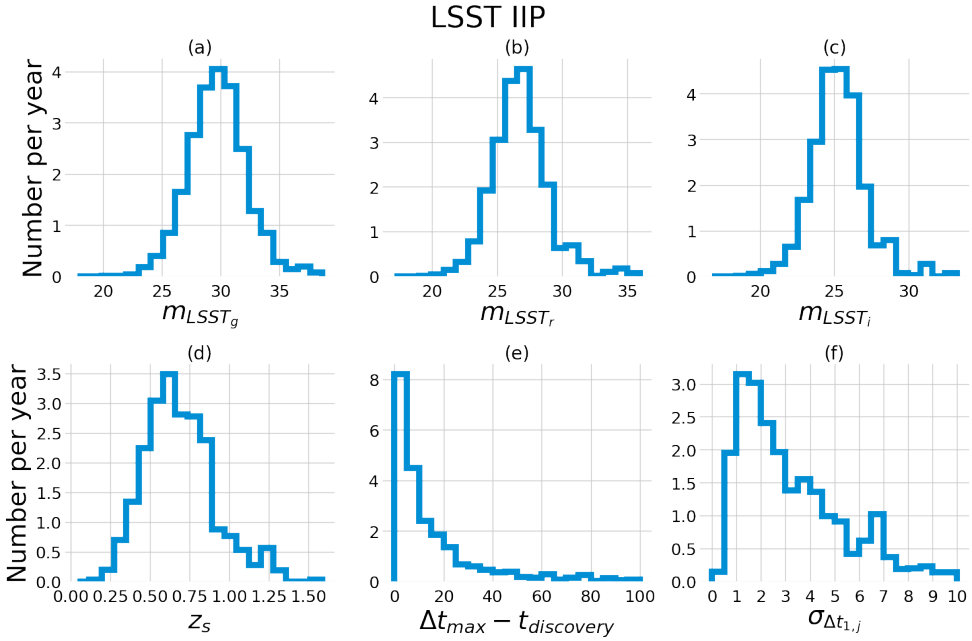

Figure 49: Distributions and annual rates of LSST-discovered Type IIP gLSNe containing trailing images with unexploded SNe. See Table 6 for descriptions of the subplots.

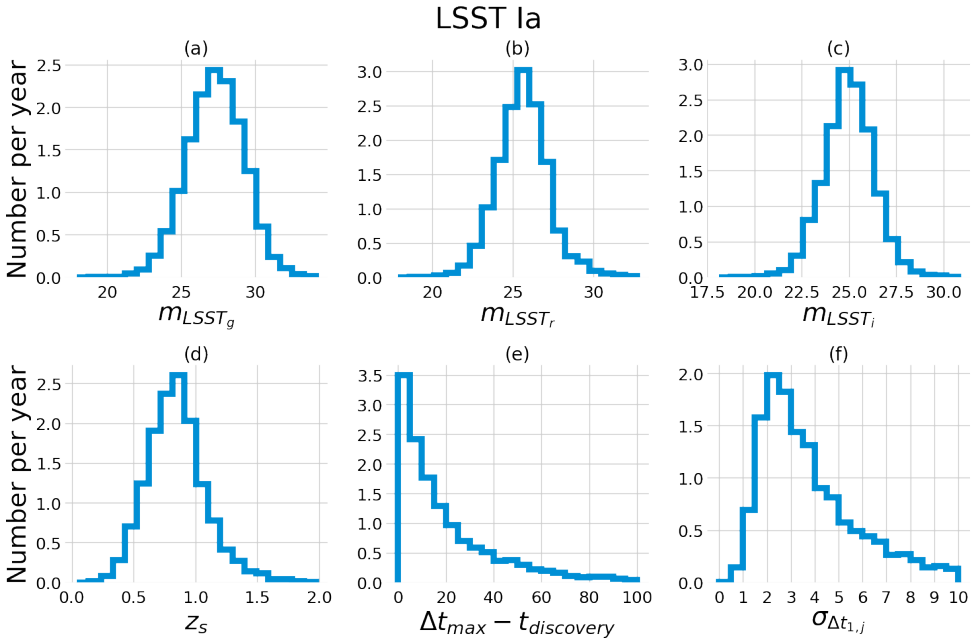

Figure 50: Distributions and annual rates of LSST-discovered Type Ia gLSNe containing trailing images with unexploded SNe. See Table 6 for descriptions of the subplots.

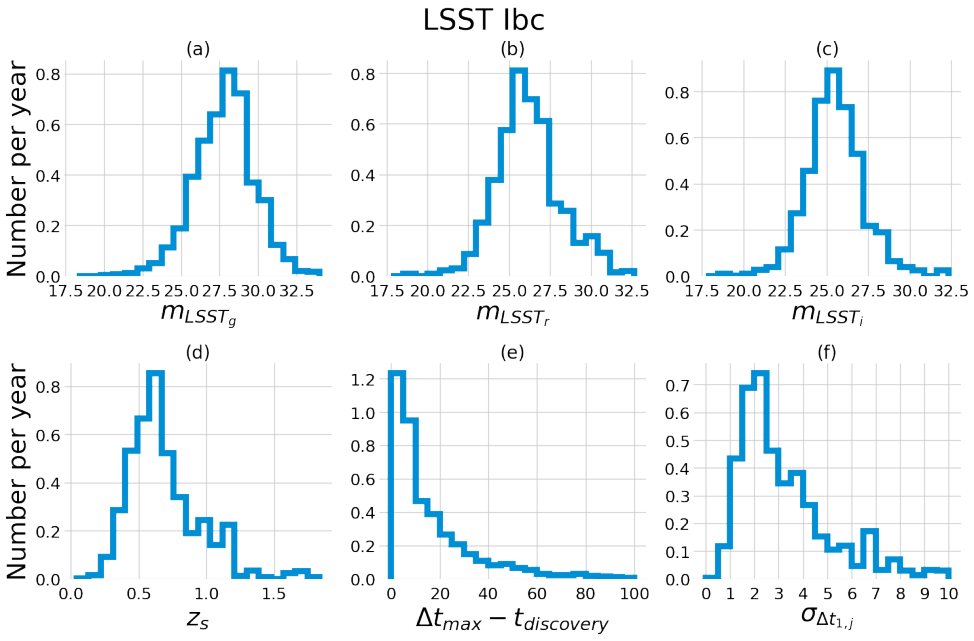

Figure 51: Distributions and annual rates of LSST-discovered Type Ibc gLSNe containing trailing images with unexploded SNe. See Table 6 for descriptions of the subplots.

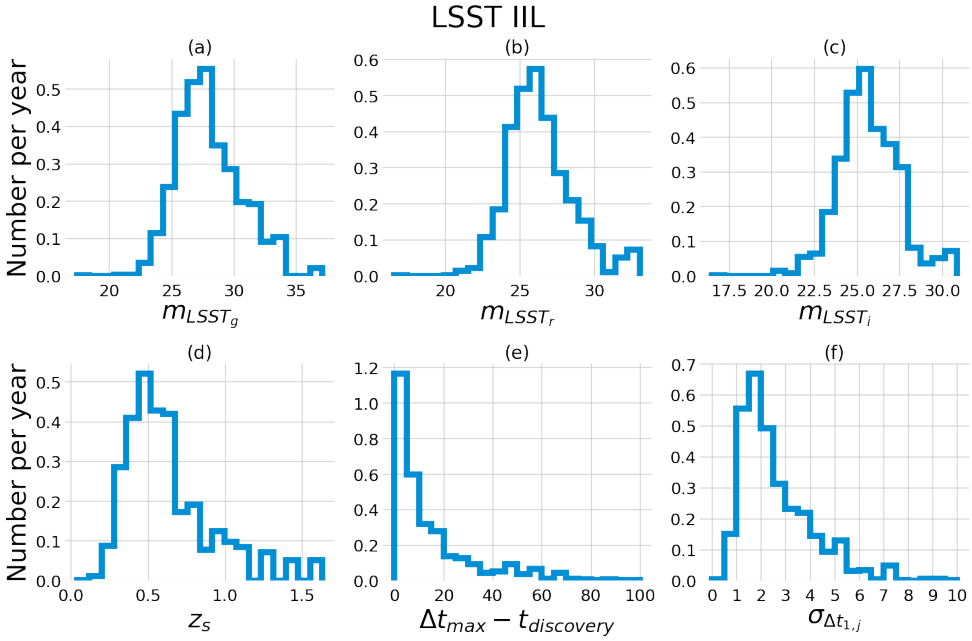

Figure 52: Distributions and annual rates of LSST-discovered Type IIL gLSNe containing trailing images with unexploded SNe. See Table 6 for descriptions of the subplots.

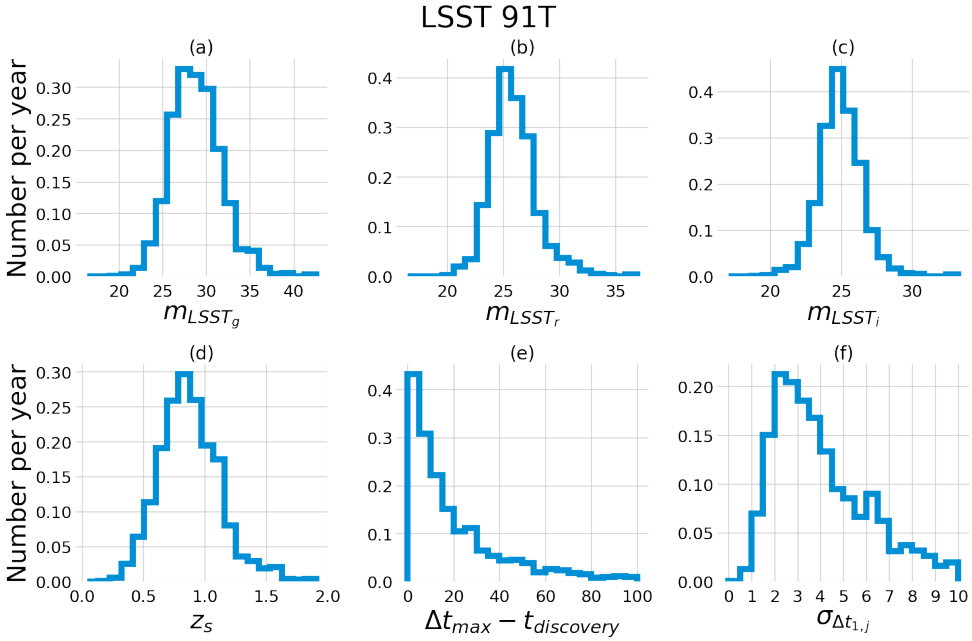

Figure 53: Distributions and annual rates of LSST-discovered 91T-like gLSNe containing trailing images with unexploded SNe. See Table 6 for descriptions of the subplots.

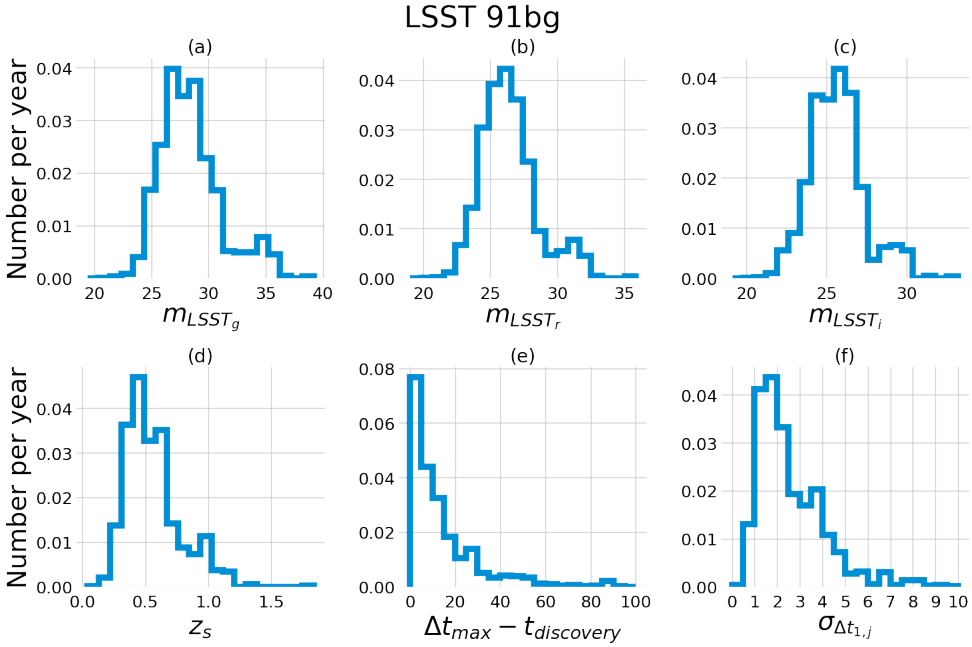

Figure 54: Distributions and annual rates of LSST-discovered 91bg-like gLSNe containing trailing images with unexploded SNe. See Table 6 for descriptions of the subplots.

Part III

CONCLUSIONS

I have no idea what I'm doing, but I know I'm doing it really, really well.

— Andy Dwyer, Parks and Recreation

6

CONCLUSIONS

Strong gravitational lensing has the potential to pave the way for major advances in the field of cosmology and astrophysics. They can be used to probe the Hubble constant (H_0) independently of the cosmic distance ladder and early-Universe physics through time delay cosmography. Additionally, measurements of H_0 through this method are relatively insensitive to the chosen cosmology when compared with other probes (see Figure 6). The latest result from TDCOSMO (Millon et al., 2019) best estimates $H_0 = 74.2^{+1.6}_{-1.6}$ km s^{-1} Mpc^{-1} to 2.4% precision, using constraints from seven lensed quasars (see Section 1.4.2). This is in tension with early-Universe measurements by $\sim 4\sigma$ and in strong agreement with other late-Universe measurements, whilst being independent of the cosmological distance ladder. However, quasars are not immune to the mass-sheet degeneracy (see Section 3.6) and require long monitoring campaigns to accurately measure time delays (e.g. Bonvin et al., 2017). The strong gravitational lensing of Type Ia supernovae (gLSNe Ia) has promise to outperform strongly lensed quasars in the field of time delay cosmography (see Section 3.7). They can be used to accurately measure the time delays through much shorter monitoring campaigns than strongly lensed quasars (Holz, 2001; Oguri, Suto, and Turner, 2003; Huber et al., 2019) and the standardisable nature of Type Ia supernovae (SNe) has promise to tightly constrain lensing systematics (Holz, 2001). However, the point-like nature of Type Ia SNe introduces large sensitivities to microlensing effects that can significantly distort the SN Ia light curve (e.g. Dobler and Keeton 2006, also see Section 3.4 and Figure 33). The microlensing effect for gravitationally lensed supernovae (gLSNe) is time dependent mainly due to the expanding size of the background SN, but also partially due to transverse motion of stars in the foreground (see Section 4.2 and Figure 32). We cannot predict when microlensing events will occur and the effect is completely independent for each lensed image, hence we cannot directly correct the microlensed SN Ia light curves. In order for gLSNe Ia time delays to produce competitive H_0 estimates, microlensing needs to be accounted for.

Chapter 4 (published in Foxley-Marrable et al. 2018) proposes that the best way to overcome microlensing systematics is to be selective with the gLSNe sample used

for time delay cosmography. We find that lensing systems with asymmetric image configurations, where at least one image forms well beyond the Einstein radius in regions of low stellar matter (high dark matter), will be subject to average microlensing scatters of $\sigma_M \lesssim 0.15$ magnitudes. We deem these systems to be standardisable, since the microlensing scatters are comparable to the intrinsic dispersion of SNe Ia (see Figures 34 and 36). Additionally, constraining the absolute magnification of just one lensed image allows us to break the mass-sheet degeneracy across the whole lens. By combining microlensing models with the gLSN catalogues of Goldstein et al. 2018, we predict that ~ 22% of gLSNe discovered by the Legacy Survey of Space and Time (LSST) will be standardisable. Through a sample of ~ 650 gLSNe, we predict estimates on H_0 will be possible with the mass-sheet degeneracy constrained at the 0.5% level. If this is the dominant systematic, then this means a sub-percent measurement on H_0. Reducing the sample size to the ~ 140 standardisable gLSNe, i.e. the systems with $\sigma_M \lesssim 0.15$ magnitudes of microlensing scatter, the constraints degrade by just 0.1%. If ~ 40 standardisable quadruple image gLSNe are used, then the mass-sheet degeneracy is constrained on the ~ 1% level.

On the whole, Chapter 4 demonstrates that time delay cosmography with Type Ia gLSNe is a plausible method to probe H_0. Goldstein, Nugent, and Goobar (2019) predicts that LSST will find ~ 50 gLSNe Ia per year (see Table 2). Hence over its 10 year survey, LSST could produce a sample of ~ 110 standardisable systems, providing a ~ 0.7% constraint on the mass-sheet degeneracy. Assuming the mass-sheet degeneracy is the dominant systematic, obtaining a competitive, sub-percent measurement of H_0 using gLSNe Ia time delays is possible within the next 10 years through LSST alone, allowing a stringent test of the Λ cold dark matter (ΛCDM) model of cosmology. An interesting byproduct of this research found a sharp sensitivity to the lens galaxy initial mass function (IMF) in the standardisable fraction of the source plane (see Figure 37). Hence a statistically relevant sample of gLSNe Ia could feasibly be used to test the IMF of the lensing galaxy.

Gravitational lensing time delays also opens up the possibility of observing the earliest moments of supernovae (Suwa, 2018). If a gLSNe was discovered before the appearance of the SN explosion in any of the remaining multiple images, through rapid lens modelling and follow up observations, it might be possible to predict and observe the SN reappearance. Observations of SNe in the first/hours days could

be instrumental in furthering our understanding of SN physics (see Section 2.4.1.4). In particular observing early phase SNe Ia could allow us to discriminate between progenitor models. If the progenitor population varies with redshift and the intrinsic brightness of SNe Ia depends on the progenitor model, this could introduce significant bias into the standardisation process of SNe Ia. This is especially problematic since SNe Ia are used as cosmological distance measures on which estimates of H_0 depend on.

Chapter 5 (published in Foxley-Marrable et al. 2020) explores the viability using strong lenses to observe early phase SNe. From analysis of the Goldstein, Nugent, and Goobar (2019) gLSNe catalogues, we predict that LSST will discover ~ 110 gLSNe per year with 'trailing' images in which the SN is yet to appear (see Section 5.2 and Table 5). The 'reaction time' between discovery and the SN explosion in the last image is typically around $11.7^{+29.8}_{-9.3}$ days (Figures 39e and 40e). Assuming 5% precision on modelling time delays, we conclude the SN reappearance in final image can be predicted to an accuracy of $3.2^{+3.4}_{-1.6}$ days (Figures 39f and 40f). This presents a potential problem for the future, where a large number of trailing gLSNe systems will require a quick turnaround to both model and perform the necessary followup observations. The lens models will need to be of high enough precision to reduce observational overheads - predicting the precise day of reappearance would require sub-percent time delay predictions. The lens models will also need to be produced quick enough in time to catch the SN reappearance. Lens modelling is currently a timely task, especially for complex systems (e.g. see Shajib et al., 2020). This work provides significant motivation to optimise lens model codes in order to produce to high-precision mass models on a time scale of days. Automatic lens modelling software e.g. `AutoLens` (Nightingale, Dye, and Massey, 2018) yields promise in alleviating the time pressure, however it remains to be seen whether they can produce accurate enough time delay predictions.

In our simulated gLSNe sample, the trailing images are typically demagnified by ~ 1 or 2 magnitudes (Figure 41). The combined effect of demagnification and host extinction will make obtaining early phase observations of SN a more challenging effort than previously thought. The evolution of SN shock breakouts are extremely rapid, evolving over a timescale of ~ 30 mins (see Section 5.3.1 and Figure 42). Coupled with demagnification and extinction by dust, this means that a network of telescopes with large collecting apertures would be required to properly sample shock break-

outs at a reasonable signal-to-noise. The companion shock cooling light curves of single-degenerate SNe Ia evolve over a timescale of order days (see Section 5.3.2 and Figure 43) and could be feasibly be monitored in the trailing images of gLSNe with the next generation of 30m class telescopes. Whilst it's plausible that the unlensed SNe population will provide a better sample for early phase observations, gLSNe can probe the population at higher redshifts. As mentioned previously, this is especially important for Type Ia SN cosmology. This work has shown that it's possible to discriminate between Type Ia SNe progenitor populations, on the assumption we are able to monitor the population with deep one hour exposures using a 30m class telescope (see Section 5.4).

On the whole, Chapter 5 demonstrates that there is significant motivation to pursue the field of early-phase observations of SNe using strong lenses. However, significant investment is required to overcome the shortcomings associated with demagnification and extinction by dust. This study will require a new generation of networked telescopes with large enough mirrors to probe down to at least 24-28th magnitude with short exposures. Whilst this is a considerable demand, the ability to probe the SN progenitor population across redshift, beyond what is capable with the unlensed population, will be an invaluable asset for both SN astrophysics and cosmology.

In conclusion, the field of gLSNe is one well worth perusing by the astronomical community. The next generation of wide field, high cadence surveys (e.g. LSST) will be finding $\mathcal{O}(100)$ gLSN systems per year. Combining this data with imaging from the next generation of space-based telescopes (e.g. Euclid) provides the ideal tools to perform the cutting-edge strong lensing science presented. Over the next decade, LSST gLSNe will enable a measurement of H_0 with systematics controlled at sub-percent precision. If this confirms the current best fit from the cosmic distance ladder, it will provide definitive evidence for physics beyond ΛCDM. gLSNe are also capable of constraining SN progenitor populations across redshift. This new information will considerably strengthen Type Ia SNe as a cosmological distance indicator and hence a probe of H_0 and dark energy. The work presented in this thesis ultimately demonstrates the power of gLSNe as a future probe of both cosmology and astrophysics, with the next decade showing promise as a new golden age in astronomy.

Part IV

APPENDIX

"For a moment, nothing happened. Then, after a second or so, nothing continued to happen."

— Douglas Adams, The Hitchhiker's Guide to the Galaxy

A

PROBABILITY THEORY FOR CONSTRAINING TWO COMPONENT PROGENITOR POPULATIONS

Disclaimer: This section was written by Thomas Collett.

Constraining the underlying ratio of single-degenerate (SD) to double-degenerate (DD) SN Ia progenitors from an observed sample, is analogous to testing if a coin is fair given a finite number of flips. The mathematics of the progenitor problem is complicated slightly for two reasons: firstly, uncertainties in the observations mean that an individual observation does not perfectly discriminate between a SD and DD progenitor; secondly, whilst the DD is assumed to have no early blue flux the SD model does not predict a unique flux value due to viewing angle effects (and microlensing in the case of a strongly lensed SD Ia).

Assume a true population of Ia progenitors, where the underlying ratio of SD to DD progenitors is given by A. For any given supernova:

$$P(SD|A) = A, P(DD|A) = 1 - A. \tag{52}$$

Let us first consider the case where the data uniquely determines if the progenitor is a SD or DD. Let us denote s as the number of SD and d as the number of DD progenitors in a sample of $s + d$ events:

$$P(s, d|A) \propto A^s (1 - A)^d. \tag{53}$$

Bayes theorem tells us that:

$$P(A|s, d)P(s, d) = P(s, d|A)P(A). \tag{54}$$

Assuming a Uniform distribution for the prior on P(A) between 0 and 1 yields:

$$P(A|s, d) \propto A^s (1 - A)^d. \tag{55}$$

Let us now consider the case where the data does not uniquely determine if an event is SD or DD. For a single observation, O_i:

$$\begin{aligned} P(O_i|A) &= P(O_i|SD)P(SD|A) + P(O_i|DD)P(DD|A) \\ &= A \times P(O_i|SD) + (1 - A) \times P(O_i|DD). \end{aligned} \tag{56}$$

$P(DD|O_i|) = 1 - P(SD|O_i)$, are derived from the integral of the flux, f, predicted by the two models (a δ function at o for the DD model and a broader distribution for the SD model) over the window function consistent with the observed flux ($P(f|O_i)$):

$$P(SD|O_i) = \frac{\int_{-\infty}^{\infty} P(SD|f)P(f|O_i)df}{\int_{-\infty}^{\infty} P(SD|f)df}. \tag{57}$$

For multiple observations, O the posterior is the product of the individual probabilities:

$$P(O|A) \propto \prod_{\forall i} (A \times P(O_i|SD) + (1 - A) \times P(O_i|DD)), \tag{58}$$

which can be inverted using Bayes theorem to infer $P(A \mid O)$.

BIBLIOGRAPHY

Abbott, B. P. et al. (Feb. 2016). "Astrophysical Implications of the Binary Black-hole Merger GW150914." In: *The Astrophysical Journal* 818.2, p. L22. DOI: 10.3847/2041-8205/818/2/l22. URL: https://doi.org/10.3847\%2F2041-8205\%2F818\%2F2\%2Fl22.

Abbott, B. P. et al. (Feb. 2016). "Observation of Gravitational Waves from a Binary Black Hole Merger." In: *Phys. Rev. Lett.* 116.6, 061102, p. 061102. DOI: 10.1103/PhysRevLett.116.061102. arXiv: 1602.03837 [gr-qc].

Abbott, B. P. et al. (Nov. 2017). "A gravitational-wave standard siren measurement of the Hubble constant." In: *Nature* 551.7678, pp. 85–88. DOI: 10.1038/nature24471. arXiv: 1710.05835 [astro-ph.CO].

Abbott, T. M. C. et al. (Nov. 2018). "Dark Energy Survey Year 1 Results: A Precise H_0 Estimate from DES Y1, BAO, and D/H Data." In: *Monthly Notices of the RAS* 480.3, pp. 3879–3888. DOI: 10.1093/mnras/sty1939. arXiv: 1711.00403 [astro-ph.CO].

AbdelSalam, Hanadi M., Prasenjit Saha, and Liliya L. R. Williams (Oct. 1998). "Non-parametric Reconstruction of Abell 2218 from Combined Weak and Strong Lensing." In: *The Astronomical Journal* 116.4, pp. 1541–1552. DOI: 10.1086/300546. URL: https://doi.org/10.1086\%2F300546.

Alam, Shadab et al. (Sept. 2017). "The clustering of galaxies in the completed SDSS-III Baryon Oscillation Spectroscopic Survey: cosmological analysis of the DR12 galaxy sample." In: *Monthly Notices of the RAS* 470.3, pp. 2617–2652. DOI: 10.1093/mnras/stx721. arXiv: 1607.03155 [astro-ph.CO].

Alcock, Charles, RA Allsman, David R Alves, TS Axelrod, Andrew C Becker, DP Bennett, Kem H Cook, N Dalal, Andrew John Drake, KC Freeman, et al. (2000). "The MACHO project: microlensing results from 5.7 years of Large Magellanic Cloud observations." In: *The Astrophysical Journal* 542.1, p. 281.

Alexeyev, E. N., L. N. Alexeyeva, I. V. Krivosheina, and V. I. Volchenko (Apr. 1988). "Detection of the neutrino signal from SN 1987A in the LMC using the INR

Baksan underground scintillation telescope." In: *Physics Letters B* 205.2-3, pp. 209–214. DOI: 10.1016/0370-2693(88)91651-6.

Alsabti, Athem W. and Paul Murdin (2017). *Handbook of Supernovae*. DOI: 10.1007/978-3-319-21846-5.

Alsabti, Athem W. and Paul Murdin (2017). "Supernovae and Supernova Remnants: The Big Picture in Low Resolution." In: *Handbook of Supernovae*. Ed. by Athem W. Alsabti and Paul Murdin. Cham: Springer International Publishing, pp. 3–28. ISBN: 978-3-319-21846-5. DOI: 10.1007/978-3-319-21846-5_1. URL: https://doi.org/10.1007/978-3-319-21846-5_1.

Anguita, T. et al. (Nov. 2018). "The STRong lensing Insights into the Dark Energy Survey (STRIDES) 2016 follow-up campaign - II. New quasar lenses from double component fitting." In: *MNRAS* 480.4, pp. 5017–5028. DOI: 10.1093/mnras/sty2172. arXiv: 1805.12151 [astro-ph.GA].

Arcavi, Iair (2017). "Hydrogen-Rich Core-Collapse Supernovae." In: *Handbook of Supernovae*. Ed. by Athem W. Alsabti and Paul Murdin. Cham: Springer International Publishing, pp. 239–276. ISBN: 978-3-319-21846-5. DOI: 10.1007/978-3-319-21846-5_39. URL: https://doi.org/10.1007/978-3-319-21846-5_39.

Arnett, W. D. (Feb. 1982). "Type I supernovae. I - Analytic solutions for the early part of the light curve." In: *ApJ* 253, pp. 785–797. DOI: 10.1086/159681.

Arnett, W. David, John N. Bahcall, Robert P. Kirshner, and Stanford E. Woosley (Jan. 1989). "Supernova 1987A." In: *ARA&A* 27, pp. 629–700. DOI: 10.1146/annurev.aa.27.090189.003213.

Aubourg, Éric et al. (Dec. 2015). "Cosmological implications of baryon acoustic oscillation measurements." In: *Physical Review D* 92.12, 123516, p. 123516. DOI: 10.1103/PhysRevD.92.123516. arXiv: 1411.1074 [astro-ph.CO].

Auger, M. W., T. Treu, A. S. Bolton, R. Gavazzi, L. V. E. Koopmans, P. J. Marshall, L. A. Moustakas, and S. Burles (Nov. 2010). "The Sloan Lens ACS Survey. X. Stellar, Dynamical, and Total Mass Correlations of Massive Early-type Galaxies." In: *Astrophys. J.* 724, pp. 511–525. DOI: 10.1088/0004-637X/724/1/511. arXiv: 1007.2880.

Aznar-Siguán, G., E. García-Berro, P. Lorén-Aguilar, N. Soker, and A. Kashi (July 2015). "Smoothed particle hydrodynamics simulations of the core-degenerate sce-

nario for Type Ia supernovae." In: *MNRAS* 450.3, pp. 2948–2962. DOI: 10.1093/mnras/stv824. arXiv: 1503.02444 [astro-ph.HE].

Baade, W. and F. Zwicky (May 1934). "On Super-novae." In: *Proceedings of the National Academy of Science* 20.5, pp. 254–259. DOI: 10.1073/pnas.20.5.254.

Bagherpour, H., D. Branch, and R. Kantowski (Feb. 2006). "Effects of Gravitational Microlensing on P Cygni Profiles of Type Ia Supernovae." In: *Astrophysical Journal* 638, pp. 946–950. DOI: 10.1086/498889. eprint: astro-ph/0503460.

Barbarino, C. et al. (Apr. 2015). "SN 2012ec: mass of the progenitor from PESSTO follow-up of the photospheric phase." In: *MNRAS* 448.3, pp. 2312–2331. DOI: 10.1093/mnras/stv106. arXiv: 1410.8393 [astro-ph.SR].

Barbon, R., F. Ciatti, and L. Rosino (Feb. 1979). "Photometric properties of type II supernovae." In: *A&A* 72, pp. 287–292.

Batista, V. et al. (May 2011). "MOA-2009-BLG-387Lb: a massive planet orbiting an M dwarf." In: *A&A* 529, A102, A102. DOI: 10.1051/0004-6361/201016111. arXiv: 1102.0558 [astro-ph.EP].

Baumann, Daniel (July 2009). "TASI Lectures on Inflation." In: *arXiv e-prints*, arXiv:0907.5424, arXiv:0907.5424. arXiv: 0907.5424 [hep-th].

Beaton, Rachael L. et al. (Dec. 2016). "THE CARNEGIE-CHICAGO HUBBLE PROGRAM. I. AN INDEPENDENT APPROACH TO THE EXTRAGALACTIC DISTANCE SCALE USING ONLY POPULATION II DISTANCE INDICATORS." In: *The Astrophysical Journal* 832.2, p. 210. DOI: 10.3847/0004-637x/832/2/210. URL: https://doi.org/10.3847\%2F0004-637x\%2F832\%2F2\%2F210.

Beaton, Rachael L. et al. (Oct. 2018). "Old-Aged Primary Distance Indicators." In: *Space Science Reviews* 214.8, p. 113. ISSN: 1572-9672. DOI: 10.1007/s11214-018-0542-1. URL: https://doi.org/10.1007/s11214-018-0542-1.

Beaulieu, J. P. et al. (Jan. 2006). "Discovery of a cool planet of 5.5 Earth masses through gravitational microlensing." In: *Nature* 439.7075, pp. 437–440. DOI: 10.1038/nature04441. arXiv: astro-ph/0601563 [astro-ph].

Bellm, Eric C. et al. (June 2019). "The Zwicky Transient Facility: Surveys and Scheduler." In: *PASP* 131.1000, p. 068003. DOI: 10.1088/1538-3873/ab0c2a. arXiv: 1905.02209 [astro-ph.IM].

Bennett, C. L. et al. (Oct. 2013). "Nine-year Wilkinson Microwave Anisotropy Probe (WMAP) Observations: Final Maps and Results." In: *Astrophysical Journal, Sup-*

plement 208.2, 20, p. 20. DOI: 10.1088/0067-0049/208/2/20. arXiv: 1212.5225 [astro-ph.CO].

Betoule, M. et al. (Aug. 2014). "Improved cosmological constraints from a joint analysis of the SDSS-II and SNLS supernova samples." In: *Astronomy and Astrophysics* 568, A22, A22. DOI: 10.1051/0004-6361/201423413. arXiv: 1401.4064.

Bionta, R. M. et al. (Apr. 1987). "Observation of a neutrino burst in coincidence with supernova 1987A in the Large Magellanic Cloud." In: *Phys. Rev. Lett.* 58.14, pp. 1494–1496. DOI: 10.1103/PhysRevLett.58.1494.

Birrer, S. et al. (Apr. 2019). "HoLiCOW - IX. Cosmographic analysis of the doubly imaged quasar SDSS 1206+4332 and a new measurement of the Hubble constant." In: *Monthly Notices of the RAS* 484.4, pp. 4726–4753. DOI: 10.1093/mnras/stz200. arXiv: 1809.01274 [astro-ph.CO].

Blandford, R. and R. Narayan (Nov. 1986). "Fermat's principle, caustics, and the classification of gravitational lens images." In: *Astrophysical Journal* 310, pp. 568–582. DOI: 10.1086/164709.

Blandford, Roger and Rolf Bühler (2017). "Supernova of 1054 and its Remnant, the Crab Nebula." In: *Handbook of Supernovae*. Ed. by Athem W. Alsabti and Paul Murdin. Cham: Springer International Publishing, pp. 83–95. DOI: 10.1007/978-3-319-21846-5_46. URL: https://doi.org/10.1007/978-3-319-21846-5_46.

Bloom, Joshua S. et al. (Jan. 2012). "A Compact Degenerate Primary-star Progenitor of SN 2011fe." In: *ApJ* 744.2, L17, p. L17. DOI: 10.1088/2041-8205/744/2/L17. arXiv: 1111.0966 [astro-ph.HE].

Bolton, Adam S., Scott Burles, Léon V. E. Koopmans, Tommaso Treu, Raphaël Gavazzi, Leonidas A. Moustakas, Randall Wayth, and David J. Schlegel (Aug. 2008). "The Sloan Lens ACS Survey. V. The Full ACS Strong-Lens Sample." In: *The Astrophysical Journal* 682.2, pp. 964–984. DOI: 10.1086/589327. URL: https://doi.org/10.1086\%2F589327.

Bolton, Adam S., Scott Burles, Leon V. E. Koopmans, Tommaso Treu, and Leonidas A. Moustakas (Feb. 2006). "The Sloan Lens ACS Survey. I. A Large Spectroscopically Selected Sample of Massive Early-Type Lens Galaxies." In: *The Astrophysical Journal* 638.2, pp. 703–724. DOI: 10.1086/498884. URL: https://doi.org/10.1086\%2F498884.

Bonvin, V., M. Tewes, F. Courbin, T. Kuntzer, D. Sluse, and G. Meylan (Jan. 2016). "COSMOGRAIL: the COSmological MOnitoring of GRAvItational Lenses. XV. Assessing the achievability and precision of time-delay measurements." In: *Astronomy and Astrophysics* 585, A88, A88. DOI: 10.1051/0004-6361/201526704. arXiv: 1506.07524 [astro-ph.IM].

Bonvin, V. et al. (Mar. 2017). "HoLiCOW - V. New COSMOGRAIL time delays of HE 0435-1223: H_0 to 3.8 per cent precision from strong lensing in a flat ΛCDM model." In: *Monthly Notices of the Royal Astronomical Society* 465, pp. 4914–4930. DOI: 10.1093/mnras/stw3006. arXiv: 1607.01790.

Bromm, Volker and Naoki Yoshida (Sept. 2011). "The First Galaxies." In: *ARA&A* 49.1, pp. 373–407. DOI: 10.1146/annurev-astro-081710-102608. arXiv: 1102.4638 [astro-ph.CO].

Browne, I. W. A. et al. (May 2003). "The Cosmic Lens All-Sky Survey - II. Gravitational lens candidate selection and follow-up." In: *MNRAS* 341.1, pp. 13–32. DOI: 10.1046/j.1365-8711.2003.06257.x. arXiv: astro-ph/0211069 [astro-ph].

Brownstein, Joel R. et al. (Dec. 2011). "THE BOSS EMISSION-LINE LENS SURVEY (BELLS). I. A LARGE SPECTROSCOPICALLY SELECTED SAMPLE OF LENS GALAXIES AT REDSHIFT ~0.5." In: *The Astrophysical Journal* 744.1, p. 41. DOI: 10.1088/0004-637x/744/1/41. URL: https://doi.org/10.1088\%2F0004-637x\%2F744\%2F1\%2F41.

Bulla, Mattia et al. (Jan. 2020). "ZTF Early Observations of Type Ia Supernovae III: Early-Time Colors as a Test for Explosion Models and Multiple Populations." In: *arXiv e-prints*, arXiv:2001.00587, arXiv:2001.00587. arXiv: 2001.00587 [astro-ph.HE].

Burrows, Adam (Jan. 2013). "Colloquium: Perspectives on core-collapse supernova theory." In: *Reviews of Modern Physics* 85.1, pp. 245–261. DOI: 10.1103/RevModPhys.85.245. arXiv: 1210.4921 [astro-ph.SR].

Cappellaro, E., I. J. Danziger, M. della Valle, C. Gouiffes, and M. Turatto (Jan. 1995). "The bright linear type II SN 1990K." In: *A&A* 293, pp. 723–732.

Cardelli, Jason A., Geoffrey C. Clayton, and John S. Mathis (Oct. 1989). "The Relationship between Infrared, Optical, and Ultraviolet Extinction." In: *ApJ* 345, p. 245. DOI: 10.1086/167900.

Casey, Caitlin M., Desika Narayanan, and Asantha Cooray (Aug. 2014). "Dusty star-forming galaxies at high redshift." In: *Phys. Rep.* 541.2, pp. 45–161. DOI: 10.1016/j.physrep.2014.02.009. arXiv: 1402.1456 [astro-ph.CO].

Challinor, Anthony (Jan. 2013). "CMB anisotropy science: a review." In: *Astrophysics from Antarctica*. Ed. by Michael G. Burton, Xiangqun Cui, and Nicholas F. H. Tothill. Vol. 288. IAU Symposium, pp. 42–52. DOI: 10.1017/S1743921312016663. arXiv: 1210.6008 [astro-ph.CO].

Chang, K and S Refsdal (1979). "Flux variations of QSO 0957+ 561 A, B and image splitting by stars near the light path." In: *Nature* 282.5739, pp. 561–564.

Chen, Geoff C. F. et al. (Dec. 2019). "A SHARP view of HoLiCOW: H_0 from three time-delay gravitational lens systems with adaptive optics imaging." In: *Monthly Notices of the RAS* 490.2, pp. 1743–1773. DOI: 10.1093/mnras/stz2547. arXiv: 1907.02533 [astro-ph.CO].

Chen, Jacqueline, Eduardo Rozo, Neal Dalal, and James E. Taylor (Apr. 2007). "Astrometric Perturbations in Substructure Lensing." In: *ApJ* 659.1, pp. 52–68. DOI: 10.1086/512002. arXiv: astro-ph/0606359 [astro-ph].

Chiba, Masashi (Jan. 2002). "Probing Dark Matter Substructure in Lens Galaxies." In: *ApJ* 565.1, pp. 17–23. DOI: 10.1086/324493. arXiv: astro-ph/0109499 [astro-ph].

Childress, Michael J., Christian Wolf, and H. Jabran Zahid (Dec. 2014). "Ages of Type Ia supernovae over cosmic time." In: *MNRAS* 445.2, pp. 1898–1911. DOI: 10.1093/mnras/stu1892. arXiv: 1409.2951 [astro-ph.CO].

Chornock, R. et al. (Apr. 2013). "PS1-10afx at z = 1.388: Pan-STARRS1 Discovery of a New Type of Superluminous Supernova." In: *ApJ* 767.2, 162, p. 162. DOI: 10.1088/0004-637X/767/2/162. arXiv: 1302.0009 [astro-ph.CO].

Chugai, N. N. (June 1991). "Evidence for energizing of H alpha emission in type II supernovae by ejecta-wind interaction." In: *MNRAS* 250, p. 513. DOI: 10.1093/mnras/250.3.513.

Claeys, J. S. W., O. R. Pols, R. G. Izzard, J. Vink, and F. W. M. Verbunt (Mar. 2014). "Theoretical uncertainties of the Type Ia supernova rate." In: *A&A* 563, A83, A83. DOI: 10.1051/0004-6361/201322714. arXiv: 1401.2895 [astro-ph.SR].

Colgate, S. A. (Jan. 1968). "Prompt gamma rays and X-rays from supernovae." In: *Canadian Journal of Physics* 46, S476–S480.

Colgate, S. A. (Oct. 1975). "Prompt effects of supernovae." In: *Seventh Texas Symposium on Relativistic Astrophysics*. Ed. by P. G. Bergman, E. J. Fenyves, and L. Motz. Vol. 262, pp. 34–46. DOI: 10.1111/j.1749-6632.1975.tb31418.x.

Colgate, Stirling A. and Chester McKee (Aug. 1969). "Early Supernova Luminosity." In: *ApJ* 157, p. 623. DOI: 10.1086/150102.

Collett, T. E. and M. W. Auger (Sept. 2014). "Cosmological constraints from the double source plane lens SDSSJ0946+1006." In: *Monthly Notices of the Royal Astronomical Society* 443, pp. 969–976. DOI: 10.1093/mnras/stu1190. arXiv: 1403.5278.

Collett, Thomas E. (Sept. 2015). "The Population of Galaxy-Galaxy Strong Lenses in Forthcoming Optical Imaging Surveys." In: *Astrophysical Journal* 811.1, 20, p. 20. DOI: 10.1088/0004-637X/811/1/20. arXiv: 1507.02657 [astro-ph.CO].

Collett, Thomas E. et al. (July 2017). "Core or Cusps: The Central Dark Matter Profile of a Strong Lensing Cluster with a Bright Central Image at Redshift 1." In: *ApJ* 843.2, 148, p. 148. DOI: 10.3847/1538-4357/aa76e6. arXiv: 1703.08410 [astro-ph.CO].

Congdon, Arthur B. and Charles R. Keeton (2018). *Principles of Gravitational Lensing: Light Deflection as a Probe of Astrophysics and Cosmology*. Cham: Springer International Publishing. ISBN: 978-3-030-02122-1. DOI: 10.1007/978-3-030-02122-1_5. URL: https://doi.org/10.1007/978-3-030-02122-1_5.

Conley, A. et al. (July 2008). "SiFTO: An Empirical Method for Fitting SN Ia Light Curves." In: *ApJ* 681.1, pp. 482–498. DOI: 10.1086/588518. arXiv: 0803.3441 [astro-ph].

Cooke, Jeff, Mark Sullivan, Avishay Gal-Yam, Elizabeth J. Barton, Raymond G. Carlberg, Emma V. Ryan-Weber, Chuck Horst, Yuuki Omori, and C. Gonzalo Díaz (Nov. 2012). "Superluminous supernovae at redshifts of 2.05 and 3.90." In: *Nature* 491.7423, pp. 228–231. DOI: 10.1038/nature11521. arXiv: 1211.2003 [astro-ph.CO].

Crockett, R. M. et al. (Nov. 2008). "The type IIb SN 2008ax: the nature of the progenitor." In: *MNRAS* 391.1, pp. L5–L9. DOI: 10.1111/j.1745-3933.2008.00540.x. arXiv: 0805.1913 [astro-ph].

Cuesta, Antonio J., Licia Verde, Adam Riess, and Raul Jimenez (Apr. 2015). "Calibrating the cosmic distance scale ladder: the role of the sound-horizon scale and the local expansion rate as distance anchors." In: *Monthly Notices of the RAS* 448.4, pp. 3463–3471. DOI: 10.1093/mnras/stv261. arXiv: 1411.1094 [astro-ph.CO].

Curtin, Chris et al. (Apr. 2019). "First Release of High-redshift Superluminous Supernovae from the Subaru HIgh-Z SUpernova CAmpaign (SHIZUCA). II. Spectroscopic Properties." In: *ApJS* 241.2, 17, p. 17. DOI: 10.3847/1538-4365/ab07c8. arXiv: 1801.08241 [astro-ph.HE].

Czerny, Bożena et al. (Feb. 2018). "Astronomical Distance Determination in the Space Age. Secondary Distance Indicators." In: *Space Sci. Rev.* 214.1, 32, p. 32. DOI: 10.1007/s11214-018-0466-9. arXiv: 1801.00598 [astro-ph.GA].

Dalal, N. and C. S. Kochanek (June 2002). "Direct Detection of Cold Dark Matter Substructure." In: *ApJ* 572.1, pp. 25–33. DOI: 10.1086/340303. arXiv: astro-ph/0111456 [astro-ph].

De, Kishalay et al. (Mar. 2019). "ZTF 18aaqeasu (SN2018byg): A Massive Helium-shell Double Detonation on a Sub-Chandrasekhar-mass White Dwarf." In: *ApJ* 873.2, L18, p. L18. DOI: 10.3847/2041-8213/ab0aec. arXiv: 1901.00874 [astro-ph.HE].

Decourchelle, Anne (2017). "Supernova of 1572, Tycho's Supernova." In: *Handbook of Supernovae*. Ed. by Athem W. Alsabti and Paul Murdin. Cham: Springer International Publishing, pp. 117–137. DOI: 10.1007/978-3-319-21846-5_48. URL: https://doi.org/10.1007/978-3-319-21846-5_48.

Delchambre, L. et al. (Feb. 2019). "Gaia GraL: Gaia DR2 Gravitational Lens Systems. III. A systematic blind search for new lensed systems." In: *A&A* 622, A165, A165. DOI: 10.1051/0004-6361/201833802. arXiv: 1807.02845 [astro-ph.CO].

Delgado, Francisco, Abhijit Saha, Srinivasan Chand rasekharan, Kem Cook, Catherine Petry, and Stephen Ridgway (2014). "The LSST operations simulator." In: *Proc. SPIE*. Vol. 9150. Society of Photo-Optical Instrumentation Engineers (SPIE) Conference Series, p. 915015. DOI: 10.1117/12.2056898.

Dessart, Luc, Stéphane Blondin, D. John Hillier, and Alexei Khokhlov (June 2014). "Constraints on the explosion mechanism and progenitors of Type Ia supernovae." In: *MNRAS* 441.1, pp. 532–550. DOI: 10.1093/mnras/stu598. arXiv: 1310.7747 [astro-ph.SR].

Dhawan, S. et al. (Jan. 2020). "Magnification, dust, and time-delay constraints from the first resolved strongly lensed Type Ia supernova iPTF16geu." In: *MNRAS* 491.2, pp. 2639–2654. DOI: 10.1093/mnras/stz2965. arXiv: 1907.06756 [astro-ph.GA].

Diehl, H. T. et al. (Sept. 2017). "The DES Bright Arcs Survey: Hundreds of Candidate Strongly Lensed Galaxy Systems from the Dark Energy Survey Science Verifica-

tion and Year 1 Observations." In: *The Astrophysical Journal Supplement Series* 232.1, p. 15. DOI: 10.3847/1538-4365/aa8667. URL: https://doi.org/10.3847\%2F1538-4365\%2Faa8667.

Dimitriadis, G. et al. (Jan. 2019). "K2 Observations of SN 2018oh Reveal a Two-component Rising Light Curve for a Type Ia Supernova." In: *Astrophysical Journal, Letters* 870.1, L1, p. L1. DOI: 10.3847/2041-8213/aaedb0. arXiv: 1811.10061 [astro-ph.HE].

Dobler, Gregory and Charles R. Keeton (2006). "Microlensing of Lensed Supernovae." In: *Astrophys. J.* 653, pp. 1391–1399. DOI: 10.1086/508769. arXiv: astro-ph/0608391 [astro-ph].

Dobler, Gregory and Charles R. Keeton (Dec. 2006). "Microlensing of Lensed Supernovae." In: *ApJ* 653.2, pp. 1391–1399. DOI: 10.1086/508769. arXiv: astro-ph/0608391 [astro-ph].

Dyson, F. W., A. S. Eddington, and C. Davidson (1920). "A Determination of the Deflection of Light by the Sun's Gravitational Field, from Observations Made at the Total Eclipse of May 29, 1919." In: *Royal Society of London Philosophical Transactions Series A* 220, pp. 291–333. DOI: 10.1098/rsta.1920.0009.

Einstein, Albert (Jan. 1915). "Die Feldgleichungen der Gravitation." In: *Sitzungsberichte der Königlich Preußischen Akademie der Wissenschaften (Berlin*, pp. 844–847.

— (Jan. 1917). "Kosmologische Betrachtungen zur allgemeinen Relativitätstheorie." In: *Sitzungsberichte der Königlich Preußischen Akademie der Wissenschaften (Berlin*, pp. 142–152.

— (Dec. 1936). "Lens-Like Action of a Star by the Deviation of Light in the Gravitational Field." In: *Science* 84.2188, pp. 506–507. DOI: 10.1126/science.84.2188.506.

Eisenstein, Daniel J. and Wayne Hu (Mar. 1998). "Baryonic Features in the Matter Transfer Function." In: *ApJ* 496.2, pp. 605–614. DOI: 10.1086/305424. arXiv: astro-ph/9709112 [astro-ph].

Eisenstein, Daniel J. et al. (Nov. 2005). "Detection of the Baryon Acoustic Peak in the Large-Scale Correlation Function of SDSS Luminous Red Galaxies." In: *ApJ* 633.2, pp. 560–574. DOI: 10.1086/466512. arXiv: astro-ph/0501171 [astro-ph].

Ensman, Lisa and Adam Burrows (July 1992). "Shock Breakout in SN 1987A." In: *ApJ* 393, p. 742. DOI: 10.1086/171542.

Epstein, R. I. (Mar. 1981). "The eruption of supernova shock waves." In: *ApJ* 244, pp. L89–L91. DOI: 10.1086/183486.

Ezquiaga, Jose María and Miguel Zumalacárregui (Dec. 2018). "Dark Energy in light of Multi-Messenger Gravitational-Wave astronomy." In: *Frontiers in Astronomy and Space Sciences* 5, 44, p. 44. DOI: 10.3389/fspas.2018.00044. arXiv: 1807.09241 [astro-ph.CO].

Falco, E. E., M. V. Gorenstein, and I. I. Shapiro (Feb. 1985). "On model-dependent bounds on H(0) from gravitational images Application of Q0957 + 561A,B." In: *The Astrophysical Journal Letters* 289, pp. L1–L4. DOI: 10.1086/184422.

Falk, S. W. (Nov. 1978). "Shock steepening and prompt thermal emission in supernovae." In: *ApJ* 225, pp. L133–L136. DOI: 10.1086/182810.

Faure, Cecile et al. (May 2008). "First Catalog of Strong Lens Candidates in the COSMOS Field." In: 176.1, pp. 19–38. DOI: 10.1086/526426. URL: https://doi.org/10.1086\%2F526426.

Fausnaugh, M. M. et al. (Apr. 2019). "Early Time Light Curves of 18 Bright Type Ia Supernovae Observed with TESS." In: *arXiv e-prints*, arXiv:1904.02171, arXiv:1904.02171. arXiv: 1904.02171 [astro-ph.SR].

Filippenko, Alexei V. et al. (Jan. 1992a). "The Peculiar Type IA SN 1991T: Detonation of a White Dwarf?" In: *ApJ* 384, p. L15. DOI: 10.1086/186252.

Filippenko, Alexei V. et al. (Oct. 1992b). "The Subluminous, Spectroscopically Peculiar Type 1a Supernova 1991bg in the Elliptical Galaxy NGC 4374." In: *AJ* 104, p. 1543. DOI: 10.1086/116339.

Fink, M., W. Hillebrandt, and F. K. Röpke (Dec. 2007). "Double-detonation supernovae of sub-Chandrasekhar mass white dwarfs." In: *A&A* 476.3, pp. 1133–1143. DOI: 10.1051/0004-6361:20078438. arXiv: 0710.5486 [astro-ph].

Fink, M., F. K. Röpke, W. Hillebrandt, I. R. Seitenzahl, S. A. Sim, and M. Kromer (May 2010). "Double-detonation sub-Chandrasekhar supernovae: can minimum helium shell masses detonate the core?" In: *A&A* 514, A53, A53. DOI: 10.1051/0004-6361/200913892. arXiv: 1002.2173 [astro-ph.SR].

Firth, R. E. et al. (Feb. 2015). "The rising light curves of Type Ia supernovae." In: *MNRAS* 446.4, pp. 3895–3910. DOI: 10.1093/mnras/stu2314. arXiv: 1411.1064 [astro-ph.HE].

Folatelli, Gastón, Melina C. Bersten, Omar G. Benvenuto, Schuyler D. Van Dyk, Hanindyo Kuncarayakti, Keiichi Maeda, Takaya Nozawa, Ken'ichi Nomoto, Mario Hamuy, and Robert M. Quimby (Oct. 2014). "A Blue Point Source at the Location of Supernova 2011dh." In: *ApJ* 793.2, L22, p. L22. DOI: 10.1088/2041-8205/793/2/L22. arXiv: 1409.0700 [astro-ph.SR].

Folatelli, Gastón, Melina C. Bersten, Hanindyo Kuncarayakti, Omar G. Benvenuto, Keiichi Maeda, and Ken'ichi Nomoto (Oct. 2015). "The Progenitor of the Type IIb SN 2008ax Revisited." In: *ApJ* 811.2, 147, p. 147. DOI: 10.1088/0004-637X/811/2/147. arXiv: 1509.01588 [astro-ph.SR].

Foxley-Marrable, Max, Thomas E. Collett, Chris Frohmaier, Daniel A. Goldstein, Daniel Kasen, Elizabeth Swann, and David Bacon (May 2020). "Observing the earliest moments of supernovae using strong gravitational lenses." In: *MNRAS*. DOI: 10.1093/mnras/staa1289. arXiv: 2003.14340 [astro-ph.HE].

Foxley-Marrable, Max, Thomas E. Collett, Georgios Vernardos, Daniel A. Goldstein, and David Bacon (Aug. 2018). "The impact of microlensing on the standardization of strongly lensed Type Ia supernovae." In: *Monthly Notices of the RAS* 478.4, pp. 5081–5090. DOI: 10.1093/mnras/sty1346. arXiv: 1802.07738 [astro-ph.CO].

Freedman, Wendy L. (June 2017). "Correction: Cosmology at a crossroads." In: *Nature Astronomy* 1, 0169, p. 0169. DOI: 10.1038/s41550-017-0169. arXiv: 1706.02739 [astro-ph.CO].

Freedman, Wendy L. and Barry F. Madore (2010). "The Hubble Constant." In: *Annual Review of Astronomy and Astrophysics* 48.1, pp. 673–710. DOI: 10.1146/annurev-astro-082708-101829. eprint: https://doi.org/10.1146/annurev-astro-082708-101829. URL: https://doi.org/10.1146/annurev-astro-082708-101829.

Freedman, Wendy L., Barry F. Madore, Victoria Scowcroft, Chris Burns, Andy Monson, S. Eric Persson, Mark Seibert, and Jane Rigby (Oct. 2012). "Carnegie Hubble Program: A Mid-infrared Calibration of the Hubble Constant." In: *ApJ* 758.1, 24, p. 24. DOI: 10.1088/0004-637X/758/1/24. arXiv: 1208.3281 [astro-ph.CO].

Freedman, Wendy L. et al. (Sept. 2019). "The Carnegie-Chicago Hubble Program. VIII. An Independent Determination of the Hubble Constant Based on the Tip of the Red Giant Branch." In: *Astrophysical Journal* 882.1, 34, p. 34. DOI: 10.3847/1538-4357/ab2f73. arXiv: 1907.05922 [astro-ph.CO].

Friedmann, A. (Jan. 1922). "Über die Krümmung des Raumes." In: *Zeitschrift fur Physik* 10, pp. 377–386. DOI: 10.1007/BF01332580.

Frohmaier, C. et al. (June 2019). "The volumetric rate of normal type Ia supernovae in the local Universe discovered by the Palomar Transient Factory." In: *MNRAS* 486.2, pp. 2308–2320. DOI: 10.1093/mnras/stz807. arXiv: 1903.08580 [astro-ph.HE].

Fujimoto, M. Y. (June 1982). "A Theory of Hydrogen Shell Flashes on Accreting White Dwarfs - Part Two - the Stable Shell Burning and the Recurrence Period of Shell Flashes." In: *ApJ* 257, p. 767. DOI: 10.1086/160030.

Gaia Collaboration et al. (Aug. 2018). "Gaia Data Release 2. Summary of the contents and survey properties." In: *Astronomy and Astrophysics* 616, A1, A1. DOI: 10.1051/0004-6361/201833051. arXiv: 1804.09365 [astro-ph.GA].

Gal-Yam, A. and D. C. Leonard (Apr. 2009). "A massive hypergiant star as the progenitor of the supernova SN 2005gl." In: *Nature* 458.7240, pp. 865–867. DOI: 10.1038/nature07934.

Gal-Yam, A. et al. (Dec. 2009). "Supernova 2007bi as a pair-instability explosion." In: *Nature* 462.7273, pp. 624–627. DOI: 10.1038/nature08579. arXiv: 1001.1156 [astro-ph.CO].

Gal-Yam, Avishay (Aug. 2012). "Luminous Supernovae." In: *Science* 337.6097, p. 927. DOI: 10.1126/science.1203601. arXiv: 1208.3217 [astro-ph.CO].

Gal-Yam, Avishay et al. (Feb. 2007). "On the Progenitor of SN 2005gl and the Nature of Type IIn Supernovae." In: *The Astrophysical Journal* 656.1, pp. 372–381. DOI: 10.1086/510523. URL: https://doi.org/10.1086\%2F510523.

García-Berro, Enrique and Pablo Lorén-Aguilar (2017). "Dynamical Mergers." In: *Handbook of Supernovae*. Ed. by Athem W. Alsabti and Paul Murdin. Cham: Springer International Publishing, pp. 1237–1255. ISBN: 978-3-319-21846-5. DOI: 10.1007/978-3-319-21846-5_60. URL: https://doi.org/10.1007/978-3-319-21846-5_60.

Gaskell, C. M., E. Cappellaro, H. L. Dinerstein, D. R. Garnett, R. P. Harkness, and J. C. Wheeler (July 1986). "Type Ib Supernovae 1983n and 1985f: Oxygen-rich Late Time Spectra." In: *ApJ* 306, p. L77. DOI: 10.1086/184709.

Gaudi, B. S. et al. (Jan. 2008). "Discovery of a Jupiter/Saturn Analog with Gravitational Microlensing." In: *Science* 319.5865, p. 927. DOI: 10.1126/science.1151947. arXiv: 0802.1920 [astro-ph].

Gaudi, B. Scott (Sept. 2012). "Microlensing Surveys for Exoplanets." In: *ARA&A* 50, pp. 411–453. DOI: 10.1146/annurev-astro-081811-125518.

Geach, J. E., R. J. Ivison, S. Dye, and I. Oteo (Oct. 2018). "A Magnified View of Circumnuclear Star Formation and Feedback around an Active Galactic Nucleus at z = 2.6." In: *The Astrophysical Journal* 866.1, p. L12. DOI: 10.3847/2041-8213/aae375. URL: https://doi.org/10.3847\%2F2041-8213\%2Faae375.

Goldstein, D. A. and P. E. Nugent (Jan. 2017). "How to Find Gravitationally Lensed Type Ia Supernovae." In: *The Astrophysical Journal Letters* 834, L5, p. L5. DOI: 10.3847/2041-8213/834/1/L5. arXiv: 1611.09459 [astro-ph.IM].

Goldstein, Daniel A., Peter E. Nugent, and Ariel Goobar (July 2019). "Rates and Properties of Supernovae Strongly Gravitationally Lensed by Elliptical Galaxies in Time-domain Imaging Surveys." In: *Astrophysical Journal, Supplement* 243.1, 6, p. 6. DOI: 10.3847/1538-4365/ab1fe0. arXiv: 1809.10147 [astro-ph.GA].

Goldstein, Daniel A., Peter E. Nugent, Daniel N. Kasen, and Thomas E. Collett (Mar. 2018). "Precise Time Delays from Strongly Gravitationally Lensed Type Ia Supernovae with Chromatically Microlensed Images." In: *Astrophysical Journal* 855.1, 22, p. 22. DOI: 10.3847/1538-4357/aaa975. arXiv: 1708.00003 [astro-ph.CO].

Goobar, A., M. Kromer, R. Siverd, K. G. Stassun, J. Pepper, R. Amanullah, M. Kasliwal, J. Sollerman, and F. Taddia (Jan. 2015). "Constraints on the Origin of the First Light from SN 2014J." In: *ApJ* 799.1, 106, p. 106. DOI: 10.1088/0004-637X/799/1/106. arXiv: 1410.1363 [astro-ph.HE].

Goobar, A. et al. (Mar. 2014). "The Rise of SN 2014J in the Nearby Galaxy M82." In: *ApJ* 784.1, L12, p. L12. DOI: 10.1088/2041-8205/784/1/L12. arXiv: 1402.0849 [astro-ph.GA].

Goobar, A. et al. (2017). "iPTF16geu: A multiply imaged, gravitationally lensed type Ia supernova." In: *Science* 356, pp. 291–295. DOI: 10.1126/science.aal2729. arXiv: 1611.00014 [astro-ph.CO].

Goobar, A. et al. (Apr. 2017). "iPTF16geu: A multiply imaged, gravitationally lensed type Ia supernova." In: *Science* 356.6335, pp. 291–295. DOI: 10.1126/science.aal2729. arXiv: 1611.00014 [astro-ph.CO].

Grassberg, E. K., V. S. Imshennik, and D. K. Nadyozhin (Jan. 1971). "On the Theory of the Light Curves of Supernovae." In: *Ap&SS* 10.1, pp. 28–51. DOI: 10.1007/BF00654604.

Graur, O. et al. (Mar. 2014). "Type-Ia Supernova Rates to Redshift 2.4 from CLASH: The Cluster Lensing And Supernova Survey with Hubble." In: *ApJ* 783.1, 28, p. 28. DOI: 10.1088/0004-637X/783/1/28. arXiv: 1310.3495 [astro-ph.CO].

Graur, Or and Dan Maoz (Apr. 2013). "Discovery of 90 Type Ia supernovae among 700 000 Sloan spectra: the Type Ia supernova rate versus galaxy mass and star formation rate at redshift ~0.1." In: *MNRAS* 430.3, pp. 1746–1763. DOI: 10.1093/mnras/sts718. arXiv: 1209.0008 [astro-ph.CO].

Green, David A. (2017). "Historical Supernovae in the Galaxy from AD 1006." In: *Handbook of Supernovae*. Ed. by Athem W. Alsabti and Paul Murdin, p. 37. DOI: 10.1007/978-3-319-21846-5_2.

Greggio, L. (Oct. 2005). "The rates of type Ia supernovae. I. Analytical formulations." In: *A&A* 441.3, pp. 1055–1078. DOI: 10.1051/0004-6361:20052926. arXiv: astro-ph/0504376 [astro-ph].

Grillo, C. et al. (June 2018). "Measuring the Value of the Hubble Constant "à la Refsdal"." In: *ApJ* 860.2, 94, p. 94. DOI: 10.3847/1538-4357/aac2c9. arXiv: 1802.01584 [astro-ph.CO].

Gutierrez, Jordi, Enrique Garcia-Berro, Jr. Iben Icko, Jordi Isern, Javier Labay, and Ramon Canal (Mar. 1996). "The Final Evolution of ONeMg Electron-Degenerate Cores." In: *ApJ* 459, p. 701. DOI: 10.1086/176934.

Guy, J. et al. (Apr. 2007). "SALT2: using distant supernovae to improve the use of type Ia supernovae as distance indicators." In: *A&A* 466.1, pp. 11–21. DOI: 10.1051/0004-6361:20066930. arXiv: astro-ph/0701828 [astro-ph].

Hachisu, I., M. Kato, and K. Nomoto (Oct. 1996). "A New Model for Progenitor Systems of Type IA Supernovae." In: *ApJ* 470, p. L97. DOI: 10.1086/310303.

Hamuy, Mario, M. M. Phillips, Nicholas B. Suntzeff, Robert A. Schommer, Jose Maza, and R. Aviles (Dec. 1996). "The Absolute Luminosities of the Calan/Tololo Type IA Supernovae." In: *Astronomical Journal* 112, p. 2391. DOI: 10.1086/118190. arXiv: astro-ph/9609059 [astro-ph].

Hamuy, Mario, Nicholas B. Suntzeff, Ricardo Gonzalez, and Gabriel Martin (Jan. 1988). "SN 1987A in the LMC: UBVRI Photometry at Cerro Tololo." In: *AJ* 95, p. 63. DOI: 10.1086/114613.

Hamuy, Mario, S. C. Trager, Philip A. Pinto, M. M. Phillips, R. A. Schommer, Valentin Ivanov, and Nicholas B. Suntzeff (Sept. 2000). "A Search for Environmental Effects on Type IA Supernovae." In: *AJ* 120.3, pp. 1479–1486. DOI: 10.1086/301527. arXiv: astro-ph/0005213 [astro-ph].

Hamuy, Mario et al. (Aug. 2003). "An asymptotic-giant-branch star in the progenitor system of a type Ia supernova." In: *Nature* 424.6949, pp. 651–654. DOI: 10.1038/nature01854. arXiv: astro-ph/0306270 [astro-ph].

Heger, A., C. L. Fryer, S. E. Woosley, N. Langer, and D. H. Hartmann (July 2003). "How Massive Single Stars End Their Life." In: *ApJ* 591.1, pp. 288–300. DOI: 10.1086/375341. arXiv: astro-ph/0212469 [astro-ph].

Hennawi, Joseph F. et al. (Jan. 2008). "A NEW SURVEY FOR GIANT ARCS." In: *The Astronomical Journal* 135.2, pp. 664–681. DOI: 10.1088/0004-6256/135/2/664. URL: https://doi.org/10.1088\%2F0004-6256\%2F135\%2F2\%2F664.

Herrnstein, J. R., J. M. Moran, L. J. Greenhill, P. J. Diamond, M. Inoue, N. Nakai, M. Miyoshi, C. Henkel, and A. Riess (Aug. 1999). "A geometric distance to the galaxy NGC4258 from orbital motions in a nuclear gas disk." In: *Nature* 400.6744, pp. 539–541. DOI: 10.1038/22972. arXiv: astro-ph/9907013 [astro-ph].

Hezaveh, Y. D. et al. (Apr. 2013). "ALMA Observations of SPT-discovered, Strongly Lensed, Dusty, Star-forming Galaxies." In: *ApJ* 767.2, 132, p. 132. DOI: 10.1088/0004-637X/767/2/132. arXiv: 1303.2722 [astro-ph.CO].

Hezaveh, Yashar D. and Gilbert P. Holder (June 2011). "Effects of Strong Gravitational Lensing on Millimeter-wave Galaxy Number Counts." In: *ApJ* 734.1, 52, p. 52. DOI: 10.1088/0004-637X/734/1/52. arXiv: 1010.0998 [astro-ph.CO].

Hicken, Malcolm et al. (July 2009). "CfA3: 185 Type Ia Supernova Light Curves from the CfA." In: *ApJ* 700.1, pp. 331–357. DOI: 10.1088/0004-637X/700/1/331. arXiv: 0901.4787 [astro-ph.CO].

Hillebrandt, W., M. Kromer, F. K. Röpke, and A. J. Ruiter (Apr. 2013). "Towards an understanding of Type Ia supernovae from a synthesis of theory and observations." In: *Frontiers of Physics* 8.2, pp. 116–143. DOI: 10.1007/s11467-013-0303-2. arXiv: 1302.6420 [astro-ph.CO].

Hillman, Y., D. Prialnik, A. Kovetz, and M. M. Shara (Mar. 2016). "GROWING WHITE DWARFS TO THE CHANDRASEKHAR LIMIT: THE PARAMETER SPACE OF THE SINGLE DEGENERATE SN Ia CHANNEL." In: *The Astrophysical Journal* 819.2, p. 168. DOI: 10.3847/0004-637x/819/2/168. URL: https://doi.org/10.3847\%2F0004-637x\%2F819\%2F2\%2F168.

Hinshaw, G. et al. (Oct. 2013). "Nine-year Wilkinson Microwave Anisotropy Probe (WMAP) Observations: Cosmological Parameter Results." In: *Astrophysical Journal, Supplement* 208.2, 19, p. 19. DOI: 10.1088/0067-0049/208/2/19. arXiv: 1212.5226 [astro-ph.CO].

Hirata, K. et al. (Apr. 1987). "Observation of a neutrino burst from the supernova SN1987A." In: *Phys. Rev. Lett.* 58.14, pp. 1490–1493. DOI: 10.1103/PhysRevLett.58.1490.

Hoeflich, P. and A. Khokhlov (Feb. 1996). "Explosion Models for Type IA Supernovae: A Comparison with Observed Light Curves, Distances, H 0, and Q 0." In: *ApJ* 457, p. 500. DOI: 10.1086/176748. arXiv: astro-ph/9602025 [astro-ph].

Hoeflich, Peter (2017). "Explosion Physics of Thermonuclear Supernovae and Their Signatures." In: *Handbook of Supernovae*. Ed. by Athem W. Alsabti and Paul Murdin. Cham: Springer International Publishing, pp. 1151–1184. ISBN: 978-3-319-21846-5. DOI: 10.1007/978-3-319-21846-5_56. URL: https://doi.org/10.1007/978-3-319-21846-5_56.

Holz, Daniel E. (Aug. 2001). "Seeing Double: Strong Gravitational Lensing of High-Redshift Supernovae." In: *The Astrophysical Journal* 556.2, pp. L71–L74. DOI: 10.1086/322947. URL: https://doi.org/10.1086\%2F322947.

Holz, Daniel E. and Scott A. Hughes (Aug. 2005). "Using Gravitational-Wave Standard Sirens." In: *ApJ* 629.1, pp. 15–22. DOI: 10.1086/431341. arXiv: astro-ph/0504616 [astro-ph].

Hosseinzadeh, Griffin et al. (Aug. 2017). "Early Blue Excess from the Type Ia Supernova 2017cbv and Implications for Its Progenitor." In: *ApJ* 845.2, L11, p. L11. DOI: 10.3847/2041-8213/aa8402. arXiv: 1706.08990 [astro-ph.HE].

Howell, D. A. et al. (Jan. 2009). "The Effect of Progenitor Age and Metallicity on Luminosity and ^{56}Ni Yield in Type Ia Supernovae." In: *ApJ* 691.1, pp. 661–671. DOI: 10.1088/0004-637X/691/1/661. arXiv: 0810.0031 [astro-ph].

Howell, D. Andrew (2017). "Superluminous Supernovae." In: *Handbook of Supernovae*. Ed. by Athem W. Alsabti and Paul Murdin. Cham: Springer International Publishing, pp. 431–458. DOI: 10.1007/978-3-319-21846-5_41. URL: https://doi.org/10.1007/978-3-319-21846-5_41.

Hsiao, E. Y., A. Conley, D. A. Howell, M. Sullivan, C. J. Pritchet, R. G. Carlberg, P. E. Nugent, and M. M. Phillips (July 2007). "K-Corrections and Spectral Templates of Type Ia Supernovae." In: *Astrophysical Journal* 663.2, pp. 1187–1200. DOI: 10.1086/518232. arXiv: astro-ph/0703529 [astro-ph].

Hsueh, J.-W., G. Despali, S. Vegetti, D. Xu, C. D. Fassnacht, and R. B. Metcalf (July 2017). "Flux-ratio anomalies from discs and other baryonic structures in the Illustris simulation." In: *ArXiv e-prints*. arXiv: 1707.07680.

Hu, Wayne and Martin White (Feb. 2004). "The Cosmic Symphony." In: *Scientific American* 290.2, pp. 44–53. DOI: 10.1038/scientificamerican0204-44.

Huang, Fang, Xiaofeng Wang, Jujia Zhang, Peter J. Brown, Luca Zampieri, Maria Letizia Pumo, Tianmeng Zhang, Juncheng Chen, Jun Mo, and Xulin Zhao (July 2015). "SN 2013ej IN M74: A LUMINOUS AND FAST-DECLINING TYPE II-P SUPERNOVA." In: *The Astrophysical Journal* 807.1, p. 59. DOI: 10.1088/0004-637x/807/1/59. URL: https://doi.org/10.1088\%2F0004-637x\%2F807\%2F1\%2F59.

Hubble, Edwin (Mar. 1929). "A Relation between Distance and Radial Velocity among Extra-Galactic Nebulae." In: *Proceedings of the National Academy of Science* 15.3, pp. 168–173. DOI: 10.1073/pnas.15.3.168.

Huber, S. et al. (Nov. 2019). "Strongly lensed SNe Ia in the era of LSST: observing cadence for lens discoveries and time-delay measurements." In: *A&A* 631, A161, A161. DOI: 10.1051/0004-6361/201935370. arXiv: 1903.00510 [astro-ph.IM].

Humphreys, E. M. L., M. J. Reid, J. M. Moran, L. J. Greenhill, and A. L. Argon (Sept. 2013). "Toward a New Geometric Distance to the Active Galaxy NGC 4258. III. Final Results and the Hubble Constant." In: *Astrophysical Journal* 775.1, 13, p. 13. DOI: 10.1088/0004-637X/775/1/13. arXiv: 1307.6031 [astro-ph.CO].

Huterer, Dragan and Daniel L. Shafer (Jan. 2018). "Dark energy two decades after: observables, probes, consistency tests." In: *Reports on Progress in Physics* 81.1, 016901, p. 016901. DOI: 10.1088/1361-6633/aa997e. arXiv: 1709.01091 [astro-ph.CO].

Iben Jr., I. and A. V. Tutukov (Feb. 1984). "Supernovae of type I as end products of the evolution of binaries with components of moderate initial mass (M not greater

than about 9 solar masses)." In: *Astrophysical Journal, Supplement* 54, pp. 335–372. DOI: 10.1086/190932.

Ilkov, Marjan and Noam Soker (Jan. 2012). "Type Ia supernovae from very long delayed explosion of core-white dwarf merger." In: *MNRAS* 419.2, pp. 1695–1700. DOI: 10.1111/j.1365-2966.2011.19833.x. arXiv: 1106.2027 [astro-ph.SR].

Imshennik, V. S. and V. P. Utrobin (Feb. 1977). "Light curves of type II supernovae." In: *Soviet Astronomy Letters* 3, p. 34.

Inserra, C. and S. J. Smartt (Dec. 2014). "Superluminous Supernovae as Standardizable Candles and High-redshift Distance Probes." In: *ApJ* 796.2, 87, p. 87. DOI: 10.1088/0004-637X/796/2/87. arXiv: 1409.4429 [astro-ph.SR].

Inserra, C. et al. (Jan. 2018). "Euclid: Superluminous supernovae in the Deep Survey." In: *A&A* 609, A83, A83. DOI: 10.1051/0004-6361/201731758. arXiv: 1710.09585 [astro-ph.CO].

Jackson, Neal (Sept. 2008). "Gravitational lenses and lens candidates identified from the COSMOS field." In: *MNRAS* 389.3, pp. 1311–1318. DOI: 10.1111/j.1365-2966.2008.13629.x. arXiv: 0806.3693 [astro-ph].

— (Sept. 2015). "The Hubble Constant." In: *Living Reviews in Relativity* 18.1, 2, p. 2. DOI: 10.1007/lrr-2015-2.

Jacobs, C. et al. (Apr. 2019). "Finding high-redshift strong lenses in DES using convolutional neural networks." In: *MNRAS* 484.4, pp. 5330–5349. DOI: 10.1093/mnras/stz272. arXiv: 1811.03786 [astro-ph.GA].

Jacobson-Galan, Wynn V. et al. (Oct. 2019). "Ca hnk: Calcium-rich Transient SN 2016hnk from the Helium Shell Detonation of a Sub-Chandrasekhar White Dwarf." In: *arXiv e-prints*, arXiv:1910.05436, arXiv:1910.05436. arXiv: 1910.05436 [astro-ph.HE].

Janka, Hans-Thomas (Nov. 2012). "Explosion Mechanisms of Core-Collapse Supernovae." In: *Annual Review of Nuclear and Particle Science* 62.1, pp. 407–451. DOI: 10.1146/annurev-nucl-102711-094901. arXiv: 1206.2503 [astro-ph.SR].

Janka, Hans-Thomas, Tobias Melson, and Alexander Summa (Oct. 2016). "Physics of Core-Collapse Supernovae in Three Dimensions: A Sneak Preview." In: *Annual Review of Nuclear and Particle Science* 66.1, pp. 341–375. DOI: 10.1146/annurev-nucl-102115-044747. arXiv: 1602.05576 [astro-ph.SR].

Jee, Inh, Sherry H. Suyu, Eiichiro Komatsu, Christopher D. Fassnacht, Stefan Hilbert, and Léon V. E. Koopmans (Sept. 2019). "A measurement of the Hubble con-

stant from angular diameter distances to two gravitational lenses." In: *Science* 365.6458, pp. 1134–1138. DOI: 10.1126/science.aat7371. arXiv: 1909.06712 [astro-ph.CO].

Jha, Saurabh, Adam G. Riess, and Robert P. Kirshner (Apr. 2007). "Improved Distances to Type Ia Supernovae with Multicolor Light-Curve Shapes: MLCS2k2." In: *ApJ* 659.1, pp. 122–148. DOI: 10.1086/512054. arXiv: astro-ph/0612666 [astro-ph].

Jiang, Ji-An et al. (Oct. 2017). "A hybrid type Ia supernova with an early flash triggered by helium-shell detonation." In: *Nature* 550.7674, pp. 80–83. DOI: 10.1038/nature23908. arXiv: 1710.01824 [astro-ph.HE].

Joglekar, Hrishikesh, M N Vahia, and Aniket Sule (2011). "Oldest sky-chart with Supernova record." In: *Puratattva: Journal of the Indian Archaeological Society* 41, pp. 207–211. URL: https://www.tifr.res.in/~archaeo/papers/Prehistoricastronomy/OldestSupernovarecordinKashmir.pdf.

Johansson, J. et al. (Apr. 2020). "Spectroscopy of the first resolved strongly lensed Type Ia supernova iPTF16geu." In: *arXiv e-prints*, arXiv:2004.10164, arXiv:2004.10164. arXiv: 2004.10164 [astro-ph.GA].

Jones, D. O. et al. (Apr. 2018). "Measuring Dark Energy Properties with Photometrically Classified Pan-STARRS Supernovae. II. Cosmological Parameters." In: *ApJ* 857.1, 51, p. 51. DOI: 10.3847/1538-4357/aab6b1. arXiv: 1710.00846 [astro-ph.CO].

Kasen, Daniel (Jan. 2010). "Seeing the Collision of a Supernova with Its Companion Star." In: *Astrophysical Journal* 708.2, pp. 1025–1031. DOI: 10.1088/0004-637X/708/2/1025. arXiv: 0909.0275 [astro-ph.HE].

Kasen, Daniel and S. E. Woosley (Feb. 2007). "On the Origin of the Type Ia Supernova Width-Luminosity Relation." In: *The Astrophysical Journal* 656.2, pp. 661–665. DOI: 10.1086/510375. URL: https://doi.org/10.1086\%2F510375.

Kashi, Amit and Noam Soker (Oct. 2011). "A circumbinary disc in the final stages of common envelope and the core-degenerate scenario for Type Ia supernovae." In: *MNRAS* 417.2, pp. 1466–1479. DOI: 10.1111/j.1365-2966.2011.19361.x. arXiv: 1105.5698 [astro-ph.SR].

Katsuda, Satoru (2017). "Supernova of 1006 (G327.6+14.6)." In: *Handbook of Supernovae*. Ed. by Athem W. Alsabti and Paul Murdin. Cham: Springer International Pub-

lishing, pp. 63–81. ISBN: 978-3-319-21846-5. DOI: 10.1007/978-3-319-21846-5_45. URL: https://doi.org/10.1007/978-3-319-21846-5_45.

Kattner, ShiAnne et al. (Feb. 2012). "The Standardizability of Type Ia Supernovae in the Near-Infrared: Evidence for a Peak-Luminosity Versus Decline-Rate Relation in the Near-Infrared." In: *Publications of the Astronomical Society of the Pacific* 124.912, pp. 114–127. DOI: 10.1086/664734. URL: https://doi.org/10.1086\%2F664734.

Katz, Boaz and Subo Dong (Nov. 2012). "The rate of WD-WD head-on collisions may be as high as the SNe Ia rate." In: *arXiv e-prints*, arXiv:1211.4584, arXiv:1211.4584. arXiv: 1211.4584 [astro-ph.SR].

Kayser, R., S. Refsdal, and R. Stabell (Sept. 1986). "Astrophysical applications of gravitational micro-lensing." In: *Astronomy and Astrophysics* 166, pp. 36–52.

Keeton, Charles R. and Leonidas A. Moustakas (June 2009). "A NEW CHANNEL FOR DETECTING DARK MATTER SUBSTRUCTURE IN GALAXIES: GRAVITATIONAL LENS TIME DELAYS." In: *The Astrophysical Journal* 699.2, pp. 1720–1731. DOI: 10.1088/0004-637x/699/2/1720. URL: https://doi.org/10.1088\%2F0004-637x\%2F699\%2F2\%2F1720.

Kelly, P. L. et al. (Mar. 2016). "Deja Vu All Over Again: The Reappearance of Supernova Refsdal." In: *ApJ* 819.1, L8, p. L8. DOI: 10.3847/2041-8205/819/1/L8. arXiv: 1512.04654 [astro-ph.CO].

Kelly, Patrick L. et al. (Mar. 2015). "Multiple images of a highly magnified supernova formed by an early-type cluster galaxy lens." In: *Science* 347.6226, pp. 1123–1126. DOI: 10.1126/science.aaa3350. arXiv: 1411.6009 [astro-ph.CO].

Klein, R. I. and R. A. Chevalier (Aug. 1978). "X-ray bursts from type II supernovae." In: *ApJ* 223, pp. L109–L112. DOI: 10.1086/182740.

Kochanek, C. S. (Apr. 2004). "Quantitative Interpretation of Quasar Microlensing Light Curves." In: *The Astrophysical Journal* 605.1, pp. 58–77. DOI: 10.1086/382180. URL: https://doi.org/10.1086\%2F382180.

Kochanek, C. S. (Mar. 2019). "The physics of flash (supernova) spectroscopy." In: *MNRAS* 483.3, pp. 3762–3772. DOI: 10.1093/mnras/sty3363. arXiv: 1807.09778 [astro-ph.SR].

Kochanek, Christopher S. (June 1995). "Evidence for Dark Matter in MG 1654+134." In: *ApJ* 445, p. 559. DOI: 10.1086/175721.

Kolatt, T. S. and M. Bartelmann (May 1998). "Gravitational lensing of type IA supernovae by galaxy clusters." In: *Monthly Notices of the RAS* 296, pp. 763–772. DOI: 10.1046/j.1365-8711.1998.01466.x. eprint: astro-ph/9708120.

Koopmans, L. V. E., A. Bolton, T. Treu, O. Czoske, M. W. Auger, M. Barnabè, S. Vegetti, R. Gavazzi, L. A. Moustakas, and S. Burles (Sept. 2009). "The Structure and Dynamics of Massive Early-Type Galaxies: On Homology, Isothermality, and Isotropy Inside One Effective Radius." In: *ApJ* 703.1, pp. L51–L54. DOI: 10.1088/0004-637X/703/1/L51. arXiv: 0906.1349 [astro-ph.CO].

Kormann, R., P. Schneider, and M. Bartelmann (Apr. 1994). "Isothermal elliptical gravitational lens models." In: *A&A* 284, pp. 285–299.

Kothes, Roland (2017). "Supernova of AD 1181 and its Remnant: 3C 58." In: *Handbook of Supernovae*. Ed. by Athem W. Alsabti and Paul Murdin. Cham: Springer International Publishing, pp. 97–115. ISBN: 978-3-319-21846-5. DOI: 10.1007/978-3-319-21846-5_47. URL: https://doi.org/10.1007/978-3-319-21846-5_47.

Kravtsov, Andrey (Jan. 2010). "The Dark Matter Annihilation Signal from Dwarf Galaxies and Subhalos." In: *Advances in Astronomy* 2010, 281913, p. 281913. DOI: 10.1155/2010/281913. arXiv: 0906.3295 [astro-ph.CO].

Kubo, Jeffrey M., Sahar S. Allam, James Annis, Elizabeth J. Buckley-Geer, H. Thomas Diehl, Donna Kubik, Huan Lin, and Douglas Tucker (Apr. 2009). "THE SLOAN BRIGHT ARCS SURVEY: SIX STRONGLY LENSED GALAXIES AT z = 0.4-1.4." In: *The Astrophysical Journal* 696.1, pp. L61–L65. DOI: 10.1088/0004-637x/696/1/l61. URL: https://doi.org/10.1088\%2F0004-637x\%2F696\%2F1\%2Fl61.

Kunkel, W. et al. (Feb. 1987). "Supernova 1987A in the Large Magellanic Cloud." In: *IAU Circ.* 4316, p. 1.

Kushnir, Doron, Boaz Katz, Subo Dong, Eli Livne, and Rodrigo Fernández (Nov. 2013). "HEAD-ON COLLISIONS OF WHITE DWARFS IN TRIPLE SYSTEMS COULD EXPLAIN TYPE Ia SUPERNOVAE." In: *The Astrophysical Journal* 778.2, p. L37. DOI: 10.1088/2041-8205/778/2/l37. URL: https://doi.org/10.1088\%2F2041-8205\%2F778\%2F2\%2Fl37.

Lasher, G. J. and K. L. Chan (June 1979). "A method for predicting the soft X-ray flux from supernovae." In: *ApJ* 230, pp. 742–754. DOI: 10.1086/157133.

Lasher, G. and K. L. Chan (Sept. 1975). "A Prediction of Soft X-Ray Emission from Type I Supernovae." In: *BAAS*. Vol. 7, p. 505.

Leavitt, Henrietta S. (Jan. 1908). "1777 variables in the Magellanic Clouds." In: *Annals of Harvard College Observatory* 60, pp. 87–108.3.

Leavitt, Henrietta S. and Edward C. Pickering (Mar. 1912). "Periods of 25 Variable Stars in the Small Magellanic Cloud." In: *Harvard College Observatory Circular* 173, pp. 1–3.

Leibundgut, Bruno et al. (Jan. 1993). "SN 1991bg: A Type IA Supernova With a Difference." In: *AJ* 105, p. 301. DOI: 10.1086/116427.

Lemaître, G. (Jan. 1927). "Un Univers homogène de masse constante et de rayon croissant rendant compte de la vitesse radiale des nébuleuses extra-galactiques." In: *Annales de la Société Scientifique de Bruxelles* 47, pp. 49–59.

Lemon, Cameron A., Matthew W. Auger, and Richard G. McMahon (Mar. 2019). "Gravitationally lensed quasars in Gaia - III. 22 new lensed quasars from Gaia data release 2." In: *MNRAS* 483.3, pp. 4242–4258. DOI: 10.1093/mnras/sty3366. arXiv: 1810.04480 [astro-ph.GA].

Lemon, Cameron A., Matthew W. Auger, Richard G. McMahon, and Fernanda Ostrovski (Oct. 2018). "Gravitationally lensed quasars in Gaia - II. Discovery of 24 lensed quasars." In: *MNRAS* 479.4, pp. 5060–5074. DOI: 10.1093/mnras/sty911. arXiv: 1803.07601 [astro-ph.GA].

Leonard, Douglas C. (Nov. 2011). "On the progenitors of core-collapse supernovae." In: *Ap&SS* 336.1, pp. 117–122. DOI: 10.1007/s10509-010-0530-8. arXiv: 1011.0203 [astro-ph.SR].

Leonard, Douglas C., Shashi M. Kanbur, Choong C. Ngeow, and Nial R. Tanvir (Sept. 2003). "The Cepheid Distance to NGC 1637: A Direct Test of the Expanding Photosphere Method Distance to SN 1999em." In: *ApJ* 594.1, pp. 247–278. DOI: 10.1086/376831. arXiv: astro-ph/0305259 [astro-ph].

Li, Weidong et al. (Apr. 2011). "Nearby supernova rates from the Lick Observatory Supernova Search - II. The observed luminosity functions and fractions of supernovae in a complete sample." In: *Monthly Notices of the RAS* 412.3, pp. 1441–1472. DOI: 10.1111/j.1365-2966.2011.18160.x. arXiv: 1006.4612 [astro-ph.SR].

Li, X. D. and E. P. J. van den Heuvel (June 1997). "Evolution of white dwarf binaries: supersoft X-ray sources and progenitors of type IA supernovae." In: *A&A* 322, pp. L9–L12.

Liao, K. et al. (Feb. 2015a). "Strong Lens Time Delay Challenge. II. Results of TDC1." In: *Astrophysical Journal* 800, 11, p. 11. DOI: 10.1088/0004-637X/800/1/11. arXiv: 1409.1254 [astro-ph.IM].

Liao, Kai et al. (Feb. 2015b). "Strong Lens Time Delay Challenge. II. Results of TDC1." In: *ApJ* 800.1, 11, p. 11. DOI: 10.1088/0004-637X/800/1/11. arXiv: 1409.1254 [astro-ph.IM].

Liske, Jochen (2019). *E-ELT Imaging ETC: Detailed Description*. URL: http://www.eso.org/observing/etc/doc/elt/etc_img_model.pdf (visited on 03/03/2020).

Livio, Mario (1989). "Common envelope evolution of binary stars." In: *International Astronomical Union Colloquium*. Vol. 107. Cambridge University Press, pp. 299–310.

Livio, Mario and Paolo Mazzali (Mar. 2018). "On the progenitors of Type Ia supernovae." In: *Phys. Rep.* 736, pp. 1–23. DOI: 10.1016/j.physrep.2018.02.002. arXiv: 1802.03125 [astro-ph.SR].

Livio, Mario and Adam G. Riess (Aug. 2003). "Have the Elusive Progenitors of Type Ia Supernovae Been Discovered?" In: *The Astrophysical Journal* 594.2, pp. L93–L94. DOI: 10.1086/378765. URL: https://doi.org/10.1086\%2F378765.

Livio, Mario and James W. Truran (Apr. 1992). "Type I Supernovae and Accretion-induced Collapses from Cataclysmic Variables?" In: *ApJ* 389, p. 695. DOI: 10.1086/171242.

Livne, Eli (May 1990). "Successive Detonations in Accreting White Dwarfs as an Alternative Mechanism for Type I Supernovae." In: *ApJ* 354, p. L53. DOI: 10.1086/185721.

Lorén-Aguilar, P., J. Isern, and E. García-Berro (Aug. 2010). "Smoothed particle hydrodynamics simulations of white dwarf collisions and close encounters." In: *MNRAS* 406.4, pp. 2749–2763. DOI: 10.1111/j.1365-2966.2010.16878.x. arXiv: 1004.4783 [astro-ph.SR].

Lotz, J. M. et al. (Mar. 2017). "The Frontier Fields: Survey Design and Initial Results." In: *The Astrophysical Journal* 837.1, p. 97. DOI: 10.3847/1538-4357/837/1/97. URL: https://doi.org/10.3847\%2F1538-4357\%2F837\%2F1\%2F97.

Luri, X., A. G. A. Brown, L. M. Sarro, F. Arenou, C. A. L. Bailer-Jones, A. Castro-Ginard, J. de Bruijne, T. Prusti, C. Babusiaux, and H. E. Delgado (Aug. 2018).

"Gaia Data Release 2. Using Gaia parallaxes." In: *Astronomy and Astrophysics* 616, A9, A9. DOI: 10.1051/0004-6361/201832964. arXiv: 1804.09376 [astro-ph.IM].

MacLeod, Chelsea L. and Craig J. Hogan (Feb. 2008). "Precision of Hubble constant derived using black hole binary absolute distances and statistical redshift information." In: *Phys. Rev. D* 77.4, 043512, p. 043512. DOI: 10.1103/PhysRevD.77.043512. arXiv: 0712.0618 [astro-ph].

Macaulay, E., T. M. Davis, D. Scovacricchi, D. Bacon, T. Collett, and R. C. Nichol (May 2017). "The effects of velocities and lensing on moments of the Hubble diagram." In: *Monthly Notices of the RAS* 467, pp. 259–272. DOI: 10.1093/mnras/stw3339. arXiv: 1607.03966.

Macaulay, E. et al. (June 2019). "First cosmological results using Type Ia supernovae from the Dark Energy Survey: measurement of the Hubble constant." In: *Monthly Notices of the RAS* 486.2, pp. 2184–2196. DOI: 10.1093/mnras/stz978. arXiv: 1811.02376 [astro-ph.CO].

Magee, M. R., K. Maguire, R. Kotak, S. A. Sim, J. H. Gillanders, S. J. Prentice, and K. Skillen (Feb. 2020). "Determining the ^{56}Ni distribution of type Ia supernovae from observations within days of explosion." In: *A&A* 634, A37, A37. DOI: 10.1051/0004-6361/201936684. arXiv: 1912.07603 [astro-ph.HE].

Maguire, Kate (2017). "Type Ia Supernovae." In: *Handbook of Supernovae*. Ed. by Athem W. Alsabti and Paul Murdin. Cham: Springer International Publishing, pp. 293–316. ISBN: 978-3-319-21846-5. DOI: 10.1007/978-3-319-21846-5_36. URL: https://doi.org/10.1007/978-3-319-21846-5_36.

Mannucci, F., M. Della Valle, and N. Panagia (Aug. 2006). "Two populations of progenitors for Type Ia supernovae?" In: *MNRAS* 370.2, pp. 773–783. DOI: 10.1111/j.1365-2966.2006.10501.x. arXiv: astro-ph/0510315 [astro-ph].

Mannucci, F., M. Della Valle, N. Panagia, E. Cappellaro, G. Cresci, R. Maiolino, A. Petrosian, and M. Turatto (Apr. 2005). "The supernova rate per unit mass." In: *A&A* 433.3, pp. 807–814. DOI: 10.1051/0004-6361:20041411. arXiv: astro-ph/0411450 [astro-ph].

Mao, Shude (Aug. 2012). "Astrophysical applications of gravitational microlensing." In: *Research in Astronomy and Astrophysics* 12.8, pp. 947–972. DOI: 10.1088/1674-4527/12/8/005. arXiv: 1207.3720 [astro-ph.GA].

Mao, Shude and Peter Schneider (1998). "Evidence for substructure in lens galaxies?" In: *Monthly Notices of the Royal Astronomical Society* 295.3, pp. 587–594.

Maoz, D. and F. Mannucci (Jan. 2012). "Type-Ia Supernova Rates and the Progenitor Problem: A Review." In: *Publ. Astron. Soc. Australia* 29.4, pp. 447–465. DOI: 10.1071/AS11052. arXiv: 1111.4492 [astro-ph.CO].

Maoz, Dan, Filippo Mannucci, and Timothy D. Brandt (Nov. 2012). "The delay-time distribution of Type Ia supernovae from Sloan II." In: *MNRAS* 426.4, pp. 3282–3294. DOI: 10.1111/j.1365-2966.2012.21871.x. arXiv: 1206.0465 [astro-ph.CO].

Maoz, Dan, Filippo Mannucci, and Gijs Nelemans (Aug. 2014). "Observational Clues to the Progenitors of Type Ia Supernovae." In: *ARA&A* 52, pp. 107–170. DOI: 10.1146/annurev-astro-082812-141031. arXiv: 1312.0628 [astro-ph.CO].

Marietta, E., Adam Burrows, and Bruce Fryxell (June 2000). "Type IA Supernova Explosions in Binary Systems: The Impact on the Secondary Star and Its Consequences." In: *ApJS* 128.2, pp. 615–650. DOI: 10.1086/313392. arXiv: astro-ph/9908116 [astro-ph].

Marion, G. H. et al. (Apr. 2016). "SN 2012cg: Evidence for Interaction Between a Normal Type Ia Supernova and a Non-degenerate Binary Companion." In: *ApJ* 820.2, 92, p. 92. DOI: 10.3847/0004-637X/820/2/92. arXiv: 1507.07261 [astro-ph.SR].

McCray, Richard (Jan. 1993). "Supernova 1987A revisited." In: *ARA&A* 31, pp. 175–216. DOI: 10.1146/annurev.aa.31.090193.001135.

McCray, Richard (2017). "The Physics of Supernova 1987A." In: *Handbook of Supernovae*. Ed. by Athem W. Alsabti and Paul Murdin. Cham: Springer International Publishing, pp. 2181–2210. ISBN: 978-3-319-21846-5. DOI: 10.1007/978-3-319-21846-5_96. URL: https://doi.org/10.1007/978-3-319-21846-5_96.

McCray, Richard and Claes Fransson (Sept. 2016). "The Remnant of Supernova 1987A." In: *ARA&A* 54, pp. 19–52. DOI: 10.1146/annurev-astro-082615-105405.

McQuinn, Kristen. B. W., Martha Boyer, Evan D. Skillman, and Andrew E. Dolphin (July 2019). "Using the Tip of the Red Giant Branch As a Distance Indicator in the Near Infrared." In: *The Astrophysical Journal* 880.1, p. 63. DOI: 10.3847/1538-4357/ab2627. URL: https://doi.org/10.3847\%2F1538-4357\%2Fab2627.

Mennekens, N., D. Vanbeveren, J. P. De Greve, and E. De Donder (June 2010). "The delay-time distribution of Type Ia supernovae: a comparison between theory and

observation." In: *A&A* 515, A89, A89. DOI: 10.1051/0004-6361/201014115. arXiv: 1003.2491 [astro-ph.SR].

Metcalf, R. Benton and Piero Madau (Dec. 2001). "Compound Gravitational Lensing as a Probe of Dark Matter Substructure within Galaxy Halos." In: *ApJ* 563.1, pp. 9–20. DOI: 10.1086/323695. arXiv: astro-ph/0108224 [astro-ph].

Miller, A. A. et al. (Jan. 2018). "Early Observations of the Type Ia Supernova iPTF 16abc: A Case of Interaction with Nearby, Unbound Material and/or Strong Ejecta Mixing." In: *ApJ* 852.2, 100, p. 100. DOI: 10.3847/1538-4357/aaa01f. arXiv: 1708.07124 [astro-ph.HE].

Miller, A. A. et al. (Jan. 2020). "ZTF Early Observations of Type Ia Supernovae II: First Light, the Initial Rise, and Time to Reach Maximum Brightness." In: *arXiv e-prints*, arXiv:2001.00598, arXiv:2001.00598. arXiv: 2001.00598 [astro-ph.HE].

Millon, M. et al. (Dec. 2019). "TDCOSMO. I. An exploration of systematic uncertainties in the inference of H_0 from time-delay cosmography." In: *arXiv e-prints*, arXiv:1912.08027, arXiv:1912.08027. arXiv: 1912.08027 [astro-ph.CO].

Miralda-Escudé, Jordi (June 2003). "The Dark Age of the Universe." In: *Science* 300.5627, pp. 1904–1909. DOI: 10.1126/science.1085325. arXiv: astro-ph/0307396 [astro-ph].

Moll, R. and S. E. Woosley (Sept. 2013). "Multi-dimensional Models for Double Detonation in Sub-Chandrasekhar Mass White Dwarfs." In: *ApJ* 774.2, 137, p. 137. DOI: 10.1088/0004-637X/774/2/137. arXiv: 1303.0324 [astro-ph.HE].

More, A., R. Cabanac, S. More, C. Alard, M. Limousin, J-P. Kneib, R. Gavazzi, and V. Motta (Mar. 2012). "THE CFHTLS-STRONG LENSING LEGACY SURVEY (SL2S): INVESTIGATING THE GROUP-SCALE LENSES WITH THE SARCS SAMPLE." In: *The Astrophysical Journal* 749.1, p. 38. DOI: 10.1088/0004-637x/749/1/38. URL: https://doi.org/10.1088\%2F0004-637x\%2F749\%2F1\%2F38.

More, Anupreeta, Sherry H. Suyu, Masamune Oguri, Surhud More, and Chien-Hsiu Lee (2017). "Interpreting the strongly lensed supernova iPTF16geu: time delay predictions, microlensing, and lensing rates." In: *Astrophys. J.* 835.2, p. L25. DOI: 10.3847/2041-8213/835/2/L25. arXiv: 1611.04866 [astro-ph.CO].

Moriya, Takashi J., Elena I. Sorokina, and Roger A. Chevalier (Mar. 2018). "Superluminous Supernovae." In: *Space Sci. Rev.* 214.2, 59, p. 59. DOI: 10.1007/s11214-018-0493-6. arXiv: 1803.01875 [astro-ph.HE].

Moriya, Takashi J. et al. (Apr. 2019). "First Release of High-Redshift Superluminous Supernovae from the Subaru HIgh-Z SUpernova CAmpaign (SHIZUCA). I. Photometric Properties." In: *ApJS* 241.2, 16, p. 16. DOI: 10.3847/1538-4365/ab07c5. arXiv: 1801.08240 [astro-ph.HE].

Moriya, Takashi, Nozomu Tominaga, Masaomi Tanaka, Keiichi Maeda, and Ken'ichi Nomoto (July 2010). "A Core-collapse Supernova Model for the Extremely Luminous Type Ic Supernova 2007bi: An Alternative to the Pair-instability Supernova Model." In: *ApJ* 717.2, pp. L83–L86. DOI: 10.1088/2041-8205/717/2/L83. arXiv: 1004.2967 [astro-ph.HE].

Morozova, Viktoriya, Anthony L. Piro, Mathieu Renzo, Christian D. Ott, Drew Clausen, Sean M. Couch, Justin Ellis, and Luke F. Roberts (Nov. 2015). "Light Curves of Core-collapse Supernovae with Substantial Mass Loss Using the New Open-source SuperNova Explosion Code (SNEC)." In: *The Astrophysical Journal* 814.1, 63, p. 63. DOI: 10.1088/0004-637X/814/1/63. arXiv: 1505.06746 [astro-ph.HE].

Mortonson, M. J., P. L. Schechter, and J. Wambsganss (Aug. 2005). "Size Is Everything: Universal Features of Quasar Microlensing with Extended Sources." In: *Astrophysical Journal* 628, pp. 594–603. DOI: 10.1086/431195. eprint: astro-ph/0408195.

Mörtsell, E., J. Johansson, S. Dhawan, A. Goobar, R. Amanullah, and D. A. Goldstein (July 2019). "Lens modelling of the strongly lensed Type Ia supernova iPTF16geu." In: *arXiv e-prints*, arXiv:1907.06609, arXiv:1907.06609. arXiv: 1907.06609 [astro-ph.CO].

Myers, S. T. et al. (May 2003). "The Cosmic Lens All-Sky Survey - I. Source selection and observations." In: *MNRAS* 341.1, pp. 1–12. DOI: 10.1046/j.1365-8711.2003.06256.x. arXiv: astro-ph/0211073 [astro-ph].

Negrello, Mattia et al. (Nov. 2010). "The Detection of a Population of Submillimeter-Bright, Strongly Lensed Galaxies." In: *Science* 330.6005, p. 800. DOI: 10.1126/science.1193420. arXiv: 1011.1255 [astro-ph.CO].

Newton, I. (1704). *Opticks, Or a Treatise of the Reflexions, Refractions, Inflexions and Colours of Light: Also Two Treatises of the Species and Magnitude of Curvilinear Figures*. Smith and Walford. URL: https://books.google.co.uk/books?id=mxhfAAAAcAAJ.

Nightingale, J. W., S. Dye, and Richard J. Massey (Aug. 2018). "AutoLens: automated modeling of a strong lens's light, mass, and source." In: *MNRAS* 478.4, pp. 4738–4784. DOI: 10.1093/mnras/sty1264. arXiv: 1708.07377 [astro-ph.CO].

Nissanke, Samaya, Daniel E. Holz, Scott A. Hughes, Neal Dalal, and Jonathan L. Sievers (Dec. 2010). "Exploring Short Gamma-ray Bursts as Gravitational-wave Standard Sirens." In: *ApJ* 725.1, pp. 496–514. DOI: 10.1088/0004-637X/725/1/496. arXiv: 0904.1017 [astro-ph.CO].

Nomoto, K. I., K. Iwamoto, and T. Suzuki (May 1995). "The evolution and explosion of massive binary stars and Type Ib-Ic-IIb-IIL supernovae." In: *Phys. Rep.* 256.1, pp. 173–191. DOI: 10.1016/0370-1573(94)00107-E.

Nomoto, K. (Nov. 1980). "White dwarf models for type I supernovae and quiet supernovae, and presupernova evolution." In: *Space Sci. Rev.* 27.3-4, pp. 563–570. DOI: 10.1007/BF00168350.

Nomoto, K (1982). "Accreting white dwarf models for type 1 supernovae. II-Off-center detonation supernovae." In: *The Astrophysical Journal* 257, pp. 780–792.

Nomoto, K. and Jr. Iben I. (Oct. 1985). "Carbon ignition in a rapidly accreting degenerate dwarf - A clue to the nature of the merging process in close binaries." In: *ApJ* 297, pp. 531–537. DOI: 10.1086/163547.

Nomoto, K. and D. Sugimoto (Jan. 1977). "Rejuvenation of Helium White Dwarfs by Mass Accretion." In: *PASJ* 29, pp. 765–780.

Nomoto, Ken, Kyoji Nariai, and Daiichiro Sugimoto (1979). "Rapid mass accretion onto white dwarfs and formation of an extended envelope." In: *Publications of the Astronomical Society of Japan* 31, pp. 287–298.

Nomoto, Ken'ichi and Yoji Kondo (Jan. 1991). "Conditions for Accretion-induced Collapse of White Dwarfs." In: *ApJ* 367, p. L19. DOI: 10.1086/185922.

Nomoto, Ken'ichi, Hideyuki Saio, Mariko Kato, and Izumi Hachisu (July 2007). "Thermal Stability of White Dwarfs Accreting Hydrogen-rich Matter and Progenitors of Type Ia Supernovae." In: *The Astrophysical Journal* 663.2, pp. 1269–1276. DOI: 10.1086/518465. URL: https://doi.org/10.1086\%2F518465.

Nugent, Peter E. et al. (Dec. 2011). "Supernova SN 2011fe from an exploding carbon-oxygen white dwarf star." In: *Nature* 480.7377, pp. 344–347. DOI: 10.1038/nature10644. arXiv: 1110.6201 [astro-ph.CO].

Nugent, Peter (2007). *Peter Nugent's Spectral Templates*. URL: https://c3.lbl.gov/nugent/nugent_templates.html.

Oguri, M. (Aug. 2010). "The Mass Distribution of SDSS J1004+4112 Revisited." In: *Publications of the ASJ* 62, pp. 1017–1024. DOI: 10.1093/pasj/62.4.1017. arXiv: 1005.3103.

Oguri, M. and Y. Kawano (Feb. 2003). "Gravitational lens time delays for distant supernovae: breaking the degeneracy between radial mass profiles and the Hubble constant." In: *Monthly Notices of the RAS* 338, pp. L25–L29. DOI: 10.1046/j.1365-8711.2003.06290.x. eprint: astro-ph/0211499.

Oguri, M. et al. (May 2012). "The Sloan Digital Sky Survey Quasar Lens Search. VI. Constraints on Dark Energy and the Evolution of Massive Galaxies." In: *Astronomical Journal* 143, 120, p. 120. DOI: 10.1088/0004-6256/143/5/120. arXiv: 1203.1088.

Oguri, Masamune (Nov. 2019). "Strong gravitational lensing of explosive transients." In: *Reports on Progress in Physics* 82.12, p. 126901. DOI: 10.1088/1361-6633/ab4fc5. URL: https://doi.org/10.1088\%2F1361-6633\%2Fab4fc5.

Oguri, Masamune and Philip J. Marshall (July 2010). "Gravitationally lensed quasars and supernovae in future wide-field optical imaging surveys." In: *Monthly Notices of the RAS* 405.4, pp. 2579–2593. DOI: 10.1111/j.1365-2966.2010.16639.x. arXiv: 1001.2037 [astro-ph.CO].

Oguri, Masamune, Yasushi Suto, and Edwin L. Turner (Feb. 2003). "Gravitational Lensing Magnification and Time Delay Statistics for Distant Supernovae." In: *The Astrophysical Journal* 583.2, pp. 584–593. DOI: 10.1086/345431. URL: https://doi.org/10.1086\%2F345431.

Paczynski, B. and A. N. Zytkow (June 1978). "Hydrogen shell flashes in a white dwarf with mass accretion." In: *ApJ* 222, p. 604. DOI: 10.1086/156176.

Pakmor, R., M. Kromer, S. Taubenberger, S. A. Sim, F. K. Röpke, and W. Hillebrandt (Mar. 2012). "Normal Type Ia Supernovae from Violent Mergers of White Dwarf Binaries." In: *ApJ* 747.1, L10, p. L10. DOI: 10.1088/2041-8205/747/1/L10. arXiv: 1201.5123 [astro-ph.HE].

Pakmor, Rüdiger (2017). "Violent Mergers." In: *Handbook of Supernovae*. Ed. by Athem W. Alsabti and Paul Murdin. Cham: Springer International Publishing, pp. 1257–1273. DOI: 10.1007/978-3-319-21846-5_61. URL: https://doi.org/10.1007/978-3-319-21846-5_61.

Pan, Y. C. et al. (Oct. 2017). "DES15E2mlf: a spectroscopically confirmed superluminous supernova that exploded 3.5 Gyr after the big bang." In: *MNRAS* 470.4, pp. 4241–4250. DOI: 10.1093/mnras/stx1467. arXiv: 1707.06649 [astro-ph.GA].

Pastorello, A. et al. (Sept. 2008). "The Type IIb SN 2008ax: spectral and light curve evolution." In: *MNRAS* 389.2, pp. 955–966. DOI: 10.1111/j.1365-2966.2008.13618.x. arXiv: 0805.1914 [astro-ph].

Paxton, Bill, Lars Bildsten, Aaron Dotter, Falk Herwig, Pierre Lesaffre, and Frank Timmes (Jan. 2011). "Modules for Experiments in Stellar Astrophysics (MESA)." In: *ApJS* 192.1, 3, p. 3. DOI: 10.1088/0067-0049/192/1/3. arXiv: 1009.1622 [astro-ph.SR].

Paxton, Bill et al. (Sept. 2013). "Modules for Experiments in Stellar Astrophysics (MESA): Planets, Oscillations, Rotation, and Massive Stars." In: *ApJS* 208.1, 4, p. 4. DOI: 10.1088/0067-0049/208/1/4. arXiv: 1301.0319 [astro-ph.SR].

Perlmutter, S. et al. (June 1999). "Measurements of Ω and Λ from 42 High-Redshift Supernovae." In: *Astrophysical Journal* 517, pp. 565–586. DOI: 10.1086/307221. eprint: astro-ph/9812133.

Pesce, D. W. et al. (Mar. 2020). "The Megamaser Cosmology Project. XIII. Combined Hubble Constant Constraints." In: *ApJ* 891.1, L1, p. L1. DOI: 10.3847/2041-8213/ab75f0. arXiv: 2001.09213 [astro-ph.CO].

Peter, Annika H. G. (Jan. 2012). "Dark Matter: A Brief Review." In: *arXiv e-prints*, arXiv:1201.3942, arXiv:1201.3942. arXiv: 1201.3942 [astro-ph.CO].

Petrillo, C. E. et al. (Apr. 2019). "LinKS: discovering galaxy-scale strong lenses in the Kilo-Degree Survey using convolutional neural networks." In: *MNRAS* 484.3, pp. 3879–3896. DOI: 10.1093/mnras/stz189. arXiv: 1812.03168 [astro-ph.GA].

Philip D. Hall (2016). *File:Common envelope phase - ejection or merger.svg — Wikimedia Commons, the free media repository*. Online; accessed 15-May-2020. Distributed under a CC BY-SA 4.0 license. URL: https://commons.wikimedia.org/w/index.php?title=File:Common_envelope_phase_-_ejection_or_merger.svg&oldid=410491812.

— (2017). *File:Binary star system - semidetached configuration q=3.svg — Wikimedia Commons, the free media repository*. Online; accessed 15-May-2020. Distributed under a CC BY-SA 3.0 license. URL: https://commons.wikimedia.org/w/index.php?

title=File:Binary_star_system_-_semidetached_configuration_q\%3D3.svg&oldid=407381590.

Phillips, M. M. (Aug. 1993). "The absolute magnitudes of Type IA supernovae." In: *Astrophysical Journal, Letters* 413, pp. L105–L108. DOI: 10.1086/186970.

Phillips, M. M., Paulina Lira, Nicholas B. Suntzeff, R. A. Schommer, Mario Hamuy, and José Maza (Oct. 1999). "The Reddening-Free Decline Rate Versus Luminosity Relationship for Type IA Supernovae." In: *AJ* 118.4, pp. 1766–1776. DOI: 10.1086/301032. arXiv: astro-ph/9907052 [astro-ph].

Phillips, M. M., Lisa A. Wells, Nicholas B. Suntzeff, Mario Hamuy, Bruno Leibundgut, Robert P. Kirshner, and Craig B. Foltz (May 1992). "SN 1991T: Further Evidence of the Heterogeneous Nature of Type IA Supernovae." In: *AJ* 103, p. 1632. DOI: 10.1086/116177.

Pian, Elena and Paolo A. Mazzali (2017). "Hydrogen-Poor Core-Collapse Supernovae." In: *Handbook of Supernovae*. Ed. by Athem W. Alsabti and Paul Murdin. Cham: Springer International Publishing, pp. 277–292. ISBN: 978-3-319-21846-5. DOI: 10.1007/978-3-319-21846-5_40. URL: https://doi.org/10.1007/978-3-319-21846-5_40.

Piro, Anthony L., Philip Chang, and Nevin N. Weinberg (Jan. 2010). "Shock Breakout from Type Ia Supernova." In: *ApJ* 708.1, pp. 598–604. DOI: 10.1088/0004-637X/708/1/598. arXiv: 0909.2643 [astro-ph.HE].

Piro, Anthony L. and Viktoriya S. Morozova (July 2016). "Exploring the Potential Diversity of Early Type Ia Supernova Light Curves." In: *ApJ* 826.1, 96, p. 96. DOI: 10.3847/0004-637X/826/1/96. arXiv: 1512.03442 [astro-ph.HE].

Piro, Anthony L. and Ehud Nakar (Mar. 2014). "Constraints on Shallow ^{56}Ni from the Early Light Curves of Type Ia Supernovae." In: *ApJ* 784.1, 85, p. 85. DOI: 10.1088/0004-637X/784/1/85. arXiv: 1211.6438 [astro-ph.HE].

Planck Collaboration et al. (Nov. 2014). "Planck 2013 results. XVI. Cosmological parameters." In: *Astronomy and Astrophysics* 571, A16, A16. DOI: 10.1051/0004-6361/201321591. arXiv: 1303.5076 [astro-ph.CO].

— (Sept. 2016). "Planck 2015 results. XIII. Cosmological parameters." In: *Astronomy and Astrophysics* 594, A13, A13. DOI: 10.1051/0004-6361/201525830. arXiv: 1502.01589.

Planck Collaboration et al. (July 2018). "Planck 2018 results. VI. Cosmological parameters." In: *arXiv e-prints*, arXiv:1807.06209, arXiv:1807.06209. arXiv: 1807.06209 [astro-ph.CO].

Podsiadlowski, Ph., J. J. L. Hsu, P. C. Joss, and R. R. Ross (Aug. 1993). "The progenitor of supernova 1993J: a stripped supergiant in a binary system?" In: *Nature* 364.6437, pp. 509–511. DOI: 10.1038/364509a0.

Podsiadlowski, Ph., P. C. Joss, and J. J. L. Hsu (May 1992). "Presupernova Evolution in Massive Interacting Binaries." In: *ApJ* 391, p. 246. DOI: 10.1086/171341.

Podsiadlowski, Philipp (2017). "The Progenitor of SN 1987A." In: *Handbook of Supernovae*. Ed. by Athem W. Alsabti and Paul Murdin. Cham: Springer International Publishing, pp. 635–648. ISBN: 978-3-319-21846-5. DOI: 10.1007/978-3-319-21846-5_123. URL: https://doi.org/10.1007/978-3-319-21846-5_123.

Prajs, S. et al. (Jan. 2017). "The volumetric rate of superluminous supernovae at z ~ 1." In: *MNRAS* 464.3, pp. 3568–3579. DOI: 10.1093/mnras/stw1942. arXiv: 1605.05250 [astro-ph.HE].

Pskovskii, Yu. P. (Dec. 1984). "Photometric classification and basic parameters of type I supernovae." In: *Soviet Astronomy* 28, pp. 658–664.

Quimby, R. M. et al. (June 2011). "Hydrogen-poor superluminous stellar explosions." In: *Nature* 474.7352, pp. 487–489. DOI: 10.1038/nature10095. arXiv: 0910.0059 [astro-ph.CO].

Quimby, Robert M., Fang Yuan, Carl Akerlof, and J. Craig Wheeler (May 2013a). "Rates of superluminous supernovae at z ~ 0.2." In: *MNRAS* 431.1, pp. 912–922. DOI: 10.1093/mnras/stt213. arXiv: 1302.0911 [astro-ph.CO].

Quimby, Robert M. et al. (May 2013b). "Extraordinary Magnification of the Ordinary Type Ia Supernova PS1-10afx." In: *ApJ* 768.1, L20, p. L20. DOI: 10.1088/2041-8205/768/1/L20. arXiv: 1302.2785 [astro-ph.CO].

Quimby, Robert M. et al. (Apr. 2014). "Detection of the Gravitational Lens Magnifying a Type Ia Supernova." In: *Science* 344.6182, pp. 396–399. DOI: 10.1126/science.1250903. arXiv: 1404.6014 [astro-ph.CO].

Rabinak, Itay and Eli Waxman (Feb. 2011). "The Early UV/Optical Emission from Core-collapse Supernovae." In: *ApJ* 728.1, 63, p. 63. DOI: 10.1088/0004-637X/728/1/63. arXiv: 1002.3414 [astro-ph.HE].

Rakavy, G. and G. Shaviv (June 1967). "Instabilities in Highly Evolved Stellar Models." In: *ApJ* 148, p. 803. DOI: 10.1086/149204.

Rasio, Frederic A. and Mario Livio (Nov. 1996). "On the Formation and Evolution of Common Envelope Systems." In: *ApJ* 471, p. 366. DOI: 10.1086/177975. arXiv: astro-ph/9511054 [astro-ph].

Rasio, Frederic A. and Stuart L. Shapiro (Sept. 1994). "Hydrodynamics of Binary Coalescence. I. Polytropes with Stiff Equations of State." In: *ApJ* 432, p. 242. DOI: 10.1086/174566. arXiv: astro-ph/9401027 [astro-ph].

Raskin, Cody, Daniel Kasen, Rainer Moll, Josiah Schwab, and Stan Woosley (May 2014). "TYPE Ia SUPERNOVAE FROM MERGING WHITE DWARFS. II. POST-MERGER DETONATIONS." In: *The Astrophysical Journal* 788.1, p. 75. DOI: 10.1088/0004-637x/788/1/75. URL: https://doi.org/10.1088\%2F0004-637x\%2F788\%2F1\%2F75.

Raskin, Cody, Evan Scannapieco, Gabriel Rockefeller, Chris Fryer, Steven Diehl, and F. X. Timmes (Oct. 2010). "56Ni PRODUCTION IN DOUBLE-DEGENERATE WHITE DWARF COLLISIONS." In: *The Astrophysical Journal* 724.1, pp. 111–125. DOI: 10.1088/0004-637x/724/1/111. URL: https://doi.org/10.1088\%2F0004-637x\%2F724\%2F1\%2F111.

Refsdal, S. (Jan. 1964). "On the possibility of determining Hubble's parameter and the masses of galaxies from the gravitational lens effect." In: *Monthly Notices of the RAS* 128, p. 307. DOI: 10.1093/mnras/128.4.307.

— (Jan. 1966). "On the possibility of testing cosmological theories from the gravitational lens effect." In: *MNRAS* 132, p. 101. DOI: 10.1093/mnras/132.1.101.

Reid, M. J., D. W. Pesce, and A. G. Riess (Nov. 2019). "An Improved Distance to NGC 4258 and Its Implications for the Hubble Constant." In: *The Astrophysical Journal* 886.2, p. L27. DOI: 10.3847/2041-8213/ab552d. URL: https://doi.org/10.3847\%2F2041-8213\%2Fab552d.

Richardson, Dean, David Branch, Darrin Casebeer, Jennifer Millard, R. C. Thomas, and E. Baron (Feb. 2002). "A Comparative Study of the Absolute Magnitude Distributions of Supernovae." In: *The Astronomical Journal* 123.2, pp. 745–752. DOI: 10.1086/338318. URL: https://doi.org/10.1086\%2F338318.

Richardson, Dean, III Jenkins Robert L., John Wright, and Larry Maddox (May 2014). "Absolute-magnitude Distributions of Supernovae." In: *AJ* 147.5, 118, p. 118. DOI: 10.1088/0004-6256/147/5/118. arXiv: 1403.5755 [astro-ph.SR].

Riess, A. G., W. H. Press, and R. P. Kirshner (Dec. 1996). "A Precise Distance Indicator: Type IA Supernova Multicolor Light-Curve Shapes." In: *The Astrophysical Journal* 473, p. 88. DOI: 10.1086/178129. eprint: astro-ph/9604143.

Riess, Adam G., Stefano Casertano, Wenlong Yuan, Lucas M. Macri, and Dan Scolnic (May 2019). "Large Magellanic Cloud Cepheid Standards Provide a 1% Foundation for the Determination of the Hubble Constant and Stronger Evidence for Physics beyond ΛCDM." In: *Astrophysical Journal* 876.1, 85, p. 85. DOI: 10.3847/1538-4357/ab1422. arXiv: 1903.07603 [astro-ph.CO].

Riess, Adam G., Lucas Macri, Stefano Casertano, Hubert Lampeitl, Henry C. Ferguson, Alexei V. Filippenko, Saurabh W. Jha, Weidong Li, and Ryan Chornock (Apr. 2011). "A 3% Solution: Determination of the Hubble Constant with the Hubble Space Telescope and Wide Field Camera 3." In: *Astrophysical Journal* 730.2, 119, p. 119. DOI: 10.1088/0004-637X/730/2/119. arXiv: 1103.2976 [astro-ph.CO].

Riess, Adam G. et al. (1998). "Observational evidence from supernovae for an accelerating universe and a cosmological constant." In: *Astron. J.* 116, pp. 1009–1038. DOI: 10.1086/300499. arXiv: astro-ph/9805201 [astro-ph].

Riess, Adam G. et al. (July 2016). "A 2.4% Determination of the Local Value of the Hubble Constant." In: *Astrophysical Journal* 826, 56, p. 56. DOI: 10.3847/0004-637X/826/1/56. arXiv: 1604.01424.

Riess, Adam G. et al. (Jan. 2018). "New Parallaxes of Galactic Cepheids from Spatially Scanning the Hubble Space Telescope: Implications for the Hubble Constant." In: *ArXiv e-prints*. arXiv: 1801.01120 [astro-ph.SR].

Rivera, Jesus et al. (July 2019). "The Atacama Cosmology Telescope: CO(J = 3 – 2) Mapping and Lens Modeling of an ACT-selected Dusty Star-forming Galaxy." In: *The Astrophysical Journal* 879.2, p. 95. DOI: 10.3847/1538-4357/ab264b. URL: https://doi.org/10.3847\%2F1538-4357\%2Fab264b.

Rosswog, Stephan, Daniel Kasen, James Guillochon, and Enrico Ramirez-Ruiz (2009). "Collisions of white dwarfs as a new progenitor channel for type Ia supernovae." In: *The Astrophysical Journal Letters* 705.2, p. L128.

Rothchild, Daniel, Christopher Stubbs, and Peter Yoachim (Nov. 2019). "ALTSched: Improved Scheduling for Time-domain Science with LSST." In: *PASP* 131.1005, p. 115002. DOI: 10.1088/1538-3873/ab3300. arXiv: 1903.00531 [astro-ph.IM].

Rowan-Robinson, Michael (1985). "Cosmological distance ladder: distance and time in the universe." In:

Rubin, V. C., Jr. Ford W. K., and N. Thonnard (Nov. 1978). "Extended rotation curves of high-luminosity spiral galaxies. IV. Systematic dynamical properties, Sa -> Sc." In: *ApJ* 225, pp. L107–L111. DOI: 10.1086/182804.

Rubin, Vera C. and Jr. Ford W. Kent (Feb. 1970). "Rotation of the Andromeda Nebula from a Spectroscopic Survey of Emission Regions." In: *ApJ* 159, p. 379. DOI: 10.1086/150317.

Ruiz-Lapuente, P., E. Cappellaro, M. Turatto, C. Gouiffes, I. J. Danziger, M. della Valle, and L. B. Lucy (Mar. 1992). "Modeling the Iron-dominated Spectra of the Type IA Supernova SN 1991T at Premaximum." In: *ApJ* 387, p. L33. DOI: 10.1086/186299.

Rusu, Cristian E., Ciprian T. Berghea, Christopher D. Fassnacht, Anupreeta More, Erica Seman, George J. Nelson, and Geoff C. F. Chen (July 2019a). "A search for gravitationally lensed quasars and quasar pairs in Pan-STARRS1: spectroscopy and sources of shear in the diamond 2M1134-2103." In: *MNRAS* 486.4, pp. 4987–5007. DOI: 10.1093/mnras/stz1142. arXiv: 1803.07175 [astro-ph.GA].

Rusu, Cristian E. et al. (May 2019b). "HoLiCOW XII. Lens mass model of WFI2033-4723 and blind measurement of its time-delay distance and H_0." In: *arXiv e-prints*, arXiv:1905.09338, arXiv:1905.09338. arXiv: 1905.09338 [astro-ph.CO].

Saio, H. and K. Nomoto (Sept. 1985). "Evolution of a merging pair of C + O white dwarfs to form a single neutron star." In: *A&A* 150.1, pp. L21–L23.

Saio, Hideyuki and Ken'ichi Nomoto (June 1998). "Inward Propagation of Nuclear-burning Shells in Merging C-O and He White Dwarfs." In: *ApJ* 500.1, pp. 388–397. DOI: 10.1086/305696. arXiv: astro-ph/9801084 [astro-ph].

— (Nov. 2004). "Off-Center Carbon Ignition in Rapidly Rotating, Accreting Carbon-Oxygen White Dwarfs." In: *ApJ* 615.1, pp. 444–449. DOI: 10.1086/423976. arXiv: astro-ph/0401141 [astro-ph].

Sako, Masao et al. (Sept. 2011). "Photometric Type Ia Supernova Candidates from the Three-year SDSS-II SN Survey Data." In: *Astrophysical Journal* 738.2, 162, p. 162. DOI: 10.1088/0004-637X/738/2/162. arXiv: 1107.5106 [astro-ph.CO].

Sathyaprakash, B. S., B. F. Schutz, and C. Van Den Broeck (Nov. 2010). "Cosmography with the Einstein Telescope." In: *Classical and Quantum Gravity* 27.21, 215006, p. 215006. DOI: 10.1088/0264-9381/27/21/215006. arXiv: 0906.4151 [astro-ph.CO].

Sato, Yushi, Naohito Nakasato, Ataru Tanikawa, Ken'ichi Nomoto, Keiichi Maeda, and Izumi Hachisu (July 2015). "A SYSTEMATIC STUDY OF CARBON–OXYGEN WHITE DWARF MERGERS: MASS COMBINATIONS FOR TYPE Ia SUPERNOVAE." In: *The Astrophysical Journal* 807.1, p. 105. DOI: 10.1088/0004-637x/807/1/105. URL: https://doi.org/10.1088\%2F0004-637x\%2F807\%2F1\%2F105.

Scannapieco, Evan and Lars Bildsten (Aug. 2005). "The Type Ia Supernova Rate." In: *ApJ* 629.2, pp. L85–L88. DOI: 10.1086/452632. arXiv: astro-ph/0507456 [astro-ph].

Schechter, Paul L. and Joachim Wambsganss (Dec. 2002). "Quasar Microlensing at High Magnification and the Role of Dark Matter: Enhanced Fluctuations and Suppressed Saddle Points." In: *The Astrophysical Journal* 580.2, pp. 685–695. DOI: 10.1086/343856. URL: https://doi.org/10.1086\%2F343856.

Schlegel, Eric M. (May 1990). "A new subclass of type II supernovae ?" In: *MNRAS* 244, pp. 269–271.

Schneider, P. and D. Sluse (Apr. 2014). "Source-position transformation: an approximate invariance in strong gravitational lensing." In: *Astronomy and Astrophysics* 564, A103, A103. DOI: 10.1051/0004-6361/201322106. arXiv: 1306.4675.

Schutz, B. F. (Sept. 1986). "Determining the Hubble constant from gravitational wave observations." In: *Nature* 323.6086, pp. 310–311. DOI: 10.1038/323310a0.

Scovacricchi, D., R. C. Nichol, D. Bacon, M. Sullivan, and S. Prajs (Feb. 2016). "Cosmology with superluminous supernovae." In: *MNRAS* 456.2, pp. 1700–1707. DOI: 10.1093/mnras/stv2752. arXiv: 1511.06670 [astro-ph.CO].

Shajib, A. J. et al. (Mar. 2020). "STRIDES: A 3.9 per cent measurement of the Hubble constant from the strong lens system DES J0408-5354." In: *MNRAS*. DOI: 10.1093/mnras/staa828. arXiv: 1910.06306 [astro-ph.CO].

Shapiro, I. I. (Dec. 1964). "Fourth Test of General Relativity." In: *Physical Review Letters* 13, pp. 789–791. DOI: 10.1103/PhysRevLett.13.789.

Shappee, B. J. et al. (Jan. 2019). "Seeing Double: ASASSN-18bt Exhibits a Two-component Rise in the Early-time K2 Light Curve." In: *Astrophysical Journal* 870.1, 13, p. 13. DOI: 10.3847/1538-4357/aaec79. arXiv: 1807.11526 [astro-ph.HE].

Shen, Ken J. and Lars Bildsten (May 2007). "Thermally Stable Nuclear Burning on Accreting White Dwarfs." In: *The Astrophysical Journal* 660.2, pp. 1444–1450. DOI: 10.1086/513457. URL: https://doi.org/10.1086\%2F513457.

Shen, Ken J., Lars Bildsten, Daniel Kasen, and Eliot Quataert (Mar. 2012). "The Long-term Evolution of Double White Dwarf Mergers." In: *ApJ* 748.1, 35, p. 35. DOI: 10.1088/0004-637X/748/1/35. arXiv: 1108.4036 [astro-ph.HE].

Shu, Yiping et al. (June 2016). "THE BOSS EMISSION-LINE LENS SURVEY. III. STRONG LENSING OF LyαEMITTERS BY INDIVIDUAL GALAXIES." In: *The Astrophysical Journal* 824.2, p. 86. DOI: 10.3847/0004-637x/824/2/86. URL: https://doi.org/10.3847\%2F0004-637x\%2F824\%2F2\%2F86.

Sim, S. A., F. K. Röpke, W. Hillebrandt, M. Kromer, R. Pakmor, M. Fink, A. J. Ruiter, and I. R. Seitenzahl (Apr. 2010). "DETONATIONS IN SUB-CHANDRASEKHAR-MASS C+O WHITE DWARFS." In: *The Astrophysical Journal* 714.1, pp. L52–L57. DOI: 10.1088/2041-8205/714/1/l52. URL: https://doi.org/10.1088\%2F2041-8205\%2F714\%2F1\%2Fl52.

Slipher, V. M. (Jan. 1913). "The radial velocity of the Andromeda Nebula." In: *Lowell Observatory Bulletin* 1, pp. 56–57.

— (Jan. 1915). "Spectrographic Observations of Nebulae." In: *Popular Astronomy* 23, pp. 21–24.

— (Aug. 1917). "Radial velocity observations of spiral nebulae." In: *The Observatory* 40, pp. 304–306.

Smartt, Stephen J. (Sept. 2009). "Progenitors of Core-Collapse Supernovae." In: *ARA&A* 47.1, pp. 63–106. DOI: 10.1146/annurev-astro-082708-101737. arXiv: 0908.0700 [astro-ph.SR].

Smith, M. et al. (Feb. 2018). "Studying the Ultraviolet Spectrum of the First Spectroscopically Confirmed Supernova at Redshift Two." In: *ApJ* 854.1, 37, p. 37. DOI: 10.3847/1538-4357/aaa126. arXiv: 1712.04535 [astro-ph.HE].

Soldner, J (1804). "On the deflection of a light ray from its rectilinear motion, by the attraction of a celestial body at which it nearly passes by." In: *Berliner Astronomisches Jahrbuch*, pp. 161–172.

Sonnenfeld, Alessandro et al. (Jan. 2018). "Survey of Gravitationally-lensed Objects in HSC Imaging (SuGOHI). I. Automatic search for galaxy-scale strong lenses." In: *PASJ* 70, S29, S29. DOI: 10.1093/pasj/psx062. arXiv: 1704.01585 [astro-ph.GA].

Starrfield, Sumner, J. W. Truran, Warren M. Sparks, and G. S. Kutter (Aug. 1972). "CNO Abundances and Hydrodynamic Models of the Nova Outburst." In: *ApJ* 176, p. 169. DOI: 10.1086/151619.

Stephenson, F. Richard (2017). "Historical Records of Supernovae." In: *Handbook of Supernovae*. Ed. by Athem W. Alsabti and Paul Murdin. Cham: Springer International Publishing, pp. 49–62. ISBN: 978-3-319-21846-5. DOI: 10.1007/978-3-319-21846-5_44. URL: https://doi.org/10.1007/978-3-319-21846-5_44.

Stephenson, F Richard and David A Green (2002). "Historical supernovae and their remnants." In: *Europe* 2, p. 1.

Stritzinger, Maximilian D. et al. (Nov. 2011). "The Carnegie Supernova Project: Second Photometry Data Release of Low-redshift Type Ia Supernovae." In: *AJ* 142.5, 156, p. 156. DOI: 10.1088/0004-6256/142/5/156. arXiv: 1108.3108 [astro-ph.CO].

Strolger, Louis-Gregory, Steven A. Rodney, Camilla Pacifici, Gautham Narayan, and Or Graur (Feb. 2020). "Delay Time Distributions of Type Ia Supernovae from Galaxy and Cosmic Star Formation Histories." In: *ApJ* 890.2, 140, p. 140. DOI: 10.3847/1538-4357/ab6a97.

Sullivan, M. et al. (Sept. 2006). "Rates and Properties of Type Ia Supernovae as a Function of Mass and Star Formation in Their Host Galaxies." In: *ApJ* 648.2, pp. 868–883. DOI: 10.1086/506137. arXiv: astro-ph/0605455 [astro-ph].

Suwa, Yudai (Feb. 2018). "Supernova forecast with strong lensing." In: *MNRAS* 474.2, pp. 2612–2616. DOI: 10.1093/mnras/stx2953. arXiv: 1711.00183 [astro-ph.HE].

Suyu, S. H., P. J. Marshall, M. W. Auger, S. Hilbert, R. D. Blandford, L. V. E. Koopmans, C. D. Fassnacht, and T. Treu (Mar. 2010). "Dissecting the Gravitational lens B1608+656. II. Precision Measurements of the Hubble Constant, Spatial Curvature, and the Dark Energy Equation of State." In: *Astrophysical Journal* 711.1, pp. 201–221. DOI: 10.1088/0004-637X/711/1/201. arXiv: 0910.2773 [astro-ph.CO].

Suyu, S. H. et al. (May 2012). "Disentangling Baryons and Dark Matter in the Spiral Gravitational Lens B1933+503." In: *The Astrophysical Journal* 750, 10, p. 10. DOI: 10.1088/0004-637X/750/1/10. arXiv: 1110.2536.

Suyu, S. H. et al. (Apr. 2013). "Two Accurate Time-delay Distances from Strong Lensing: Implications for Cosmology." In: *Astrophysical Journal* 766, 70, p. 70. DOI: 10.1088/0004-637X/766/2/70. arXiv: 1208.6010.

Suyu, S. H. et al. (June 2014). "Cosmology from Gravitational Lens Time Delays and Planck Data." In: *Astrophysical Journal, Letters* 788.2, L35, p. L35. DOI: 10.1088/2041-8205/788/2/L35. arXiv: 1306.4732 [astro-ph.CO].

Suyu, S. H. et al. (Feb. 2020). "HOLISMOKES – I. Highly Optimised Lensing Investigations of Supernovae, Microlensing Objects, and Kinematics of Ellipticals and Spirals." In: *arXiv e-prints*, arXiv:2002.08378, arXiv:2002.08378. arXiv: 2002.08378 [astro-ph.CO].

Taam, R. E. (Apr. 1980). "Helium runaways in white dwarfs." In: *ApJ* 237, pp. 142–147. DOI: 10.1086/157852.

Taam, Ronald E. and Eric L. Sandquist (Jan. 2000). "Common Envelope Evolution of Massive Binary Stars." In: *ARA&A* 38, pp. 113–141. DOI: 10.1146/annurev.astro.38.1.113.

Takáts, K. et al. (July 2015). "SN 2009ib: a Type II-P supernova with an unusually long plateau." In: *MNRAS* 450.3, pp. 3137–3154. DOI: 10.1093/mnras/stv857. arXiv: 1504.02404 [astro-ph.SR].

Taubenberger, S. et al. (May 2011). "The He-rich stripped-envelope core-collapse supernova 2008ax." In: *MNRAS* 413.3, pp. 2140–2156. DOI: 10.1111/j.1365-2966.2011.18287.x. arXiv: 1101.1824 [astro-ph.SR].

Taubenberger, Stefan (2017). "The Extremes of Thermonuclear Supernovae." In: *Handbook of Supernovae*. Ed. by Athem W. Alsabti and Paul Murdin. Cham: Springer International Publishing, pp. 317–373. ISBN: 978-3-319-21846-5. DOI: 10.1007/978-3-319-21846-5_37. URL: https://doi.org/10.1007/978-3-319-21846-5_37.

Tewes, M. et al. (Aug. 2013a). "COSMOGRAIL: the COSmological MOnitoring of GRAvItational Lenses. XIII. Time delays and 9-yr optical monitoring of the lensed quasar RX J1131-1231." In: *Astronomy and Astrophysics* 556, A22, A22. DOI: 10.1051/0004-6361/201220352. arXiv: 1208.6009.

— (Aug. 2013b). "COSMOGRAIL: the COSmological MOnitoring of GRAvItational Lenses. XIII. Time delays and 9-yr optical monitoring of the lensed quasar RX J1131-1231." In: *A&A* 556, A22, A22. DOI: 10.1051/0004-6361/201220352. arXiv: 1208.6009 [astro-ph.CO].

The LIGO Scientific Collaboration et al. (Aug. 2019). "A gravitational-wave measurement of the Hubble constant following the second observing run of Advanced

LIGO and Virgo." In: *arXiv e-prints*, arXiv:1908.06060, arXiv:1908.06060. arXiv: 1908.06060 [astro-ph.CO].

Thomas, B. C., E. E. Engler, M. Kachelrieß, A. L. Melott, A. C. Overholt, and D. V. Semikoz (July 2016). "TERRESTRIAL EFFECTS OF NEARBY SUPERNOVAE IN THE EARLY PLEISTOCENE." In: *The Astrophysical Journal* 826.1, p. L3. DOI: 10.3847/2041-8205/826/1/l3. URL: https://doi.org/10.3847\%2F2041-8205\%2F826\%2F1\%2Fl3.

Thompson, A. C., C. J. Fluke, D. G. Barnes, and B. R. Barsdell (Jan. 2010). "Teraflop per second gravitational lensing ray-shooting using graphics processing units." In: *New Astronomy* 15, pp. 16–23. DOI: 10.1016/j.newast.2009.05.010. arXiv: 0905.2453 [astro-ph.IM].

Thompson, A. C., G. Vernardos, C. J. Fluke, and B. R. Barsdell (Mar. 2014). *GPU-D: Generating cosmological microlensing magnification maps*. Astrophysics Source Code Library. ascl: 1403.001.

Thompson, Todd A. (Oct. 2011). "ACCELERATING COMPACT OBJECT MERGERS IN TRIPLE SYSTEMS WITH THE KOZAI RESONANCE: A MECHANISM FOR "PROMPT" TYPE Ia SUPERNOVAE, GAMMA-RAY BURSTS, AND OTHER EXOTICA." In: *The Astrophysical Journal* 741.2, p. 82. DOI: 10.1088/0004-637x/741/2/82. URL: https://doi.org/10.1088\%2F0004-637x\%2F741\%2F2\%2F82.

Tisserand, P. et al. (July 2007). "Limits on the Macho content of the Galactic Halo from the EROS-2 Survey of the Magellanic Clouds." In: *A&A* 469.2, pp. 387–404. DOI: 10.1051/0004-6361:20066017. arXiv: astro-ph/0607207 [astro-ph].

Treu, T. (Sept. 2010). "Strong Lensing by Galaxies." In: *Annual Review of Astronomy and Astrophysics* 48, pp. 87–125. DOI: 10.1146/annurev-astro-081309-130924. arXiv: 1003.5567.

Treu, T. et al. (Jan. 2016). ""Refsdal" Meets Popper: Comparing Predictions of the Re-appearance of the Multiply Imaged Supernova Behind MACSJ1149.5+2223." In: *Astrophysical Journal* 817.1, 60, p. 60. DOI: 10.3847/0004-637X/817/1/60. arXiv: 1510.05750 [astro-ph.CO].

Treu, T. et al. (Nov. 2018). "The STRong lensing Insights into the Dark Energy Survey (STRIDES) 2016 follow-up campaign - I. Overview and classification of candidates selected by two techniques." In: *MNRAS* 481.1, pp. 1041–1054. DOI: 10.1093/mnras/sty2329. arXiv: 1808.04838 [astro-ph.CO].

Treu, Tommaso and Léon V. E. Koopmans (Aug. 2004). "Massive Dark Matter Halos and Evolution of Early-Type Galaxies to z ~1." In: *ApJ* 611.2, pp. 739–760. DOI: 10.1086/422245. arXiv: astro-ph/0401373 [astro-ph].

Treu, Tommaso and Philip J. Marshall (July 2016). "Time delay cosmography." In: *The Astronomy and Astrophysics Review* 24.1, p. 11. ISSN: 1432-0754. DOI: 10.1007/s00159-016-0096-8. URL: https://doi.org/10.1007/s00159-016-0096-8.

Troja, E. et al. (Oct. 2018). "A luminous blue kilonova and an off-axis jet from a compact binary merger at z = 0.1341." In: *Nature Communications* 9, 4089, p. 4089. DOI: 10.1038/s41467-018-06558-7. arXiv: 1806.10624 [astro-ph.HE].

Tsujikawa, Shinji (Apr. 2003). "Introductory review of cosmic inflation." In: *arXiv e-prints*, hep-ph/0304257, hep–ph/0304257. arXiv: hep-ph/0304257 [hep-ph].

Turatto, M., S. Benetti, E. Cappellaro, I. J. Danziger, M. Della Valle, C. Gouiffes, P. A. Mazzali, and F. Patat (Nov. 1996). "The properties of the peculiar type Ia supernova 1991bg. I. Analysis and discussion of two years of observations." In: *MNRAS* 283.1, pp. 1–17. DOI: 10.1093/mnras/283.1.1. arXiv: astro-ph/9605178 [astro-ph].

Udalski, A. et al. (Feb. 2015). "Spitzer as a Microlens Parallax Satellite: Mass Measurement for the OGLE-2014-BLG-0124L Planet and its Host Star." In: *ApJ* 799.2, 237, p. 237. DOI: 10.1088/0004-637X/799/2/237. arXiv: 1410.4219 [astro-ph.EP].

Ureña, Carlos and Iliyan Georgiev (July 2018). "Stratified Sampling of Projected Spherical Caps." In: *Computer Graphics Forum* 37, pp. 13–20. DOI: 10.1111/cgf.13471.

Vega-Ferrero, J., J. M. Diego, V. Miranda, and G. M. Bernstein (Feb. 2018). "The Hubble Constant from SN Refsdal." In: *ApJ* 853.2, L31, p. L31. DOI: 10.3847/2041-8213/aaa95f. arXiv: 1712.05800 [astro-ph.CO].

Vegetti, S., L. V. E. Koopmans, A. Bolton, T. Treu, and R. Gavazzi (Nov. 2010). "Detection of a dark substructure through gravitational imaging." In: *Monthly Notices of the RAS* 408, pp. 1969–1981. DOI: 10.1111/j.1365-2966.2010.16865.x. arXiv: 0910.0760.

Verde, Licia, Tommaso Treu, and Adam G. Riess (Sept. 2019). "Tensions between the early and late Universe." In: *Nature Astronomy* 3, pp. 891–895. DOI: 10.1038/s41550-019-0902-0. arXiv: 1907.10625 [astro-ph.CO].

Vernardos, G. and C. J. Fluke (Oct. 2014). "Adventures in the microlensing cloud: Large datasets, eResearch tools, and GPUs." In: *Astronomy and Computing* 6, pp. 1–18. DOI: 10.1016/j.ascom.2014.05.002. arXiv: 1406.0559 [astro-ph.IM].

Vernardos, G., C. J. Fluke, N. F. Bate, and D. Croton (Mar. 2014). "GERLUMPH Data Release 1: High-resolution Cosmological Microlensing Magnification Maps and eResearch Tools." In: *Astrophysical Journal, Supplement* 211, 16, p. 16. DOI: 10.1088/0067-0049/211/1/16. arXiv: 1401.7711 [astro-ph.CO].

Vernardos, G., C. J. Fluke, N. F. Bate, D. Croton, and D. Vohl (Apr. 2015). "GERLUMPH Data Release 2: 2.5 Billion Simulated Microlensing Light Curves." In: *ApJS* 217.2, 23, p. 23. DOI: 10.1088/0067-0049/217/2/23. arXiv: 1503.00770 [astro-ph.IM].

Vink, Jacco (2017). "Supernova 1604, Kepler's Supernova, and its Remnant." In: *Handbook of Supernovae*. Ed. by Athem W. Alsabti and Paul Murdin. Cham: Springer International Publishing, pp. 139–160. ISBN: 978-3-319-21846-5. DOI: 10.1007/978-3-319-21846-5_49. URL: https://doi.org/10.1007/978-3-319-21846-5_49.

Vink, Jacco, Johan Bleeker, Kurt van der Heyden, Andrei Bykov, Aya Bamba, and Ryo Yamazaki (Sept. 2006). "The X-Ray Synchrotron Emission of RCW 86 and the Implications for Its Age." In: *ApJ* 648.1, pp. L33–L37. DOI: 10.1086/507628. arXiv: astro-ph/0607307 [astro-ph].

Vuissoz, C. et al. (Sept. 2008). "COSMOGRAIL: the COSmological MOnitoring of GRAvItational Lenses. VII. Time delays and the Hubble constant from WFI J2033-4723." In: *Astronomy and Astrophysics* 488, pp. 481–490. DOI: 10.1051/0004-6361:200809866. arXiv: 0803.4015.

Walsh, D., R. F. Carswell, and R. J. Weymann (May 1979). "0957+561 A, B: twin quasistellar objects or gravitational lens?" In: *Nature* 279, pp. 381–384. DOI: 10.1038/279381a0.

Wambsganss, J. (2006). "Gravitational Microlensing." In: *Gravitational Lensing: Strong, Weak and Micro*. Berlin, Heidelberg: Springer Berlin Heidelberg, pp. 453–540. ISBN: 978-3-540-30310-7. DOI: 10.1007/978-3-540-30310-7_4. URL: https://doi.org/10.1007/978-3-540-30310-7_4.

Wang, Bo and Zhanwen Han (June 2012). "Progenitors of type Ia supernovae." In: *New Astron. Rev.* 56.4, pp. 122–141. DOI: 10.1016/j.newar.2012.04.001. arXiv: 1204.1155 [astro-ph.SR].

Wardlow, Julie L. et al. (Dec. 2012). "HerMES: CANDIDATE GRAVITATIONALLY LENSED GALAXIES AND LENSING STATISTICS AT SUBMILLIMETER WAVELENGTHS." In: *The Astrophysical Journal* 762.1, p. 59. DOI: 10.1088/0004-637x/762/1/59. URL: https://doi.org/10.1088\%2F0004-637x\%2F762\%2F1\%2F59.

Waxman, Eli and Boaz Katz (2017). "Shock Breakout Theory." In: *Handbook of Supernovae*. Ed. by Athem W. Alsabti and Paul Murdin. Cham: Springer International Publishing, pp. 967–1015. ISBN: 978-3-319-21846-5. DOI: 10.1007/978-3-319-21846-5_33. URL: https://doi.org/10.1007/978-3-319-21846-5_33.

Way, M. J. (2013). "Dismantling Hubble's Legacy?" In: *Origins of the Expanding Universe: 1912-1932. Proceedings of a conference held 13-15 September, 2012, at Flagstaff, Arizona, USA. ASP Conference Proceedings, Vol. 471. San Francisco: Astronomical Society of the Pacific, 2013., p.97*. Ed. by M. J. Way and D. Hunter. Vol. 471. Astronomical Society of the Pacific Conference Series, p. 97.

Webbink, R. F. (Feb. 1984). "Double white dwarfs as progenitors of R Coronae Borealis stars and Type I supernovae." In: *Astrophysical Journal* 277, pp. 355–360. DOI: 10.1086/161701.

Wei, Jun-Jie, Xue-Feng Wu, and Fulvio Melia (May 2015). "Testing Cosmological Models with Type Ic Super Luminous Supernovae." In: *AJ* 149.5, 165, p. 165. DOI: 10.1088/0004-6256/149/5/165. arXiv: 1503.06378 [astro-ph.CO].

Wen, Xudong and Kai Liao (Feb. 2020). "Calibrating the standard candles with strong lensing." In: *European Physical Journal C* 80.2, 94, p. 94. DOI: 10.1140/epjc/s10052-020-7677-4. arXiv: 1907.02693 [astro-ph.CO].

Whelan, J. and I. Iben Jr. (Dec. 1973). "Binaries and Supernovae of Type I." In: *Astrophysical Journal* 186, pp. 1007–1014. DOI: 10.1086/152565.

Williams, Liliya L. R. and Jori Liesenborgs (Feb. 2019). "The role of multiple images and model priors in measuring H_0 from supernova Refsdal in galaxy cluster MACS J1149.5+2223." In: *MNRAS* 482.4, pp. 5666–5677. DOI: 10.1093/mnras/sty3113. arXiv: 1806.11113 [astro-ph.CO].

Wolf, William M., Lars Bildsten, Jared Brooks, and Bill Paxton (Oct. 2013). "HYDROGEN BURNING ON ACCRETING WHITE DWARFS: STABILITY, RECURRENT NOVAE, AND THE POST-NOVA SUPERSOFT PHASE." In: *The Astrophysical Journal* 777.2, p. 136. DOI: 10.1088/0004-637x/777/2/136. URL: https://doi.org/10.1088\%2F0004-637x\%2F777\%2F2\%2F136.

Wong, Kenneth C. et al. (Mar. 2017). "HoLiCOW - IV. Lens mass model of HE 0435-1223 and blind measurement of its time-delay distance for cosmology." In: *Monthly Notices of the RAS* 465.4, pp. 4895–4913. DOI: 10.1093/mnras/stw3077. arXiv: 1607.01403 [astro-ph.CO].

Wong, Kenneth C. et al. (Nov. 2018). "Survey of Gravitationally Lensed Objects in HSC Imaging (SuGOHI). II. Environments and Line-of-Sight Structure of Strong Gravitational Lens Galaxies to z ∼ 0.8." In: *The Astrophysical Journal* 867.2, p. 107. DOI: 10.3847/1538-4357/aae381. URL: https://doi.org/10.3847\%2F1538-4357\%2Faae381.

Wong, Kenneth C. et al. (July 2019). "HoLiCOW XIII. A 2.4% measurement of H_0 from lensed quasars: 5.3σ tension between early and late-Universe probes." In: *arXiv e-prints*, arXiv:1907.04869, arXiv:1907.04869. arXiv: 1907.04869 [astro-ph.CO].

Woosley, S. E., R. E. Taam, and T. A. Weaver (Feb. 1986). "Models for Type I Supernova. I. Detonations in White Dwarfs." In: *ApJ* 301, p. 601. DOI: 10.1086/163926.

Woosley, S. E. and Thomas A. Weaver (Mar. 1994). "Sub–Chandrasekhar Mass Models for Type IA Supernovae." In: *ApJ* 423, p. 371. DOI: 10.1086/173813.

Wyrzykowski, Ł, S Kozłowski, J Skowron, A Udalski, MK Szymański, M Kubiak, G Pietrzyński, I Soszyński, O Szewczyk, K Ulaczyk, et al. (2011a). "The OGLE view of microlensing towards the Magellanic Clouds–III. Ruling out subsolar MACHOs with the OGLE-III LMC data." In: *Monthly Notices of the Royal Astronomical Society* 413.1, pp. 493–508.

Wyrzykowski, L, J Skowron, S Kozłowski, A Udalski, MK Szymański, M Kubiak, G Pietrzyński, Igor Soszyński, O Szewczyk, K Ulaczyk, et al. (2011b). "The OGLE view of microlensing towards the Magellanic Clouds–IV. OGLE-III SMC data and final conclusions on MACHOs." In: *Monthly Notices of the Royal Astronomical Society* 416.4, pp. 2949–2961.

Yahalomi, D. A., P. L. Schechter, and J. Wambsganss (Nov. 2017). "A Quadruply Lensed SN Ia: Gaining a Time-Delay...Losing a Standard Candle." In: *ArXiv e-prints*. arXiv: 1711.07919.

Yao, Yuhan et al. (Dec. 2019). "ZTF Early Observations of Type Ia Supernovae. I. Properties of the 2018 Sample." In: *ApJ* 886.2, 152, p. 152. DOI: 10.3847/1538-4357/ab4cf5. arXiv: 1910.02967 [astro-ph.HE].

Yaron, O., D. Prialnik, M. M. Shara, and A. Kovetz (Apr. 2005). "An Extended Grid of Nova Models. II. The Parameter Space of Nova Outbursts." In: *The Astrophysical Journal* 623.1, pp. 398–410. DOI: 10.1086/428435. URL: https://doi.org/10.1086\%2F428435.

Yoon, S. C. and N. Langer (June 2005). "On the evolution of rapidly rotating massive white dwarfs towards supernovae or collapses." In: *A&A* 435.3, pp. 967–985. DOI: 10.1051/0004-6361:20042542. arXiv: astro-ph/0502133 [astro-ph].

Yoon, S. C., Ph. Podsiadlowski, and S. Rosswog (Sept. 2007). "Remnant evolution after a carbon-oxygen white dwarf merger." In: *MNRAS* 380.3, pp. 933–948. DOI: 10.1111/j.1365-2966.2007.12161.x. arXiv: 0704.0297 [astro-ph].

Yuan, Wenlong, Adam G. Riess, Lucas M. Macri, Stefano Casertano, and Daniel M. Scolnic (Nov. 2019). "Consistent Calibration of the Tip of the Red Giant Branch in the Large Magellanic Cloud on the Hubble Space Telescope Photometric System and a Redetermination of the Hubble Constant." In: *ApJ* 886.1, 61, p. 61. DOI: 10.3847/1538-4357/ab4bc9. arXiv: 1908.00993 [astro-ph.GA].

Yungelson, L. and M. Livio (Apr. 1998). "Type IA Supernovae: an Examination of Potential Progenitors and the Redshift Distribution." In: *ApJ* 497.1, pp. 168–177. DOI: 10.1086/305455. arXiv: astro-ph/9711201 [astro-ph].

Zampieri, Luca (2017). "Light Curves of Type II Supernovae." In: *Handbook of Supernovae*. Ed. by Athem W. Alsabti and Paul Murdin. Cham: Springer International Publishing, pp. 737–768. DOI: 10.1007/978-3-319-21846-5_26. URL: https://doi.org/10.1007/978-3-319-21846-5_26.

Zhang, Bonnie R., Michael J. Childress, Tamara M. Davis, Natallia V. Karpenka, Chris Lidman, Brian P. Schmidt, and Mathew Smith (Oct. 2017). "A blinded determination of H_0 from low-redshift Type Ia supernovae, calibrated by Cepheid variables." In: *MNRAS* 471.2, pp. 2254–2285. DOI: 10.1093/mnras/stx1600. arXiv: 1706.07573 [astro-ph.CO].

Zhao, Fu-Yuan, R. G Strom, and Shi-Yang Jiang (Oct. 2006). "The Guest Star of AD185 must have been a Supernova." In: *Chinese Journal of Astronomy and Astrophysics* 6.5, pp. 635–640. DOI: 10.1088/1009-9271/6/5/17. URL: https://doi.org/10.1088\%2F1009-9271\%2F6\%2F5\%2F17.

Zwicky, F. (Feb. 1937a). "Nebulae as Gravitational Lenses." In: *Physical Review* 51, pp. 290–290. DOI: 10.1103/PhysRev.51.290.

Zwicky, F. (Apr. 1937b). "On the Probability of Detecting Nebulae Which Act as Gravitational Lenses." In: *Physical Review* 51.8, pp. 679–679. DOI: 10.1103/PhysRev.51.679.

de Sitter, W. (Nov. 1917). "Einstein's theory of gravitation and its astronomical consequences. Third paper." In: *Monthly Notices of the RAS* 78, pp. 3–28. DOI: 10.1093/mnras/78.1.3.

DECLARATION

Whilst registered as a candidate for the above degree, I have not been registered for any other research award. Unless indicated, the results and conclusions embodied in this thesis are the work of the named candidate and have not been submitted for any other academic award.

Portsmouth, December 2020

Max Foxley-Marrable

Word Count: 26035

COLOPHON

This document was typeset using the typographical look-and-feel `classicthesis` developed by André Miede. The style was inspired by Robert Bringhurst's seminal book on typography "*The Elements of Typographic Style*". `classicthesis` is available for both LaTeX and LyX:

https://bitbucket.org/amiede/classicthesis/

Happy users of `classicthesis` usually send a real postcard to the author, a collection of postcards received so far is featured here:

http://postcards.miede.de/